

NASA-CR-193077

21 AM  
N47 CR  
164754  
P. 276

FINAL REPORT

AN EVALUATION OF SATELLITE-DERIVED HUMIDITY  
AND ITS RELATIONSHIP TO CONVECTIVE DEVELOPMENT

NASA Grant NAG8-653

FSU ID 1338-580-26

December 1987-December 1992

Florida State University  
Henry E. Fuelberg  
Principal Investigator

Submitted May 1993

(NASA-CR-193077) AN EVALUATION OF  
SATELLITE-DERIVED HUMIDITY AND ITS  
RELATIONSHIP TO CONVECTIVE  
DEVELOPMENT Final Report, Dec. 1987  
- Dec. 1992 (Florida State Univ.)  
276 p

N93-27262

Unclass

G3/47 0164784

The objectives of this research were to

- 1) Specify mesoscale water vapor content as functions of space and time,
- 2) Evaluate satellite-derived vapor content against ground-based measurements, and
- 3) Investigate relations between fine scale water vapor fields and the presence or absence of convective development.

Initial research focussed on the VISSR Atmospheric Sounder (VAS) that is housed on the recent series of GOES satellites. Later research utilized data from the Multispectral Atmospheric Mapping Sensor (MAMS) and the High-resolution Interferometer Sounder (HIS) to investigate the same three objectives.

No patents or inventions were produced as part of this grant.

Five graduate students were supported by the research grant and supervised by Prof. Fuelberg. Each student wrote a thesis describing his portion of the overall research. Three of these theses already have been published as journal manuscripts. All publications resulting from the grant are itemized in the enclosed Table. Two of the theses were completed only recently and have not yet been submitted as journal manuscripts. That will be done during the upcoming year. The accompanying Appendix volume contains copies of the three journal manuscripts and two theses. These five reports give details of our research methodology, findings, and conclusions. Brief summaries are given below.

The Fuelberg and Olson (1991) research evaluated VAS satellite-derived temperature and humidity soundings and higher order parameters against those from conventional ground truth radiosonde data (RAOBs). VAS temperatures were found to agree closely with radiosonde values; however, VAS dewpoints showed somewhat less agreement. VAS discrepancies usually were not well correlated with first-guess errors. A disappointing finding was that the retrievals degraded the first guess about as often as they improved it. VAS did tend to improve large first-guess errors, but not even that was guaranteed. Horizontal gradients of VAS products generally were stronger than those from radiosondes. VAS precipitable water agreed better with the ground truth than did dewpoints at individual levels, but VAS thicknesses were not much improved over the already accurate VAS temperatures. Several sounding-derived parameters used in severe storms forecasting also were evaluated. Results indicated that VAS/RAOB discrepancies increased with the amount of manipulation required during computation. VAS parameters incorporating observed surface data tended to give better results than those that did not. Of all the parameters examined, VAS-derived lifted index exhibited the best agreement with RAOB versions. VAS positive buoyant energy showed disappointingly poor comparisons. VAS retrievals provided poor measures of the low-level negative buoyant energy that must be overcome before convection can begin. Agreements between VAS/RAOB versions of the K index, totals index, Showalter index, and several other parameters were intermediate to those of positive buoyant energy and lifted index.

The Fuelberg, Schudalla, and Guillory (1991) journal article describes the results of a case

study in which VAS imagery and derived soundings were used to investigate a period of sudden mesoscale drying at the surface (17 June 1986), a day during the Cooperative Huntsville Meteorological Experiment (COHMEX). Dewpoints fell as much as  $-6.3^{\circ}\text{C}$  in less than 1 h over a small portion of central Tennessee. The drying occurred prior to the onset of convective activity. The satellite retrievals detected a narrow tongue of middle tropospheric dry air that overlay moist air near the surface. The analyses indicated that heating induced surface-based mixing penetrated the middle levels, bringing drier air to the surface and resulting in the sudden decreases in surface dewpoints. The results demonstrated that VAS imagery and derived soundings were an important source of upper-air information. In spite of retrieval limitations (e.g., poor vertical resolution, unresolved cloud contamination, instrument noise, etc.), the satellite data provided mesoscale details about the middle tropospheric dry tongue that were unavailable from other sources.

The Bradshaw and Fuelberg (1993) research utilized data from the High-resolution Interferometer Sounding (HIS) which was flown over Tennessee and northern Alabama during summer 1986. HIS temperature and dewpoint soundings were examined on two flight days to determine their error characteristics and utility in mesoscale analyses. Random errors were calculated from structure functions while total errors were obtained by pairing the HIS soundings with radiosonde-derived profiles. Random temperature errors were found to be less than  $1^{\circ}\text{C}$  at most levels, but random dewpoint errors ranged from 1 to  $5^{\circ}\text{C}$ . Total errors of both parameters were considerably greater, with dewpoint errors especially large on the day having a pronounced subsidence inversion.

Cumulus cloud cover on 15 June limited HIS mesoscale analyses on that day. However, HIS dewpoints at 300 mb indicated a strong moisture gradient that was confirmed by GOES 6.7 micrometer imagery. HIS mesoscale analyses on 19 June revealed a tongue of humid air stretching across the study area. This moist region was confirmed by radiosonde data and imagery from the MAMS instrument. Convective temperatures derived from HIS retrievals helped explain the cloud formation that occurred after the HIS overflights. Crude estimates of Bowen ratio were obtained from HIS data using a mixing line approach. Values indicated that areas of large sensible heat flux were the regions of first cloud development. These locations were also suggested by GOES visible and infrared imagery. The HIS retrievals indicated that areas of thunderstorm formation were regions of greatest instability. Local landscape variability and atmospheric temperature and humidity fluctuations were found to be important factors in producing the cumulus clouds on 19 June. HIS soundings were capable of detecting some of this variability. The authors were impressed by HIS's performance on the two study days.

Richard Knabb's M.S. thesis (1993) research investigated a technique for retrieving precipitable water (PW) from high resolution split window data to determine its strengths and weaknesses. The technique relies on the relationship between PW and the ratio of spatial variances of brightness temperatures in the two split window channels. This relationship, which was determined by regression using radiosonde data, appeared to vary little for summertime conditions over the southeast United States. A case study applied the technique to data from the Multispectral Atmospheric Mapping Sensor (MAMS) on 16 October 1990 over Florida. The resulting PW images revealed horizontal moisture variability as strong as 0.5 mm per km. The sharp gradient detected in the PW imagery occurred over a smaller distance than suggested by

analysis of radiosonde-derived PW. Numerous sources of errors for the technique were evaluated. The most significant potential errors were due to variations in surface emissivity within the templates used to compute channel variances. Horizontal moisture variations within these regions, uncertainty in the regression relationship, and split window data errors also decreased the accuracy of the PW estimates. Each source of error was enhanced when channel variances were small. The magnitude of variances mostly depended on the underlying surface and varied with the template size used for retrievals. Choice of template size also was important because large sizes increasingly invalidated major assumptions of the technique.

Mike Nichols' M.S. thesis (1993) research compared three different techniques for estimating soil moisture over northern Alabama/southern Tennessee: 1) An antecedent retention index (ARI) with and without explicit evaporation physics, 2) A remotely sensed land surface temperature (LST)-modeling technique in which separate regression equations were developed at each site using a one-dimensional planetary boundary layer (PBL) model to predict soil moisture based on LST changes from 10 AM to noon; and 3) A method which exploited the relationship between soil moisture availability and the slope of normalized differenced vegetation index (NDVI) vs. LST on scatter diagrams. Observed soil moisture data were not available for the study. Therefore, results of the various methods were intercompared to assess their strengths and weaknesses. Additionally, remotely sensed LSTs from the Multispectral Atmospheric Mapping Sensor (MAMS) were compared to in situ and PBL-modeled LSTs.

Results showed significant differences between these estimation methods over complex terrain. The most reliable method was found to be the LST-modeling approach. There was a correlation of -0.9 between time changes in LST and regressed soil moisture, regardless of terrain influences. Moreover, the slope of the fitted regression line was similar to those of previous investigations where in situ measurements of soil moisture and soil temperatures were available. The ARI technique apparently underestimated root zone soil moisture when compared to PBL regressed soil moisture. Terrain slope may account for some of the differences, in addition to the simplicity of the ARI model parameters. The NDVI / LST slope procedure was found to be easily contaminated by changes in solar insolation. This solar contamination must be removed in order to infer soil moisture estimates. Both ARI-derived and LST-PBL model regressed soil moisture estimates were input to a PBL model to predict variables such as LST, mixed layer (ML) height, cloud fractions, and surface fluxes.

Comparison of MAMS LSTs with in situ soil temperatures showed agreement within 1 to 3°C. The soil moisture model producing the smallest differences between remotely sensed and modeled LST was found to be the MAMS / PBL-regressed method. No relationship was found between any soil moisture model and ML growth. There are inherent large errors in the procedure (a cloud shadow technique), and the ML observations were taken during the rapid phase of ML growth. Both ARI and model-regressed techniques led to similar errors in forecast cloud fraction when these soil moisture values were input to the PBL model. Important processes which cannot be resolved by a one-dimensional model most likely were influencing PBL cloud growth.

In summary, the research was very successful, and we believe we have achieved the goals originally proposed.

## Theses

Ronald L. Schudalla, 1988: A Case Study of Thunderstorm Development on 17 June 1986 During COHMEX.

Steven R. Olson, 1990: An Evaluation of VAS-Derived Parameters Commonly Used in Thunderstorm Forecasting.

John T. Bradshaw, 1991: High Resolution Interferometer Sounder (HIS) Analyses of Mesoscale Phenomena.

Richard D. Knabb, 1993: A Sensitivity Analysis of the Split Window Variance Ratio Technique for Precipitable Water Estimation.

Michael W. Nichols, 1993: A Comparison of Several Techniques for Estimating Soil Moisture Over Complex Terrain.

## Conference Papers

Schudalla, R. L., and H. E. Fuelberg, 1989: A mesoscale analysis of the pre-storm environment on the 17 June 1986 COHMEX day. Preprints Twelfth Conf. Wea. Analysis and Forecasting, Monterey, Amer. Meteor. Soc., 130-135.

Olson, S.R., and H.E. Fuelberg, 1990: An evaluation of VAS-derived severe storm parameters. Preprints Sixteenth Conf. Severe Local Storms, Kananaskis, Alberta, Canada, Amer. Meteor. Soc., 150-153.

Bradshaw, J.T., and H.E. Fuelberg, 1990: HIS analyses of mesoscale phenomena, Preprints Fifth Conf. Satellite Meteor. and Ocean., London, Amer. Meteor. Soc., 329-333.

## Journal Articles

Fuelberg, H.E., R. L. Schudalla, and A.R. Guillory, 1991: Analysis of sudden mesoscale drying at the surface, Mon. Wea. Rev., 119, 1391-1406.

Fuelberg, H.E., and S. R. Olson, 1991: An assessment of VAS-derived retrievals and parameters used in thunderstorm forecasting. Mon. Wea. Rev., 119, 795-814.

Bradshaw, J.T., and H.E. Fuelberg, 1993: An evaluation of HIS interferometer soundings and their use in mesoscale analyses, J. Appl. Meteor., 32, 522-538.

## An Evaluation of High-Resolution Interferometer Soundings and Their Use in Mesoscale Analyses

JOHN T. BRADSHAW\* AND HENRY E. FUELBERG

*Department of Meteorology, The Florida State University, Tallahassee, Florida*

(Manuscript received 2 December 1991, in final form 6 July 1992)

### ABSTRACT

An aircraft prototype of the High-Resolution Interferometer Sounder (HIS) was flown over Tennessee and northern Alabama during summer 1986. HIS temperature and dewpoint soundings were examined on two flight days to determine their error characteristics and utility in mesoscale analyses. Random errors were calculated from structure functions while total errors were obtained by pairing the HIS soundings with radiosonde-derived profiles. Random temperature errors were found to be less than 1°C at most levels, but random dewpoint errors ranged from 1° to 5°C. Total errors of both parameters were considerably greater, with dewpoint errors especially large on the day having a pronounced subsidence inversion.

Cumulus cloud cover on 15 June limited HIS mesoscale analyses on that day. Previously undetected clouds were found in many HIS fields of view, and these probably produced the low-level horizontal temperature and dewpoint variations observed in the retrievals. HIS dewpoints at 300 mb indicated a strong moisture gradient that was confirmed by GOES 6.7- $\mu\text{m}$  imagery.

HIS mesoscale analyses on 19 June revealed a tongue of humid air stretching across the study area. The moist region was confirmed by radiosonde data and imagery from the Multispectral Atmospheric Mapping Sensor (MAMS). Convective temperatures derived from HIS retrievals helped explain the cloud formation that occurred after the HIS overflights. Crude estimates of Bowen ratio were obtained from HIS data using a mixing-line approach. Values indicated that areas of large sensible heat flux were the areas of first cloud development. These locations were also suggested by GOES visible and infrared imagery. The HIS retrievals indicated that areas of thunderstorm formation were regions of greatest instability.

Local landscape variability and atmospheric temperature and humidity fluctuations were found to be important factors in producing the cumulus clouds on 19 June. HIS soundings were capable of detecting some of this variability. The authors were impressed by HIS's performance on the two study days.

### 1. Introduction

Meteorology faces exciting challenges and opportunities as it enters the twenty-first century. Many future activities will demand data at spatial and temporal scales that exceed those of current observing networks. For example, the coarse and uneven data coverage of the current radiosonde network will impede advancements in global numerical modeling. This data problem is particularly acute over the vast oceanic, tropical, and polar regions where observations are especially sparse. Improvements in short-term warnings and forecasts will also require higher-resolution data.

Geosynchronous satellites have a unique ability to sample vast regions of the atmosphere at high temporal and spatial resolution. Current Geostationary Operational Environmental Satellite (GOES) systems are

equipped with the VISSR (Visible-Infrared Spin Scan Radiometer) Atmospheric Sounder (VAS), a filter-wheel radiometer that measures atmospheric and terrestrial emissions in 12 infrared channels (Smith et al. 1981; Chesters et al. 1982). VAS temperature and moisture profiles are obtained operationally using the simultaneous physical retrieval algorithm (Smith et al. 1985; Hayden 1988). However, the accuracy of these soundings is seriously hampered by VAS's inadequate vertical resolution caused by its limited number of channels that only detect radiation over thick overlapping layers (e.g., Hayden 1988; Franklin et al. 1990; Fuelberg and Olson 1991; Fuelberg and Breidenbach 1992).

A remote sensor must attain a spectral resolution ( $\Delta\lambda/\lambda$ , where  $\lambda$  is wavelength) of 0.1% to avoid the smearing of individual absorption lines (Smith et al. 1979). The filter-wheel radiometers on the current GOES, as well as those for *GOES I-M*, are incapable of meeting this criterion (Smith et al. 1990). The desired vertical resolution can be achieved from a sounder utilizing Michelson interferometry (Huang 1989; Smith et al. 1990). Based on this concept, the High-Resolution Interferometer Sounder (HIS) represents a

\* Present affiliation: NOAA/NWS, Albuquerque, NM.

Corresponding author address: Henry E. Fuelberg, Florida State University, Department of Meteorology, B-161, Tallahassee, FL 32306-3034.

APPENDIX TO  
FINAL REPORT

AN EVALUATION OF SATELLITE-DERIVED HUMIDITY  
AND ITS RELATIONSHIP TO CONVECTIVE DEVELOPMENT

NASA Grant NAG8-653

FSU ID 1338-580-26

December 1987-December 1992

Florida State University  
Henry E. Fuelberg  
Principal Investigator

Submitted May 1993

Reprinted from JOURNAL OF APPLIED METEOROLOGY, Vol. 32, No. 3, March 1993  
American Meteorological Society

**An Evaluation of High-Resolution Interferometer Soundings  
and Their Use in Mesoscale Analyses**

JOHN T. BRADSHAW AND HENRY E. FUELBERG



new generation of remote sensors that will provide radiance information at literally thousands of spectral channels—a distinct advantage over their filter-wheel counterparts.

An HIS aircraft prototype was developed to test the applicability of interferometry to the atmospheric sounding problem. The prototype has been flown on dozens of missions and has collected spectra from a variety of atmospheric states. Technical aspects of the prototype as well as sounding results have been given by Huang (1989), Revercomb et al. (1988a, 1988b), and Smith et al. (1988, 1990). Smith et al. (1990) have proposed that later versions of *GOES I-M* be outfitted with an operational version of HIS, known as the GOES High-Resolution Interferometer Sounder (GHIS), in place of filter-wheel assemblies.

The current paper evaluates atmospheric soundings generated from radiances observed by the HIS aircraft prototype. Our two goals are to 1) estimate the accuracy of HIS temperature and dewpoint soundings using statistical tests and comparisons against simultaneous observations from other remote sensors and radiosondes, and 2) to exploit the high spatial and spectral resolution of the HIS dataset to glean new insights into mesoscale phenomena.

## 2. Methodology

### a. HIS sounding procedures

The HIS was flown numerous times during the Cooperative Huntsville Meteorological Experiment (COHMEX), a multiagency field experiment conducted during summer 1986 over portions of Tennessee and Alabama (Dodge et al. 1986). HIS data were utilized on 15 June and 19 June because other types of remotely sensed observations as well as mesoscale radiosonde soundings were available.

On 15 June, the HIS was mounted in the wing pod of a NASA U-2 research aircraft, while on the 19th, it was carried directly under the fuselage of a NASA ER-2 aircraft. In both cases, the sounder pointed directly toward nadir although it was not roll corrected. The contrasting mounting configurations produced small differences in data characteristics. Specifically, spectra on 19 June exhibited greater sample-position-error noise due to scan mirror vibrations imposed by the sounder's proximity to the aircraft's engines (W. L. Smith 1990, personal communication). Revercomb et al. (1988b) have described the characteristics of this error component.

Flight patterns for both mission days are presented in Fig. 1. In each case the aircraft flew a series of parallel legs over the Tennessee Valley at an altitude of 19.8 km. On 15 June, five north-south legs over COHMEX were completed between 1749 and 2002 UTC. These segments were 210–280 km long, spaced 50 km apart, and were traversed in 20–24 min each. On 19 June, four east-west legs were flown during the period 1520–

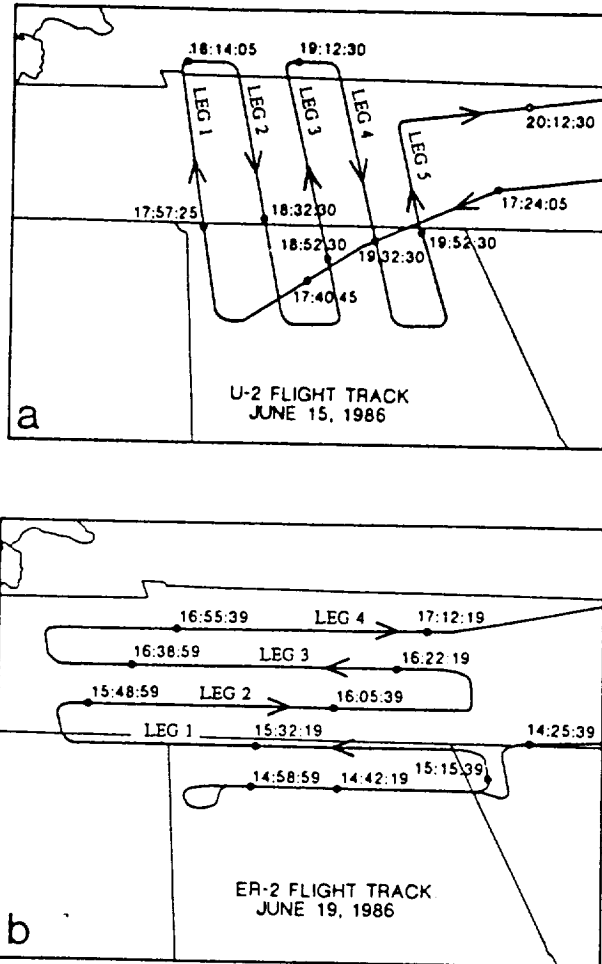


FIG. 1. Flight tracks of the aircraft carrying the HIS instrument on (a) 15 June and (b) 19 June 1986 (after Smith et al. 1990). Flight legs used in this study are numbered. Aircraft directions are indicated by the arrows, and overpass times at specific points (the dots) are given in UTC.

1713 UTC. These segments were approximately 280 km long, spaced about 45 km apart, and were completed in approximately 24 min each. We did not use data from the shorter leg traversed before 1520 UTC.

HIS instantaneous ground fields of view were 2.0 km  $\times$  2.0 km. Due to the forward speed of the aircraft, surface footprints were 2.0 km  $\times$  3.2 km. Every two minutes, the instrument underwent a calibration period lasting approximately 72 s. As a result, the retrievals were segmented into groups of six (at 2-km spacing), interspersed by calibration gaps averaging 12 km. Instrument problems and editing procedures (see section 2b) reduced the total number of retrievals and increased the variability of the data spacing.

The HIS retrievals that we examined were produced at the Cooperative Institute for Meteorological Satellite Studies (CIMSS) at the University of Wisconsin at Madison. A typical HIS radiance set may contain mea-

surements at 4000 or more spectral channels, due to the broad spectral coverage and high spectral resolution provided by the sounder. Generating soundings from a dataset of this magnitude requires a computationally efficient retrieval scheme; the simultaneous physical retrieval algorithm described by Smith et al. (1988, 1991) and Huang (1989) has been tailored to meet these requirements. Specifically, vertical profiles of temperature and humidity are obtained simultaneously from the complete set of HIS radiances. The algorithm requires a first-guess temperature–dewpoint profile, which in the current study was the average of all radiosonde soundings made during the two-month COHMEX period. This one composite guess was used at all sounding locations on both study days; no surface or upper-air data for our specific two days were utilized. The output HIS retrievals consisted of temperature data at 25 discrete levels from 1000 to 50 mb, and dewpoint information at 15 levels from 1000 to 300 mb.

### b. Preliminary HIS data preparation

We did not use some of the HIS retrievals originally calculated for 15 and 19 June. Soundings made outside the COHMEX area or while the aircraft were turning (and the HIS sensor pointed significantly away from nadir) were deleted. Since cloud contamination is a significant retrieval problem, efforts were made to isolate affected soundings. Skies were virtually clear during the 19 June flight; only a few areas of scattered cirrus were noted over the western fringes of the study area. On the 15th, however, there was an extensive cumulus cloud field over the flight region. The HIS spectra for 15 June were subjected to five cloud checks (Table 1) devised by CIMSS (H. L. Huang 1990, personal communication). The objective was to approach cloud detection from several perspectives. The first test is a gross check of brightness temperatures (TBs). Tests 2–4 are difference checks between TBs in the 3.9- and 10.3- $\mu\text{m}$  windows. A limitation here is that the shortwave window channel will have both reflected and emitted energy components during the midday COHMEX flights. Finally, the neighbor checks of TBs at adjacent fields of view (test 5) should be especially useful in locating detached cumulus clouds. Soundings that failed any of the five tests were deleted from the dataset; ninety retrievals flagged by this procedure were removed. The final dataset consisted of 248 (257) retrievals on 15 (19) June.

Radiosonde observations (RAOBs) indicated that temperature and moisture fields over the area gradually evolved on both study days. This variability, and the great difference in HIS along-track versus cross-track retrieval spacing (2 km versus 45–50 km), precluded the use of two-dimensional objective analysis. Therefore, we examined the HIS data on a leg-by-leg basis. Data along each flight leg were objectively analyzed at 5-km intervals using a one-dimensional version of the

TABLE 1. Cloud detection tests performed on the HIS data where TB denotes brightness temperature.

Test	Criteria
1	$TB(963.0\text{ cm}^{-1}) \leq 288.0\text{ K}$
2	$TB(1015.2\text{ cm}^{-1}) - TB(2395.2\text{ cm}^{-1}) \leq -2.5\text{ K}$
3	$TB(963.7\text{ cm}^{-1}) - TB(2527.8\text{ cm}^{-1}) \leq -12.0\text{ K}$ and $TB(1015.2\text{ cm}^{-1}) \leq TB(2395.0\text{ cm}^{-1})$
4	$TB(2527.8\text{ cm}^{-1}) - TB(2616.0\text{ cm}^{-1}) \leq -8.0\text{ K}$ and $TB(1015.2\text{ cm}^{-1}) \leq TB(2395.2\text{ cm}^{-1})$
5	Neighbor checks [checks are against forward and backward fields of view (FOV)]: $TB^0(963.7\text{ cm}^{-1}) - TB^{+1}(963.7\text{ cm}^{-1}) \leq -2.0\text{ K}$ , $TB^0(2611.2\text{ cm}^{-1}) - TB^{-1}(2611.2\text{ cm}^{-1}) \geq 3.0\text{ K}$ , $TB^0(963.7\text{ cm}^{-1}) - TB^{+1}(963.7\text{ cm}^{-1}) \leq -2.0\text{ K}$ , and $TB^0(2611.2\text{ cm}^{-1}) - TB^{+1}(2611.2\text{ cm}^{-1}) \geq 3.0\text{ K}$ , where superscripts: 0: center FOV -1: forward FOV +1: backward FOV

Barnes scheme (Barnes 1964, 1973). Classical sampling theory (e.g., Peterson and Middleton 1963) states that observation spacing must not exceed half the horizontal wavelength of the feature being investigated. Since individual HIS sounding groups were separated by gaps averaging 12 km, 25 km was determined to be the minimum resolvable wavelength. The response of the Barnes analysis was specified to be 0.3 at this distance.

### c. Other data sources

Special COHMEX RAOBs served as the primary comparison for the HIS retrievals. The network had a spacing of approximately 50 km, and releases were made at 3-h intervals (Williams et al. 1987). The sounding data were available at 25-mb increments from the surface to 25 mb. On 15 June, seven sites released a total of 10 sondes during the flight period; on the 19th, 16 soundings were obtained from nine sites.

The Multispectral Atmospheric Mapping Sensor (MAMS; Jedlovec et al. 1986, 1989) was flown on both days of interest. The MAMS is a high-resolution scanning spectrometer that measures radiances in eight visible and three infrared channels. With a ground resolution of 100 m at its typical flight altitude of 20 km, MAMS imagery are useful for examining small-scale temperature and moisture structures at the surface and in the lower troposphere. In addition, the instrument's high resolution is useful for detecting small clouds that might be missed by GOES imagery. On 15 June, HIS and MAMS were aboard the same aircraft, while on 19 June, the U-2 aircraft carrying MAMS followed the HIS ER-2 mission by 5–10 min.

### 3. Statistical studies

One of our primary objectives was to evaluate the accuracy of HIS retrievals. Factors that contribute to

retrieval uncertainty include imperfect radiance measurements, undetected cloud contamination, minor imperfections in the transmittance calculations, and imprecise numerical techniques for solving the radiative transfer equations. In addition, there is the inherent uncertainty from inadequate spectral resolution in the input radiance data.

There has been little quantitative evaluation of HIS retrievals. Huang (1989) examined retrievals obtained from observed radiances and those synthetically generated from COHMEX RAOBs. He related retrieval errors to several factors including data noise, choice of spectral band, a priori statistics, spectral data resolution, and cloudiness. Smith et al. (1990) have examined similar aspects. Huang et al. (1992) quantified HIS's vertical resolution. The current HIS evaluations supplement this previous research in two ways: random retrieval errors are estimated using structure function analysis, and total sounding error is determined from comparisons with COHMEX RAOBs.

#### a. Random-error estimates

Statistical structure function analysis is an attractive method for estimating random error because it does not require comparisons with another data source. It is a simple technique in which each observation is paired with all others in the data region. Our methodology was similar to that used in the satellite data evaluations of Hillger and Vonder Haar (1979) and Fuelberg and Meyer (1986). The structure function (STR) of quantity  $f$  is given by

$$\text{STR}(R) = \frac{1}{N} \sum [f(\mathbf{r}_i) - f(\mathbf{r}_j)]^2, \quad (1)$$

where  $\mathbf{r}_i$  and  $\mathbf{r}_j$  are position vectors of observation sites  $i$  and  $j$ , and  $N$  is the number of station pairs whose scalar separation distance

$$\rho = |\mathbf{r}_i - \mathbf{r}_j| \quad (2)$$

is within the range  $R$ . We calculated structure values at 5-km intervals between 0- and 300-km separation.

Homogeneous and isotropic data were assumed in (1), that is, the calculations were performed independent of the orientation and position of the paired observations, with results depending only on the scalar separation distance between the two paired points. These assumptions are made frequently in mesoscale structure studies although they have questionable validity at scales larger than the microscale (Barnes and Lilly 1975; Fuelberg and Meyer 1984).

We slightly modified (1) to account for elapsed time during the 2-h HIS sounding missions. Specifically, we assumed unchanging conditions during the 20–25 min that each flight leg was traversed. Structure calculations still utilized sounding data along all legs of each flight.

However, only data pairings along the same leg were allowed; that is, no cross-leg pairings were included in the summations and therefore no information about cross-track gradients was obtained.

Noise estimates were obtained from the structure functions following the methods of Gandin (1963) and Hillger and Vonder Haar (1979). With the further assumption of no spatially correlated errors, the structure function approaches twice the inherent variance of the measuring system as the data separation approaches zero ( $\rho = 0$ ), that is,

$$\text{STR}(0) = 2\sigma^2, \quad (3)$$

which can be solved for  $\sigma$ , the rms error. Estimates of  $\text{STR}(0)$  were obtained by linearly extrapolating the structure values to zero separation. Alternative extrapolation procedures produced almost identical results. It should be emphasized that structure-derived uncertainties do not include any type of bias or systematic error.

Results (Fig. 2) indicate that HIS random temperature errors (solid lines) generally are similar for the two study days. Values for 15 June (Fig. 2a) range from 0.3° to 1.0°C at the various levels, while those on 19 June (Fig. 2b) vary from 0.7° to 1.0°C. Both temperature error profiles display maxima near 950 mb, with secondary maxima near 500 mb. Smallest errors are located near 700 mb and between 350 and 400 mb. The slightly greater errors observed on 19 June probably are related to the different placement of the HIS instrument aboard the aircraft (section 2a). Retrieval errors due to aircraft engine vibrations would be absent in a space environment (Smith et al. 1990).

Our estimates of HIS random temperature errors are comparable to those given for operational satellite retrievals. Fuelberg and Meyer (1986) used a similar structure function methodology to investigate mesoscale VAS soundings. They found rms temperature errors ranging from 0.5° to 1.2°C at five pressure levels. When a structure function procedure was applied to temperature data from the NOAA-4 Vertical Temperature Profile Radiometer (VTPR), random errors averaged 0.5°C at three levels (Hillger and Vonder Haar 1979).

Figure 2 also displays random errors for HIS dewpoints (dashed lines). These rms errors are considerably larger than those of temperature, ranging from 1.0° to 5.0°C on both days, with pronounced maxima near 500 mb. Dewpoint errors near the surface are much smaller than those aloft—values near 950 mb are approximately 1.0°C. The HIS errors are comparable to those for VAS; Fuelberg and Meyer (1986) cited a 3.0°C average for the 500-, 700-, and 850-mb levels.

#### b. Total-error estimates

Total HIS retrieval error includes a systematic component in addition to the random uncertainty described

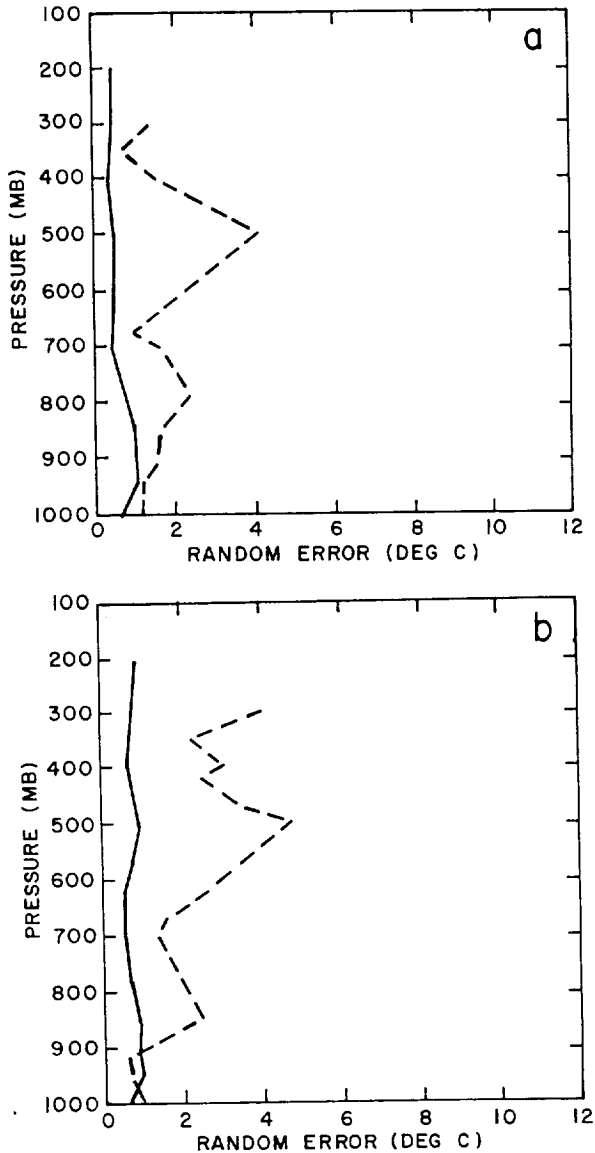


FIG. 2. Values of rms random errors ( $^{\circ}\text{C}$ ) for HIS-derived temperatures (solid) and dewpoints (dashed) on (a) 15 June and (b) 19 June 1986. Values were estimated from structure function analyses.

above. We obtained total error estimates by comparing HIS retrievals with COHMEX RAOBs. Although there is ample precedent for using RAOBs as the "ground truth" for statistically evaluating remotely sensed soundings (e.g., Moyer et al. 1978; Schlatter 1981; Jedlovec 1985; Fuelberg and Olson 1991), several factors limit the effectiveness of the procedure.

RAOBs are seldom collocated in space or time with the retrievals being scrutinized; however, our procedures (described below) should minimize, but not eliminate, this factor. In addition, the RAOBs themselves contain errors; rms errors of radiosonde temperatures have been estimated to range from  $0.4^{\circ}$  to

$0.8^{\circ}\text{C}$  (Hoehne 1980; Pratt 1985). The National Weather Service specifies that sonde hygrometer errors be within 5% relative humidity at values above 30%, and within 7% at values below 30% (Nordahl 1982); however, Pratt (1985) found that errors could be considerably greater than these amounts under certain conditions. By lifting pairs of radiosondes on single balloons, Hoehne (1980) found that dewpoint differences were within about  $20^{\circ}\text{C}$  for 54% of the ascents.

Finally, radiosonde data represent point measurements, that is, they describe the air immediately surrounding the sensors and may not represent conditions only a few kilometers away if there are strong gradients. In contrast, remote sensors such as HIS sample large atmospheric volumes encompassing many cubic kilometers. The detected signals represent composites of all variabilities within the sampling domains. This fundamental difference in sampling, even among otherwise error-free systems, will produce discrepancies between the two systems being compared. Bruce et al. (1977) concluded that RAOB-satellite temperature differences of  $1.4^{\circ}$ – $1.7^{\circ}\text{C}$  could be attributed solely to this effect.

Our pairing methodology was relatively simple. All HIS retrievals located within a 15-km radius of each COHMEX RAOB were flagged. These six or seven retrievals were then averaged to produce a single HIS profile that was compared with the RAOB. All HIS retrievals comprising each average were made within 2 min of one another. This aspect of the methodology is similar to that used on satellite retrievals by McMillin et al. (1983), Rabin et al. (1991), and Fuelberg and Breidenbach (1992). Balloon drift was negligible on both days and was neglected. Since the HIS flights occurred between the 3-h radiosonde observations, the RAOBs were linearly time interpolated to the HIS observation times. The time-interpolated RAOB profiles were then vertically interpolated to the HIS data levels.

Only a very small number of HIS-RAOB pairings was available—four on 15 June and five on 19 June. This sample size unquestionably reduces the statistical significance of the results, and firm conclusions about this aspect of HIS retrieval accuracy cannot be drawn. Nonetheless, the procedure does provide tentative error estimates for comparison with previous results from different procedures.

Estimates of total rms error on 15 June are presented in Fig. 3a. The profiles end at 500 mb because of missing RAOB data at higher levels. Temperature errors (solid) range from  $0.5^{\circ}$  to  $2.6^{\circ}\text{C}$ , with maximum uncertainties near the surface and minimum errors near 670 mb. The temperature errors for 19 June (Fig. 3b) range from  $0.8^{\circ}$  to  $3.5^{\circ}\text{C}$ . These values exceed those of 15 June at many levels, due likely to the effects of aircraft vibration noise. The errors again are greatest in the lower troposphere, reach a minimum near 650 mb, then increase slightly at higher altitudes. The magnitudes of total error on both days surpass their random-error counterparts (Fig. 2a) at nearly every level,

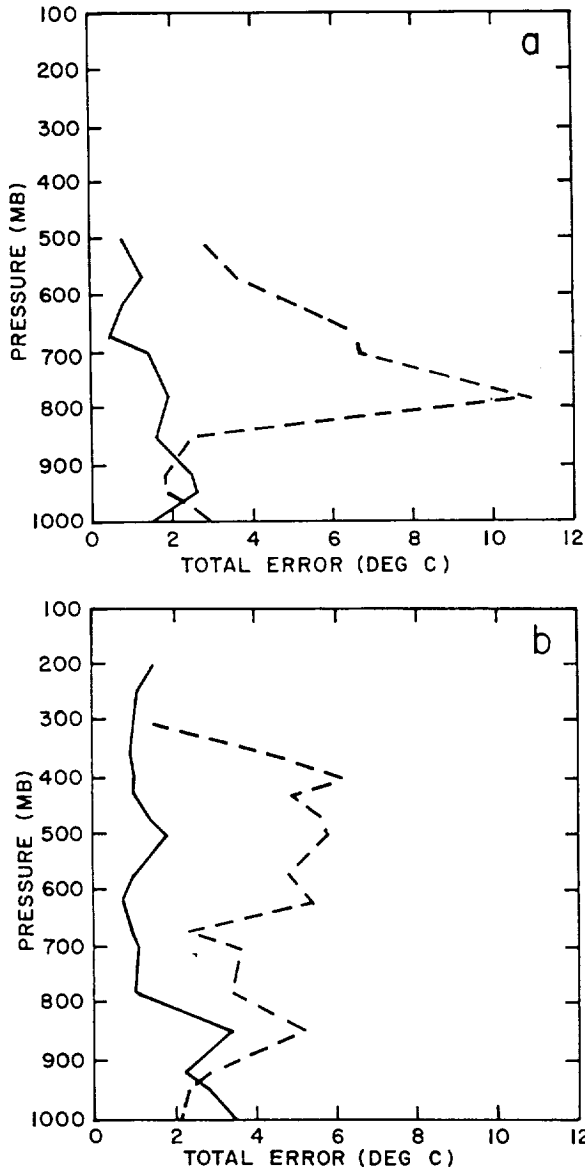


FIG. 3. Total rms errors ( $^{\circ}\text{C}$ ) for HIS-derived temperatures (solid) and dewpoints (dashed) on (a) 15 June and (b) 19 June 1986. Values were estimated by pairing HIS retrievals with nearby radiosonde soundings.

sometimes by a factor of 2; however, the altitudes of maxima and minima agree closely.

Dewpoint rms errors on 15 June (Fig. 3a, dashed) are much greater than those of temperature at most levels. Relatively small uncertainties are found near the surface, but there is a striking  $11.0^{\circ}\text{C}$  maximum near 780 mb that decreases to less than  $3.0^{\circ}\text{C}$  near 500 mb. These total dewpoint errors (Fig. 3a) are considerably greater than the random errors (Fig. 2a). In particular, the  $11.0^{\circ}\text{C}$  error at 780 mb dwarfs the  $2.5^{\circ}\text{C}$  random-error estimate. On 19 June (Fig. 3b), maxima of  $5.0^{\circ}\text{C}$ – $6.0^{\circ}\text{C}$  occur at 850 mb and between 620 and 400 mb. The minimum of  $1.5^{\circ}\text{C}$  occurs at 300 mb,

and there are secondary minima of  $2.0^{\circ}\text{C}$ – $3.0^{\circ}\text{C}$  near the surface and 670 mb. These error estimates also exceed the random error versions.

Some error characteristics on 15 June (Fig. 3a) can be attributed to a strong temperature inversion over the COHMEX area between 780 and 850 mb that was accompanied by a significant decrease in dewpoint. The relatively large HIS temperature errors centered on 950 mb, and especially the large dewpoint errors near 780 mb, likely represent the sounder's inability to adequately resolve these vertical gradients. Thermodynamic diagrams showing pairings of individual HIS and RAOB profiles have been presented by Smith et al. (1990) and Bradshaw (1991). Cumulus cloud contamination is another source of HIS error on 15 June, and this will be discussed in section 4. No temperature inversions or major vertical humidity gradients were present on 19 June, and no cloud contamination was detected in the retrievals being examined.

It is informative to compare current error estimates with earlier findings. Smith et al. (1990) and Huang et al. (1992) presented rms errors of HIS retrievals that had been prepared from radiances synthesized from COHMEX RAOBs. Details about the procedure are given in Huang (1989). The simulated temperature errors ranged from  $0.6^{\circ}$  to  $1.4^{\circ}\text{C}$ , while dewpoint errors ranged from  $1.5^{\circ}$  to  $3.2^{\circ}\text{C}$ . Our random-error estimates (Fig. 2) are similar to their simulated values; however, our total-error estimates (Fig. 3) are considerably greater than their simulated errors. Their estimates of temperature error differ most from our total errors below 850 mb; the two versions of dewpoint errors contrast most in the middle troposphere. Altitudes of maximum and minimum errors are similar between the two studies. Smith et al. (1990) stated that their evaluation methodology yielded the lower limits of error using the simultaneous algorithm. Conversely, our pairing procedure tends to exaggerate HIS retrieval errors, that is, a portion of our HIS–RAOB discrepancies can be ascribed to collocation and RAOB errors. Other differences between the two studies may represent systematic error and retrieval bias which appear to be highly dependent on the nature of the atmosphere being sampled. Finally, our small sample size is a limitation to the comparisons.

**4. Mesoscale studies**

Only limited mesoscale analyses were possible on 15 June because of widespread cumulus clouds. Virtually clear conditions during the flight of 19 June enabled more extensive studies.

*a. 15 June*

Synoptic analyses for 15 June (not shown) depicted no large-scale forcing mechanisms near the COHMEX area; however, GOES satellite imagery did reveal two interesting smaller-scale phenomena. Aloft, there was

a prominent gradient in VAS  $6.7\text{-}\mu\text{m}$  water vapor imagery over the Tennessee Valley; at lower levels, an extensive cumulus cloud field contained several elongated regions of enhanced cloudiness. Middle and high clouds were not observed during the period.

Figure 4 is a GOES 1-km visible image for 1900 UTC 15 June; leg 3 of the HIS mission is superimposed (see Fig. 1). Three areas of enhanced clouds intersect the leg at the indicated points. A plot of HIS 920-mb temperature deviations about the mean for leg 3 is shown in Fig. 5a, while a similar diagram of 920-mb dewpoint deviations is in Fig. 5b. A comparison of sounding features in Fig. 5 with positions of the enhanced cloud features in Fig. 4 shows excellent agreement. Specifically, the locations of moisture maxima, temperature minima, and cloud areas match almost perfectly when adjustments are made for temporal differences between the GOES image and the HIS data. Comparisons at other lower troposphere levels (not shown) reveal similar agreement.

An important question is whether the temperature and dewpoint perturbations in Fig. 5 represent true atmospheric structures, or are merely artifacts of cloud contamination. While one expects small-scale temperature and moisture gradients in association with the enhanced cloud areas, the relatively large amplitudes in Fig. 5 are suspicious because they exceed those commonly observed during benign atmospheric conditions.

Thus, cumulus clouds could have escaped detection by the initial screening tests described in section 2b (Table 1), influencing the HIS radiances and resulting retrievals to produce the observed fluctuations.

A two-step procedure was used to determine effects of the low-level clouds on the HIS retrievals. The first step was to use MAMS high-resolution (100-m) visible and infrared imagery to ascertain whether undetected clouds were within the HIS fields of view (FOVs). MAMS data were utilized because HIS contains no visible channels. The MAMS and HIS instruments flew aboard the same aircraft on 15 June; however, we had to employ several techniques to account for differing navigation systems and instrument configurations (see Bradshaw 1991). The resulting HIS-MAMS FOV collocations probably are accurate only to within 1 km. Thus, calculated cloud fractions within the HIS  $2.0\text{-km} \times 3.2\text{-km}$  FOVs contain some uncertainty.

Results from the MAMS cloud detection procedure (not shown) indicate that some HIS FOVs that passed the original cloud checks (Table 1) still contain significant cloudiness. Fractional coverages range from 0% to 75%, with greatest amounts within the three regions of enhanced clouds (Fig. 4). The presence of undetected cumulus is not surprising since they are very difficult to locate with infrared data. The cumulus clouds on 15 June were small and detached. Furthermore, since surface reports indicated that their tops

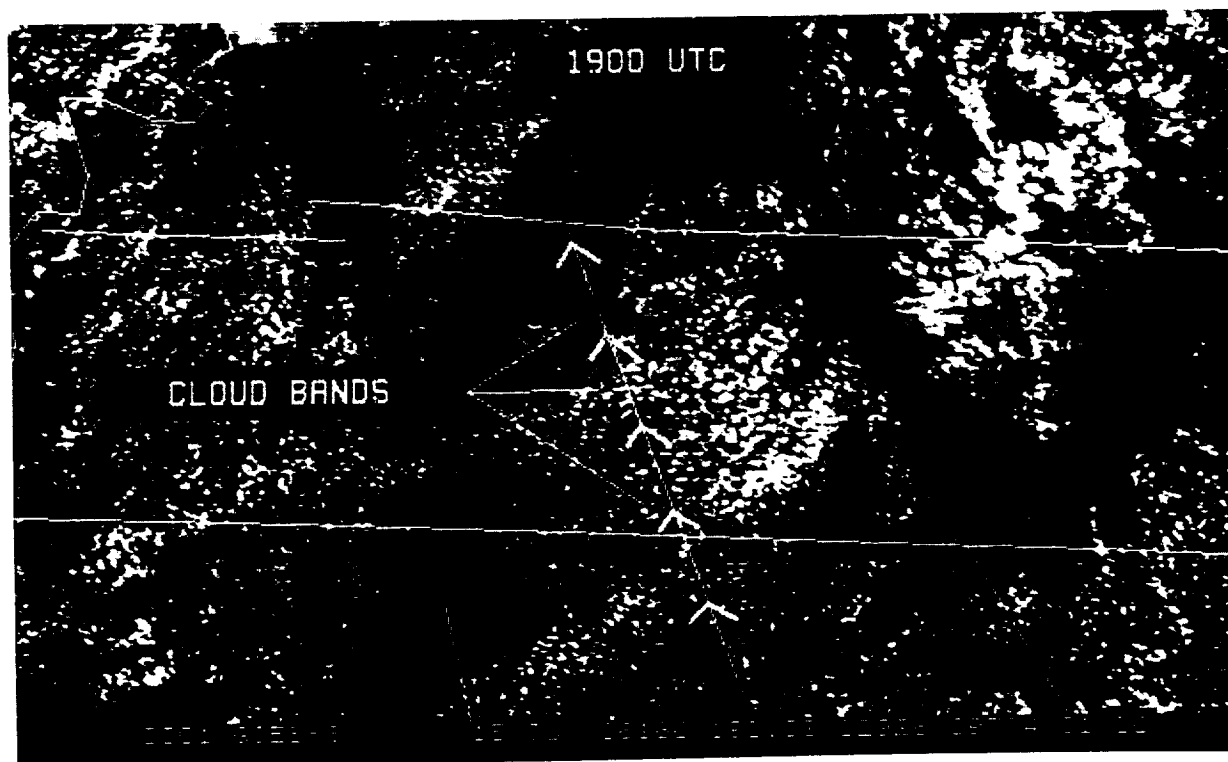


FIG. 4. GOES 1-km visible image at 1900 UTC 15 June 1986. Flight leg 3 and locations of three areas of enhanced cumulus clouds are indicated. Distances from the southernmost point are given at 50-km intervals by the arrows.

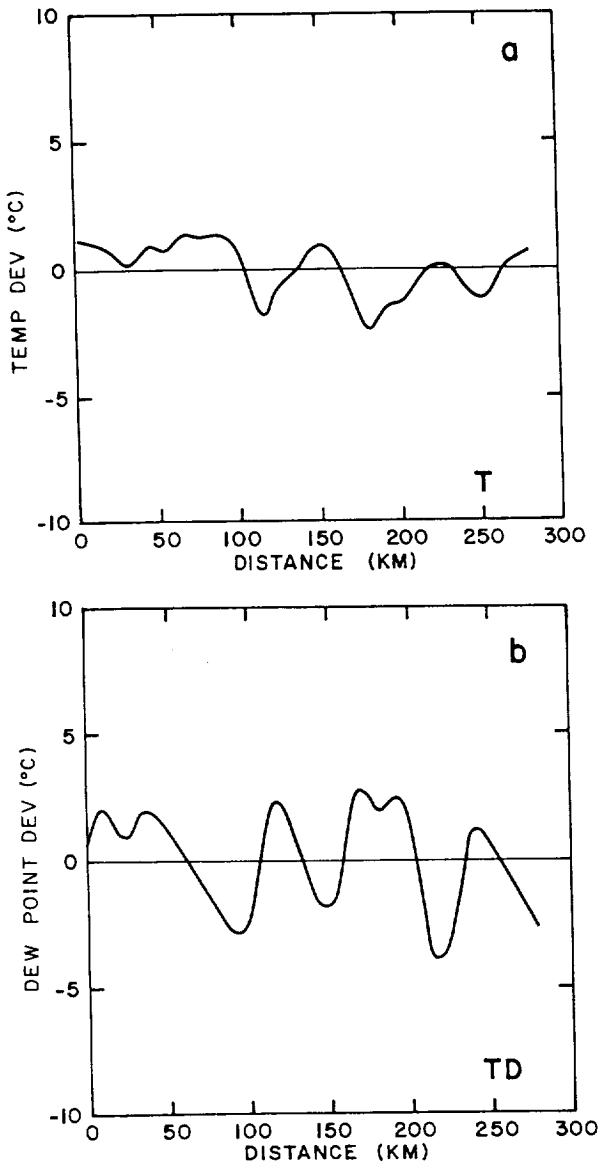


FIG. 5. Deviations of HIS (a) temperatures ( $^{\circ}\text{C}$ ) and (b) dewpoints ( $^{\circ}\text{C}$ ) at 920 mb from their respective means along leg 3 on 15 June (see Fig. 4). The original data have been objectively analyzed onto a 5-km grid. Distances increase from south to north.

were within 2 km of the ground, cloud-top temperatures were not greatly different from temperatures at the ground. It is clear that improved schemes for cumulus detection are needed.

The second step was to determine the effects of the undetected clouds on the HIS retrievals. The procedure was to prepare synthetic soundings using a modified version of the HIS retrieval algorithm. The calculations were performed by Dr. Allen Huang at the University of Wisconsin (personal communication). The modified code incorporated fractional cloud amounts in calculating atmospheric transmittance, and included a separate cloud term in the radiative transfer equation.

Details of this methodology can be found in Huang (1989). A typical COHMEX radiosonde profile on 15 June was used as input, with the bottom and top of the cumulus clouds specified to be 850 and 780 mb, respectively, based on observations. Huang simulated five different situations: clear, overcast, and cloud fractions of 25%, 50%, and 75%. The HIS synthetic spectra that were prepared for each situation were used to generate temperature and moisture retrievals.

Results, seen in Fig. 6, show that cumulus cloud contamination exerts considerable influence on the HIS retrievals of 15 June, particularly just above and below the assumed cloud layer. Clouds produce a strong cold bias in the temperature profiles below 850 mb, and there are equally robust moist dewpoint biases from the surface to 400 mb. The temperature (dewpoint) biases reach  $8^{\circ}\text{C}$  ( $10^{\circ}\text{C}$ ). Since these cloud-induced effects are similar to the spatial variations seen in the observed HIS retrievals (Fig. 5), lower tropospheric HIS data have not been used in mesoscale diagnostic studies of 15 June. As a final point, the cloud contamination on 15 June helped produce the errors described in Figs. 2 and 3; however, with the exception of the inversion layer, most errors actually are smaller on the cloudy day (15 June) than the clear one (19 June). Thus, the greater aircraft vibrations on 19 June appear to be a major cause of the uncertainties.

The simulations (Fig. 6) indicate that low-level clouds have little effect on upper-tropospheric portions of the HIS retrievals. Thus, we have analyzed HIS upper-tropospheric dewpoint data. VAS  $6.7\text{-}\mu\text{m}$  water vapor imagery for 1900 UTC (Fig. 7) depicts a large-scale southeast-to-northwest moisture gradient over the Tennessee Valley (the most humid air is denoted by the lightest shades of gray). The five north-south HIS

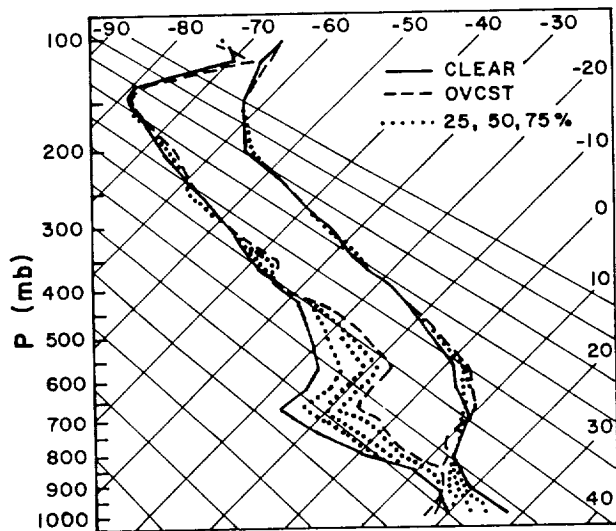


FIG. 6. Simulated effects of cumulus clouds on HIS retrievals for 15 June (Huang, personal communication). Clear, overcast, and partly cloudy (25%, 50%, and 75% coverages) are indicated. Cumulus cloud base and top were assumed to be 850 and 780 mb, respectively.

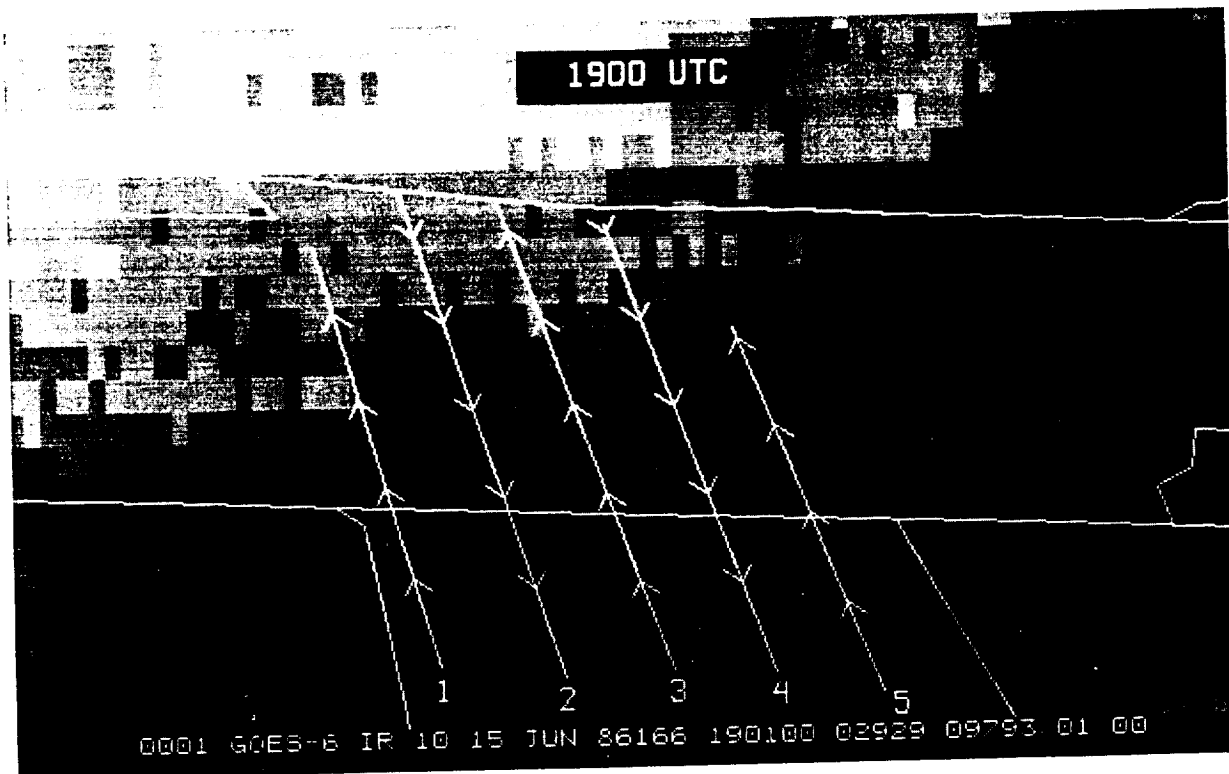


FIG. 7. GOES 6.7- $\mu\text{m}$  water vapor image for 1900 UTC 15 June. HIS flight tracks are superimposed. Distances from the southernmost points are given at 50-km intervals by the arrows.

flight tracks across this gradient are superimposed. Since significant VAS 6.7- $\mu\text{m}$  radiance may emanate anywhere from 250 to 700 mb depending on the vertical water vapor distribution (e.g., Chesters et al. 1982), we had to select an optimum HIS level for comparison. We utilized a set of transmittance and radiative transfer algorithms collectively known as "forward code" to determine the levels of maximum radiance contribution on 15 June. Further details about this forward code, a key component of the VAS operational retrieval algorithm, are given by Hayden (1988). Results showed that the moisture gradient over the Tennessee Valley primarily occurred between 250 and 400 mb.

HIS 350-mb dewpoints are plotted in Fig. 8. Since the flight legs are numbered from west to east (see Fig. 7) and the distances along them increase from south to north, the diagram represents a simplified horizontal depiction. HIS dewpoint gradients in the first 100 km (southernmost parts) of legs 4 and 5 are comparatively weak, and this agrees with the VAS imagery. The HIS data for all flight tracks indicate the large-scale moisture gradient seen in the image; dewpoints vary approximately 10°C over each leg. Differences between VAS imagery and HIS dewpoints are expected because HIS, and especially VAS, radiances represent conditions over depths of several hundred millibars. Thus, the comparison of dewpoints at a single level with the in-

tegrated radiative effect of moisture through a deep layer will not yield a perfect correlation. Although the largest-scale HIS moisture structures (Fig. 8) agree

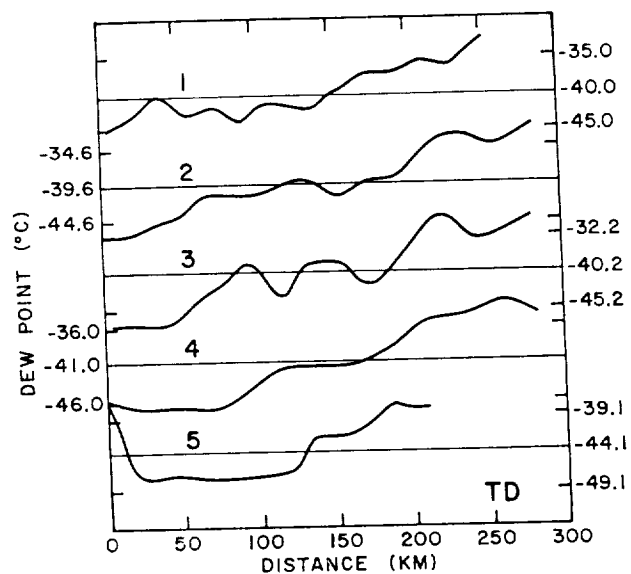


FIG. 8. HIS dewpoints ( $^{\circ}\text{C}$ ) at 350 mb for all five flight legs (see Fig. 7) on 15 June. Distances along each leg increase from south to north (see Fig. 7). The middle number given along the ordinate for each leg is the mean along that flight segment.



closely with RAOB dewpoint analyses (not shown), differences of  $1.0^{\circ}$ – $2.0^{\circ}\text{C}$  are present at individual locations. In addition to the radiative aspects previously described, some of these discrepancies could be due to RAOB uncertainties at such high altitudes.

To summarize, the 15 June case suggests that HIS retrievals can define upper-level moisture features with a skill comparable to those of VAS and mesoscale radiosonde observations. The following case study of 19 June will show that HIS products are useful in mesoscale analyses of lower-tropospheric features during clear sky conditions.

### b. 19 June

GOES visible imagery on 19 June (Fig. 9) depicts clear skies over the southernmost three flight legs during the HIS mission (1520–1645 UTC). A cumulus cloud field then develops 1–2 h later over the southeastern half of the study area. The sharp demarcation separating the cloudy and clear regions is an especially interesting image feature. The cloud boundary remains distinct and quasi-stationary throughout the afternoon, and isolated thunderstorms develop later in the day near the southern and eastern edges of the flight area. Jedlovec (1990) gives additional details about meteorological conditions on this day.

We used HIS, MAMS, and RAOB data to investigate the thermodynamics associated with the low-level cloud field and precipitation areas. As a first step, precipitable water (PW) was calculated from the special network of COHMEX radiosondes. Figure 10 shows the PW pattern at 1800 UTC 19 June. A ridge of maximum PW is oriented nearly southwest–northeast over central Tennessee, with values ranging from 26 to 33 mm across the flight area. The axis of this moist region coincides closely with the clear–cloudy boundary in Fig. 9.

It is difficult to validate the high-spatial-resolution HIS PWs because appropriate ground-truth data are unavailable; however, comparing MAMS and HIS PWs is a step in this direction. Although the HIS and MAMS instruments were carried on different aircraft, their flight tracks were virtually identical, and temporal differences between the MAMS–HIS observations rarely exceeded 10 min. The three legs to be examined here are superimposed on the RAOB PW analysis (Fig. 10). The two versions of PW were derived via different methods. HIS PW was obtained by vertically integrating humidity data at the 15 retrieval levels between 1000 and 300 mb. Thus, the HIS PWs were derived from thousands of radiance measurements. In contrast, the MAMS PWs were deduced from 11- and 12- $\mu\text{m}$  “split window” imagery using the split-window variance-ratio technique described by Jedlovec (1990). Jedlovec provided the MAMS PW data in a digital image format at 100-m resolution. We then used a computer workstation to obtain an average MAMS

value within each  $2.0\text{-km} \times 3.2\text{-km}$  footprint comprising the HIS retrievals. Both the HIS and MAMS PWs were then objectively analyzed, as described in section 2. Additional details about these procedures are given in Bradshaw (1991).

Figure 11 contains objectively analyzed plots of HIS and MAMS PW along the three east–west flight legs shown in Fig. 10. Differences between the MAMS and HIS values are also given. Both versions of PW agree with the RAOB-derived pattern in defining the moisture ridge that is oriented southwest–northeast over central Tennessee. As noted earlier, this feature is approximately parallel to the westernmost edge of the cumulus cloud field (Fig. 9). Both the MAMS and HIS PWs indicate much greater small-scale variability than the coarsely spaced radiosonde data.

The HIS and MAMS PWs generally agree favorably (Fig. 11). Although both remotely sensed estimates are usually too moist in comparison to the RAOB version (Fig. 10), HIS produces a smaller range of values. Over most of the western (left) two-thirds of each leg PWs from the two sounders agree to within  $\pm 5$  mm; however, differences approaching 10 mm are seen at the eastern (right) part of leg 1. There are some locations (e.g., leg 1 near 250 km) where trends from the two data sources go in different directions. Nonetheless, the general agreements between HIS and MAMS lend credibility to both sounding systems. The PW discrepancies probably are due mostly to the major differences in data and methodologies that were described earlier.

The convective temperature  $T_c$  is the surface temperature required to form cumulus clouds by solar heating. HIS retrievals were used to calculate  $T_c$ 's with results shown in Fig. 12. The plots indicate  $T_c$ 's ranging from approximately  $26^{\circ}$  to  $33^{\circ}\text{C}$ . The horizontal  $T_c$  gradients agree qualitatively with the areal extent and onset time of the observed cloudiness (Fig. 9). Clouds initially form at about 1630 UTC over the eastern (right) portions of the flight legs where  $T_c$ 's are relatively cool. Later cloud development (around 1830 UTC) occurs over the warmer  $T_c$  areas in the centers of the flight legs (between 100 and 200, 140 and 225, and 210 and 240 km of legs 1, 2, and 3, respectively). Over the westernmost (left) portions of the legs, where  $T_c$ 's range from  $30^{\circ}$  to  $33^{\circ}\text{C}$  because of decreased low-level moisture, skies remain clear all day because of insufficient surface heating. This absence of clouds over western portions of the COHMEX area may also be influenced by a weak low-level thermal “cap” or inversion that is indicated in both RAOB and HIS sounding profiles (not shown).

Satellite imagery reveals that the clouds initially form over a rather small region, not simultaneously over the entire HIS flight area. Cumulus clouds first appear in the 1700 UTC image over east-central and south-central Tennessee (Fig. 9). Over the next 1.5 h, small streetlike formations develop within this area as the clouds expand westward to cover the entire southeast

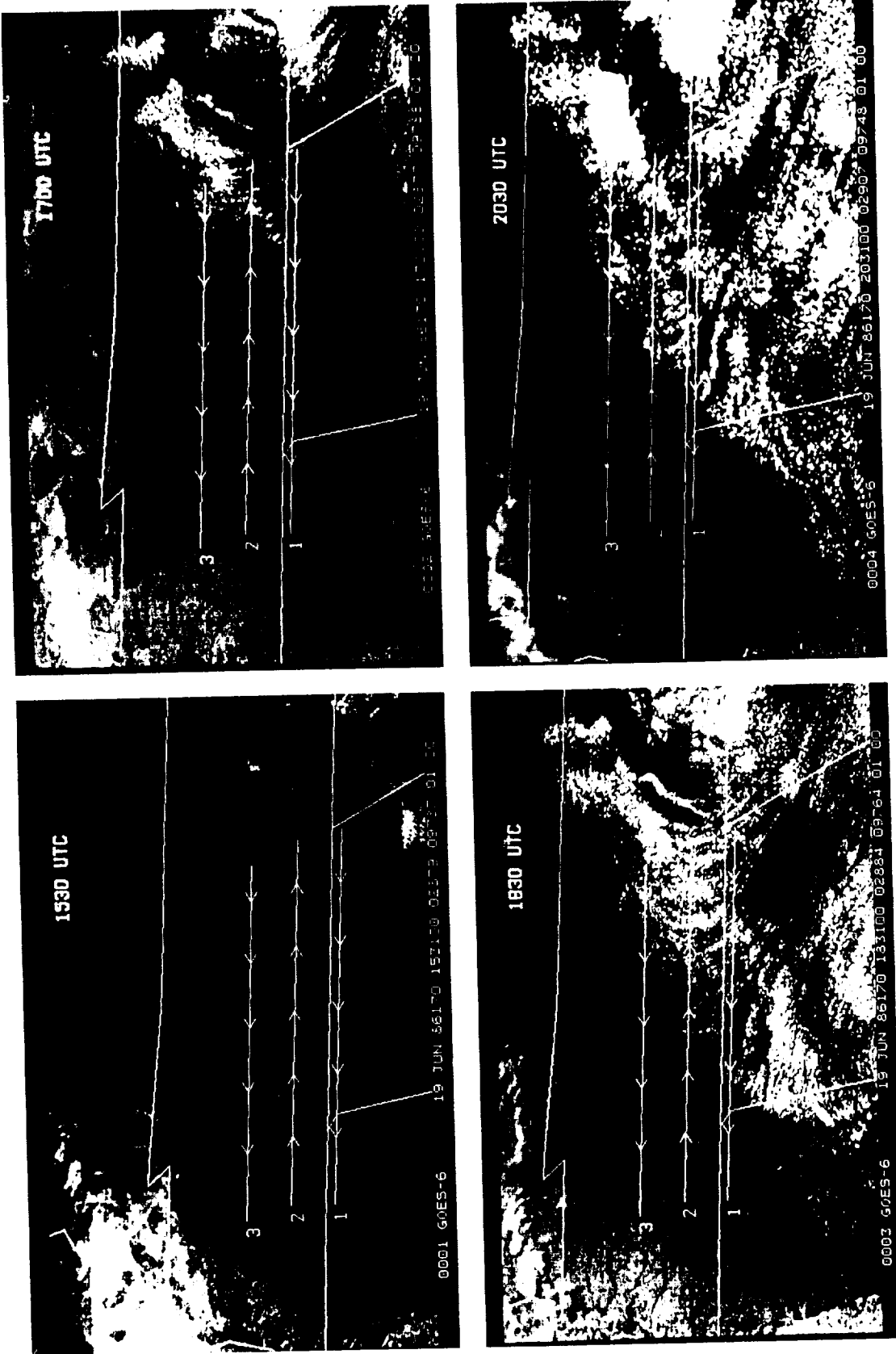


Fig. 9. GOES 1-km visible imagery for 1530, 1700, 1830, and 2030 UTC 19 June 1986. HIS flight legs are superimposed on all images; however, the overflights actually occurred between 1520 and 1645 UTC. Distances from the westernmost points are given at 50-km intervals by the arrows.

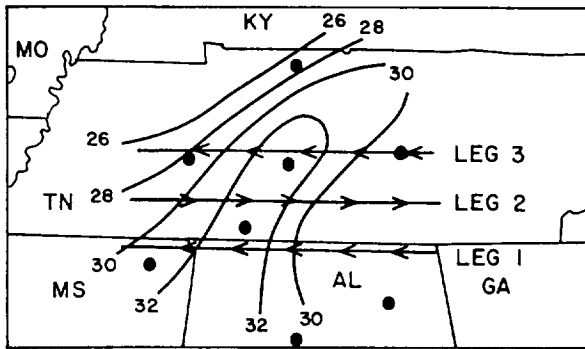


FIG. 10. Radiosonde-derived precipitable water (mm) for 1800 UTC 19 June. Station locations are indicated by darkened circles. HIS flight legs are superimposed as in Fig. 9.

half of the domain by 2030 UTC. HIS  $T_c$  data (Fig. 12) identified the eastern portions of the study area as preferred regions for cloud formation; however, local factors (described below) appear to focus initial development over selected areas within this larger favored region.

Cumulus cloud formation is closely related to characteristics of the surface and planetary boundary layer (PBL) in which air parcels rise. Wilde et al. (1985) noted that cumulus onset occurs when the entrainment zone (EZ), representing the top of the mixed layer, sufficiently overlaps the "LCL zone" containing the lifting condensation levels (LCLs) of the varying surface-based parcels. The vertical growth rates of the PBL and EZ are directly proportional to the intensity of sensible heat flux at the earth's surface (Tennekes 1973). Thus, initial cloud formation is expected in areas where relatively low LCL heights coincide with regions of greatest mixing-layer depth and, hence, increased sensible heat flux.

We did not calculate predicted mixed-layer heights; however, relative EZ heights were inferred from HIS-derived estimates of Bowen ratio (the ratio between sensible and latent heat fluxes). The procedure utilized mixing-line analysis in a saturation-point coordinate system (Betts 1982, 1985; Betts and Albrecht 1987) and is based on work by Sugita and Brutsaert (1990), Betts (1992), and E. A. Smith et al. (1991). Coordinates of a mixing line are  $q_T$ , the parcel's total water mixing ratio, and  $\theta_e$ , the parcel's equivalent potential temperature.

Mixing-line analysis is useful for examining air parcels originating from sublayers of the PBL. Surface-layer air will possess unique thermodynamic properties that differ from those of the overlying well-mixed layer. This can cause the mixing lines of the two sublayers to have different slopes. The slope of the surface-layer mixing line can be used to infer the relative contribution of surface fluxes. Specifically,  $\Delta\theta_e$  will exceed  $\Delta q_T$  in areas dominated by large sensible heat flux because  $\theta_e$  will decrease more rapidly with height than  $q_T$

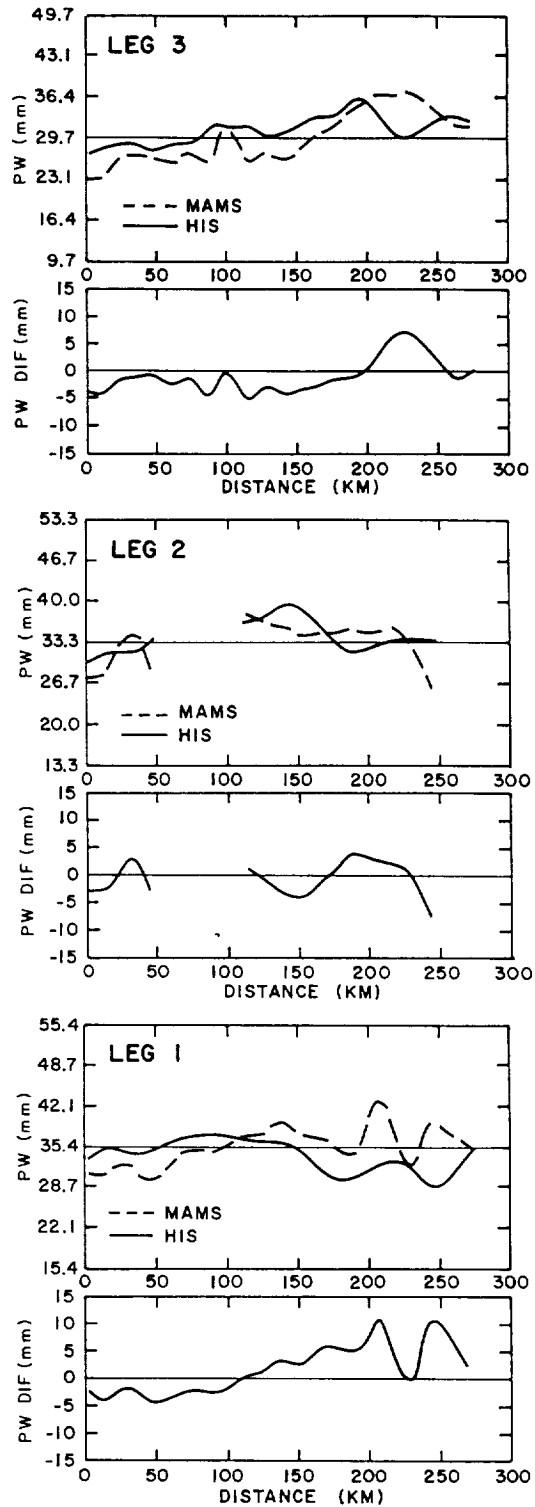


FIG. 11. HIS- (solid) and MAMS-derived (dashed) precipitable water (PW) plots (both in millimeters) for flight legs 1, 2, and 3 on 19 June (see Fig. 10). The middle number given along the ordinate for each leg is the mean MAMS value along that flight segment. Differences between HIS and MAMS values (mm) are given in the bottom panel of each diagram pair. Distances along each leg increase from west to east. The gap in leg 2 is due to missing data.

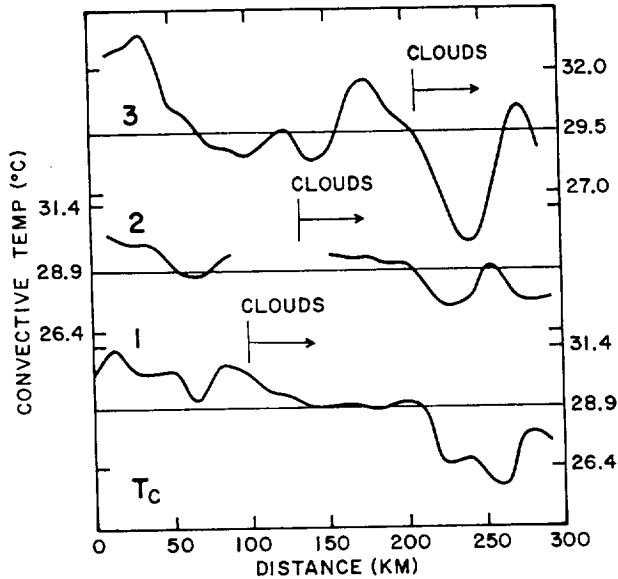


FIG. 12. HIS-derived convective temperatures  $T_c$  ( $^{\circ}\text{C}$ ) along flight legs 1, 2, and 3 on 19 June (see Figs. 9 and 10). The greatest extent of cloud cover is indicated for each leg. The gap in leg 2 is due to missing data. The middle number given along the ordinate for each leg is the mean along that flight segment.

due to superadiabatic lapse rates very near the surface. Conversely, when latent heat flux represents a greater share of the total flux term,  $\Delta q_T$  will be large relative to  $\Delta\theta_e$  since greatest moisture will exist just above the surface. E. A. Smith et al. (1991) indicated that the Bowen ratio (BR) can be related to  $\Delta\theta_e$  and  $\Delta q_T$  by

$$\text{BR} = \left( \frac{c_p}{L_v} \right) \left( \frac{\Delta\theta_e}{\Delta q_T} \right) - 1, \quad (4)$$

where  $c_p$  is the specific heat of air at constant pressure and  $L_v$  is the latent heat of fusion.

The Bowen ratio can be estimated by calculating  $\theta_e$  and  $q_T$  at levels within the boundary layer, fitting a mixing line to these data, and determining its slope. E. A. Smith et al. (1991) used (4) with slow-launched radiosondes that provided high vertical resolution within the PBL; however, the HIS retrievals that we employed for the current study contained data at only two near-surface levels—950 mb and the surface itself. This much coarser resolution reduces the likelihood that the true mixing line is well approximated. In addition, 950 mb probably resides within the well-mixed layer instead of the surface layer. As a result, these data likely fall along a mixing line whose slope differs from that of the surface layer. In light of these limitations, current Bowen ratios should be considered only crude approximations to the true values along the HIS flight tracks.

Plots of HIS-derived Bowen ratios along three flight legs are given in Fig. 13. Relatively large ratios indicate enhanced sensible heat flux which, in turn, should re-

sult in faster growth of the EZ and earlier cloud development. Horizontal fluctuations in the Bowen ratios agree with the observed imagery (Fig. 9). Specifically, the maxima on each leg (i.e., at 215, 240, and 225–260 km on legs 1, 2, and 3, respectively) are near the locations of initial cloud development. Conversely, many of the minima (e.g., at 285 km on leg 1) correspond to regions of suppressed convection. Although our Bowen ratios are crude estimates, they do agree qualitatively with the areas of initial cloud development, thereby suggesting that localized areas of enhanced sensible heat flux were important in determining locations of initial cumulus development on 19 June.

GOES imagery also supports the role of sensible heating in initial cloud formation. Figure 14 shows GOES 11- $\mu\text{m}$  TBs along flight leg 1 (occurring near 1530 UTC) for the period 1300–1600 UTC; skies were clear at these times. The relatively flat profile between 0 and 210 km at 1300 UTC is replaced in time by distinct maxima at 40 and 210 km. Although atmospheric moisture absorption affects 11- $\mu\text{m}$  TBs, sensitivity tests utilizing the forward code described in section 4a indicate that the trends observed in Fig. 14 are primarily manifestations of surface skin temperature. The warm TB region that develops at 210 km in leg 1 corresponds to the Bowen-ratio maximum seen in Fig. 13, and the area of initial cloud formation seen in Fig. 9.

The relatively warm TB area (Fig. 14) agrees with GOES visible imagery at 1630 UTC (Fig. 15). This image has been enhanced to highlight subtle differences in surface reflectance. The brightest features, over

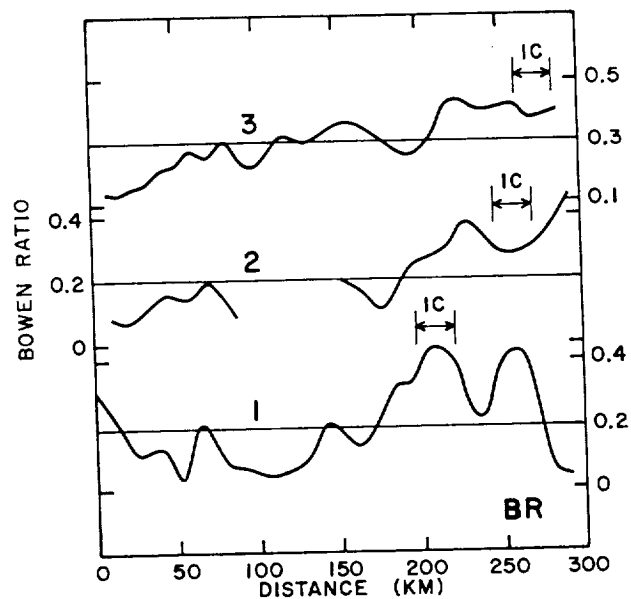


FIG. 13. As in Fig. 12, but for Bowen ratio (BR). Locations of initial cloud formation (IC) are indicated.

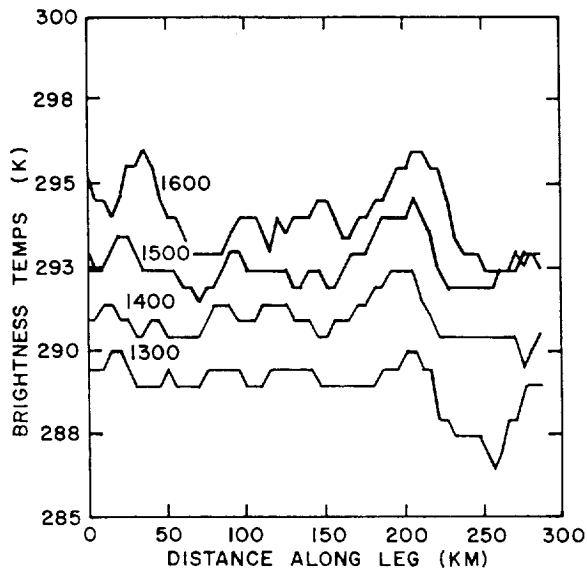


FIG. 14. GOES 11- $\mu$ m brightness temperatures (K) along flight leg 1 (see Figs. 9 and 10) at 1300, 1400, 1500, and 1600 UTC 19 June.

northwestern and extreme southeastern Tennessee, are cirrus and cumulus clouds; however, the white area stretching northeastward from north-central Alabama represents open farmland. Mountains covered by thick forest vegetation are found immediately east of this

region, while areas of mixed forest and farmland are located to the west. Cumulus clouds form preferentially over the open cultivated region where the local sensible heat flux should be comparatively greater than the latent heat flux. Small cumulus clouds are forming along the eastern margins of this area at 1700 UTC (Fig. 9). Rabin et al. (1990) presented similar findings in a study of landscape variability and its effect on cumulus onset over Oklahoma. When the air was relatively dry, cumulus clouds were found to develop preferentially over areas characterized by large sensible and small latent heat fluxes. The presence of strong small-scale gradients of sensible heat flux also may foster the development of thermally direct circulations, further enhancing low-level convergence over the region. In addition to land-surface variations, there are numerous large lakes in the region (Fig. 9). The associated land-water temperature contrasts will lead to low-level mesoscale circulations that will inhibit cloud development over the lakes, but enhance it in the surroundings.

We examined HIS-derived stability indices in the vicinities of thunderstorms that occurred on 19 June. Two storm areas developed near the flight tracks after 2000 UTC (Fig. 9): one just east of the eastern end of leg 3 (over eastern Tennessee), and the other approximately 100 km east-southeast of the western end of leg 1 (over extreme northwest Alabama, not yet developed in the 2030 UTC image). Plots of HIS lifted index (LI) are shown in Fig. 16. Distinct LI minima

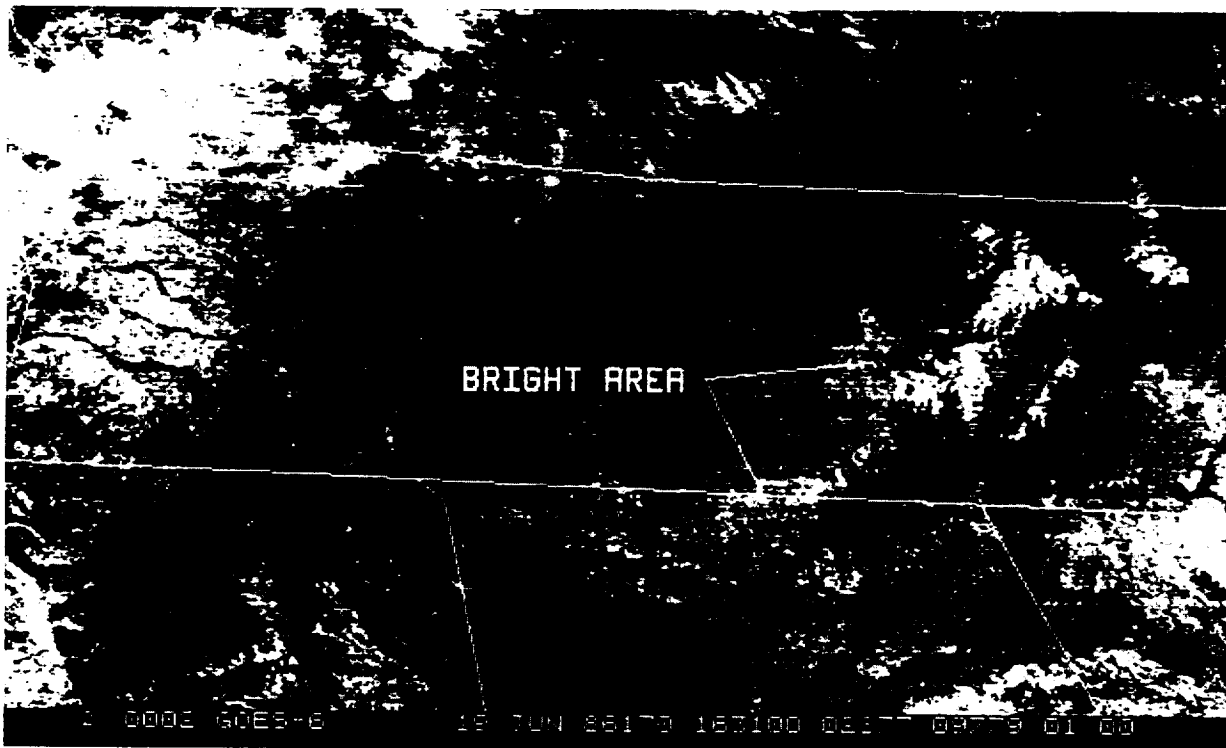


FIG. 15. Enhanced GOES 1-km visible image for 1630 UTC 19 June. Bright areas representing agricultural regions are indicated.

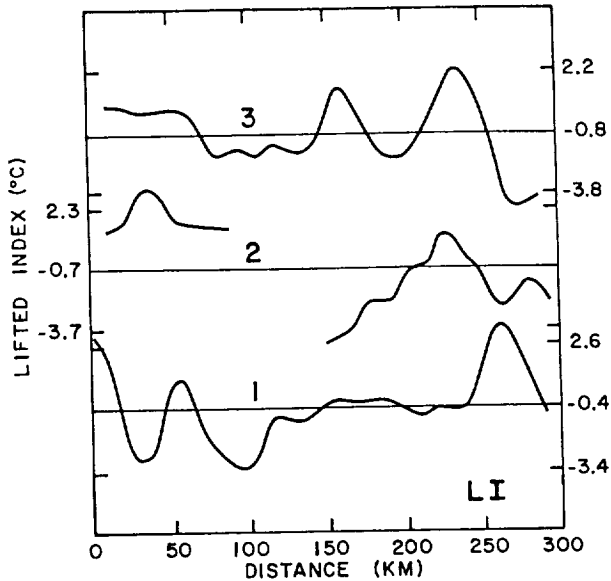


FIG. 16. As in Fig. 12, but for lifted index (LI, °C).

near  $-3^{\circ}\text{C}$  along the western (left-most) third of leg 1, the eastern end of leg 3, and near the center of leg 2. The minima along legs 1 and 3 indicate substantial instability in the vicinity of the subsequent thunderstorm areas. The LI minimum near the center of leg 2 is not associated with storm development. Trends of HIS-derived  $K$  index (KI) (not shown) are very similar to those of LI in that large values are present near the areas of later thunderstorm development. Thus, the storms develop within regions of abundant moisture (Figs. 10 and 11) and greatest instability.

## 5. Summary and conclusions

An aircraft prototype of the High-Resolution Interferometer Sounder (HIS) was flown over Tennessee and northern Alabama during Summer 1986. We have calculated random and total errors for HIS retrievals prepared on 15 and 19 June and have used the retrievals in mesoscale analyses. Structure-function calculations indicated that random rms temperature errors were approximately  $1^{\circ}\text{C}$ , with greatest values in the lower troposphere. Random dewpoint errors were much larger, ranging from  $1^{\circ}$  to  $5^{\circ}\text{C}$ . Largest errors were found in the middle troposphere. Both temperature and dewpoint errors were greater on 19 June than 15 June, probably because the HIS was mounted at a location of enhanced aircraft vibration.

Total rms error includes a systematic component in addition to random error. Our total error estimates were obtained by pairing HIS retrievals with nearby radiosonde sites. Conclusions are very tentative because of the small sample size. Total rms temperature errors ranged from  $0.5^{\circ}$  to  $3.5^{\circ}\text{C}$ , generally 1.5 to 2 times

larger than the random-error estimates. Largest values were in the lower troposphere. Total dewpoint errors were even greater—ranging from  $1.5^{\circ}$  to  $11^{\circ}\text{C}$ . The largest dewpoint discrepancies occurred near the altitude of a pronounced subsidence inversion on 15 June. Thus, errors are linked to the presence of particular atmospheric features, especially those that are difficult to resolve vertically. Cumulus cloud contamination on the 15th was also undoubtedly a factor in producing the observed errors; however, except for midtropospheric dewpoints, temperature and dewpoint errors generally were smaller on the 15th than the 19th.

Our total errors are greater than errors reported by Smith et al. (1990) and Huang et al. (1992) for synthetically derived HIS retrievals; our random errors are comparable to their errors. The pairing procedure that we used will overestimate HIS errors because of RAOB-HIS collocation discrepancies and errors in the radiosonde soundings. Conversely, Smith et al. stated that their values represent the lower limit of error because of the methodology involved. Additional evaluations should be performed using both types of procedures in order to better establish HIS retrieval characteristics.

We did not compare HIS retrievals with those from the current VAS system. Smith et al. (1990) performed such analyses, while they and Huang et al. (1992) considered HIS in relation to the upcoming *GOES I-M* system. These studies concluded that HIS would be superior to both VAS and *GOES I-M*, and on that basis recommended that an interferometer sounder be placed on future *GOES* platforms. Further comparisons between HIS, VAS, and *GOES I-M* should be undertaken.

Only limited mesoscale analysis could be performed with the 15 June HIS data because extensive cumulus clouds blanketed the flight region. Although the HIS radiances had been screened for cloud contamination, MAMS imagery indicated considerable cumulus remaining in those HIS fields of view used to prepare retrievals. Thus, the original cloud screening checks probably need to be refined. Sensitivity tests showed that the cumulus contamination on 15 June would produce fictitious cooling and moistening in lower-tropospheric portions of the retrievals that was comparable to that actually observed. On the other hand, these sensitivity checks indicated that upper-tropospheric dewpoints would not be affected significantly by undetected cumulus. HIS dewpoints at 350 mb indicated a pronounced horizontal gradient of water vapor that was confirmed by VAS  $6.7\text{-}\mu\text{m}$  imagery.

Additional HIS mesoscale analyses could be performed on 19 June because clouds were virtually non-existent during the overflights. Cumulus clouds did develop 1–2 h later. HIS precipitable water data indicated an axis of moist air stretching northeast to southwest over the flight area. This agreed with values from a

mesoscale radiosonde network, as well as PW analyses derived from MAMS. The moist area was parallel to the cloud-no-cloud boundary that existed during the afternoon.

Convective temperatures were also calculated from the HIS retrievals on 19 June. Cumulus clouds formed over the southeastern portion of the flight area where  $T_c$ 's were coolest. Farther west, the drier air apparently never warmed sufficiently to produce clouds.

The cumulus clouds on 19 June did not form simultaneously over all areas that ultimately contained them. Instead, they first developed in selected regions before expanding in areal coverage. To investigate this observation, we computed crude estimates of Bowen ratio using the HIS retrievals as input to a scheme based on mixing-line theory (E. A. Smith et al. 1991). Areas of initial cloud formation were found to agree with regions of large Bowen ratio which indicated enhanced sensible heat flux. Furthermore, the regions of large HIS-derived Bowen ratios corresponded with areas of comparatively warm GOES 11- $\mu\text{m}$  TBs and enhanced visible reflectance. Thus, results indicate that local landscape variability as well as atmospheric temperature-humidity variations were important factors in producing the cumulus clouds. Furthermore, it appears that HIS is capable of detecting at least some of this variability.

Finally, thunderstorms formed along the fringes of the study area during the late afternoon of 19 June. Stability indices computed from HIS data showed that this development occurred in areas of greatest instability.

We are impressed by HIS's performance on the two study days. The small spacing of the HIS retrievals (as close as 2 km) allowed us to examine mesoscale sounding features that cannot be resolved with current operational sounders such as VAS. The aircraft prototype has been flown on many additional missions, and we believe that these data should be utilized in future studies. These investigations should further document error characteristics of HIS soundings and utilize them as a high-resolution data source to examine atmospheric phenomena.

*Acknowledgments.* We greatly appreciate the help of Drs. William Smith and Allen Huang at CIMSS, University of Wisconsin for providing the HIS data and answering numerous questions about their use. We particularly want to thank Dr. Huang for preparing the cloud sensitivity study. Dr. Christopher Hayden and Mr. Chris Moeller of CIMSS also offered many useful comments about the research.

Dr. Gary Jedlovec at NASA/Marshall Space Flight Center provided the MAMS imagery, assistance with its use, and helpful discussions. Mr. Steve Williams graciously provided COHMEX data and GOES imagery. Several persons at Florida State assisted in our

efforts: Jeff Orrock with data processing, Dewey Rudd with figure preparation, Anthony Guillory with countless computer matters, and Rick Knabb with preparing the satellite imagery.

This research was sponsored by the National Aeronautics and Space Administration. Headquarters program managers Drs. John Theon, Jim Dodge, and Ramesh Kakar were very supportive of these activities. Our grant NAG8-653 was coordinated through the Remote Sensing Branch of NASA's Marshall Space Flight Center.

#### REFERENCES

- Barnes, S. L., 1964: A technique for maximizing details in numerical weather map analysis. *J. Appl. Meteor.*, **3**, 396-409.
- , 1973: Mesoscale objective analysis using weighted time-series observations. NOAA Tech. Memo., ERL NSSL-62, 60 pp. [NTIS COM-73-10781.]
- , and D. K. Lilly, 1975: Covariance analysis of severe storm environments. Preprints, *Ninth Conf. on Severe Local Storms*, Norman, Amer. Meteor. Soc., 301-306.
- Betts, A. K., 1982: Saturation point analysis of moist convective overturning. *J. Atmos. Sci.*, **39**, 1484-1505.
- , 1985: Mixing line analysis of clouds and cloudy boundary layers. *J. Atmos. Sci.*, **42**, 2751-2763.
- , 1992: FIFE atmospheric boundary layer budget methods. *J. Geophys. Res.*, in press.
- , and B. A. Albrecht, 1987: Conserved variable analysis of the convective boundary layer thermodynamic structure over the tropical oceans. *J. Atmos. Sci.*, **44**, 83-99.
- Bradshaw, J. T., 1991: High resolution interferometer sounder (HIS) analyses of mesoscale phenomena. M.S. thesis, Department of Meteorology, Florida State University, Tallahassee, 146 pp. [Available from H. E. Fuelberg, Department of Meteorology, Florida State University, Tallahassee, FL 32306-3034.]
- Bruce, R. E., L. D. Duncan, and J. H. Pierluissi, 1977: Experimental study of the relationship between radiosonde temperatures and satellite-derived temperatures. *Mon. Wea. Rev.*, **105**, 493-496.
- Chesters, D. L., W. Uccellini, and A. Mostek, 1982: VISSR Atmospheric Sounder (VAS) simulation experiment for a severe storm environment. *Mon. Wea. Rev.*, **110**, 370-387.
- Dodge, J., J. Arnold, G. Wilson, J. Evans, and T. Fujita, 1986: The Cooperative Huntsville Meteorological Experiment (COHMEX). *Bull. Amer. Meteor. Soc.*, **67**, 417.
- Franklin, J. L., C. S. Velden, J. Kaplan, and C. M. Hayden, 1990: Some comparisons of VAS and dropwindsonde data over the subtropical Atlantic. *Mon. Wea. Rev.*, **118**, 1869-1887.
- Fuelberg, H. E., and P. J. Meyer, 1984: An analysis of the AVESESAME I period using statistical structure and correlation functions. *Mon. Wea. Rev.*, **112**, 1562-1576.
- , and —, 1986: An analysis of mesoscale VAS retrievals using statistical structure functions. *J. Climate Appl. Meteor.*, **25**, 59-76.
- , and S. R. Olson, 1991: An assessment of VAS-derived retrievals and parameters used in thunderstorm forecasting. *Mon. Wea. Rev.*, **119**, 795-814.
- , and J. P. Breidenbach, 1992: Time trends of VAS satellite-derived soundings. *Mon. Wea. Rev.*, **120**, 1603-1615.
- Gandin, L. S., 1963: *Objective Analysis of Meteorological Fields*. Translated from Russian, Israel Program for Scientific Translations, 242 pp. [NTIS TT-65-50007].
- Hayden, C. M., 1988: GOES-VAS simultaneous temperature-moisture retrieval algorithm. *J. Appl. Meteor.*, **27**, 705-733.
- Hilger, D. W., and T. H. Vonder Haar, 1979: An analysis of satellite infrared soundings at the mesoscale using statistical structure and correlation functions. *J. Atmos. Sci.*, **36**, 287-305.

- Hoehne, W. E., 1980: Precision of National Weather Service upper-air measurements. NOAA Tech. Memo., NWS T&ED-16, 23 pp. [NTIS PB81-108136.]
- Huang, H.-L., 1989: An analysis of the characteristics of atmospheric profiles obtained with the high-resolution interferometer sounder (HIS). Ph.D. dissertation, University of Wisconsin-Madison, 145 pp.
- , W. L. Smith, and H. M. Woolf, 1992: Vertical resolution and accuracy of atmospheric infrared sounding spectrometers. *J. Appl. Meteor.*, **31**, 265–274.
- Jedlovec, G. J., 1985: An evaluation and comparison of vertical profile data from the VISSR Atmospheric Sounder (VAS). *J. Atmos. Oceanic Technol.*, **2**, 559–581.
- , 1990: Precipitable water estimation from high-resolution split window radiance measurements. *J. Appl. Meteor.*, **29**, 863–877.
- , W. P. Menzel, R. J. Atkinson, and G. S. Wilson, 1986: The Multispectral Atmospheric Mapping Sensor (MAMS): Instrument description, calibration, and data quality. NASA Tech. Memo., 86565, 37 pp. [Available from G. J. Jedlovec, ES-43, Marshall Space Center, Huntsville, AL 35812.]
- , K. B. Batson, R. J. Atkinson, C. C. Moeller, W. P. Menzel, and M. W. James, 1989: Improved capabilities of the Multispectral Atmospheric Mapping Sensor (MAMS). NASA Tech. Memo., 100352, 80 pp. [Available from G. J. Jedlovec, ES-43, Marshall Space Center, Huntsville, AL 35812.]
- McMillin, L. M., D. G. Gray, H. F. Drahos, M. W. Chalfant, and C. S. Novak, 1983: Improvements in the accuracy of operational satellite soundings. *J. Climate Appl. Meteor.*, **22**, 1948–1955.
- Moyer, V., J. R. Scoggins, N. M. Chou, and G. S. Wilson, 1978: Atmospheric structure deduced from routine Nimbus 6 satellite data. *Mon. Wea. Rev.*, **106**, 1340–1351.
- Nordahl, L. S., 1982: Response to correspondence by R. W. Shaffer. *Bull. Amer. Meteor. Soc.*, **63**, 1394.
- Peterson, D. P., and D. Middleton, 1963: On representative observations. *Tellus*, **15**, 387–405.
- Pratt, R. W., 1985: Review of radiosonde humidity and temperature errors. *J. Atmos. Oceanic Technol.*, **2**, 404–407.
- Rabin, R. M., S. J. Stadler, P. J. Wetzel, D. J. Stensrud, and M. Gregory, 1990: Observed effects of landscape variability on convective clouds. *Bull. Amer. Meteor. Soc.*, **71**, 272–280.
- , L. A. McMurdie, C. M. Hayden, and G. S. Wade, 1991: Monitoring precipitable water and surface wind over the Gulf of Mexico from microwave and VAS satellite imagery. *Wea. Forecasting*, **6**, 227–243.
- Revercomb, H. E., H. Buijs, H. B. Howell, D. D. LaPorte, W. L. Smith, and L. A. Sromovsky, 1988a: Radiometric calibration of IR Fourier transform spectrometers: Solution to a problem with the high-resolution interferometer sounder. *Appl. Opt.*, **27**, 3210–3218.
- , D. D. LaPorte, W. L. Smith, H. Buijs, D. G. Murcray, F. J. Murcray, and L. A. Sromovsky, 1988b: High-altitude aircraft measurements of upwelling IR radiance: Prelude to FTIR from geosynchronous satellite. *Mikrochimica Acta*, 439–444.
- Schlatter, T. W., 1981: An assessment of operational TIROS-N temperature retrievals over the United States. *Mon. Wea. Rev.*, **109**, 110–119.
- Smith, E. A., H. J. Cooper, W. L. Crosson, and D. D. Delorey, 1991: Retrieval of surface heat and moisture fluxes from slow-launched radiosondes. *J. Appl. Meteor.*, **30**, 1613–1626.
- Smith, W. L., H. B. Howell, and H. M. Woolf, 1979: The use of interferometric radiance measurements of sounding the atmosphere. *J. Atmos. Sci.*, **36**, 566–575.
- , V. E. Suomi, W. P. Menzel, H. M. Woolf, L. A. Sromovsky, H. E. Revercomb, C. M. Hayden, D. N. Erickson, and F. R. Mosher, 1981: First sounding results from VAS-D. *Bull. Amer. Meteor. Soc.*, **62**, 232–236.
- , H. M. Woolf, and A. J. Schreiner, 1985: Simultaneous retrieval of surface atmospheric parameters: A physical and analytically direct approach. *Advances in Remote Sensing*, A. Deepak, H. E. Fleming, and M. T. Chahine, Eds., A. Deepak Publishing, 221–232.
- , —, H. B. Howell, H. E. Revercomb, and H. L. Huang, 1988: High resolution interferometer sounder—The retrieval of atmospheric temperature and water vapor profiles. Preprints, *Third Conf. Satellite Meteorology*, Anaheim, Amer. Meteor. Soc., 266–271.
- , H. E. Revercomb, H. B. Howell, H. L. Huang, R. O. Knuteson, E. W. Koenig, D. D. LaPorte, S. Silverman, L. A. Sromovsky, and H. M. Woolf, 1990: GHIS—The GOES high-resolution interferometer sounder. *J. Appl. Meteor.*, **29**, 1189–1204.
- , H. M. Woolf, and H. E. Revercomb, 1991: A linear simultaneous solution for temperature and absorbing constituent profiles from radiance spectra. *Appl. Opt.*, **30**, 1117–1123.
- Sugita, M., and W. Brutsaert, 1990: How similar are temperature and humidity profiles in the unstable boundary layer? *J. Appl. Meteor.*, **29**, 489–497.
- Tennekes, H., 1973: A model for the dynamics of the inversion above a convective boundary layer. *J. Atmos. Sci.*, **30**, 558–567.
- Wilde, N. P., R. B. Stull, and E. W. Eloranta, 1985: The LCL zone and cumulus onset. *J. Climate Appl. Meteor.*, **24**, 640–657.
- Williams, S. F., H. M. Goodman, K. R. Knupp, and J. E. Arnold, 1987: Space/COHMEX Data Inventory Document. NASA Tech Memo., 4006, 480 pp. [Available from J. Arnold, ES-43, Marshall Space Center, Huntsville, AL 35812.]



## An Assessment of VAS-Derived Retrievals and Parameters Used in Thunderstorm Forecasting

HENRY E. FUELBERG AND STEVEN R. OLSON

*Department of Meteorology, Florida State University, Tallahassee, Florida*

(Manuscript received 11 June 1990, in final form 21 September 1990)

### ABSTRACT

Operational VAS satellite retrievals and derived parameters used in forecasting severe local storms were evaluated against corresponding radiosonde values. VAS products also were compared with the first-guess input to the retrieval algorithm. The evaluation methodology was to pair each radiosonde observation (RAOB) with the closest VAS retrieval within 50 km during a 4-month period in 1986.

VAS temperatures were found to agree closely with radiosonde values; however, VAS dewpoints showed somewhat less agreement. VAS/RAOB sounding differences were poorly correlated with the number of pixels from which the retrievals were prepared. VAS discrepancies usually were not well correlated with first-guess errors. A disappointing finding is that the retrievals degraded the first guess about as often as they improved it. VAS did tend to improve large first-guess errors, but not even this was guaranteed. Horizontal gradients of VAS products generally were stronger than those from radiosondes. VAS precipitable water agreed better with the ground truth than did dewpoints at individual levels, but VAS thicknesses were not much improved over the already accurate VAS temperatures.

Results for the severe storms forecasting parameters indicated that VAS/RAOB discrepancies increased with the amount of manipulation required during computation. VAS parameters incorporating observed surface data tended to give better results than those that did not. Of all the parameters examined, VAS-derived lifted index exhibited the best agreement with RAOB versions. VAS positive buoyant energy showed disappointingly poor comparisons. VAS retrievals provided poor measures of the low-level negative buoyant energy that must be overcome before convection can begin. Agreements between VAS/RAOB versions of the *K* index, total totals index, Showalter index, and several other parameters were intermediate to those of positive buoyant energy and lifted index.

### 1. Introduction

Geostationary meteorological satellites launched by the United States since September 1980 have contained the Visible Infrared Spin Scan Radiometer (VISSR) Atmospheric Sounder (VAS). With seven temperature, three water vapor, and two window channels, VAS provides infrared radiances from which vertical profiles of temperature and humidity (i.e., retrievals) can be derived. Details about the VAS instrument can be found in Menzel et al. (1981), Smith et al. (1981), and Chesters and Uccellini (1982).

VAS retrievals have been made using both statistical and physical algorithms. Although the statistical algorithm (Lee et al. 1983) has not been used operationally, case studies have demonstrated that its soundings can help define the preconvective environment (e.g., Mostek et al. 1986). Soundings based on the current version of the physical algorithm, the simultaneous form (Smith et al. 1985; Hayden 1988), have been employed in specific case studies by several

groups and in the operational mode by personnel at the National Severe Storms Forecast Center (NSSFCC). NSSFCC forecasters generally use VAS retrievals to better locate stability and humidity features and their evolutions—not to determine their absolute magnitudes (Wade et al. 1985; Mosher and Schoeni 1988; Zehr et al. 1988; Fuelberg et al. 1991; and Ellrod 1989)—have used simultaneous physical retrievals in case studies to detect mesoscale aspects of the preconvective environment.

VAS retrievals obtained from the current simultaneous algorithm have been evaluated to a limited extent. Hayden (1988) compared them against a special set of radiosonde data (RAOBs) on 6 March 1982. He noted the weakness of bias errors and a dependence on the numerically derived temperature/dewpoint profiles that serve as first-guess input to the algorithm. Strengths included the capacity to improve horizontal patterns and gradients from the first guess. Velden et al. (1984) presented statistical comparisons between VAS retrievals and dropwindsonde data over the tropical Atlantic Ocean. Franklin and Lord (1988) and Franklin et al. (1989) found that synoptic-scale horizontal fields and gradients of VAS data over the same

---

*Corresponding author address:* Professor Henry E. Fuelberg, Dept. of Meteorology, The Florida State University, Tallahassee, FL 32306.

region were not consistently better than those derived from dropwindsondes on the two days examined. Their VAS-derived patterns also were not consistently improved over those from the first guess.

There has been little evaluation of VAS-derived parameters frequently used in forecasting severe thunderstorms. Wade et al. (1985) compared VAS and RAOB versions of precipitable water, total totals index, and lifted index over a period of several days. Taking a considerably different approach, Kitzmiller and McGovern (1989) related the two versions of thunderstorm forecasting parameters with the actual occurrence of convective activity. The relative information content of the first-guess input also was considered. Although some VAS parameters were found to be more useful than others in forecasting thunderstorm development, they provided little additional predictive information over the first-guess data.

The current paper should interest those who plan to use VAS retrievals in diagnostic studies or in numerical prediction models because it presents a detailed evaluation of operational VAS retrievals by comparing them against RAOBs. It differs from the previously cited studies in that retrievals over a several month period are examined. The paper will be of special interest for those planning to use VAS retrievals in severe storm activities because it also assesses VAS-derived parameters commonly used in forecasting convection (e.g., positive buoyant energy, lifted index, height of the wet-bulb zero). Other sections of the paper describe correlations between VAS discrepancies and first-guess errors, VAS improvements over first-guess data, comparative magnitudes of VAS horizontal gradients, and advantages of using VAS vertically integrated parameters such as precipitable water.

## 2. Methodology

The evaluation methodology was to pair RAOBs with their closest VAS retrievals. The period for study was 21 March–23 July 1986, i.e., when the National Environmental Satellite, Data, and Information Service (NESDIS) prepared VAS retrievals operationally for the NSSFC during 1986. The area of interest was the United States east of the Rocky Mountains. Since the Rapid Interval Scan Operations Plan (RISOP) mode interrupts VAS sounding procedures during convective storm outbreaks, 0000 UTC VAS data frequently were unavailable. Consequently, this study only evaluated early morning retrievals near 1200 UTC.

The VAS retrievals were prepared operationally by personnel of the NESDIS Advanced Satellite Products Project in Madison, Wisconsin, using the Smith et al. (1985) simultaneous physical algorithm. Hayden (1988) presents an excellent description of the procedures involved. Retrievals between 1100–1148 UTC were closest to the 1200 UTC radiosonde soundings. Soundings in areas without extensive cloud cover were

available at separations of approximately 100 km. The VAS profiles consisted of temperature and dewpoint at the surface: 1000, 950, 920, 850, 780, 700, 670, 500, 400, 300, 250, 200, 150, and 100 mb. First-guess temperature and dewpoint data also were available at these levels. The first-guess information consisted of the 12-h (1200 UTC) forecast from the 0000 UTC run of the limited-area fine mesh (LFM) model. Observed surface data from 1100 UTC had been blended into the first-guess LFM profiles through 850 mb. NESDIS procedures denoted the VAS retrievals made in cloudy areas as well as those that did not satisfy quality control criteria. These types of retrievals were not used in the current study; however, the remaining data were accepted at face value, i.e., without additional screening.

RAOBs from the standard National Weather Service network were utilized. They were obtained from archives at the National Climatic Data Center. Although called 1200 UTC data, the sondes generally are released between 1100–1115 UTC, requiring approximately 20 min to reach 500 mb and 60 min to reach 100 mb. Temperature and relative humidity were provided as functions of pressure at both mandatory and significant levels. Dewpoint temperatures were calculated using standard techniques.

The specification of VAS/RAOB pairs followed simple criteria. Only the 1100–1148 UTC retrievals were used, and only the single closest VAS retrieval was matched with each radiosonde report. To minimize VAS/RAOB differences arising from horizontal gradients, the pairings were required to be collocated within 50 km. A total of 1108 VAS/RAOB sounding pairs met these requirements.

VAS and radiosondes sample the atmosphere in fundamentally different ways. Sondes are direct sensors, producing virtually point-source measurements, while VAS is a remote sensor that provides only volume-averaged data. Since VAS has only 12 channels, each sampling a broad layer of the atmosphere, it is unable to resolve finescale vertical structures such as inversions and shallow humidity features. VAS retrievals also represent horizontal averages since radiances from a number of individual fields-of-view (pixels) are combined.

Discrepancies between VAS and radiosonde soundings will overestimate the true VAS retrieval error because the discrepancies also include error due to VAS/RAOB noncollocation in space and time, as well as errors in the sonde data. An attempt to minimize collocation errors has been made through the pairing procedures described above; however, they have not been eliminated. Root-mean-square errors of radiosonde temperatures have been estimated to range from 0.5° to 0.8°C, and generally under 20% for relative humidity (Hoehne 1980; Pratt 1985). Bruce et al. (1977) and McMillin et al. (1983) discuss in greater detail the roles of collocation and sonde errors in satellite sounding evaluation.

3. Temperature and dewpoint evaluations

Before evaluating the VAS-derived severe storm forecasting parameters, it is informative to examine the VAS temperature and dewpoint data that serve as input for those parameters. Solid lines in Fig. 1 describe VAS/RAOB temperature comparisons for the 1108 paired soundings near 1200 UTC. Mean differences (VAS minus RAOB) range from  $-1.0^{\circ}$  to  $1.5^{\circ}\text{C}$ . The near-zero value at the surface probably represents the favorable influence of the observed 1100 UTC surface data. The levels of maximum positive bias, where VAS

values are too warm, are just above the surface and near 200 mb. These levels probably occur because VAS is unable to adequately resolve temperature inversions. At the surface, radiation inversions are very common in the early morning, and many of the radiosonde soundings also depicted lids or capping layers at slightly higher levels which were most common during the spring. The positive maximum near 200 mb and the layer of strong cold bias near 100 mb are associated with the tropopause. Standard deviations of VAS/RAOB temperature discrepancies (Fig. 1) are near  $1.8^{\circ}\text{C}$  showing little variation with height. This value

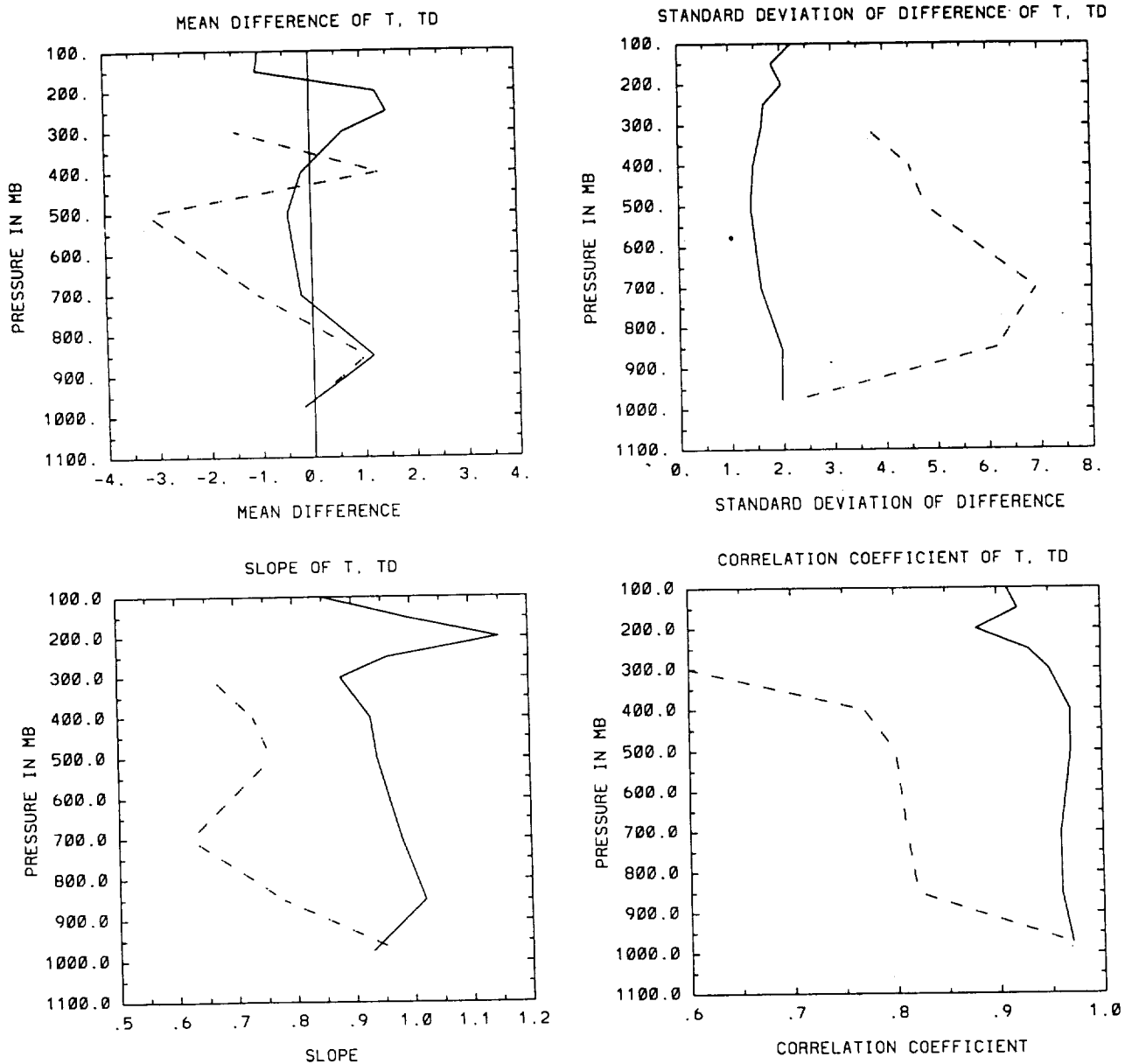


FIG. 1. Mean difference ( $^{\circ}\text{C}$ ), standard deviation of differences ( $^{\circ}\text{C}$ ), slope, and correlation coefficient between VAS and RAOB temperature (solid) and dewpoint (dashed) as functions of pressure.

is similar to those for the TIROS and NOAA series of polar orbiting sounders (McMillin et al. 1983; Schlatter 1981).

A least squares procedure was used to calculate linear best-fit regression lines between the VAS and RAOB temperatures. A slope of 1.0 indicates that VAS values always agree with the sonde-derived versions or that they are uniformly warm or cold biased over all temperature values. Slopes not equal to 1.0 imply a differential bias. For example, if the slope exceeds 1.0, VAS values are too warm at cold RAOB temperatures and/or too cold at warm RAOB temperatures. The current results (Fig. 1), ranging between 0.85 and 1.15, suggest that differential bias is not pronounced. Linear correlation coefficients between the two sources of temperature also were calculated. These values (Fig. 1) are quite large, only varying between 0.88 and 0.97, with minima near the tropopause.

Scatter diagrams of VAS/RAOB temperatures at individual levels show the range of RAOB temperatures that occur with a particular VAS value. Figure 2 (top) contains panels for levels of comparatively good (500 mb) and poor (200 mb) agreement where each dot represents a VAS/RAOB pairing. At 200 mb (500 mb) a VAS temperature of 220 K (260 K) corresponds to RAOB temperatures between 215 and 225 K (258 and 264 K). Such discrepancies obviously will affect the values of derived parameters that are discussed in later sections.

VAS/RAOB dewpoint evaluations are denoted by the dashed lines in Fig. 1. Compared to the temperatures, VAS dewpoints do not compare as favorably with the sonde data. Mean differences indicate greatest moisture bias in the middle troposphere where VAS averages are as much as 3°C too cold (dry). Standard deviations of differences are largest near 700 mb where values approach 7°C. These values also are consistent with those from polar orbiting sounders (e.g., Moyer et al. 1978). Magnitudes of linear slope decrease upward from the surface, reaching a minimum of 0.62 at 700 mb. Correlations are less than 0.8, except near the surface. Each of the four dewpoint statistics indicates best VAS/RAOB agreement near the surface, again reflecting the favorable influence of the 1100 UTC surface data that are blended into the first guess through 850 mb. The relatively poor values in the lower and middle troposphere coincide with increasing distance from the observed surface data and with large vertical gradients of water vapor that occur in many soundings (e.g., subsidence or capping inversions).

Scatter diagrams of 700 mb (400 mb) dewpoints (Fig. 2 bottom) illustrate levels of relatively poor (better) agreement in terms of standard deviations of differences. Compared to the temperature panels, the greater degree of scatter is readily apparent. For a VAS 700 mb (400 mb) dewpoint of 265 K (240 K), RAOB values range from 250–280 K (230–255 K). The linear slopes of 0.62 and 0.73 indicate considerable differential

bias. Specifically, VAS dewpoints tend to be cold biased (too dry) for cold RAOB values and warm biased (too humid) for warm RAOB values.

#### 4. Factors associated with discrepancies

VAS/RAOB discrepancies were related to two factors. The first is the number of fields-of-view (FOVs) comprising each retrieval. A maximum of 121 FOVs had been used, i.e., an  $11 \times 11$  array of 7-km pixels (Hayden 1988). Cloud contaminated FOVs were excluded from this maximum number with the retrieval then calculated from the average of the remaining FOV radiances. Theoretically, retrievals from more (fewer) FOVs should exhibit smaller (larger) VAS/RAOB discrepancies because random error is reduced by the inverse of the square root of the number of FOVs employed. In addition, one can hypothesize that undetected cloud contaminated FOVs would be more likely in the cloudier areas where many pixels already had been detected and excluded.

Scatter diagrams relating the number of FOVs utilized in a retrieval to the corresponding VAS/RAOB discrepancy are given in Fig. 3. The panels for 700-mb temperature (top) and dewpoint (bottom) are typical of those at other levels. Results for both actual differences (left) and absolute values of differences (right) are shown. Each panel shows a large amount of scatter with slopes near zero. Thus, errors associated with 121 FOVs are only slightly smaller (or sometimes even larger) than those associated with far fewer FOVs. This lack of correlation suggests that the algorithm's cloud detection scheme is performing well, although it does not explain the range of VAS/RAOB discrepancies observed in Figs. 1 and 2. The results also suggest that useful retrievals could be generated from fewer FOVs than currently used, supporting the results of Hillger and Vonder Haar (1988).

This study also considers whether VAS retrieval errors were correlated with errors of the first guess (FG). Specifically, correlation coefficients were calculated between absolute values of VAS/RAOB discrepancies and FG/RAOB discrepancies at five levels between 850 and 200 mb. In the case of temperature, the correlations ranged from 0.80 at 200 mb to 0.28 at 700 mb with the average for the five levels being 0.51. The values did not vary with height in a clearly identifiable manner. For dewpoints, the correlations were even smaller, ranging from 0.53 at 850 mb to  $-0.09$  at 400 mb, with a vertical average of 0.31. These correlations decreased with altitude through 400 mb and then increased again at higher levels. The results suggest that VAS dewpoints are less first-guess dependent than VAS temperatures.

Scatter diagrams for 200- and 700-mb temperature (the levels of greatest and smallest correlation) as well as 400- and 700-mb dewpoint are shown in Fig. 4. Retrievals at 850 mb are influenced by the surface data;

therefore, the dewpoint diagram at 700 mb is shown because it had the second greatest correlation. Since slopes of linear best-fit regression lines are less than 1.0, VAS discrepancies tend to be relatively large at small values of FG difference, and relatively small at large values of FG difference. As an example of the scatter, a 700-mb FG dewpoint error of 5°C (Fig. 4) is associated with VAS discrepancies ranging from 0° to 20°C. Current results indicate considerably less correlation between the FG and VAS discrepancies than

observed on 6 March 1982 (Hayden 1988). Nonetheless, it is clear that good FG data are vital to the retrieval process, i.e., a good first guess helps produce a good VAS retrieval.

5. Improvements over the first guess

Operational numerical models such as the LFM and nested grid model are providing valuable and increasingly accurate forecast guidance. Although one hopes

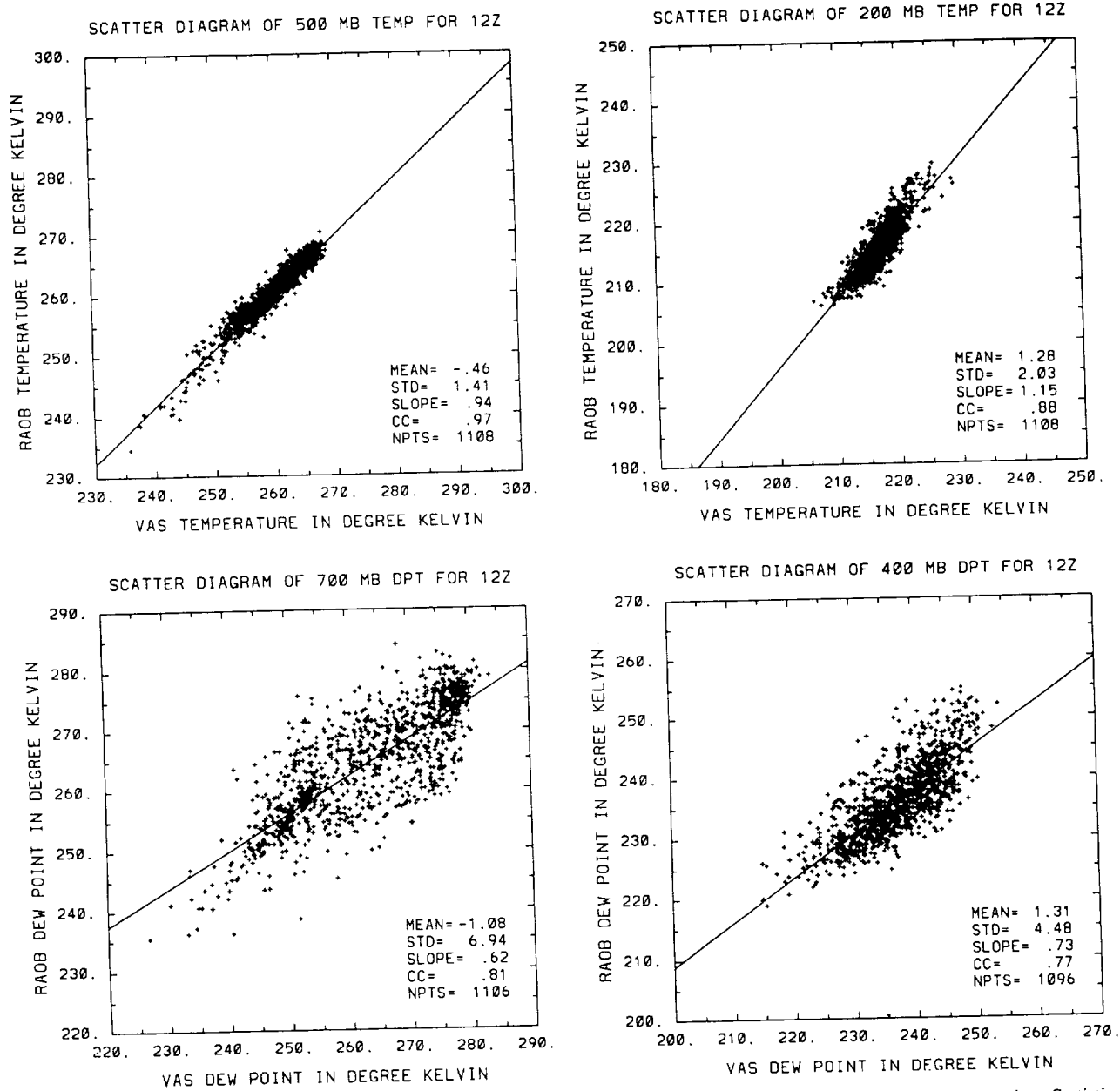


FIG. 2. Scatter diagrams of RAOB versus VAS (top) 500- and 200-mb temperatures (°C); (bottom) 700- and 400-mb dewpoints. Statistics and best fit regression lines are shown. "Mean" denotes mean differences between VAS/RAOB data; STD is the standard deviation of differences; "slope" is the linear best fit slope between VAS/RAOB values; CC is the linear correlation between values; and NPTS is the number of VAS/RAOB data pairs comprising the sample.

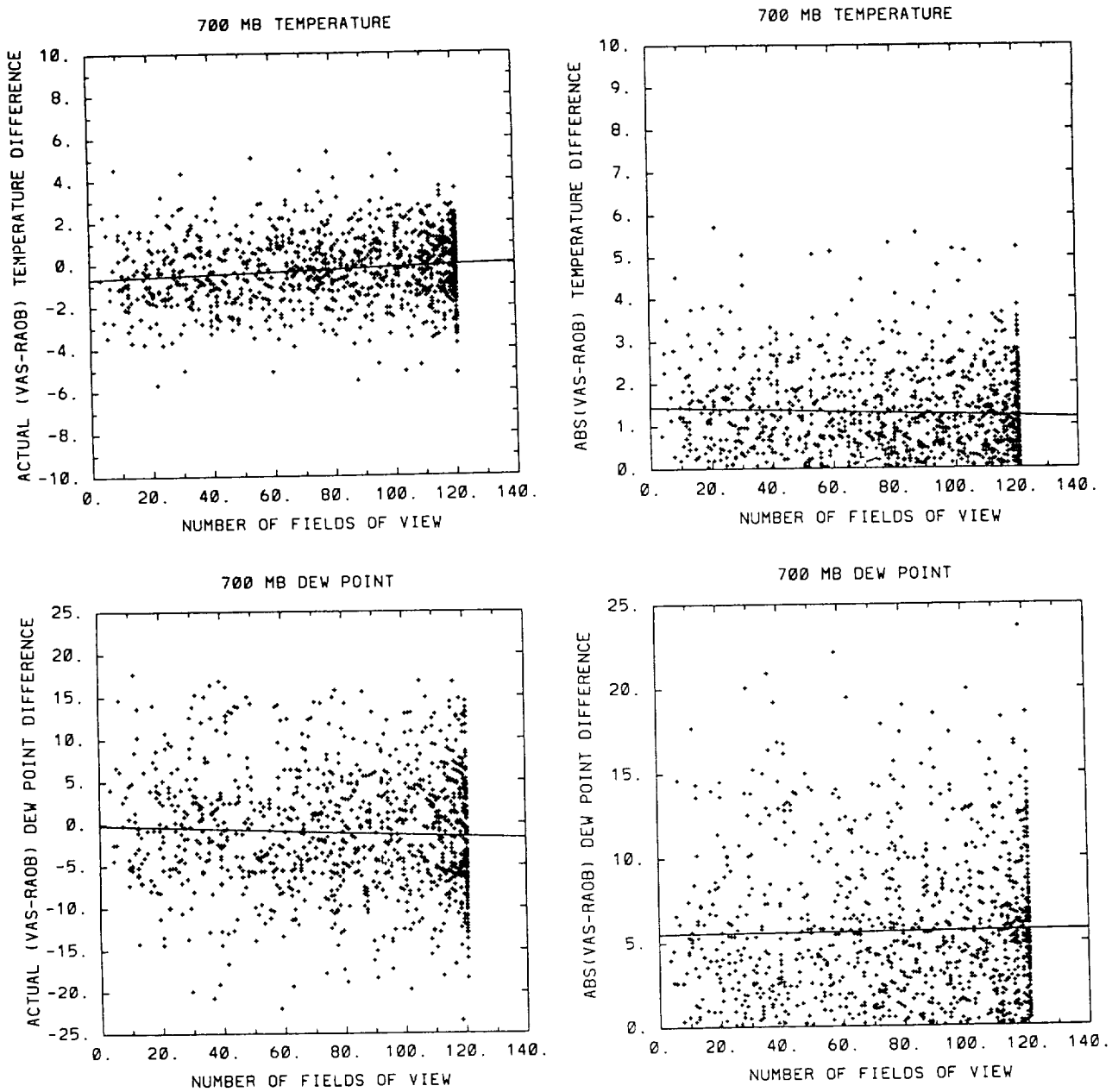


FIG. 3. Scatter diagrams of (left) actual and (right) absolute values of (VAS-RAOB) (top) 700-mb temperature differences ( $^{\circ}\text{C}$ ) versus number of fields-of-view; (bottom) 700-mb dewpoint differences ( $^{\circ}\text{C}$ ) versus number of fields of view. Best fit regression lines are shown.

that VAS retrievals are superior to soundings from numerical models, the results were mixed for the south-central United States on 6 March 1982 (Hayden 1988) and the tropical Atlantic on two case days (Franklin and Lord 1988; Franklin et al. 1989). By considering a 4-month period, the current study includes situations ranging from accurate to poor LFM-FG data. The current procedure differed from that of earlier studies since calculations indicate the degree to which retrievals are an improvement on the 12-h LFM-FG data. Improvement is defined as any sounding change that brings the

VAS retrieval closer than the FG to the RAOB profile. Using temperatures as an example, if  $\text{VAS} = 4^{\circ}\text{C}$ ,  $\text{FG} = 7^{\circ}\text{C}$ , and  $\text{RAOB} = 5^{\circ}\text{C}$ , the difference between VAS and the FG is  $3^{\circ}\text{C}$ ; however, VAS provides only a  $1^{\circ}\text{C}$  improvement over the FG. Negative improvements signify that VAS data compare less favorably with the RAOBs than do the FG. Calculations were made at five levels between 850 and 200 mb.

In the case of temperature, histograms for 700 mb (200 mb) (top of Fig. 5) illustrate the levels of greatest (least) improvement over the FG. Results for 700 mb

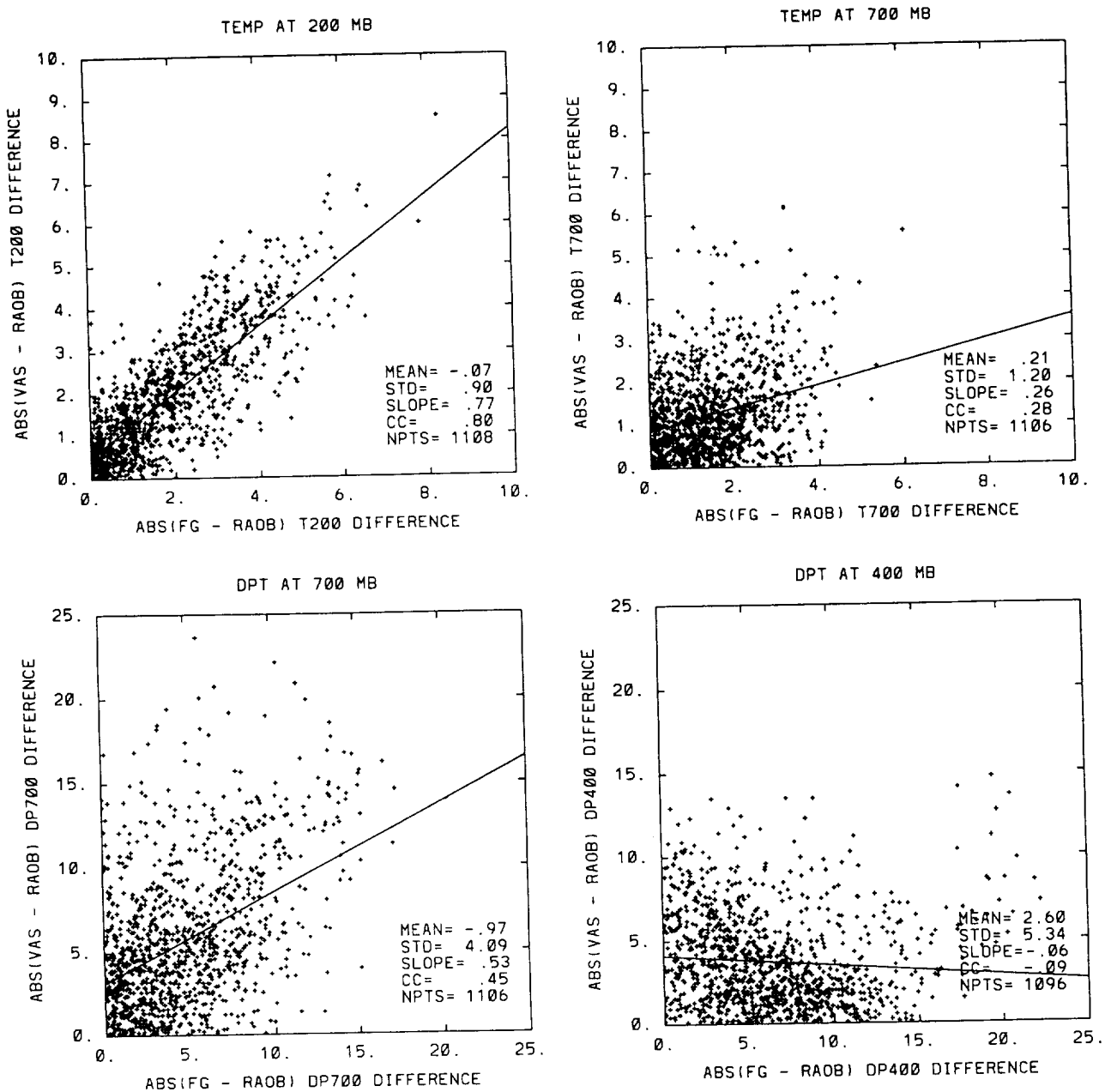


FIG. 4. Scatter diagrams of VAS absolute error versus FG absolute error for (top) 200- and 700-mb temperature ( $^{\circ}\text{C}$ ) and (bottom) 700- and 400-mb dewpoint ( $^{\circ}\text{C}$ ).

show a peak at positive values, and there are more cases of improvement than degradation of the FG. Conversely, at 200 mb, there are more cases when VAS temperatures are inferior to the FG. These levels represent the extreme cases, but when all levels are considered (not shown), the general finding is that VAS improvements are normally distributed about zero. Thus, the first guess is degraded about as often as it is improved—a more disappointing finding than occurred on 6 March 1982 (Hayden 1988).

To explore this issue in greater detail, VAS/FG im-

provements were related to errors in the FG data. With a perfect FG, VAS cannot provide a better sounding; however, VAS could yield improvement when the FG does not agree with the RAOB. Results for temperature at 700 and 200 mb are given at the top of Fig. 6. At 700 mb, the slope and correlation values are 0.74 and 0.63, respectively, while corresponding statistics at 200 mb are only 0.23 and 0.36. The diagrams show that large FG errors generally are associated with the greatest amount of VAS improvement; however, the relation is not as strong as one would like, and there is a large

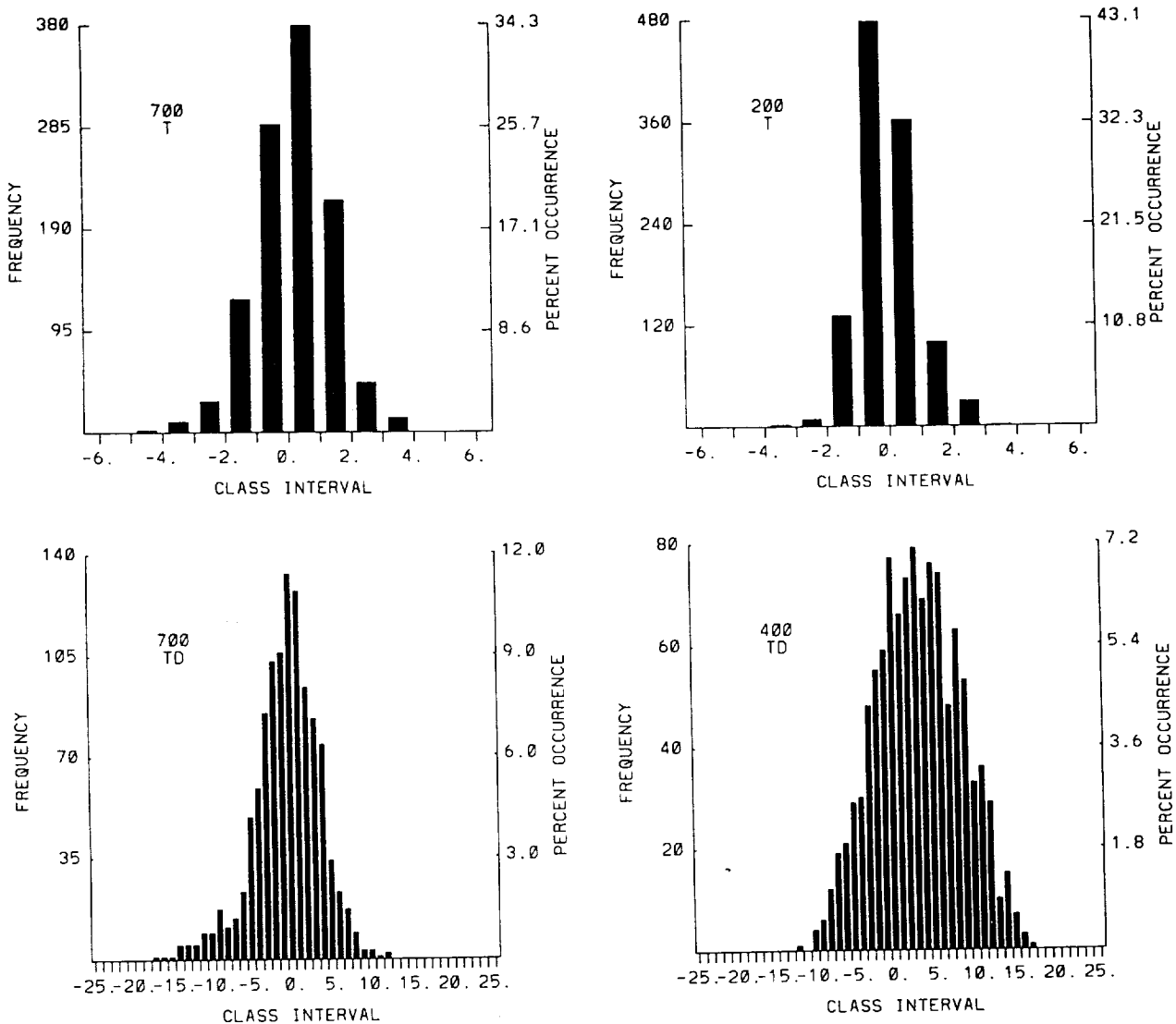


FIG. 5. Histograms of (top) VAS improvement over FG for 700- and 200-mb temperatures ( $^{\circ}\text{C}$ ); (bottom) VAS improvement over FG for 700- and 400-mb dewpoints ( $^{\circ}\text{C}$ ).

amount of scatter. Thus, improvement (positive values) is not guaranteed even for large FG errors. At 200 mb, for example, VAS retrievals sometimes are worse than the FG even when the guess error is more than  $4^{\circ}\text{C}$ .

For the dewpoints, the histograms at 400 mb (700 mb) (bottom of Fig. 5) represent the levels of greatest (least) VAS improvement over the FG. The histogram for 700 mb shows that VAS retrievals are inferior to the FG 61% of the time, and superior to the FG in only 39% of the cases. The situation is reversed at 400 mb, perhaps due to VAS's  $6.7\text{-}\mu\text{m}$  water-vapor channel whose weighting function peaks near 400 mb in standard atmospheric conditions.

When VAS dewpoint improvements are related to FG errors (bottom of Fig. 6), the results at 700 mb are

comparable to those for temperature, i.e., the variables have only the modest correlation of 0.40. At 400 mb, however, VAS improvements are more highly correlated (0.85) with FG errors. In fact, retrievals always are superior to the FG when the FG error exceeds  $10^{\circ}\text{C}$ . From the perspective of severe storm forecasting, greater improvements would have been desired in the lower troposphere (e.g., 700 mb) since vapor content in that region is a major factor in determining convective instability.

## 6. Horizontal gradients

Regions of strong horizontal temperature and/or dewpoint gradients are preferred regions of convective formation (e.g., Miller 1972). The relative strengths



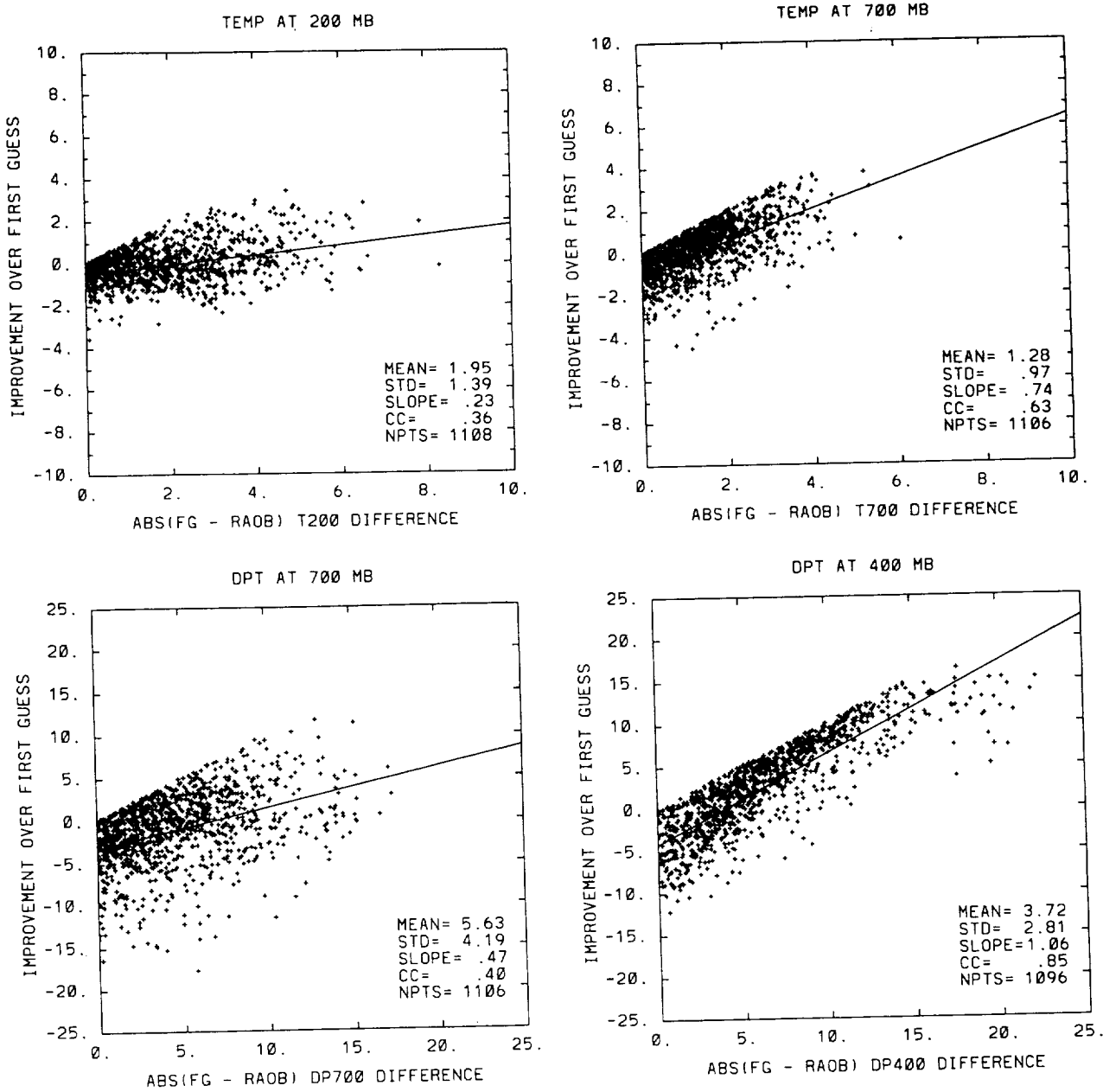


FIG. 6. Scatter diagrams of VAS improvement over FG for (top) 200- and 700-mb temperature ( $^{\circ}\text{C}$ ) and (bottom) 700- and 400-mb dewpoint ( $^{\circ}\text{C}$ ).

of VAS and RAOB gradients were examined in a manner similar to that of Hayden (1988). Specifically, the slope of the linear regression best-fit line between VAS/RAOB data (e.g., those in Fig. 2) gives the relative strengths. A slope less than 1.0 (greater than 1.0) implies an overestimate (underestimate) of the mean observed RAOB gradient. Similarly, the comparative magnitudes of FG and RAOB gradients can be evaluated from their linear slope.

Table 1 shows that VAS retrievals generally overestimate the observed temperature gradients. First-

guess temperature gradients at and below 500 mb also are stronger than observed, while above 500 mb the FG data produce weaker than observed gradients. The VAS and FG overestimates are comparable and relatively small, i.e., slopes are near 1.0. There are some levels where the VAS gradient differs more from the observed gradient (further from 1.0 slope) than does the FG variety. However, there are many more levels where the VAS temperature gradient is somewhat closer to the observed gradient than is the FG input.

VAS dewpoint gradients (Table 1) are a considerable

TABLE 1. Slopes of VAS and FG temperatures and dewpoints used to determine horizontal gradients. Values less than 1.0 indicate that VAS or the FG has overestimated the observed gradient.

Pressure (mb)	VAS slope	FG slope
Temperature		
100	0.85	1.03
150	0.99	1.12
200	1.15	1.32
250	0.96	1.16
300	0.88	1.07
400	0.93	1.07
500	0.94	0.98
700	0.98	0.90
850	1.02	0.96
Sfc	0.93	0.93
Dewpoint		
300	0.66	0.61
400	0.73	0.69
500	0.76	0.60
700	0.62	0.82
850	0.78	0.96
Sfc	0.96	0.97

overestimate of the observed gradients. The FG data also overestimate the gradients. In the lower troposphere, VAS gradients are stronger than the already too strong FG values. However, in the middle and upper troposphere, VAS gradients are slightly weaker than those of FG input, although they still overestimate the observed strength. It is discouraging that VAS does not consistently improve the FG gradients.

Current results contrast with those on 6 March 1982 (Hayden 1988) when VAS retrievals underestimated both the observed temperature and dewpoint gradients. An earlier version of the VAS physical algorithm (Smith 1983) also produced weaker gradients on that same date (Fuelberg and Meyer 1986; Jedlovec 1985). The 6 March case was colder and drier than probably any day in the current 4-month period. This and the general goodness of the FG on 6 March may explain the differing findings. Franklin et al. (1989) suggested the VAS retrievals were an improvement on the phase, but not necessarily the placement of horizontal variations. However, these aspects were not considered in the current study.

### 7. Vertically integrated parameters

Vertically integrated VAS parameters, rather than level specific data, are assumed to compare more favorably with their respective sonde-derived counterparts because integration should minimize VAS's problem of poor vertical resolution (e.g., Zehr et al. 1988). To quantify this hypothesis, thickness and precipitable water were calculated over various layers from both sounding sources. Data from all available levels were utilized. Table 2 contains evaluation statistics for

thickness and temperature as well as precipitable water and dewpoint. The temperature and dewpoint statistics are averages of those at pressure levels common to both the VAS and RAOB soundings used in the vertical integration.

Results for precipitable water (Table 2) support the use of vertical integration since its slopes and correlations are greater than those of the dewpoints. As an example, VAS surface to 300-mb precipitable water has a 0.94 correlation with the corresponding radiosonde values, while the average dewpoint correlation for the intervening levels of this layer is only 0.81. The greater slope for precipitable water (0.88 versus 0.82) indicates an improvement over the excessively large gradients observed with the level specific data (Table 1). In general, the degree to which integration improves the slopes and correlations is directly proportional to the depth of the layer considered.

Results for thickness (Table 2) are less impressive than those of dewpoint. Slopes and correlation coefficients for thickness only are slightly greater than those of temperature. Because the temperature statistics already exceed 0.9 at most levels (Fig. 1), it would be difficult for integration to yield much additional improvement.

### 8. Thunderstorm forecasting parameters

Many parameters have been developed to help forecasters diagnose the humidity and stability conditions that are conducive to convective development (Miller 1972; Pepler 1988). With the differences in sensing methodology between VAS and radiosondes, and the

TABLE 2. A comparison of slope and correlation coefficients for thickness and precipitable water (*P* water) with temperature and dewpoint statistics averaged over the same layers.

<i>P</i> water layer (mb)	Slope		Correlation	
	Average dewpoint	<i>P</i> water	Average dewpoint	<i>P</i> water
Sfc-300	0.82	0.88	0.81	0.94
850-300	0.71	0.73	0.76	0.89
850-500	0.72	0.72	0.81	0.88
850-700	0.70	0.70	0.82	0.85
700-400	0.70	0.74	0.79	0.87
500-400	0.75	0.88	0.79	0.82

Thickness layer (mb)	Slope		Correlation	
	Average temperature	Thickness	Average temperature	Thickness
1000-500	0.93	0.95	0.93	0.98
1000-700	0.93	0.99	0.93	0.98
700-500	0.96	0.93	0.97	0.98
500-300	0.92	0.94	0.96	0.98
850-300	0.95	0.95	0.96	0.99
1000-850	0.94	1.04	0.93	0.96
1000-300	0.92	0.95	0.94	0.99

resulting discrepancies between the two sets of sounding data, some thunderstorm parameters with VAS input should agree better with their sonde-derived counterparts than others. This section investigates that issue.

#### a. Stability parameters involving lifting

The lifted index (Galway 1956) and positive/negative buoyant energy are widely used stability parameters that involve the lifting of subcloud air parcels. Although the low-level parcel has been defined in various ways, this study followed the procedure of Zehr et al. (1988) who specified it to be the mean lowest kilometer of the atmosphere. The mean lowest kilometer (MLK) temperatures and mixing ratios were simple averages of those within 1000 m of the surface. VAS retrievals usually contained fewer of these data levels than the RAOBs. Discrepancies between VAS/RAOB MLK data will be described first, followed by discrepancies of intermediate parameters used in obtaining the lifted index and energies, and ending with the stability parameters themselves. The propagation of errors through the various steps of calculation will be examined.

Figure 7 contains scatter diagrams and associated statistics comparing VAS/RAOB versions of MLK temperatures and dewpoints calculated from the MLK mixing ratios. The agreements for both parameters are quite good with slopes and correlation coefficients near or exceeding 0.9. The use of observed hourly temperature and dewpoint data in the VAS retrieval process undoubtedly aids in producing these favorable results. High correlations do not rule out the possibility for considerable differences, especially for dewpoints. As an example, a MLK RAOB temperature (dewpoint) of  $0^{\circ}\text{C}$  ( $0^{\circ}\text{C}$ ) corresponds to VAS values ranging from  $-5^{\circ}$  to  $5^{\circ}\text{C}$  ( $-12^{\circ}$  to  $12^{\circ}\text{C}$ ). These differences will be important in the positive buoyant energy evaluations that follow.

The lifted index (LI) is obtained by lifting the MLK parcel dry adiabatically without entrainment to its lifting condensation level (LCL), then continuing pseudoadiabatically to 500 mb where the parcel temperature is subtracted from the environmental value. Figure 7 indicates that VAS LCL pressures do not agree as closely with their RAOB-derived counterparts as did the MLK data. Slope and correlation values are approximately 0.1 smaller than those for the MLK, and standard deviations of differences are near 60 mb. Putting the discrepancies into perspective, a VAS LCL pressure of 800 mb corresponds to RAOB values between 690 and 910 mb.

VAS/RAOB lifted indices (Fig. 7) show rather good agreement. VAS LIs are slightly too small (unstable) in the mean ( $-0.39^{\circ}\text{C}$ ), while the standard deviation of differences is  $3.15^{\circ}\text{C}$ . These values are comparable to those reported by Wade et al. (1985). Although the correlation is 0.90, a particular value of VAS LI can correspond to a broad range of RAOB values. With a

slope of 1.03, there is little differential bias such that horizontal gradients of VAS LIs should agree closely with those from the conventional data. The correlation and slope values would not be as favorable if only pairs with unstable RAOB LIs (i.e., those less than zero) had been considered.

The Showalter index (SW) (Showalter 1953) is similar to the LI, except that the parcel being raised to 500 mb is defined by 850-mb data, not the MLK. Thus, the SW does not include the MLK vertical averaging that characterizes the LI, and perhaps more importantly, the SW does not incorporate observed hourly surface data. Comparing the VAS/RAOB, LI, and SW statistics (Fig. 7), SW exhibits smaller slope and correlation, and its mean difference and standard deviation of differences are larger. Thus, the LI is superior to the SW in terms of agreement with RAOB data.

Positive and negative buoyant energy depend on the level of free convection (LFC), defined as the altitude where the rising (MLK) parcel first becomes warmer than its environment. The statistics and scatter diagram for LFC pressure (Fig. 8) are based on those cases when both soundings of each VAS/RAOB pair exhibited an LFC (only 235 out of 1108 possible pairs). The results reveal that VAS LFC values are poorly correlated (0.39) with their sonde-derived counterparts. The standard deviation of differences is 113 mb, and there is a large differential bias indicated by a linear slope of only 0.46. As an example of the poor agreements, a VAS LFC pressure of 600 mb corresponds to RAOB values between 500 and 850 mb. Those cases where it corresponded to a nonexistent LFC are not indicated. The agreement between VAS/RAOB LFCs is considerably worse than that for LCL pressure (Fig. 7), probably due to the additional mathematical manipulation; i.e., the saturated ascent to where the parcel and environmental temperatures are equal.

Positive buoyant energy (PBE) is obtained by vertically integrating positive parcel/environmental temperature differences between the LFC and equilibrium level. Figure 8 shows agreements between VAS/RAOB PBE for those cases where both soundings of each pair exhibited nonzero PBE, i.e., the same 235 pairs shown for the LFC. The statistics indicate major discrepancies between the two versions. VAS-derived PBE is negatively biased ( $-158\text{ J kg}^{-1}$ ); the standard deviation of differences is  $564\text{ J kg}^{-1}$ ; and both slope and correlation statistics (each 0.20) are worse than those of the LFC (0.46 and 0.39, respectively). Zehr et al. (1988) noted that VAS tended to overestimate PBE during their case study, and current results suggest that this is most likely at the larger values. PBE statistics probably are worse than those for the LFC because there is the additional step of vertically integrating the parcel/environmental temperature differences. The PBE statistics are much worse than those of the LI (Fig. 7) whose calculation did not involve the integration of temperature contrasts.

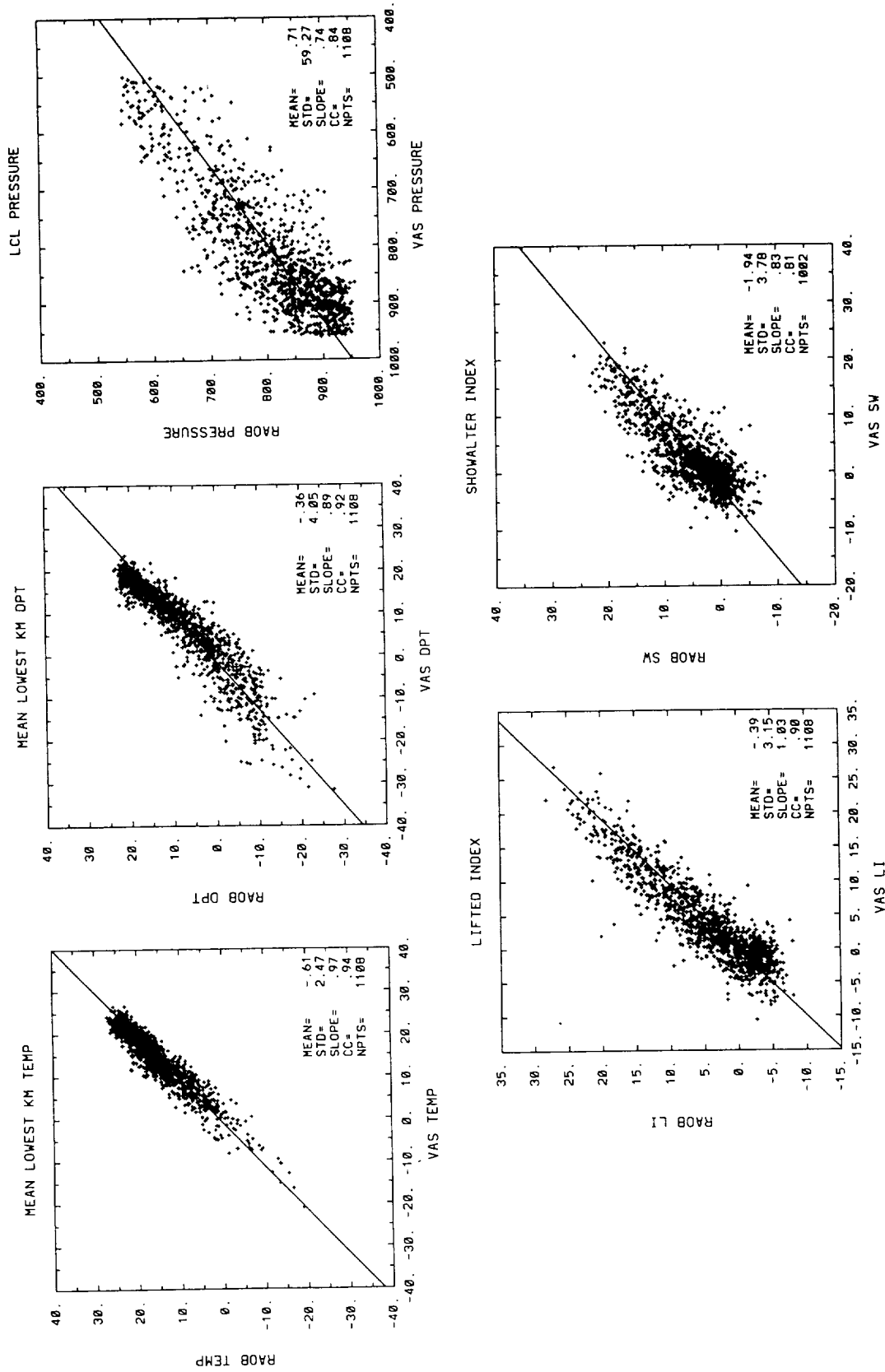


FIG. 7. Scatter diagrams of RAOB versus VAS (top) mean lowest kilometer temperature (°C) and dewpoint (°C) and LCL pressure (mb); (bottom) LI and SW index (°C). Statistics and best fit regression lines are shown as in Fig. 2.

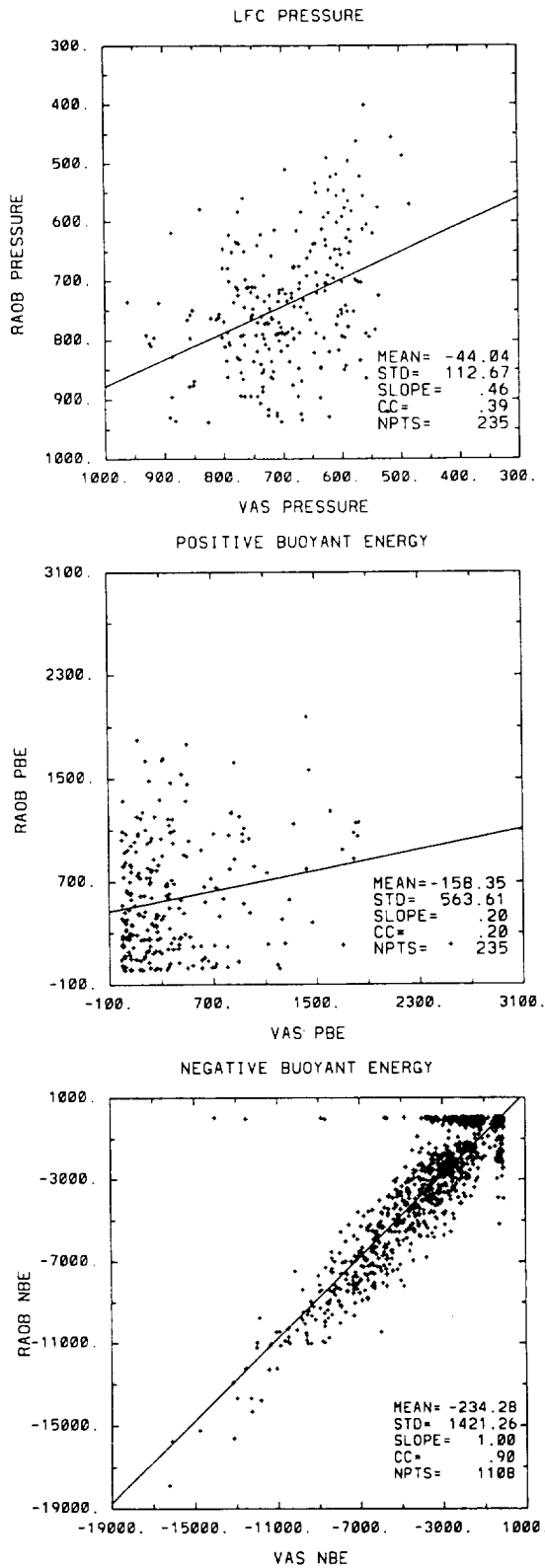


FIG. 8. Scatter diagrams of RAOB versus VAS LFC pressure (mb), PBE ( $J\ kg^{-1}$ ), and NBE ( $J\ kg^{-1}$ ). Statistics and best fit regression lines are as in Fig. 2. Only those sounding pairs with an LFC (235 points) are shown in the PBE and LFC panels.

Figure 9 shows results when all VAS/RAOB pairs are considered, not just the nonzero versions shown in Fig. 8. Although the various statistics suggest somewhat better agreement than observed for the limited sample (Fig. 8), forecasters considering the use of the VAS PBE probably will not be impressed. For example, when VAS yields zero PBE, RAOB values range from 0 to  $2800\ J\ kg^{-1}$ . Conversely, VAS PBE ranges from 0 to  $1250\ J\ kg^{-1}$  when the RAOB value is zero.

We were surprised by the poor VAS/RAOB PBE agreements since the vertical integration was expected to counter VAS's weakness of coarse vertical resolution. To examine the issue further, thermodynamic charts were plotted for a large sample of paired soundings. Figure 10 contains skew  $T$ - $\log p$  diagrams for two representative sounding pairs whose PBE values are circled in Fig. 9. For point A, VAS/RAOB temperatures in the middle troposphere are similar although the RAOB exhibits greater vertical detail. Important sounding differences related to PBE are found just above the surface where the VAS retrieval indicates much drier conditions than the RAOB. Although VAS also smears the surface-based temperature inversion, lifted parcels are more sensitive to their originating dewpoints than their temperatures (Sanders 1986). As a result of these MLK differences, the LCL pressure and wet-bulb potential temperature of the rising VAS-defined parcel are less than those of the RAOB parcel. Thus, the VAS sounding has no PBE, whereas the RAOB version yields  $1600\ J\ kg^{-1}$ . It should be noted that VAS captures major trends of the RAOB dewpoint trace in the middle and upper troposphere; however, these are not factors in determining PBE.

The bottom pair of sounding diagrams in Fig. 10 describes circled point B along the abscissa of the PBE scatter diagram (Fig. 9). Although VAS/RAOB temperatures show close agreement near the surface, the VAS dewpoints indicate more humid conditions just above the surface. The pseudoadiabatic ascent of the VAS MLK parcel therefore occurs at warmer temperatures than for the RAOB case. To compound the problem, VAS middle-tropospheric environmental temperatures are several degrees cooler than indicated by the RAOB. The result is VAS PBE =  $1250\ J\ kg^{-1}$  whereas RAOB PBE = 0.

Table 3 quantifies the factors producing PBE values along the coordinate axes of Fig. 9. The various entries represent simple averages for all points along each particular axis. Results show that the sounding examples in Fig. 10 are common occurrences. When VAS PBE = 0 but RAOB PBE is nonzero, VAS MLK temperatures and especially the dewpoints are too cold. When RAOB PBE = 0 and VAS PBE is nonzero, VAS MLK temperatures and especially dewpoints are too warm. Differences in parcel temperatures, e.g., 500 mb in Table 3, result from these discrepancies in the MLK data. The environmental temperature discrepancy at 500 mb (Table 3) is a secondary factor contributing to the PBE errors.

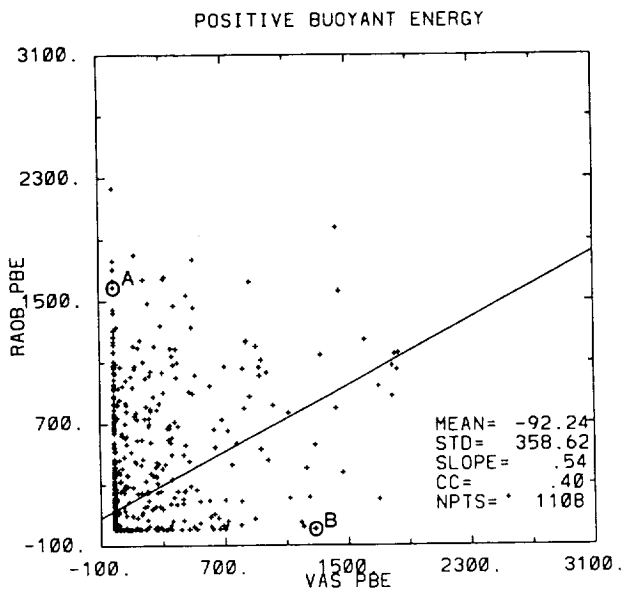


FIG. 9. RAOB versus VAS PBE ( $\text{J kg}^{-1}$ ) as in Fig. 8, except that all sounding pairs are shown. Circled points are described further in Fig. 10. Statistics and regression lines are as in Fig. 2.

In summary, current results indicate that VAS-derived PBE is not as appropriate as the lifted index in diagnosing the instability required for convective storm formation, at least not in terms of its agreement with RAOB values. PBE is critically dependent on the detailed structure of humidity in the lowest levels, and VAS simply cannot provide the needed information.

Negative buoyant energy (NBE) is the energy that must be overcome for a parcel to ascend dry adiabatically to its LCL, i.e., a hurdle to convective initiation. The scatter diagram and statistics comparing VAS/RAOB NBE (Fig. 8) are encouraging at first glance. Although the mean difference and standard deviation of differences are larger than those of PBE (Figs. 8 and 9), the slope and correlation are near 1.0. The improved statistics result from good agreements at large NBE values, but unfortunately, this is not the situation that most interests severe storm forecasters.

Convective environments frequently are characterized by inversions or stable layers in the lower levels and unstable regions aloft. The low-level negative area acts as a cap or lid to convective initiation although its magnitude may be small, e.g., only a few hundred joules per kilogram or less. Accurately describing the evolution of this small NBE region is a crucial component of many storm forecasting scenarios. To examine the suitability of VAS retrievals in this regard, a NBE scatter diagram was prepared for those sounding pairs where the RAOB contained both PBE and NBE (Fig. 11). The diagram shows that RAOB NBE values usually are only a few hundred joules per kilogram; however, corresponding VAS amounts range from 0 to over  $-3000 \text{ J kg}^{-1}$ . Although the statistics are influenced greatly by the few very large discrepancies, the poor

correlation is obvious. VAS tends to greatly overestimate the NBE due to its poor vertical resolution. Thus, VAS retrievals do not appear to be useful for diagnosing the small amounts of NBE that frequently are found in the preconvective environment.

#### b. Level-specific stability parameters

Some stability parameters are calculated from data at specific levels without any vertical averaging, lifting, and/or vertical integration. Many of these parameters were investigated and results will be described for the  $K$  index, total totals index, and 700–500 mb temperature lapse rate.

The  $K$  index (KI) (George 1960) often is used to locate possible areas of nonsevere thunderstorm activity. It is defined as

$$\text{KI} = T_{850} - T_{500} + \text{TD}_{850} - \text{DD}_{700}, \quad (1)$$

where  $\text{DD}_{700}$  is the dewpoint depression at 700 mb. VAS/RAOB KIs (Fig. 12) exhibit rather high correlation (0.83) with a standard deviation of differences approximately  $10^\circ\text{C}$ . VAS-derived values are somewhat too large (unstable) in the mean, and the slope of 0.71 indicates that the VAS version is too stable (small) for RAOB-defined stable conditions and too unstable (large) for RAOB-defined unstable conditions.

The total index (TT, Miller 1972) is defined as

$$\text{TT} = T_{850} + \text{TD}_{850} - 2T_{500}. \quad (2)$$

Its various statistics (Fig. 12) are similar to those of KI, indicating similar biases and scatter. Wade et al. (1985) reported an average difference of  $0.4^\circ\text{C}$  and an rms difference of  $8.5^\circ\text{C}$  for a several day period during May 1985.

The 700–500 mb temperature lapse rate gives forecasters a measure of parcel stability in the lower troposphere. Figure 12 indicates that VAS/RAOB lapse rates exhibit somewhat poorer correlations (0.68) than those of KI or TT (0.83 and 0.76, respectively), although its linear slope (0.76) is slightly greater (0.71 and 0.72). Zehr et al. (1988) noted that VAS tended to overestimate lower-tropospheric lapse rates during their case study, but that is not a major factor in the composite dataset.

The agreements between VAS/RAOB versions of KI, TT, and lapse rate (Fig. 12) are much better than those of PBE (Figs. 8–9). The superiority of these three indices probably is due to their simplicity of calculation; i.e., they do not involve integrated parcel/environmental temperature differences. The simple addition and subtraction that are required apparently do not magnify the VAS temperature/dewpoint discrepancies to the extent of the PBE calculation. Conversely, the statistics for LI (Fig. 7) are superior to those of any of the three-level specific indices (Fig. 12). In this case, the LI's inclusion of observed surface data apparently is a major factor leading to improved results. Kitzmiller and McGovern (1989) found that versions of KI and

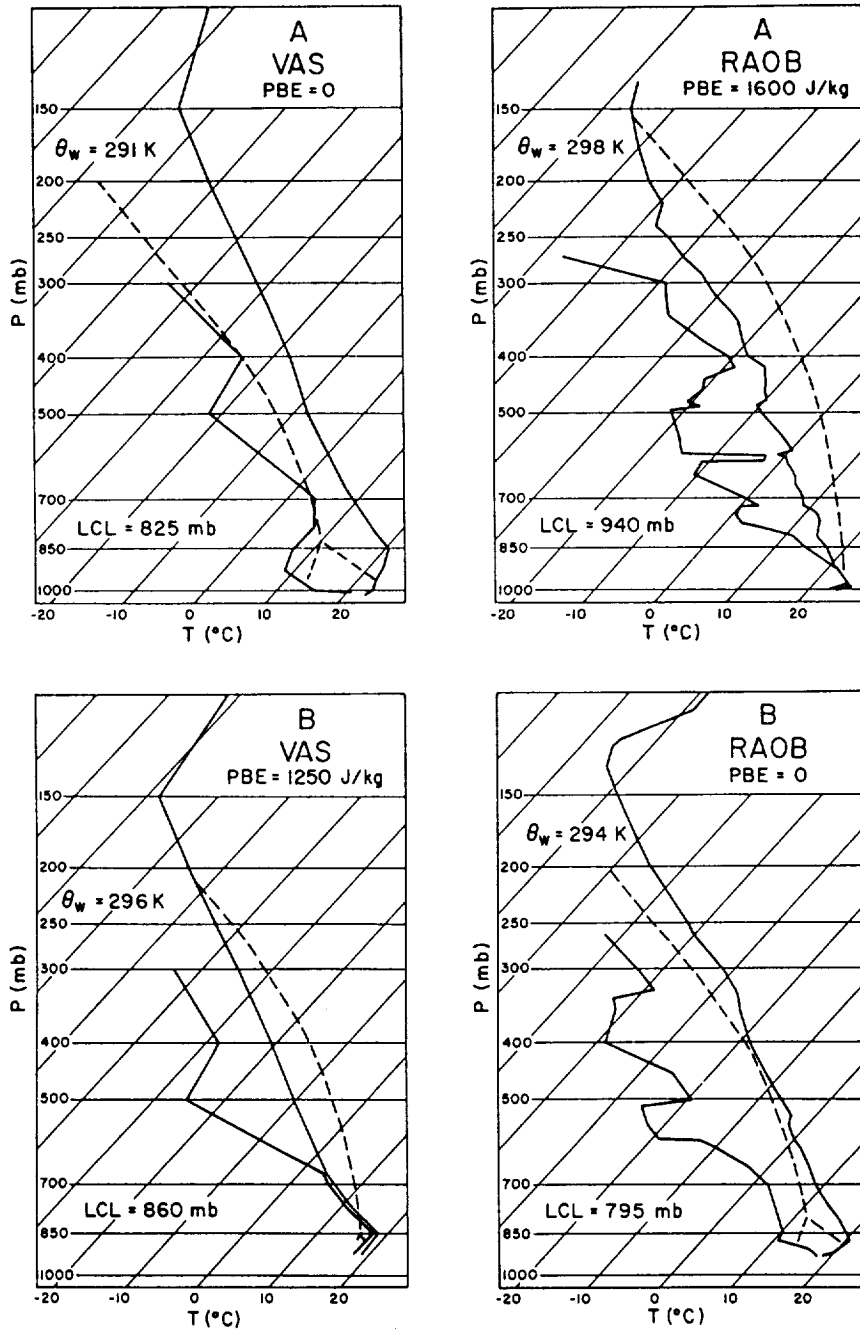


FIG. 10. Skew  $T$ -log  $p$  diagrams for points A and B in Fig. 9. Ascent of the MLK parcel is indicated by the dashed line.

TT that had been modified to include observed surface data produced better agreements with observed storm reports than did the versions defined by (1) and (2).

*c. Other parameters*

Severe storm forecasters also use some parameters that are not direct measures of stability. The convective condensation level (CCL) is the height to which a parcel

of air, if heated sufficiently from below, will rise dry adiabatically until just saturated. On a thermodynamic diagram, it is obtained by following the mixing ratio isoline from the surface (or MLK in this case) to its intersection with the temperature profile. Figure 12 shows that VAS-derived values are low biased (-15.7 mb) with a standard deviation of differences of 85.1 mb. The slope and correlation coefficients of 0.85 and 0.77, respectively, are comparable to those of the KI,

TABLE 3. Mean temperature and dewpoint differences ( $^{\circ}\text{C}$ ) in the MLK, and mean 500-mb parcel and environmental temperatures differences ( $^{\circ}\text{C}$ ) for (top) VAS PBE equal zero but RAOB PBE not equal to zero and (bottom) VAS PBE not equal to zero but RAOB PBE equal to zero.

VAS PBE = 0 and RAOB PBE $\neq$ 0	
$T$ (MLK) =	-0.91
TD (MLK) =	-2.39
$T_{\text{par}}$ (500) =	-3.09
$T_{\text{env}}$ (500) =	-0.29
VAS PBE $\neq$ 0 and RAOB PBE = 0	
$T$ (MLK) =	0.57
TD (MLK) =	2.55
$T_{\text{par}}$ (500) =	3.37
$T_{\text{env}}$ (500) =	-1.38

TT, and lapse rate. The convection temperature represents the minimum temperature needed for subcloud parcels to reach the CCL. VAS-derived values (Fig. 12) are slightly warm biased ( $0.3^{\circ}\text{C}$ ), with a standard deviation of differences of  $5.6^{\circ}\text{C}$ . The blending of observed surface data into the FG through 850 mb is a favorable influence on the VAS-derived CCL and convection temperature.

The height of the  $0^{\circ}\text{C}$  wet-bulb temperature is useful to forecasters because it has been associated with the occurrence of hail and severe thunderstorms (Miller 1972). VAS/RAOB versions show reasonably good statistical agreement (Fig. 12). Slope and correlation values both exceed 0.9, and there is only a small bias (13.9 m) and standard deviation of differences (372.7 m). Nonetheless, a particular RAOB value can be associated with a wide range of VAS amounts.

#### d. Improvements over the first guess

Previous sections demonstrated that VAS temperatures and dewpoints are not consistent improvements over the LFM data that serve as first-guess input (Fig. 5). Similar calculations were made for the thunderstorm forecasting parameters, with selected results shown in Fig. 13. As expected, the VAS derived parameters exhibit similarly poor improvements over the FG. The histogram peaks occur near zero, again indicating that VAS products provide little consistent improvement over those from the FG.

### 9. Summary and conclusions

This study has investigated operationally derived VAS retrievals for the period 31 March–23 July 1986, employing a total of 1108 paired VAS/RAOB soundings near 1200 UTC that were collocated within 50 km and approximately 15 min. Temperature and dewpoint data from the two sources were compared and then used to calculate various parameters used in forecasting severe local storms. VAS retrievals also were compared with the first-guess LFM input to determine relationships and/or improvement.

Comparisons between VAS and observed RAOB temperatures showed correlations greater than 0.95 at most pressure levels. Magnitudes of mean discrepancies were less than  $1.5^{\circ}\text{C}$ , and standard deviations of discrepancies were small ( $1.4^{\circ}$  to  $2.2^{\circ}\text{C}$ ). There was little differential bias. Conversely, VAS and RAOB dewpoints did not correlate as well, with standard deviations of differences ranging from  $2.5^{\circ}$  to  $6.9^{\circ}\text{C}$  and biases as great as  $-3^{\circ}\text{C}$ .

VAS/RAOB differences were poorly correlated with the number of FOVs on which the retrievals were based. Thus, it appears that the algorithm's cloud detection scheme performs adequately. These results also imply that useful retrievals can be prepared from fewer FOVs than is currently done.

The various VAS/FG comparisons generally produced rather discouraging results. VAS discrepancies usually were poorly correlated with FG errors, and the retrievals were not consistent improvements over the FG numerical input. In fact, histograms of improvement were normally distributed about zero, with VAS retrievals being inferior to the FG about as often as not. VAS retrievals tended to be an improvement over large FG errors, but not even this was guaranteed.

Horizontal gradients of VAS data were compared with those from radiosondes and the FG. VAS-derived temperature gradients generally were overestimates of the RAOB variety. However, there were many levels where the VAS temperature gradient was closer to the observed than was the FG gradient. The VAS moisture gradient was found to be an even greater overestimate of the observed.

VAS/RAOB versions of precipitable water exhibited better agreement than did dewpoints at individual levels. The improvements of thickness over individual

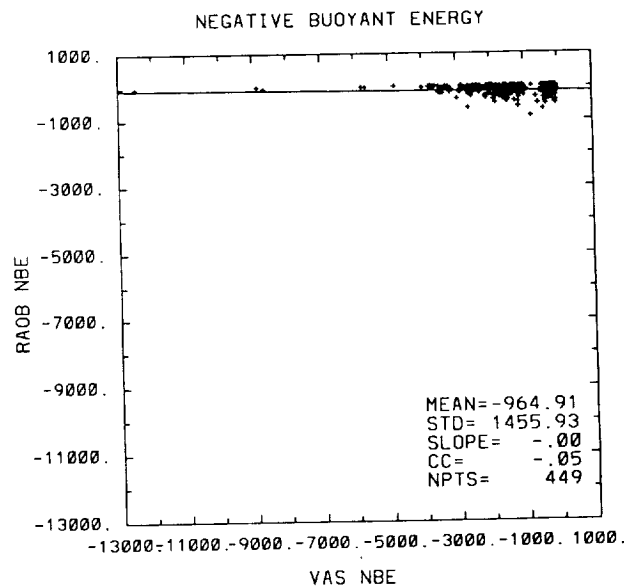


FIG. 11. RAOB versus VAS NBE ( $\text{J kg}^{-1}$ ) as in Fig. 8 except that only those points where the RAOB had both PBE and NBE are indicated. Statistics are as in Fig. 2.



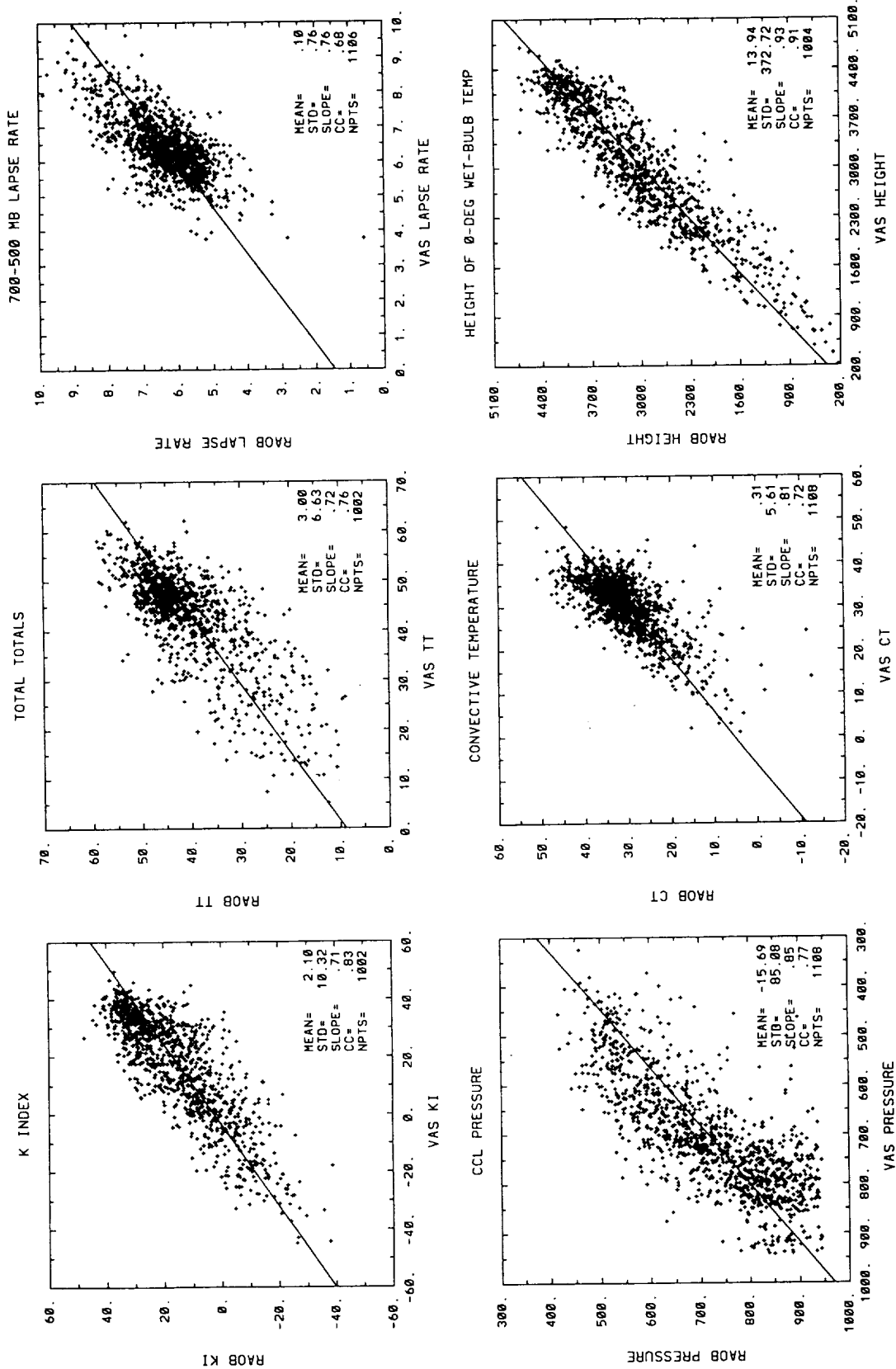


FIG. 12. Scatter diagrams of RAOB versus VAS (top) KI and TT ( $^{\circ}\text{C}$ ) and 700-500 mb lapse rate ( $^{\circ}\text{C km}^{-1}$ ); (bottom) CCL pressure (mb), convection temperature ( $^{\circ}\text{C}$ ), and height of the  $0^{\circ}$  wet-bulb temperature (m). Statistics are as in Fig. 2.

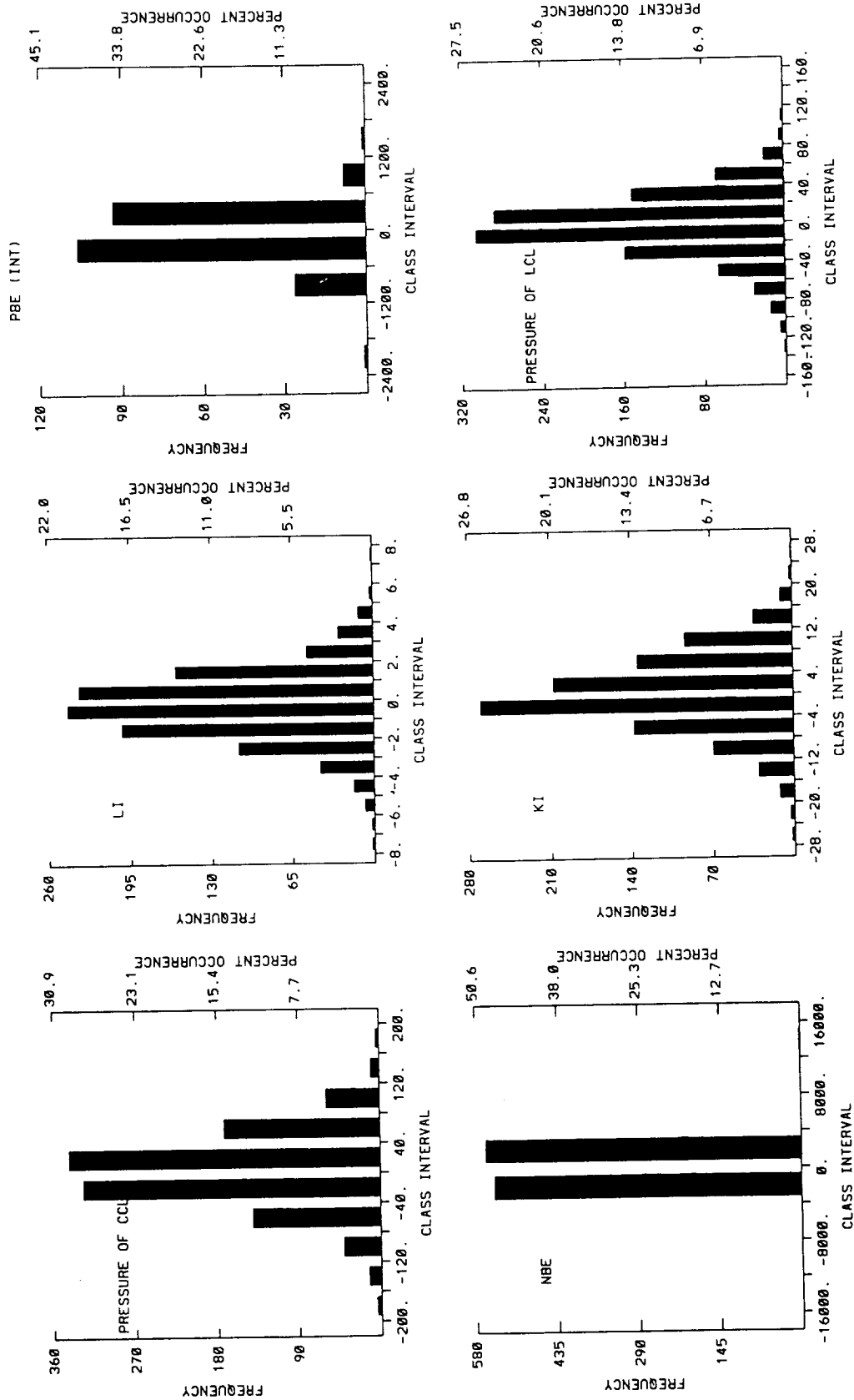


FIG. 13. Histograms of VAS improvement over FG for (top) LCL pressure (mb), LI ( $^{\circ}$ C), and PBE ( $J\ kg^{-1}$ ); and (bottom) NBE ( $J\ kg^{-1}$ ), KI ( $^{\circ}$ C), and CCL pressure (mb).

level temperatures were not as pronounced, perhaps because the temperatures already showed good agreement with sonde data. Greatest improvements in both vertically integrated parameters occurred over deep layers.

Numerous diagnostic parameters used in severe storms forecasting were calculated with VAS and RAOB input. Results showed that discrepancies increased with the greater amount of mathematical manipulation required during computation. Of all the derived parameters investigated, VAS lifted index exhibited the best agreement with RAOB versions. Slopes and correlations were near 1.0, and the standard deviation of differences was only about 3°C. Agreements between VAS/RAOB Showalter index were not as good as those of LI. The LI's advantage is its use of a vertically averaged (MLK) parcel that includes observed surface data.

VAS/RAOB versions of positive buoyant energy exhibited disappointingly poor agreements. It was common for either VAS or RAOB data to produce zero PBE, while the other data source yielded a large nonzero result. Accurate PBE depends critically on a detailed representation of low-level humidity that VAS is unable to provide. VAS-derived PBE does not appear as useful as the LI in diagnosing the preconvective environment. VAS/RAOB versions of NBE showed good correlations when all sounding pairs were considered; however, this agreement was based largely on pairs having large values. A common severe storm scenario consists of a small negative region in the lower troposphere with a large positive region aloft. When the statistics were recalculated for RAOBs having this energy distribution, the agreements were much less favorable. The satellite's poor vertical resolution once again is the limiting factor.

Agreements between VAS/RAOB versions of the  $K$  index, total totals index, and lower tropospheric temperature lapse rate were intermediate to those of PBE and LI. These parameters do not involve lifting or parcel/environmental temperature differences that can magnify VAS/RAOB temperature and dewpoint discrepancies; however, they also do not incorporate the observed surface data that appear to be a positive influence on the LI. VAS-derived convective condensation levels and temperatures showed good agreement with RAOB versions; however, surface data again play a major role in their calculation.

All VAS-derived forecasting parameters showed little consistent improvement over those obtained from the first-guess LFM input. VAS degraded the FG about as often as it improved it.

One important aspect of VAS retrievals, their improved horizontal and temporal resolution, has not been considered in the current study. VAS retrievals typically are made at approximately 100-km and 3-h intervals, considerably closer than the 400-km and 12-h intervals of the United States radiosonde network.

VAS has the potential for providing mesoscale patterns, gradients, and evolutions of features that are not available from ground-based soundings. Several case studies have suggested that VAS physical and statistical retrievals can provide useful mesoscale details in severe storm situations (e.g., Mostek et al. 1986; Zehr et al. 1988; Ellrod 1989; Andrews and Fuelberg 1988; Fuelberg et al. (1991)). VAS-derived horizontal analyses also appear to improve upon FG analyses in some, but not all situations (Hayden 1988; Franklin et al. 1989). These types of evaluations are hampered by the lack of ground-truth sounding data at comparable resolutions. Furthermore, it is not certain whether the mesoscale detail in the satellite analyses results from the VAS radiances or the observed surface data that are part of the first guess and which do have mesoscale resolution.

There is evidence that modifications to the physical retrieval process can produce VAS soundings that are superior to the operationally derived versions described here. These schemes involve selecting fields-of-view such that gradients are maintained (Hillger and Purdom 1989) and preparing retrievals from fewer fields-of-view for some channels (Hillger and Vonder Haar 1988). These modifications should be considered for operational use if scheduling constraints permit.

The upcoming GOES-NEXT satellites, together with field projects such as STORM, offer the potential for careful evaluation of satellite data in severe storm environments. We hope that such investigations will be conducted. The current study can serve as a benchmark for some of the future evaluations.

*Acknowledgments.* This research was sponsored by the National Aeronautics and Space Administration (NASA) through Grant NAG8-653 under the auspices of the Remote Sensing Branch of the Marshall Space Flight Center. We appreciate the assistance of the following persons during the course of the research: Dr. David Kitzmiller (NOAA/NWS/TDL) for supplying the VAS retrievals; Dr. James Purdom (NOAA/NESDIS) for providing the sounding analysis program; Mr. Gary Wade and Drs. Christopher Hayden and Paul Menzel (NOAA/NESDIS) for answering many questions about the VAS retrievals and providing helpful comments; and Dr. Gary Jedlovec (NASA/Marshall) for sharing his insight into VAS retrievals. Finally, we appreciate the help of Mr. David Parker, Mr. Jeff Orrock, and Mr. Dewey Rudd in preparing the manuscript.

#### REFERENCES

- Andrews, M. J., and H. E. Fuelberg, 1988: Satellite-derived stability parameters during a convective outbreak. Preprints, *Fifteenth Conference Severe Local Storms*, Baltimore, Amer. Meteor. Soc., 178-181.
- Bruce, R. E., L. D. Duncan and J. H. Pierluissi, 1977: Experimental study of the relationships between radiosonde temperatures and satellite-derived temperatures. *Mon. Wea. Rev.*, **105**, 493-496.

- Chesters, D., and L. W. Uccellini, 1982: VISSR Atmospheric Sounder (VAS) simulation experiment for a severe storm environment. *Mon. Wea. Rev.*, **110**, 198–216.
- Ellrod, G., 1989: Environmental conditions associated with the Dallas microburst storm determined from satellite soundings. *Wea. and Forecasting*, **4**, 469–484.
- Franklin, J. L., and S. C. Lord, 1988: Comparisons of VAS and omega dropwindsonde thermodynamic data in the environment of Hurricane Debby (1982). *Mon. Wea. Rev.*, **116**, 1690–1701.
- , C. S. Velden, C. M. Hayden and J. Kaplan, 1989: A comparison of VAS and ODW data around a subtropical cold low. Preprints, *Fourth Conference on Satellite Meteor./Oceanography*, San Diego, Amer. Meteor. Soc., 141–144.
- Fuelberg, H. E., and P. J. Meyer, 1986: An analysis of mesoscale VAS retrievals using statistical structure functions. *J. Climate Appl. Meteor.*, **25**, 60–75.
- , R. L. Schudalla and A. R. Guillory, 1991: Analysis of sudden mesoscale drying at the surface. *Mon. Wea. Rev.*, **119**, in press.
- Galway, J. G., 1956: The lifted index as a predictor of latent instability. *Bull. Amer. Meteor. Soc.*, **37**, 528–529.
- George, J. J., 1960: *Weather Forecasting for Aeronautics*. Academic Press, 407–415.
- Hayden, C. M., 1988: GOES-VAS simultaneous temperature—moisture retrieval algorithm. *J. Appl. Meteor.*, **27**, 705–733.
- Hillger, D. W., and T. H. Vonder Haar, 1988: Estimating noise levels of remotely sensed measurements from satellites using spatial structure analysis. *J. Atmos. Ocean. Tech.*, **5**, 206–214.
- , and J. F. W. Purdom, 1989: Using VAS data to add mesoscale detail to synoptic-scale radiosonde data. Preprints, *Twelfth Conference Weather Analysis and Forecasting*, Monterey, Amer. Meteor. Soc., 412–415.
- Hoehn, W. E., 1980: Precision of National Weather Service upper-air measurements. NOAA Tech Memo, NWS T&ED-16, 23 pp. [NTIS PB81-108136].
- Jedlovec, G. J., 1985: An evaluation and comparison of vertical profile data from the VISSR Atmospheric Sounder (VAS). *J. Atmos. Ocean. Tech.*, **2**, 559–581.
- Kitzmilller, D. H., and W. E. McGovern, 1989: VAS retrievals as a source of information for convective weather forecasts: An objective assessment and comparison with other sources of upper-air observations. *Mon. Wea. Rev.*, **117**, 2095–2109.
- Lee, T. H., D. Chesters and A. Mostek, 1983: The impact of conventional surface data upon VAS regression retrievals in the lower troposphere. *J. Climate Appl. Meteor.*, **22**, 1853–1874.
- McMillin, L. M., D. G. Gray, H. F. Drahos, M. W. Chalfant and C. S. Novak, 1983: Improvements in the accuracy of operational satellite soundings. *J. Climate Appl. Meteor.*, **22**, 1948–1955.
- Menzel, W. P., W. L. Smith and L. D. Herman, 1981: Visible infrared spin-scan radiometer atmospheric sounder radiometric calibration: An inflight evaluation from intercomparisons with HIRS and radiosonde measurements. *Appl. Opt.*, **20**, 3641–3644.
- Miller, R. C., 1972: Notes on analysis and severe storm forecasting procedures of the Air Force Global Weather Central. Air Weather Service Tech. Rep. 200 (Rev.), 102 pp. [NTIS AD 744 042.]
- Mosher, F. R., and T. Schoeni, 1988: Assessment of the utility of VAS data products for severe local storms forecasting. Preprints, *Fifteenth Conference Severe Local Storms*, Baltimore, Amer. Meteor. Soc., 182–185.
- Mostek, A., L. W. Uccellini, R. A. Petersen and D. Chesters, 1986: Assessment of VAS soundings in the analysis of a preconvective environment. *Mon. Wea. Rev.*, **114**, 62–87.
- Moyer, V., J. R. Scoggins, N.-M. Chou and G. S. Wilson, 1978: Atmospheric structure deduced from Nimbus-6 satellite data. *Mon. Wea. Rev.*, **106**, 1340–1352.
- Peppler, R. A., 1988: A review of static stability indices and related thermodynamic parameters. Illinois State Water Survey, SWS Miss. Pub. 104, 88 pp. [Available from the author at Champaign, IL 61820.]
- Pratt, R. W., 1985: Review of radiosonde humidity and temperature errors. *J. Atmos. Ocean. Tech.*, **2**, 404–407.
- Sanders, F., 1986: Temperatures of air parcels lifted from the surface: Background, application and nomograms. *Wea. and Forecasting*, **3-4**, 190–205.
- Schlatter, T. W., 1981: An assessment of operational TIROS-N temperature retrievals over the United States. *Mon. Wea. Rev.*, **109**, 110–119.
- Showalter, A. K., 1953: A stability index of thunderstorm forecasting. *Bull. Amer. Meteor. Soc.*, **34**, 250–252.
- Smith, W. L., 1983: The retrieval of atmospheric profiles from VAS geostationary radiance observations. *J. Atmos. Sci.*, **40**, 2025–2035.
- , H. M. Woolf and A. J. Schreiner, 1985: Simultaneous retrieval of surface atmospheric parameters: A physical and analytically direct approach. *Advances in Remote Sensing*, A. Deepak, H. E. Fleming and M. T. Chahine, Eds., A. Deepak Pub., 221–232.
- , V. E. Suomi, W. P. Menzel, H. M. Woolf, L. A. Sromovsky, H. E. Revercomb, C. M. Hayden, D. N. Erickson and F. R. Mosher, 1981: First sounding results from VAS-D. *Bull. Amer. Meteor. Soc.*, **62**, 232–236.
- Velden, C. S., W. L. Smith and M. Mayfield, 1984: Application of VAS and TOVS to tropical cyclones. *Bull. Amer. Meteor. Soc.*, **65**, 1059–1067.
- Wade, G. S., A. L. Siebers and R. W. Anthony, 1985: An examination of current atmospheric stability and moisture products retrieved from VAS measurements in real time for the NSSFC. Preprints, *Fourteenth Conference on Severe Local Storms*, Indianapolis, Amer. Meteor. Soc., 105–108.
- Zehr, R. A., J. F. W. Purdom, J. F. Weaver and R. N. Green, 1988: Use of VAS data to diagnose the mesoscale environment of convective storms. *Wea. and Forecasting*, **3**, 33–49.

## Analysis of Sudden Mesoscale Drying at the Surface

HENRY E. FUELBERG, RONALD L. SCHUDALLA\* AND ANTHONY R. GUILLORY

*Department of Meteorology, Florida State University, Tallahassee, Florida*

(Manuscript received 24 July 1990, in final form 6 December 1990)

### ABSTRACT

Mesoscale surface data and special satellite-derived soundings from the Visible Infrared Spin Scan Radiometer (VISSR) Atmospheric Sounder (VAS) are used to investigate a case of sudden mesoscale drying at the surface on 17 June 1986, a day during the Cooperative Huntsville Meteorological Experiment (COHMEX). Dewpoints fall as much as  $-6.3^{\circ}\text{C}$  in less than 1 h over a small portion of central Tennessee. The drying occurs prior to the onset of convective activity. The satellite retrievals detect a narrow tongue of midtropospheric dry air that overlays moist air near the surface. The analyses indicate that heating-induced surface-based mixing penetrates the midlevels, bringing drier air to the surface and resulting in the sudden decreases in surface dewpoints.

### 1. Introduction

New mesoscale data sources such as wind profilers, satellite imagery and retrieved soundings, Doppler radar, and dense surface networks are revealing a host of atmospheric phenomena that have been poorly resolved by conventional data. Many of these phenomena are accompanied by rapidly varying small-scale humidity features. Barnes and Lilly (1975) found that 37% of the horizontal variance of water vapor at 1500-m altitude on nonstorm days occurred at separations less than 200 km. Even more dramatic was that 68% of the variance occurred at separations below 200 km during stormy periods. These values have been confirmed by Fuelberg and Meyer (1984).

Thunderstorms have been observed to form in regions of strong and rapidly changing humidity gradients (e.g., Miller 1972; Petersen et al. 1984). McGinley (1986) urged operational forecasters to monitor hourly surface humidity data. He noted that a rapid drop in dewpoint often indicates that a stable layer aloft has been eliminated by heating, thereby enhancing the possibility of convective development.

Sudden, localized surface drying occurred over central Tennessee on 17 June 1986, one of the days of the Cooperative Huntsville Meteorological Experiment (COHMEX). We have used the special mesoscale surface data and special satellite-derived soundings available during COHMEX to describe the drying event and propose a hypothesis for its formation.

\* Present affiliation: NOAA/FSL/PROFS, Boulder, CO.

Corresponding author address: Professor Henry E. Fuelberg, Dept. of Meteorology, The Florida State University, Tallahassee FL 32306-3034.

### 2. Synoptic conditions

The Tennessee River valley was characterized by weak large-scale dynamic forcing on the morning of 17 June 1986. At the surface (Fig. 1), an east-west cold front extended from Virginia into Missouri. The front advanced southward during the morning and by 1700 UTC was located over central Tennessee (Fig. 2). The diffuse frontal boundary exhibited little troughing, with northerly or northwesterly winds on both of its sides. Horizontal temperature gradients across the front were weak, with temperatures generally near  $30^{\circ}\text{C}$  at midday. Contrasting dewpoint temperatures were the primary tool for frontal placement. Values exceeded  $20^{\circ}\text{C}$  over Alabama and Mississippi but were only in the teens over Kentucky.

At 500 mb (Fig. 1), anticyclonic flow dominated the central United States while a trough was located along the East Coast and Appalachians. A closed cyclonic circulation was located over northwest Texas. Very dry conditions were associated with the anticyclone, with an axis of low dewpoints extending from Nebraska to the Carolinas. Dry air also stretched along the Great Lakes. The jet stream was far north of the COHMEX region, along the Canadian border. Winds at most levels over Alabama and Tennessee were northerly or northeasterly at only  $5\text{--}15\text{ m s}^{-1}$ .

Radiosonde soundings (Fig. 3) at 1200 UTC 17 June for both Nashville (BNA) and Redstone Arsenal (RSA, near Huntsville, Alabama shown in Fig. 1) contained nearly dry-adiabatic layers between approximately 950 and 800 mb that were capped by stable regions. Conditions immediately above the inversions were drier with nearly dry-adiabatic layers again evident near 700 mb. Lifted indices for Nashville and Redstone were  $-2^{\circ}$  and  $-3^{\circ}\text{C}$ , respectively, and their convective tem-

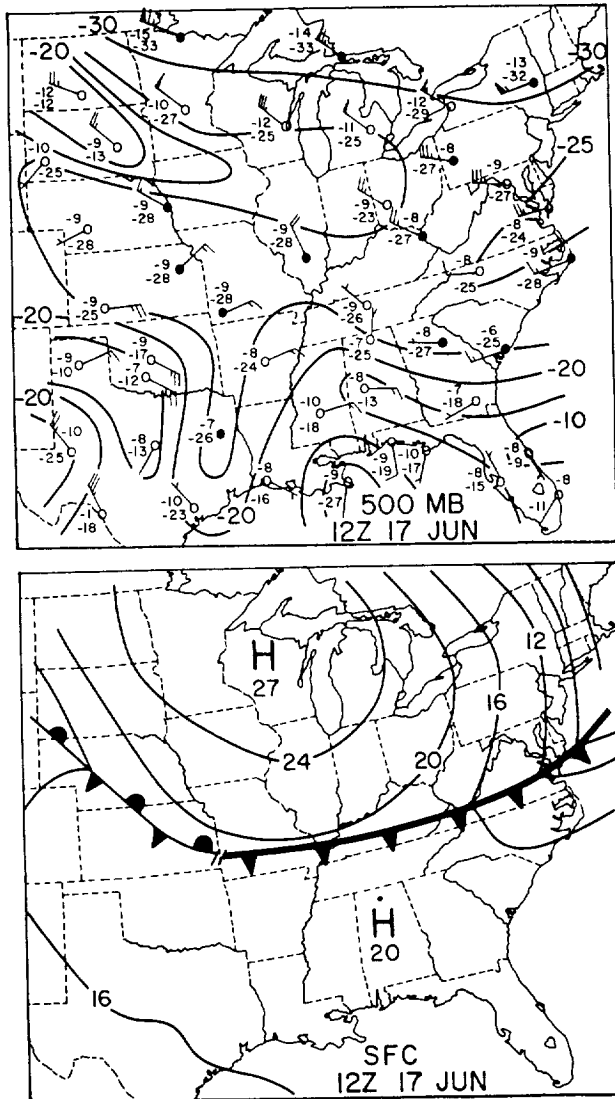


FIG. 1. Synoptic conditions at 1200 UTC 17 June 1986. At the surface, 16 represents 1016 mb; at 500 mb, temperatures and dewpoints are in degrees Celsius, while winds are in meters per second, where full (half) barbs represent 5 (2.5)  $m s^{-1}$  and flags represent 25  $m s^{-1}$ . Huntsville, Alabama is denoted by the dark circle on the surface map. Isodrosotherms at 500 mb are at intervals of 5°C. The National Weather Service reports a 30°C dewpoint depression for any relative humidity less than 20%. Since the actual depression can be either greater or less than this value, we calculated our own dewpoints based on a relative humidity equal to 20%. This was done at the locations having darkened station circles.

peratures near 31°C were expected to be reached during the afternoon. North of the COHMEX area, at Salem, Illinois (SLO, Fig. 3), the atmosphere was comparatively dry and more stable with a lifted index of +6°C.

Early morning skies over the COHMEX area were mostly clear, but cumulus clouds developed by mid-morning. Towering cumulus began to appear by 1700 UTC, and radar echoes first were noted at 1720 UTC (Williams et al. 1987), initially appearing over the

southern third of Tennessee approximately 100 km north of Redstone. Visible satellite imagery shows storm locations at 1801 and 2201 UTC (Fig. 4). The convection slowly moved southward, forming a broken line from northern Mississippi through northern Alabama and into Georgia, near the leading edge of the cold front. Maximum echo tops reached 17.5 km (57 400 ft).

### 3. Surface drying event

Dewpoint patterns undergo major variations during the morning of 17 June 1986. The subjective analysis of National Weather Service dewpoint data at 1500 UTC (Fig. 5) reveals relatively dry air north of the front. South of the front, a broad moist tongue protrudes northeastward through southern Kentucky. The moist region becomes more narrow and focused through the morning, and by 1800 UTC is oriented parallel to the Tennessee–Alabama border in advance of the front. The enhanced moisture along the front probably is an important factor in producing the nearby convection (Fig. 4).

The especially interesting feature at 1800 UTC (Fig. 5) is the southward extension of relatively dry air over central Tennessee. First noted at 1700 UTC (Fig. 2), it is best depicted by hourly surface dewpoint changes between 1600–1700 UTC (Fig. 6). Large dewpoint falls occur at several observing sites in central Tennessee and Kentucky, but Nashville (in north-central Tennessee) has the largest value of  $-4^{\circ}C$ . The convection

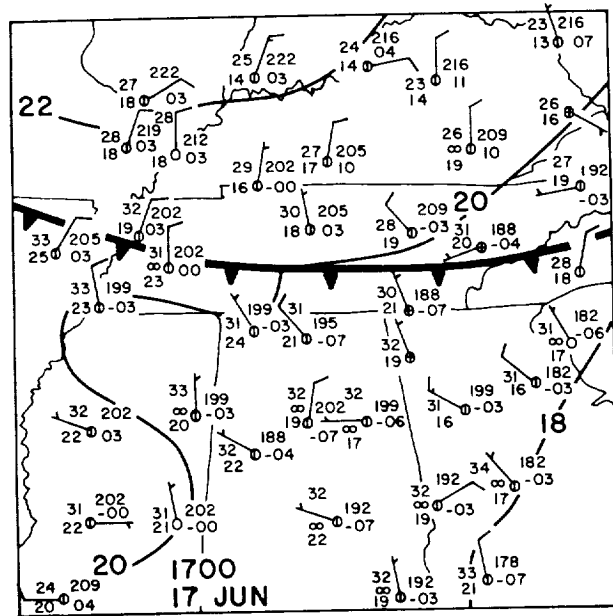


FIG. 2. Surface analysis at 1700 UTC 17 June 1986. Temperatures and dewpoints are in degrees Celsius, while winds are in meters per second, where half (full) barbs represent 2.5 (5)  $m s^{-1}$ . Isobars are at intervals of 2 mb.

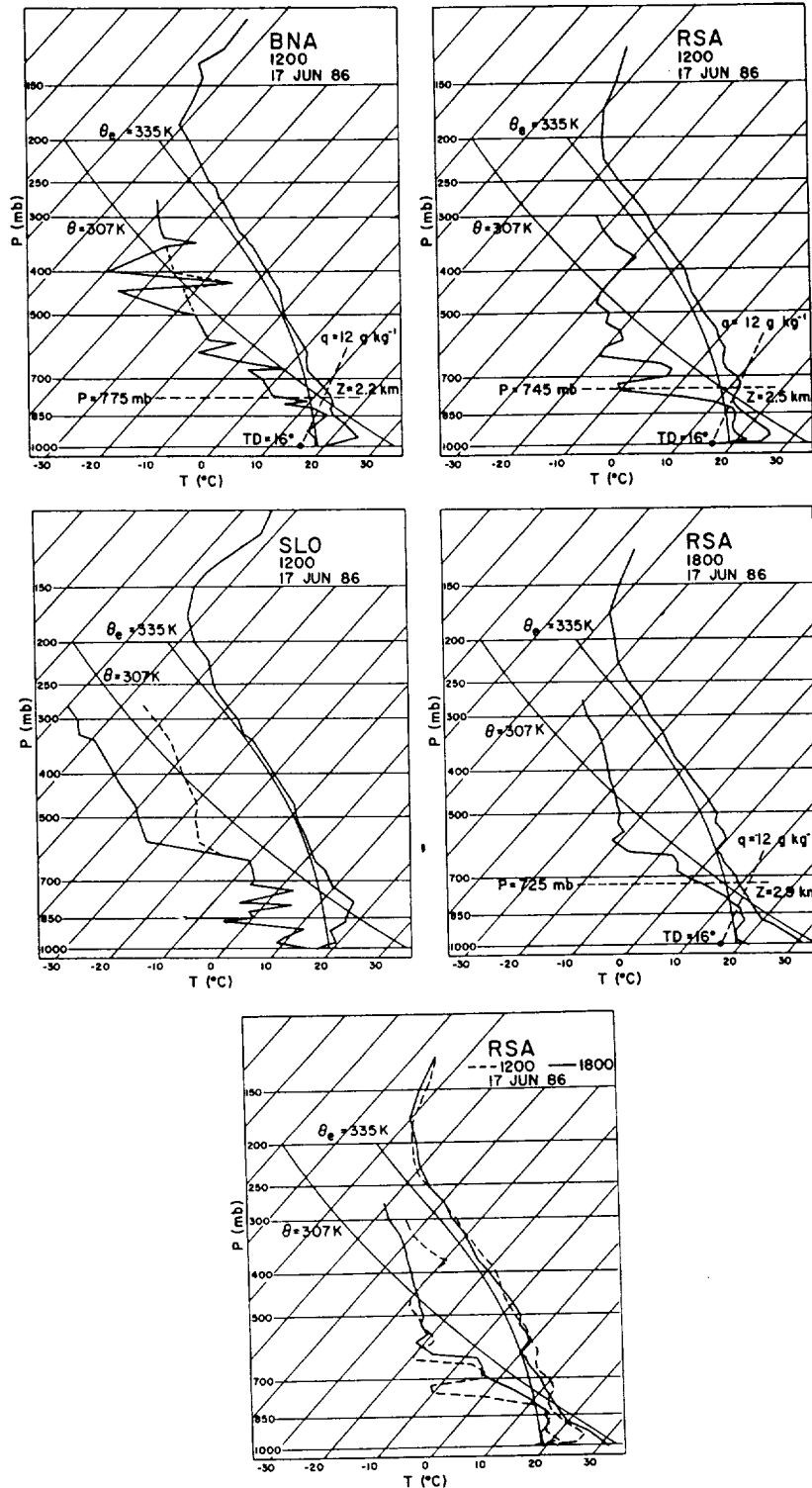


FIG. 3. Skew  $T$ -log  $p$  diagrams of soundings at Nashville, Tennessee (BNA), Redstone Arsenal, Alabama (RSA), and Salem, Illinois (SLO) for 1200 UTC 17 June 1986 and RSA at 1800 UTC. Dewpoints originally based on a  $30^\circ\text{C}$  depression have been recalculated based on 20% relative humidity. These sections of the soundings are denoted by dashed dewpoint traces (except on the bottom panel). Also indicated are the levels to which surface-based vertical mixing would have to extend to produce a surface dewpoint of  $16^\circ\text{C}$ ; i.e., a mixing ratio of  $12 \text{ g kg}^{-1}$ .

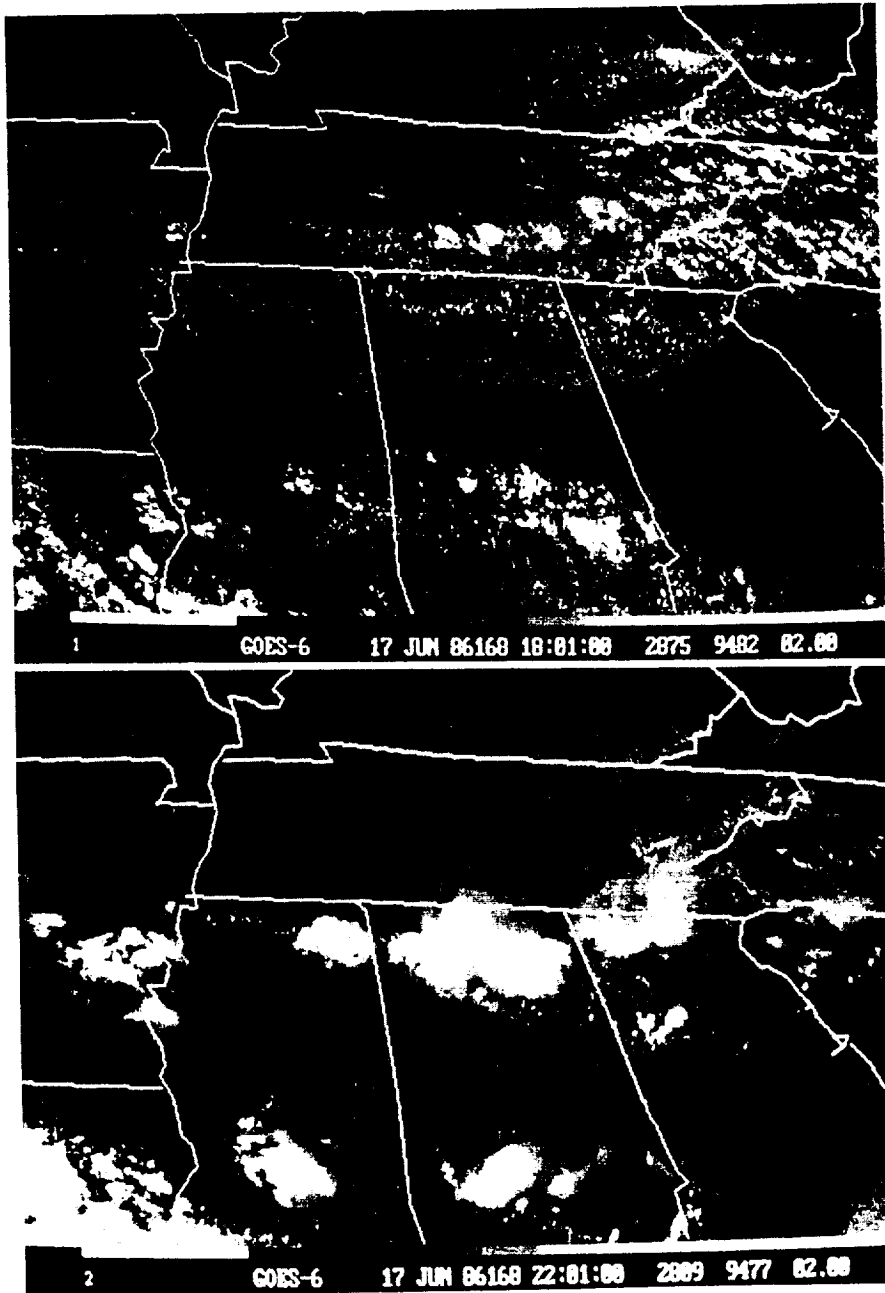


FIG. 4. GOES visible imagery at 1801 UTC (top) and 2201 UTC (bottom) 17 June 1986.

(Fig. 4) forms after 1700 UTC, to the south of Nashville in the strong dewpoint gradient that results from the drying. Surface drying during the morning is a common event as moisture is mixed up into the developing boundary layer. Except for the frontal region, most of the area in Fig. 6 experiences decreasing dewpoints. However, the drying over Tennessee is especially strong and focused, an aspect that is further documented in later paragraphs. Surface temperature analyses for this period (not shown) exhibit only normal diurnal warming with no unusual features or fluctuations.

A more detailed description of the drying event is provided by the COHMEX surface mesonetwork. Information about network instrumentation is given in Arnold et al. (1986). Time traces of 5-min-averaged data are given in Fig. 7, while locations of the mesonetwork sites and spatial maps of hourly dewpoint changes are given in Fig. 8. The average spacing of the sites is 65 km.

Continuous dewpoint data were not available at Nashville's National Weather Service Forecast Office where the dewpoint decreases  $-4.0^{\circ}\text{C}$  between 1600-



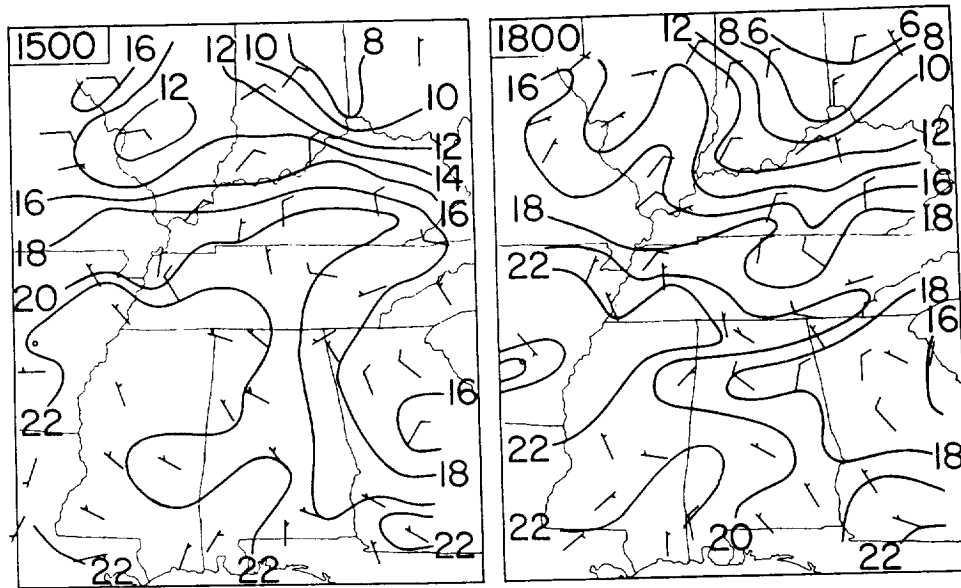


FIG. 5. Surface isodrosotherm analyses (intervals of 2°C) at 1500 and 1800 UTC 17 June. The superimposed winds are plotted as in Fig. 2.

1700 UTC (Fig. 6). However, at nearby sites N9, P8, and P7, the drying begins between 1630 and 1700 UTC and ranges from  $-2.2^{\circ}$  to  $-3.2^{\circ}\text{C}$  (Fig. 7). The greatest dewpoint decrease occurs at site N7, located approximately 65 km southwest of Nashville. The strong drop begins near 1650 UTC and continues for about 1 h, producing a total drying of  $-6.3^{\circ}\text{C}$  and a minimum

dewpoint of  $16^{\circ}\text{C}$  near 1800 UTC. It is followed by increasing dewpoint and then a sharp decrease beginning near 1840 UTC. Farther south, site P9 experiences a sudden  $-3.4^{\circ}\text{C}$  drop in dewpoint beginning near 1740 UTC. The trace for site P5 is typical of those remaining locations that exhibit only minor variations in dewpoint.

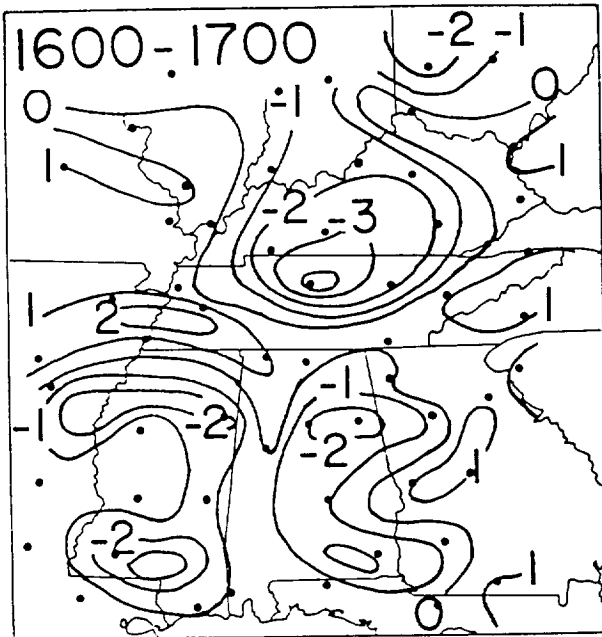


FIG. 6. One-hourly changes in surface dewpoint ( $^{\circ}\text{C}$ ) between 1600–1700 UTC. Contours are at intervals of  $1^{\circ}\text{C h}^{-1}$ . Station locations are denoted by dots.

The spatial distribution of hourly dewpoint changes (Fig. 8) indicates that the area of surface drying is very small and that it advances southward. The location of maximum dewpoint falls between 1600–1700 UTC moves to central Tennessee during the following hour, and some of the initial falls in the northern portion of the area are replaced by weaker rises. The thunderstorm development near 1720 UTC (Figs. 4, 8) occurs near the southern boundary of major dewpoint falls. The region of drying never reaches northern Alabama (Fig. 8), but remains in the Nashville area and even strengthens, as suggested by the second round of decreasing dewpoints at several sites between 1800–1900 UTC (Fig. 7). Although sites P5 and P9 are located relatively near the convection at 1800 UTC (Fig. 8), the absence of falling temperatures, gusty winds, and windshifts suggests that they did not experience convectively induced downdrafts.

#### 4. Upper-air observations

Upper-air conditions will be examined before considering explanations for the surface drying event. A mesoscale radiosonde network had been established over the COHMEX area, but, unfortunately, it was not operating on 17 June. Therefore, we explored mesoscale conditions above the surface using satellite-de-

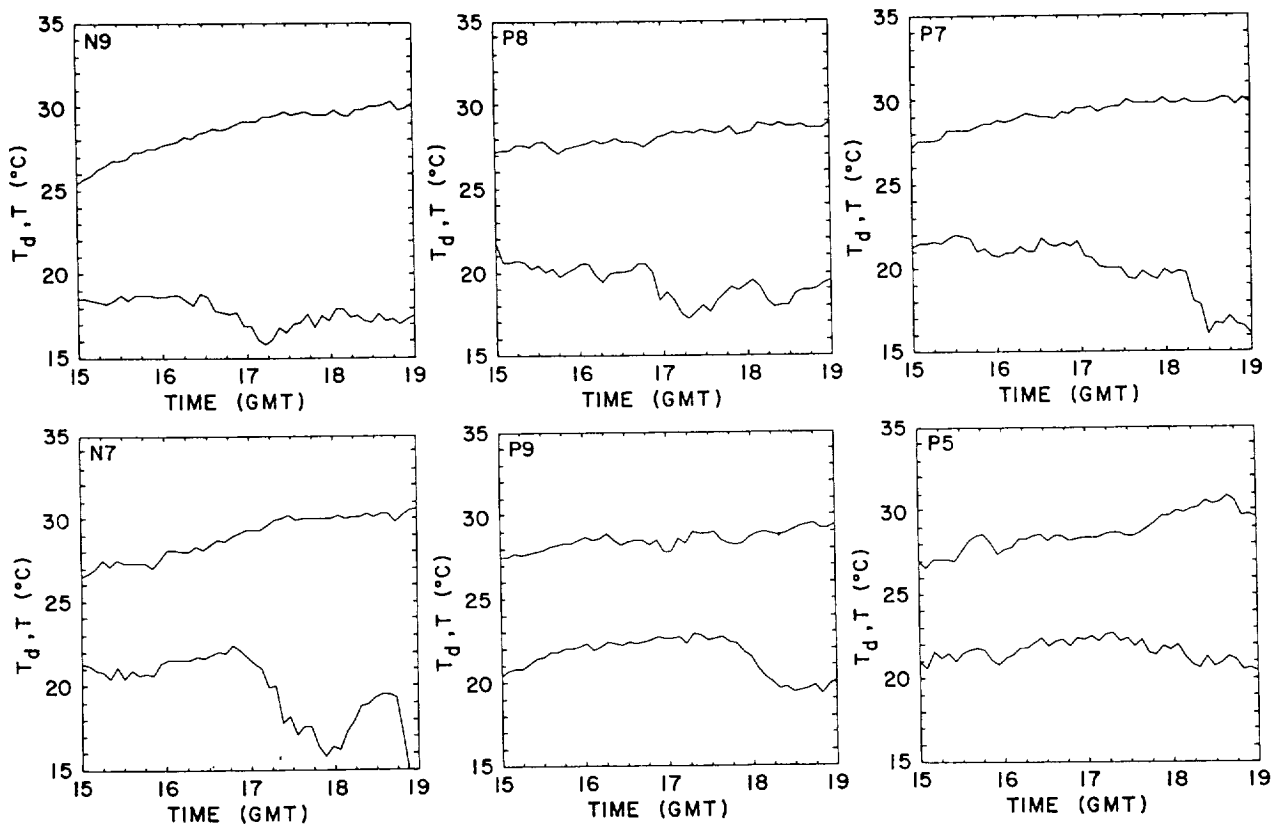


FIG. 7. Time series of surface temperature (upper trace) and dewpoint (lower trace) ( $^{\circ}\text{C}$ ) for selected COHMEX mesonetwork sites. The rapid surface drying is most prominent at site N7. Station locations are given in Fig. 8.

rived soundings from the GOES VISSR Atmospheric Sounder (VAS). Instead of utilizing retrievals prepared operationally in real time, we employed a special dataset prepared later by the Cooperative Institute for Meteorological Satellite Studies (CIMSS) at the University of Wisconsin. These retrievals were described by Velden et al. (1988) and were based on the standard "simultaneous" physical retrieval algorithm (Hayden 1988). The algorithm utilized  $5 \times 5$  arrays of 8 km (nadir) fields of view instead of the customary  $11 \times 11$  arrays, resulting in a horizontal sounding resolution of approximately 40 km. First-guess data above the surface were interpolated between the 1200 UTC Limited-area Fine-mesh Model (LFM) analyses and 12 h LFM prognoses. This contrasts with the operational procedure of interpolating between the 12- and 24-h LFM forecasts prepared from 0000 UTC input. Since VAS retrievals are highly first-guess dependent (Hayden 1988; Fuelberg and Olson 1991), this modification should yield improved results. The retrievals underwent a greater than usual degree of editing at Wisconsin after their preparation and were available at 1318, 1448, 1618, 1748, and 1918 UTC 17 June.

VAS retrievals and radiosonde-derived profiles have considerably different characteristics. VAS retrievals are available only in cloud-free locations since infrared

sensing is employed. The retrievals have relatively coarse vertical resolution, approximately 1–2 km, because the VAS instrument only has seven  $\text{CO}_2$  channels for thermal detection and three channels for water vapor, with each channel sensing radiation from a broad atmospheric layer (e.g., Chesters et al. 1982). VAS retrievals represent a horizontal area, not a single point, since each is based on an array of areal views. Although error characteristics of the special VAS retrievals have not been reported, they probably are somewhat better than those cited for an earlier operational VAS algorithm [the Smith (1983) formulation], i.e., approximately  $\pm 2^{\circ}\text{C}$  (Jedlovec 1985; Fuelberg and Meyer 1986). Advantages of VAS products over routine operational radiosonde releases include closer horizontal spacing and more frequent observations.

Moisture patterns in the middle to lower troposphere are depicted by subjectively analyzed VAS dewpoints at 620 mb (Fig. 9), the only VAS data level between 700 and 500 mb. At 1448 UTC, there is a dry tongue along the Ohio River as well as a narrow dry zone farther south, from Georgia through Arkansas. Although cloud cover has reduced sounding coverage over Tennessee and southern Kentucky, the available data indicate the area to be relatively moist. This dewpoint analysis is not at the same time or level as the 500-mb

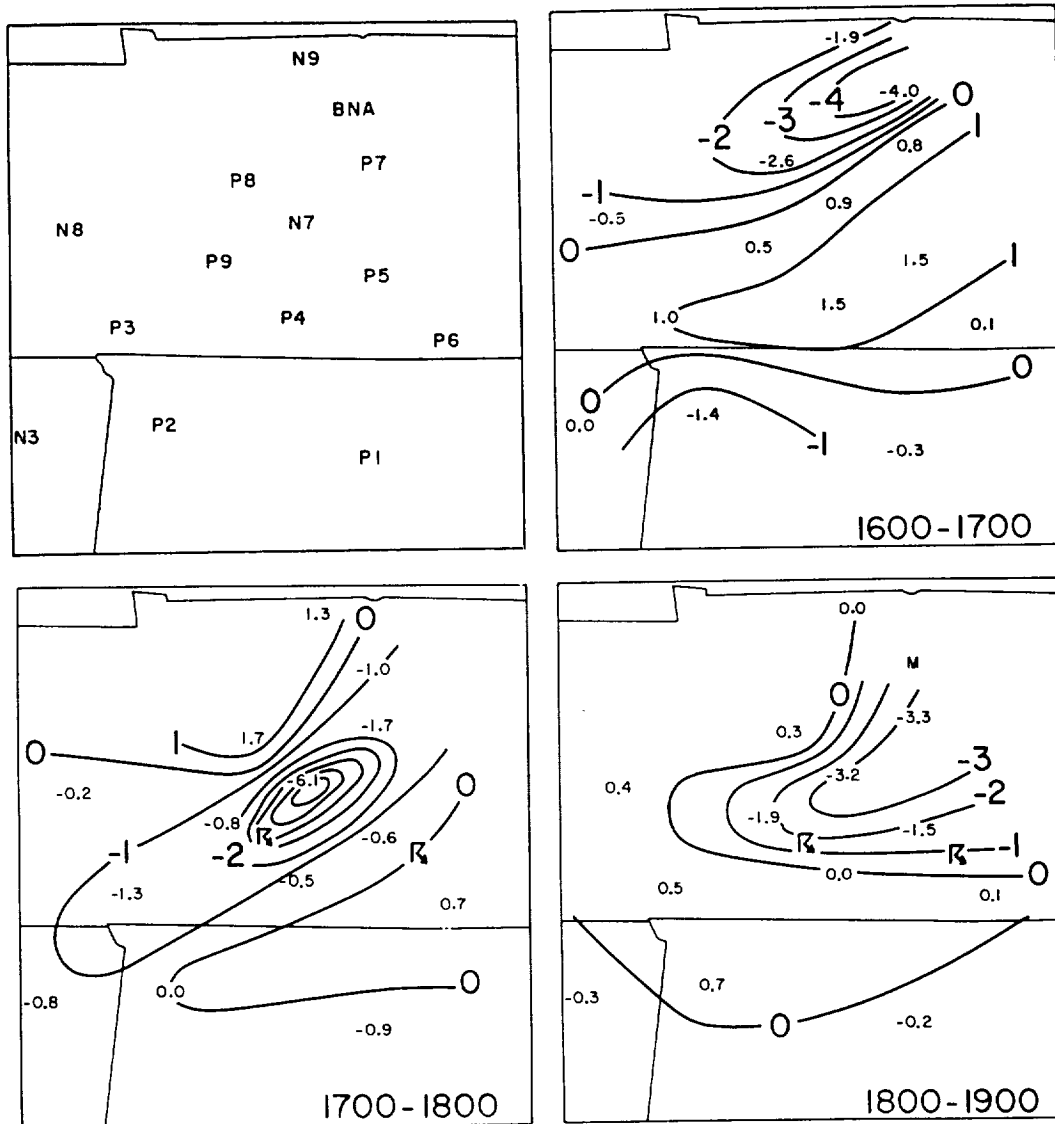


FIG. 8. One-hourly changes in surface dewpoint for the UTC times indicated. Contours are at intervals of  $1^{\circ}\text{C h}^{-1}$ . Designators for the COHMEX mesonetwork sites are given in the upper left panel. Locations of thunderstorms at 1800 and 1830 UTC were obtained from satellite imagery and are indicated on the bottom left and right panels, respectively.

sonde-derived version at 1200 UTC (Fig. 1), but the closer-spaced satellite data do suggest that the west-east dry tongue over the Ohio Valley is much more narrow and complex than indicated by the traditional data. The VAS analysis features are confirmed by  $6.7\text{-}\mu\text{m}$  water-vapor imagery (Fig. 10), where the brightest areas represent mid- and upper-level clouds. The clouds also are evident in the standard infrared ( $11\ \mu\text{m}$ ) images (Fig. 10).

Most VAS dewpoint features change little by 1618 UTC (Fig. 9); the exception is north-central Tennessee and adjoining parts of Kentucky where a narrow dry tongue is now protruding southward. If this feature existed at 1448 UTC, its location is uncertain because

of reduced sounding coverage in the area due to cloudiness, and because the 1448 UTC retrievals are displaced approximately 40 km from the 1618 UTC locations. By 1748 UTC, the dry area has moved slightly east of the Ohio River, and there are sufficient sounding sites to conclude that the narrow tongue over central Tennessee has advanced deeper into the state, bisecting the previously moist area of only 3 h ago. It is important to note that this midlevel dry tongue over central Tennessee is nearly coincident with the area of rapid surface drying occurring between 1600–1700 UTC (Figs. 6, 8).

VAS soundings over north-central Tennessee (Fig. 11) show the dry air aloft. Retrieval sites at 1448 and

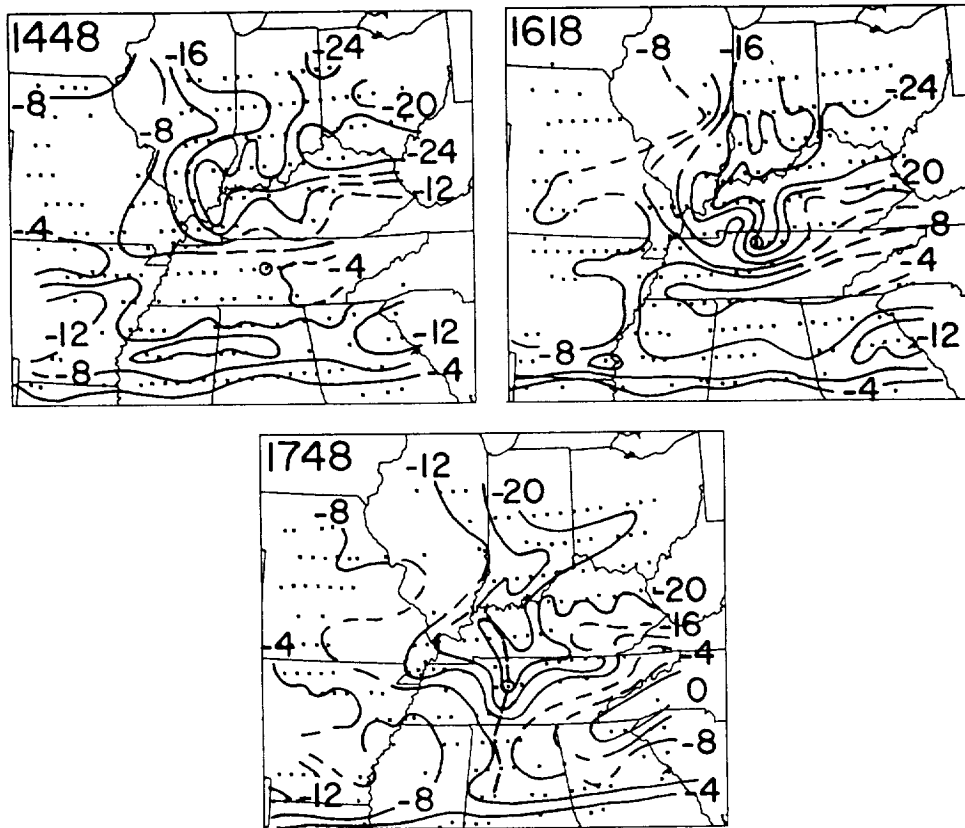


FIG. 9. VAS-derived isodrosotherm analyses (intervals of  $4^{\circ}\text{C}$ ) at 620 mb. Dashed lines are drawn in areas of relatively sparse data. VAS retrieval sites are indicated by dots, where the circled dot in north-central Tennessee at each time indicates the sounding locations in Fig. 11. The north-south line segments through Kentucky, Tennessee, and Alabama at 1748 UTC denote a cross section shown in Fig. 12.

1748 UTC (circled dots in Fig. 9) are very close to one another, and during this 3-h period the important change is the drying, especially near 600 mb. The sounding site near the dry protrusion at 1618 UTC (Fig. 9) is located about 45 km north of the other two sites. A cross section of VAS-derived equivalent potential temperatures at 1748 UTC (Fig. 12) shows conditions along the north-south axis in Fig. 9. The northern region, located behind the cold front, exhibits only slight convective instability because there is dry air at both the surface and aloft. However, on the warm side of the front, near the Alabama-Tennessee border, there is considerable convective instability since the dry protrusion aloft overlays moist air, resulting in a rapid decrease of equivalent potential temperatures with height.

The southward extension of dry air (Fig. 9) creates strong midtropospheric dewpoint gradients over northern Tennessee. At 1618 UTC, for example, dewpoints range from  $-25^{\circ}\text{C}$  near the Kentucky border to  $-12^{\circ}\text{C}$  over the Nashville area. Petersen et al. (1984) and others have made the empirical observation that convection tends to form at the edges of midtropospheric dry regions when there is sufficient low-level

moisture. This tendency is apparent in current water-vapor imagery at 2201 UTC (Fig. 10). Muller and Fuelberg (1990) described a case in which the leading edge of a dry image feature contained ascending motion that could destabilize the atmosphere and initiate convection. In the current case, however, synoptic-scale vertical motion patterns (not shown) are very weak and poorly defined.

Effects of the surface drying on stability are indicated by surface parcel lifted indices (Hales and Doswell 1982; Sanders 1986). Values were calculated using surface mesonetwork data and VAS 500-mb data subjectively interpolated to the mesonetwork sites. The parcels were lifted from the surface. Since VAS 500-mb temperatures varied little over the COHMEX domain, the lifted index patterns are dominated by surface variations detected by the conventional data.

The lifted indices (Fig. 13) show the most unstable region, with values as low as  $-6^{\circ}\text{C}$  to be located along the Alabama-Tennessee border. The stability fields are influenced by the mesoscale area of surface drying, corresponding to values of only  $-1^{\circ}\text{C}$  at 1748 UTC. This area of relatively dry surface air and comparatively small instability coincides with an area of diminished

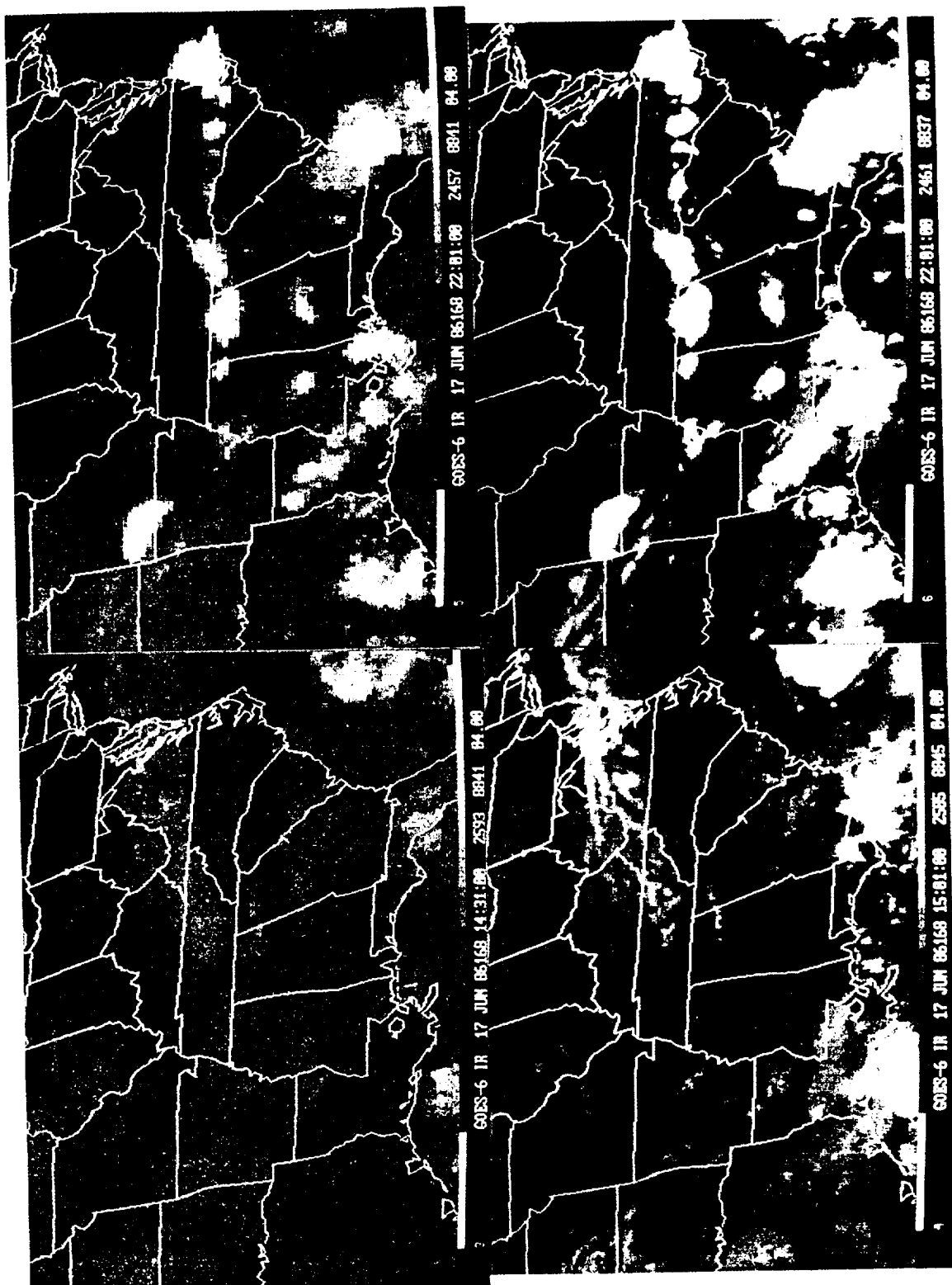


FIG. 10. Enhanced infrared imagery at 1501 and 2201 UTC 17 June (bottom) and 6.7- $\mu\text{m}$  water-vapor imagery (top) for 1431 and 2201 UTC.

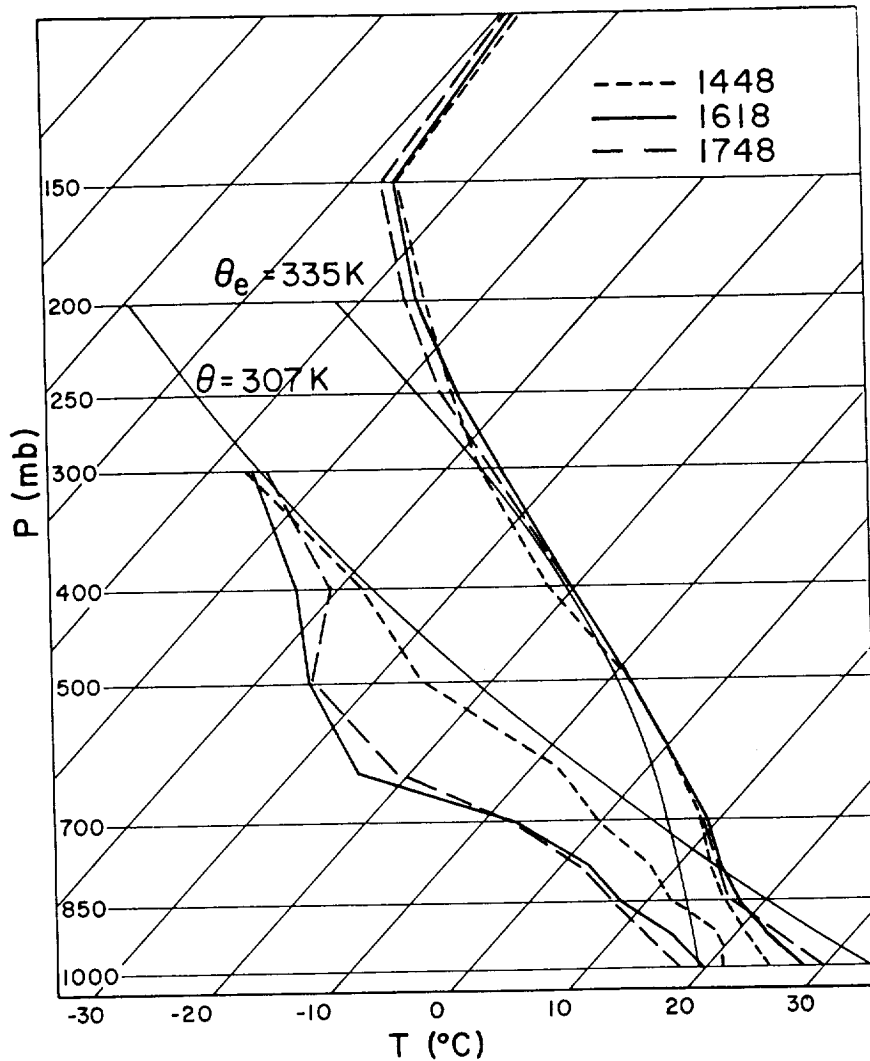


FIG. 11. Skew  $T$ -log  $p$  diagram of VAS retrievals over north-central Tennessee at the three times indicated. Sounding locations are the circled dots in Fig. 9.

convective cloudiness in the 1801 UTC visible image (Fig. 4). The thunderstorms (Figs. 4, 13) form near the southern edge of the drying that produces the strong stability gradients.

### 5. Hypothesis for surface drying

The sudden drying near Nashville cannot be attributed solely to horizontal transport since horizontal dewpoint advection over central Tennessee at 1500 UTC is only  $-0.7^{\circ}\text{C h}^{-1}$  when manually calculated from the subjective analysis (Fig. 5). This value is much smaller than the observed variations in Figs. 6 and 8. The important daytime processes of evaporation from the surface and transpiration from vegetation will tend to moisten the air, not dry it. Thus, mechanisms for surface drying must involve vertical processes. The roles

of subsidence and vertical mixing will be examined in this section.

#### a. Subsidence

Subsidence, by itself, will not cause surface drying due to the kinematic boundary condition at the earth's surface. However, subsidence may contribute to surface drying by bringing dry air aloft closer to the surface than otherwise possible, such that the dry air becomes more accessible to surface-based mixing processes. Small organized descent such as a microburst or "heat burst" (Johnson 1983; Johnson et al. 1989) is unlikely in the current case since satellite and radar data indicate that the drying event occurred prior to the onset of convection in an area of only scattered cumulus clouds. Although we did not have the necessary data to compute mesoscale fields of vertical motion, two procedures

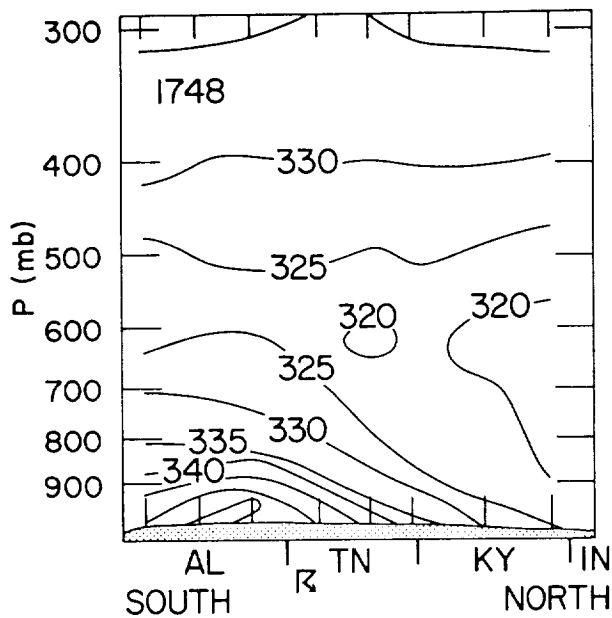


FIG. 12. Vertical cross section of satellite-derived equivalent potential temperature (intervals of 5 K) at 1748 UTC. The cross section's axis is shown in Fig. 9; tick marks along the abscissa of the cross section denote retrieval sites. Locations of thunderstorms are indicated.

were used to calculate surface horizontal divergence from the routine hourly reports that have an average spacing of approximately 100 km. One involved objective interpolation of observations to a grid of 66-km spacing, followed by simple centered finite differencing. The second procedure, outlined by Bellamy (1949), ordered the surface sites into groups of three, with relative inflow and outflow of station triangles being related to divergence. Results from the two procedures were similar, with those from the Bellamy approach given in Fig. 14.

Divergence patterns (Fig. 14) reveal an area of positive values over western Tennessee at 1200 UTC. The area moves little during the morning but expands in areal coverage by 1700 UTC when it is located near the area of rapid surface drying in central Tennessee that develops between 1600–1700 UTC (Figs. 5–6). The weak low-level subsidence that is suggested by the small divergence values over Tennessee may have aided in the formation of the surface drying event by transporting dry air aloft closer to the surface.

We also calculated surface divergence from the COHMEX mesonetwork data (average spacing of 65 km). Although the Bellamy (1949) approach was again employed, the input winds underwent a special adjustment procedure. Since Smith et al. (1988) noted that sheltering from obstructions such as trees can cause errors in COHMEX winds, we used their procedure to estimate unobstructed wind speeds at the 9 (of 12) sites for which they had prepared obstruction data. Al-

though the technique assumes that wind directions are unaffected by obstructions, the sheltering at some COHMEX sites may be extensive enough to invalidate this assumption (Fujita, personal communication). The adjustment procedure produced unobstructed winds that never were more than  $1.5 \text{ m s}^{-1}$  greater than observed values; however, in some cases of very light winds, this corresponded to as much as a 50% increase. A comparison of divergence fields produced from adjusted and unadjusted data revealed that patterns were not affected greatly because the adjustments tended to be relatively uniform across the area; however, magnitudes at some locations were reduced by as much as one half.

The fields of mesoscale divergence (Fig. 15) show northern Tennessee to be an area of persistent weak divergence. These patterns and those at earlier times and more frequent intervals (not shown) indicate no unusual change in patterns or magnitudes corresponding to the surface drying that began around 1630 UTC. However, as noted earlier, the implied subsidence may have brought drier air aloft closer to the ground where it then could be entrained by surface-based mixing.

It is interesting to note that the mesoscale divergence patterns (Fig. 15) contain a focused and persistent region of convergence just north of the most unstable region (Fig. 13) and near the area of convective initiation (Fig. 4). The convergence already is well established by 1430 UTC (not shown), several hours before the convection began. The greatest value prior to 1700 UTC ( $-2 \times 10^{-5} \text{ s}^{-1}$ ) (Fig. 15) would produce vertical motions of only a few centimeters per second in the lower troposphere. Therefore, surface heating probably was the major mechanism leading to storm development since noontime temperatures were near the convection temperatures. Nonetheless, the mesoscale patterns of convergence and instability probably helped to focus storm development in the west–east band in southern Tennessee (Fig. 4). The sudden increase in convergence after 1700 UTC, actually occurring between 1730 and 1745 UTC (not shown), probably is due to the developing storms.

#### b. Vertical mixing

Although the surface divergence (Figs. 14–15) suggests that the dry air aloft (Fig. 9) may have descended somewhat, we hypothesize that surface-based vertical mixing penetrated the dry tongue, bringing the drier air to the surface to produce the drying event noted in Figs. 5–8. We do not have direct measurements of the mixing so that our conclusions should be regarded largely as inferential. Three aspects of the hypothesis will be explored: 1) How high must surface-based mixing extend to produce the surface dewpoints observed during the drying event? 2) Does the mixed layer extend to these required altitudes? and 3) Why is the surface drying confined to the area of central Tennessee?

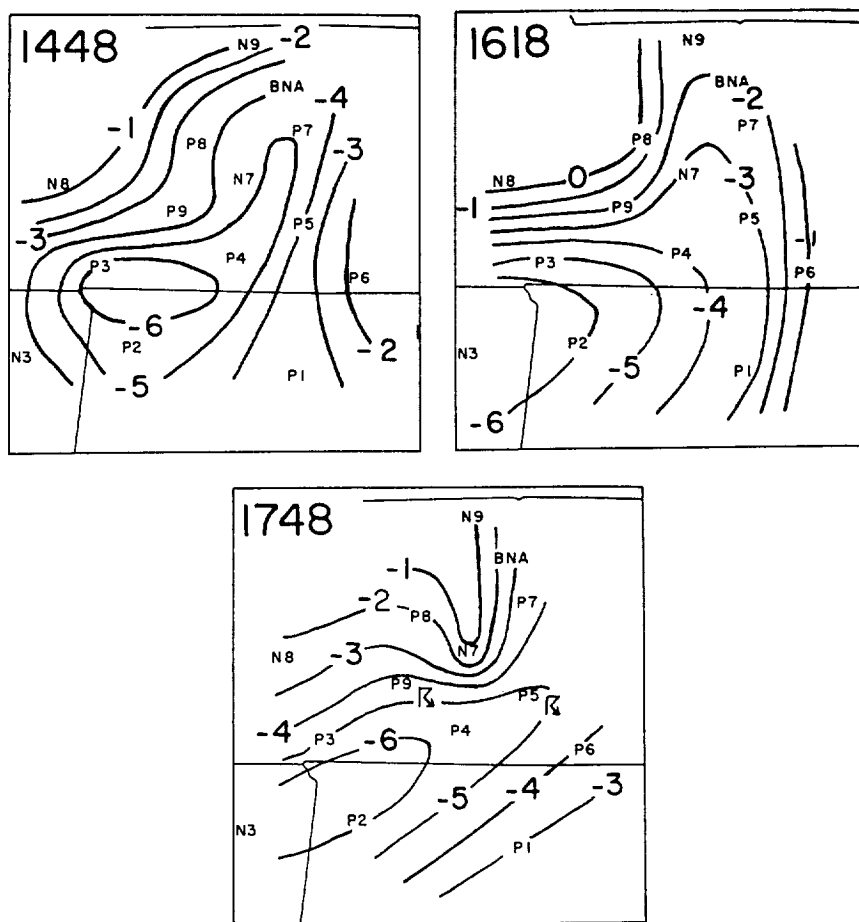


FIG. 13. Analyses of lifted index ( $1^{\circ}\text{C}$  intervals) employing COHMEX mesonetwork data at the surface and VAS retrievals interpolated to mesonetwork sites at 500 mb. Locations of thunderstorms are indicated at 1748 UTC.

Soundings were used to estimate the height to which surface-based mixing would have to extend to produce the minimum observed surface dewpoint; i.e., the  $16^{\circ}\text{C}$  value at station N7 (Fig. 7). The assumption was that vertical mixing yields a constant mixing ratio in the layer that is the average of preexisting values within it; i.e., the  $12\text{ g kg}^{-1}$  value corresponding to the  $16^{\circ}\text{C}$  dewpoint. Based on the 1200 UTC radiosonde observation at Nashville (Fig. 3), the height is 2.2 km or 775 mb. (All heights are above ground level.) This level is near the top of the weakly stable layer.

Radiosonde data were not available over central Tennessee near 1700 UTC, the time of rapid surface drying. Therefore, VAS retrievals were employed, keeping in mind their characteristics noted earlier. The retrievals indicated that midtropospheric drying had not yet occurred at 1448 UTC (Fig. 9). Based on the circled retrieval near Nashville at that time (Figs. 9, 11), the mixed layer still would have had to reach 2.6 km (740 mb), slightly higher than the 2.2 km (775 mb) value obtained from the earlier radiosonde report.

The narrow dry protrusion does extend through Tennessee at 1618 UTC (Fig. 9), and the circled retrieval site in Fig. 9 (slightly displaced from that at 1448 UTC) indicates that the mixed layer (Fig. 11) would now only have to reach 1.4 km (850 mb) to produce the  $16^{\circ}\text{C}$  surface dewpoint. This represents a decrease of 1.2 km from that of 90 min earlier.

The second question is whether the boundary layer actually extends to the required mixing height estimates. To explore this issue, the one-dimensional planetary boundary-layer model of Troen and Mahrt (1986) was used to obtain the depth of the planetary boundary layer over Tennessee at midday. The model predicts the horizontal wind components, potential temperature, and specific humidity as a function of turbulent diffusion, with horizontal and vertical advection neglected (Ruscher 1988). The eddy viscosity is stability dependent and exhibits a cubic profile with height. Boundary-layer height is diagnosed as a function of the bulk Richardson number. The boundary-layer model also integrates a separate model for the surface



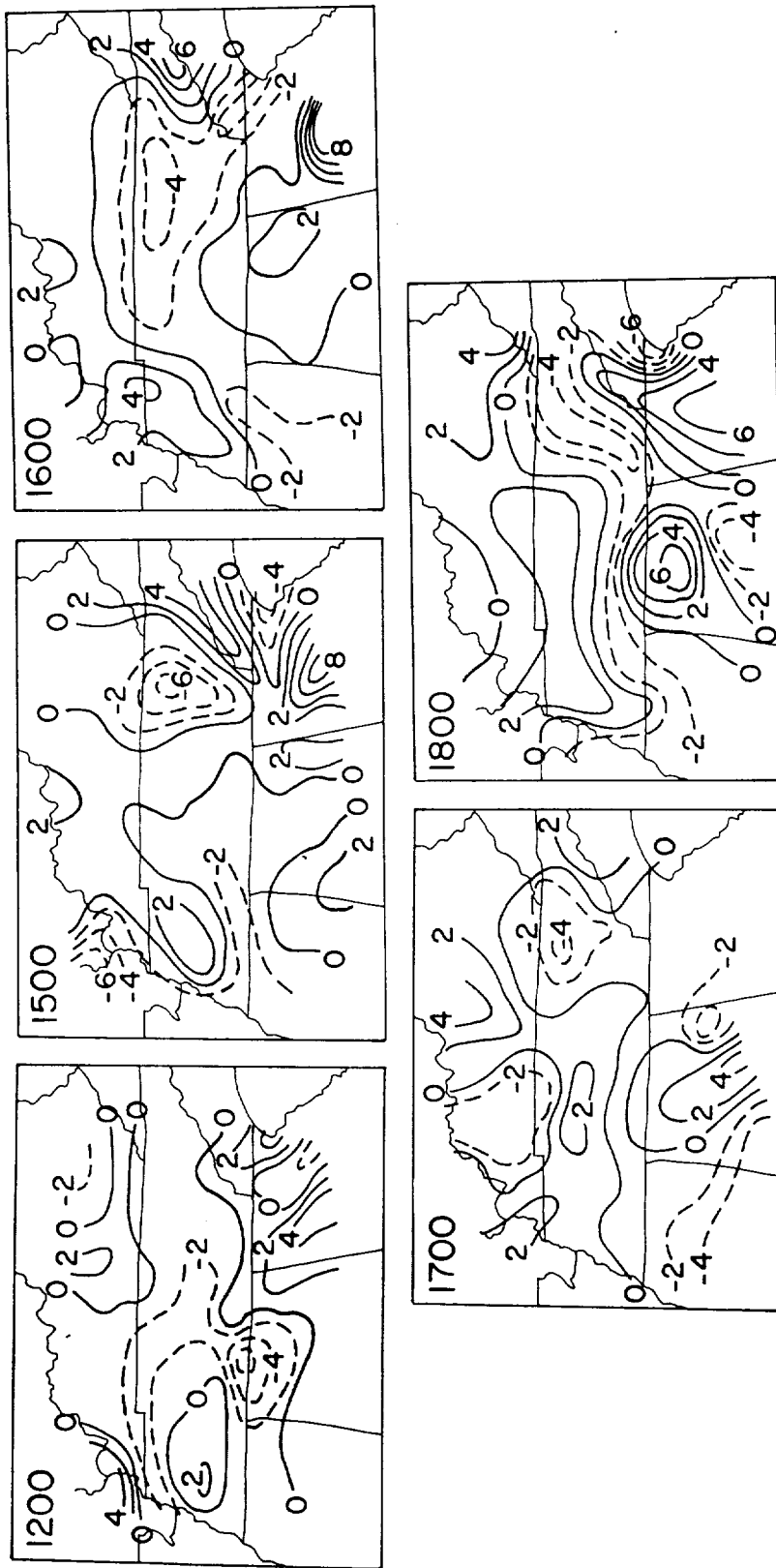


FIG. 14. Horizontal divergence (intervals of  $2 \times 10^{-3} \text{ s}^{-1}$ ) at the surface, based on routine hourly data and employing the Bellamy (1949) procedure as described in the text. Dashed isolines indicate negative values.

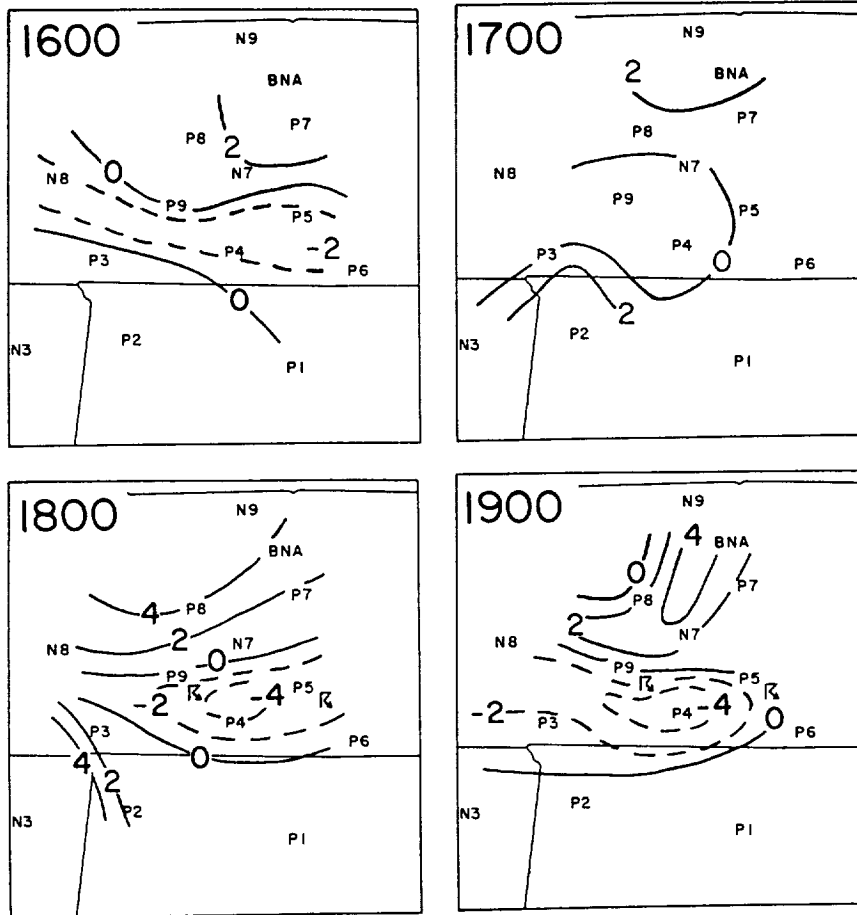


FIG. 15. Horizontal divergence (intervals of  $2 \times 10^{-5} \text{ s}^{-1}$ ) at the surface, based on COHMEX mesonetwork data and employing the Bellamy (1949) procedure. Dashed isolines indicate negative values. Locations of thunderstorms at 1800 and 1830 UTC are indicated in the bottom left and right panels, respectively.

layer, and a surface energy balance is coupled to a canopy and soil model.

The model was initialized with the 1200 UTC sounding from Nashville and run for 12 h. Clay soil was assumed, and soil moisture was based on an antecedent precipitation index (Saxton and Lenz 1967) using Nashville rainfall data. There were two soil layers—a shallow layer 5 cm deep and an underlying deep layer 95 cm deep. Shallow (deep) layer moisture availability was 0.11 (0.22) (volumetric units), corresponding to approximately 25% (50%) of field capacity. The albedo was assumed to be 0.23.

The model produces an initial boundary-layer height of 332 m (Table 1). This height is attributable to wind speeds that increase from  $3 \text{ m s}^{-1}$  at the surface to  $9.8 \text{ m s}^{-1}$  at 124 m above ground and remain near this strength through 713 m before diminishing. As the morning progresses, the boundary layer grows rapidly—to a value of 1.7 km (823 mb) by 1700 UTC. This height exceeds the 1.4 km (850 mb) value previously estimated to be required from the 1618 UTC

VAS retrieval. It is only 500 m lower than the 2.2-km value obtained from the 1200 UTC Nashville radiosonde sounding that was made before midlevel drying had occurred. Thus, model results indicate that mixing did extend to the levels required to produce the  $16^\circ\text{C}$  surface dewpoint.

The third question considers the location of the surface drying. The vertical mixing hypothesis implies that the surface drying will coincide with the dry area aloft since it is the penetration of mixing into the dry air

TABLE 1. Heights of the planetary boundary layer at Nashville on 17 June 1986 based on the model of Troen and Mahrt (1986) and Ruscher (1988).

Time (UTC)	1200	1300	1400	1500	1600	1700	1800	1900
Height (m)	332	539	795	1104	1412	1696	1832	1953
Pressure (mb)	963	937	913	881	850	823	810	798

that produces the decreasing surface dewpoints. As noted earlier, a comparison of Figs. 6, 8, and 9 indicates that the midlevel dry protrusion is nearly coincident with the surface feature and has similar dimensions. The area of surface drying moves slightly southward during the afternoon (Fig. 8), and we hypothesize that this corresponds to the movement of the upper-level dry tongue (Fig. 9). One also can speculate that the southward advance of dewpoint falls might be inhibited by boundary-layer cooling due to outflow from the convection to the south. The increasing dewpoints in the northern portion of the mesonet network between 1700–1800 UTC (Fig. 8) may be related to movement of the dry area aloft. That is, with passage of the midlevel dry tongue, the surface-based mixing entrains more humid air into the mixed layer than before. The spacing of the VAS retrieval sites (Fig. 9) is too coarse to fully verify these aspects.

It is informative to consider why northern Alabama did not experience the surface drying observed farther north. Redstone was the only COHMEX site to make an 1800 UTC radiosonde release. Located only 150 km south of Nashville, the sounding (Fig. 3) was taken only about 1 h after the surface drying began in Tennessee. The dewpoint trace does not show midtropospheric drying occurring during the morning, and this is consistent with the VAS retrievals (Fig. 9) not indicating midlevel drying this far south. Using the procedure described earlier, the 1800 UTC sounding (Fig. 3) indicates that mixing would have to extend to at least 2.9 km (725 mb) to produce a 16°C surface dewpoint; i.e., an average mixing ratio of 12 g kg<sup>-1</sup> between the surface and 2.9 km. Concerning the observed mixing depth, the sounding shows that nearly dry-adiabatic conditions extend only through about 875 mb, with the layer of constant mixing ratios only extending between approximately 950 and 875 mb. Thus, mixing does not appear to reach the level required to produce the major dewpoint falls that are observed over central Tennessee. Sudden surface drying does not occur at Redstone at any time on 17 June, thereby supporting the mixing hypothesis for central Tennessee.

## 6. Summary and conclusions

A mesoscale area of surface drying developed rapidly over central Tennessee near 1700 UTC on 17 June 1986. This was one of the days of the Cooperative Huntsville Meteorological Experiment (COHMEX) when special mesoscale surface data and special satellite-derived soundings were available. The greatest dewpoint drop of -6.3°C occurred during a 1-h period near 1700 UTC. Horizontal moisture transport at the surface was too weak to explain the drying event.

We believe that surface-based mixing penetrated the drier midlevels, entraining some of that air into the surface-based mixed layer, and leading to the sudden decreases in surface dewpoints. Radiosonde reports

showed a broad region of dry air in the midtroposphere over the Ohio River valley in the early morning. The special satellite retrievals indicated that this region developed a small-scale southward protrusion over Tennessee during midmorning that was coincident with the region of surface drying. Due to its small size, standard 12-h radiosonde data could not have resolved the feature adequately. Just prior to the drying event, surface-based mixing in the vicinity of the dry tongue would only have had to extend to approximately 1.4 km (850 mb) to produce the observed surface dewpoints. Boundary-layer modeling indicated that noon-time mixing-layer heights probably were near 1.7 km (823 mb). Thus, mixing apparently extended to the levels required to produce the observed surface dewpoints. Surface divergence patterns suggested weak subsidence over the area that might have contributed to the surface drying event by bringing the midlevel dry air nearer to the ground. In agreement with the mixing hypothesis, the size and placement of surface drying corresponded to that of the midlevel dry region. South of this region, the 1800 UTC Redstone sounding indicated that mixing did not extend to the height needed to produce the sudden surface drying.

The surface drying was not directly related to the nearby convective development except to focus the area of storm formation. Lifted indices based on the combination of COHMEX surface mesonet network data and VAS 500-mb temperatures isolated a small region that was especially conducive to storm development. The area of surface drying appeared as a region of comparatively stable conditions where convection was less likely to occur. Patterns of horizontal divergence derived from COHMEX mesonet network data revealed a persistent and well-defined area of convergence in south-central Tennessee. The convergence was located near the region of greatest instability, and this was the area of storm development.

In agreement with previous research (e.g., Chesters et al. 1982; Mostek et al. 1986; Zehr et al. 1988) current results demonstrate that VAS imagery and derived soundings were an important source of upper-air information. In spite of retrieval limitations (e.g., poor vertical resolution, unresolved cloud contamination, instrument noise, etc.), the satellite data provided mesoscale details about the midtropospheric dry tongue that were unavailable from other sources.

Local weather forecast offices of the future will focus on mesoscale conditions (Friday 1988). These offices will be able to monitor similar kinds of rapidly changing features in real time. It will be an exciting period as we use the new data sources to understand the many phenomena that previously have been hidden from our view.

*Acknowledgments.* This research was sponsored by the National Aeronautics and Space Administration (NASA) through Grant NAG8-653 under the auspices

of the Remote Sensing Branch of the Marshall Space Flight Center. Additional support was provided to Anthony Guillory under NASA's Graduate Student Researchers Program (Grant NGT-70095). Professor Paul Ruscher (FSU) and Captain T. J. Borland (FSU) graciously provided boundary-layer model runs and suggestions for their use. We also appreciate the comments of Professors Fred Sanders (MIT) and Ted Fujita (University of Chicago). Suggestions by the anonymous reviewers greatly clarified portions of the text. Steve Williams, Gary Jedlovec, and Paul Meyer, all of NASA/Marshall, provided most of the needed data and answered numerous questions about them. Chris Velden of CIMSS (University of Wisconsin) furnished the VAS retrievals along with valuable information. Figures were prepared by Dewey Rudd, and computational assistance was provided by Brad Diehl, David Parker, and Alex Orr. Tom Bradshaw helped prepare figures of the satellite imagery.

## REFERENCES

- Arnold, J., G. Wilson, S. Williams and R. McNider, 1986: Satellite precipitation and cloud experiment, experiment design document. 150 pp. [Available from Atmospheric Sciences Laboratory, Johnson Research Center, University of Alabama at Huntsville, Huntsville, AL 35899.]
- Barnes, S. L., and D. K. Lilly, 1975: Covariance analysis of severe storm environments, Preprints, *Ninth Conf. Severe Local Storms*, Norman, OK, Amer. Meteor. Soc., 301-306.
- Bellamy, J. C., 1949: Objective calculation of divergence, vertical velocity, and vorticity. *Bull. Amer. Meteor. Soc.*, **30**, 45-49.
- Chesters, D., L. W. Uccellini and A. Mostek, 1982: VISSR Atmospheric Sounder (VAS) simulation experiment for a severe storm environment. *Mon. Wea. Rev.*, **110**, 198-216.
- Friday, E. W., Jr., 1988: The National Weather Service severe storm program: Year 2000: Preprints, *15th Conf. Severe Local Storms*, Baltimore, Amer. Meteor. Soc., J1-J8.
- Fuelberg, H. E., and P. J. Meyer, 1986: An analysis of mesoscale VAS retrievals using statistical structure functions. *J. Climate Appl. Meteor.*, **25**, 59-76.
- , and —, 1984: An analysis of the AVE-SESAME I period using statistical structure and correlation functions. *Mon. Wea. Rev.*, **112**, 1562-1576.
- , and S. R. Olson, 1991: An assessment of VAS-derived retrievals and parameters used in thunderstorm forecasting. *Mon. Wea. Rev.*, **119**, 795-814.
- Hales, J. E., Jr., and C. A. Doswell III, 1982: High resolution diagnosis of instability using hourly surface lifted parcel temperatures. Preprints, *15th Conf. Severe Local Storms*, San Antonio, Amer. Meteor. Soc., 172-175.
- Hayden, C. M., 1988: GOES-VAS simultaneous temperature-moisture retrieval algorithm. *J. Appl. Meteor.*, **27**, 705-733.
- Jedlovec, G. J., 1985: An evaluation and comparison of vertical profile data from the VISSR Atmospheric Sounder (VAS). *J. Atmos. Oceanic Technol.*, **2**, 559-581.
- Johnson, B. C., 1983: The heat burst of 29 May 1976. *Mon. Wea. Rev.*, **111**, 1776-1792.
- Johnson, R. H., S. Chen and J. J. Toth, 1989: Circulations associated with a mature-to-decaying midlatitude mesoscale convective system. Part I: Surface features—heat bursts and mesowave development. *Mon. Wea. Rev.*, **117**, 942-959.
- McGinley, J., 1986: Nowcasting mesoscale phenomena. *Mesoscale Meteorology and Forecasting*, P. S. Ray, Ed., Amer. Meteor. Soc., 657-688.
- Miller, R., 1972: Notes on analysis and severe storm forecasting procedures of the Air Force Global Weather Central. AWS TR 200 (Rev.), Air Weather Service, Scott AFB, IL, 190 pp. [Available from Headquarters, AWS, Scott AFB, IL, 62225.]
- Mostek, A., L. W. Uccellini, R. A. Petersen and D. Chesters, 1986: Assessment of VAS soundings in the analysis of a preconvective environment. *Mon. Wea. Rev.*, **114**, 62-87.
- Muller, B. M., and H. E. Fuelberg, 1990: A simulation and diagnostic study of water vapor image dry bands. *Mon. Wea. Rev.*, **118**, 705-722.
- Petersen, R. A., L. W. Uccellini, A. Mostek and D. A. Keyser, 1984: Delineating mid- and low-level water vapor patterns in pre-convective environments using VAS moisture channels. *Mon. Wea. Rev.*, **112**, 2178-2198.
- Ruscher, P. H., 1988: Parameterization of the very stable atmospheric boundary layer in a simple model. Preprints, *Eighth Symposium on Turbulence and Diffusion*, San Diego, Amer. Meteor. Soc., 299-301.
- Sanders, F., 1986: Temperatures of air parcels lifted from the surface: Background, application, and nomograms. *Wea. Forecasting*, **3**, 190-205.
- Saxton, K. E., and A. T. Lenz, 1967: Antecedent retention indexes predict soil moisture. *J. Hydraul. Div. Am. Soc. Civ. Eng.*, **HY4**, 223-241.
- Smith, B. B., T. T. Fujita and J. W. Partacz, 1988: A method of correcting PAM winds based on obstructions and measured wind speeds. Preprints, *15th Conf. Severe Local Storms*, Baltimore, Amer. Meteor. Soc., 339-342.
- Smith, W. L., 1983: The retrieval of atmospheric profiles from VAS geostationary radiance observations. *J. Atmos. Sci.*, **40**, 2025-2035.
- Troen, I., and L. Mahrt, 1986: A simple model of the atmospheric boundary layer: Sensitivity to surface evaporation. *Bound. Layer Meteor.*, **37**, 129-148.
- Velden, C. S., B. M. Goodman and W. L. Smith, 1988: *Meteorological satellite products support for project COHMEX*. Final report to NASA on contract NAS8-36168, 11 pp. [Available from the authors at Space Science and Engineering Center, University of Wisconsin, 1225 West Dayton Street, Madison, WI 53706.]
- Williams, S. F., H. M. Goodman, K. R. Knupp and J. E. Arnold, 1987: *SPACE/COHMEX data inventory document*. NASA Tech. Memo. 4006, 480 pp. [Available from the authors at NASA, ES-43, Marshall Space Flight Center, AL 35812.]
- Zehr, R. M., J. F. W. Purdom, J. F. Weaver and R. N. Green, 1988: Use of VAS data to diagnose the mesoscale environment of convective storms. *Wea. Forecasting*, **3**, 33-49.

THE FLORIDA STATE UNIVERSITY  
COLLEGE OF ARTS AND SCIENCES

A SENSITIVITY ANALYSIS OF  
THE SPLIT WINDOW VARIANCE RATIO TECHNIQUE  
FOR PRECIPITABLE WATER ESTIMATION

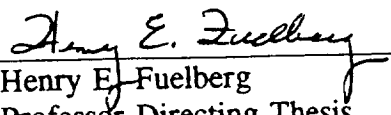
By

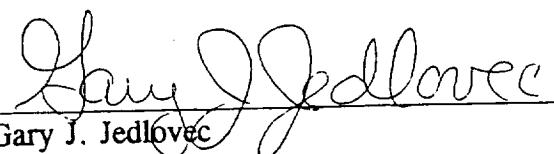
RICHARD D. KNABB

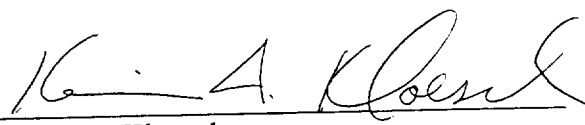
A Thesis submitted to the  
Department of Meteorology  
in partial fulfillment of the  
requirements for the degree of  
Master of Science

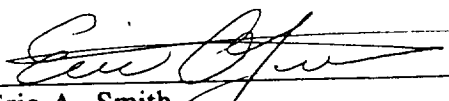
Degree Awarded:  
Spring Semester, 1993

The members of the Committee approve the thesis of Richard D. Knabb defended  
on December 3, 1992.

  
Henry E. Fuelberg  
Professor Directing Thesis

  
Gary J. Jedlovec  
Committee Member

  
Kevin A. Kloesel  
Committee Member

  
Eric A. Smith  
Committee Member

In Loving Memory of Kenneth K. Knabb

## ACKNOWLEDGEMENTS

I extend my gratitude first of all to my major professor, Dr. Henry Fuelberg, for providing me the opportunity to pursue an exciting area of meteorological research. I also thank him for his patient direction during this project. I also thank Dr. Gary Jedlovec for allowing me to freely investigate a scientific technique which he developed. His expert guidance along the way was most helpful. Thanks to my entire advisory committee for their suggestions and their careful examination of this work. Anthony Guillory was always generous with his time and information during this entire project, and for that, as well as for the tour of Huntsville last August, I thank him very much.

To my parents, I would like to express my thankfulness for their neverending support and interest in what I do, and I wish to reassure them that I will be out of school for good someday. This project also would not have been successful without the love, support, patience, and friendship of my wife Rhonda. No accomplishment would be worthwhile without someone with whom to share it. Finally, I acknowledge the daily presence of God, who reminds me that in "whatever you do, work at it with all your heart..... It is the Lord Christ you are serving."

Funding for this research was provided by the NASA Marshall Space Flight Center under grant NAG8-653.



## TABLE OF CONTENTS

LIST OF TABLES.....	vii
LIST OF FIGURES.....	viii
ABSTRACT.....	xi
1. Introduction.....	1
2. Description of the split window variance ratio technique.....	5
3. Data.....	9
4. The relationship between precipitable water and the variance ratio.....	19
<i>a. Developing the regression line.....</i>	19
<i>b. Uncertainty in the regression relationship.....</i>	25
5. Application of the technique to split window imagery.....	32
<i>a. Split window data errors.....</i>	32
<i>b. Violating the invariant emissivity assumption.....</i>	35
<i>c. Violating the invariant atmosphere assumption.....</i>	41
<i>d. Case study overview.....</i>	46
<i>e. Application to MAMS data on 16 October 1990.....</i>	51
6. Analysis of precipitable water imagery.....	55
<i>a. Comparison of results using different template sizes.....</i>	55
<i>b. 8 bit versus 10 bit input data.....</i>	65

<i>c. Evaluation of observed surface features and precipitable water gradients....</i>	66
<b>7. Summary and conclusions.....</b>	<b>75</b>
<b>REFERENCES.....</b>	<b>79</b>
<b>BIOGRAPHICAL SKETCH.....</b>	<b>81</b>

## LIST OF TABLES

Table	Page
1	MAMS instrument characteristics for the 16 October 1990 flight (from Jedlovec <i>et al.</i> 1989).....10
2	Maximum errors (K) in MAMS split window brightness temperatures due to truncation error in both calibration counts and scene temperatures. Errors for both 8 and 10 bit digitization correspond to a scene temperature of 300 K.....15
3	Single sample noise estimates based on structure function analysis of 16 October 1990 MAMS split window data with 8 and 10 bit digitization.....16
4	Comparison of vertical moisture structure among soundings having similar amounts of precipitable water. Transmittances are for the total atmospheric column.....26
5	Typical PW retrieval errors (mm) due to major sources of error for the application of the SWVR technique on 16 October 1990.....45
6	Comparison of statistics from all retrievals made with five different template sizes, from 10 bit input data, within the 37x50 km region represented in Figs. 16-20. The precipitable water statistics represent only those retrievals with 11 $\mu\text{m}$ channel variance above 1.0 K <sup>2</sup> . Statistics for 11 $\mu\text{m}$ channel variance include all values above and below 1.0 K <sup>2</sup> .....58

## LIST OF FIGURES

Figure	Page
1	Normalized spectral response function for the MAMS split window bands. The boxed values above each curve indicate the central wavelengths of the bands.....12
2	MAMS flight track over the Florida peninsula on 16 October 1990. The locations and directions of flight at various UTC times are indicated by the arrows. The dashed box represents the region displayed in the images in Fig. 22, while the shaded area is the region for Figs. 16-20.....13
3	Locations of National Weather Service radiosonde sites from which temperature and dewpoint profiles were obtained.....18
4	PW versus (A) split window variance ratio and (B) squared transmittance ratio for simulations using radiosonde data from 15-17 October 1990 (Fig. 3). The boxed equations represent the least squares fit regression line (drawn through the points) between PW and the natural logarithm of each ratio. Standard errors correspond to these regression lines. The circled points in (B) are discussed in Section 4b.....21
5	PW versus squared transmittance ratio for simulations using original radiosonde soundings (+) and modified versions of some soundings (X). The regression line from Fig. 4b is drawn through the data points.....24
6	Profiles of split window channel transmittances (A-C) and normalized weighting functions (D-F) for the three soundings in Table 4 with similar amounts of PW. Solid lines are for the 11 $\mu\text{m}$ channel, and dashed for the 12 $\mu\text{m}$ channel.....28
7	Error in PW retrieval versus percentage of PW contributed by the layer between the surface and 850 mb in the original soundings. Retrievals were calculated from the regression (Fig. 4b) relating PW to the squared transmittance ratio computed from the radiosonde soundings. Positive retrieval errors indicate overestimates of radiosonde values.....30

8	11 $\mu\text{m}$ channel variance versus retrieved PW for simulations using the CKL sounding at 1200 UTC on 16 October 1990. Curves represent retrievals using input split window data with no errors (X), instrument noise with 8 bit digitization (+), and instrument noise with 10 bit digitization (*).....	34
9	11 $\mu\text{m}$ channel variance versus average absolute retrieval error from simulations using each of the 34 original radiosonde soundings. Curves represent retrievals using a 25x25 template of channel brightness temperatures. The temperatures were subjected to instrument noise as well as 8 bit (dotted) and 10 bit (solid) digitization.....	36
10	11 $\mu\text{m}$ channel variance versus retrieved PW for simulations using the CHS sounding at 1200 UTC 16 October 1990. The various lines represent retrievals using a 25x25 template of channel brightness temperatures. The straight line with Xs indicates a template with an invariant surface emissivity of 0.96. The curved lines indicate templates where the emissivity is normally distributed about a mean of 0.96 with standard deviations of 0.005 (+), 0.01 (*), 0.02 ( $\square$ ).....	38
11	11 $\mu\text{m}$ channel variance versus retrieved PW for simulations using the AYS sounding at 1200 UTC 16 October 1990. The various lines represent retrievals using a 25x25 template of channel brightness temperatures. Surface emissivity was constant at 0.96. The straight line with Xs indicates a template with invariant PW. Curved lines indicate retrievals from templates with one-dimensional horizontal PW gradients of 1 mm (+), 2 mm (*), and 3 mm ( $\square$ ). Gradients were applied such that average PW in the template was equal to the original value from the sounding.....	43
12	Synoptic conditions for the surface at 1200 UTC 16 October 1990. Solid contours indicate sea level pressure. Note the center of high pressure over the border between Virginia and West Virginia. Station model plots at radiosonde sites provide surface temperature (F), dewpoint (F), and wind speed (kts).....	47
13	Analysis of total column PW (mm) computed from radiosonde sites (indicated by the circles and identified in Fig. 3) at 1200 UTC 16 October 1990.....	48
14	GOES visible image at 1630 UTC on 16 October 1990 over northern Florida. The MAMS flight track is superimposed with times in UTC next to arrows indicating the position and direction of flight.....	50

15	MAMS visible image for the 1635-1650 UTC flight leg on 16 October 1990, corresponding to the dashed rectangle in Fig. 2.....	52
16	Images of retrieved PW (A) and 11 $\mu\text{m}$ channel variance (B) for retrievals made with a 9x9 template over the 37x50 km region hatched in Fig. 2. In (A), lighter regions indicate greater PW. Darkest regions indicate PW below 12 mm. Each shade represents a range of about 3 mm. In (B), black regions denote variances below 1 $\text{K}^2$ , while white regions denote variances above 1 $\text{K}^2$ .....	57
17	As in Fig. 16 but for retrievals made with a 17x17 template.....	60
18	As in Fig. 16 but for retrievals made with a 25x25 template.....	61
19	As in Fig. 16 but for retrievals made with a 33x33 template.....	62
20	As in Fig. 16 but for retrievals made with a 41x41 template.....	63
21	Retrieved PW (prior to applying the variance threshold test and using a 25x25 template) versus distance of the retrieval from nadir. Retrievals are along a single scan line located 59.7 km south of the beginning of the flight leg. Negative distances indicate locations west of nadir. The solid line represents retrievals made from 10 bit data, and the dotted line indicates 8 bit data.....	67
22	Images of retrieved PW (A) and 11 $\mu\text{m}$ channel variance (B) for retrievals made with a 25x25 template over the 37x120 km region (dashed rectangle in Fig. 2) mapped during the entire 1635-1650 UTC flight leg. In (A), lighter regions indicate greater PW. The darkest shade indicates PW below 12 mm, and the lightest shade denotes values greater than 40 mm. Each shade represents a range of about 3 mm. In (B), lighter shades indicate larger variance. The lightest shade denotes variance greater than 10 $\text{K}^2$ , and each shade represents a range of about 1 $\text{K}^2$ .....	69
23	Scatter plot of retrieved PW versus 11 $\mu\text{m}$ channel variance for all actual retrievals made at 300 m spacing in the 1635-1650 UTC MAMS flight leg (corresponding to the 37x120 km dashed region in Fig. 2).....	71
24	Retrieved PW averaged along each scan line in the 1635-1650 UTC flight leg versus the distance along the flight leg.....	73

# A SENSITIVITY ANALYSIS OF THE SPLIT WINDOW VARIANCE RATIO TECHNIQUE FOR PRECIPITABLE WATER ESTIMATION

Richard D. Knabb, M. S.  
Florida State University, 1993  
Major Professor: Henry E. Fuelberg, Ph. D.

A technique for retrieving precipitable water (PW) from high resolution split window data is examined to determine its strengths and weaknesses. The technique relies on the relationship between PW and the ratio of spatial variances of brightness temperature in the two split window channels. This relationship, which is determined by regression using radiosonde data, appears to vary little for summertime conditions over the southeast United States.

This case study applies the technique to data from the Multispectral Atmospheric Mapping Sensor (MAMS) on 16 October 1990 over Florida. The resulting PW images reveal horizontal moisture variability as strong as 0.5 mm per km. The sharp gradient detected in the PW imagery occurs over a smaller distance than suggested by analysis of radiosonde-derived PW.

Numerous sources of error for the technique are evaluated. The most significant potential errors are due to variations in surface emissivity within the templates used to compute channel variances. Horizontal moisture variations within these regions, uncertainty in the regression relationship, and split window data errors also decrease

the accuracy of the PW estimations. Each source of error is enhanced when channel variances are small. The magnitude of variances is mostly dependent on the underlying surface and varies with the template size used for retrievals. Choice of template size is also important because larger sizes increasingly invalidate major assumptions of the technique.



## 1. Introduction

An important task in meteorology today is to describe the variability of atmospheric water vapor at increasingly smaller spatial and temporal scales. A primary goal is to locate and predict the evolution of horizontal and vertical moisture gradients which cannot presently be well resolved with routinely available data. Such a capability would improve skill in forecasting convective cloud cover and precipitation, particularly since the water vapor field can signify the locations of mesoscale boundaries such as sea breeze fronts, drylines, and thunderstorm outflows.

The current radiosonde network only supplies temperature, moisture, and wind profiles at 12-hour intervals and at locations spaced approximately 200 km apart. Satellites have provided a means for increasing data coverage. Over the last two decades, the accuracy and resolution of temperature and moisture profiles retrieved from satellite-borne instruments has steadily improved. For example, mesoscale retrieval data has been obtained with the VISSR Atmospheric Sounder (VAS). As part of the Geostationary Operational Environmental Satellite (GOES) platform, the VAS can monitor the same locations at half-hourly intervals. Numerous studies (Smith 1983; Jedlovec 1985; Fuelberg and Meyer 1986; McMillin et al. 1983; Hayden 1988) have addressed the use of VAS-derived soundings for improving our understanding of

moisture variability at scales below that resolvable with the radiosonde network.

Various schemes have been developed to calculate integrated water vapor content, or total column precipitable water (PW), from soundings derived from VAS. While PW does not describe vertical structure, the horizontal gradients in PW images have proven to be a valuable diagnostic and forecasting tool. A technique developed by Smith *et al.* (1985) calculates PW from VAS-derived profiles of water vapor mixing ratio. Hayden (1988) described the successful operational use of this technique. Birkenheuer (1991) introduced a procedure which merges PW data calculated from VAS-derived soundings with measurements from ground-based dual-channel passive microwave radiometers, thus providing an improved PW field.

PW is also commonly retrieved via techniques which use only the two infrared split window channels on VAS. These algorithms exploit the differential water vapor absorption within adjacent bandpasses at 11 and 12  $\mu\text{m}$ . Among the techniques is one developed by Chesters *et al.* (1983) from a single-layer physical radiative transfer model. Their case study showed that areas of relatively large PW were often associated with the development of convective clouds. A disadvantage of the method is that it requires knowledge of the average air temperature as determined from radiosonde data. Baker (1992) applied an optimized version of this algorithm described by Chesters *et al.* (1987) to VAS data over Florida. His results showed that thunderstorm formation corresponded closely with areas of enhanced mesoscale moisture gradients.

Jedlovec (1987) developed the Physical Split Window (PSW) technique for

deriving PW within the constraints of the radiative transfer equation. This method is not statistically based, but it does require a first guess profile obtained from radiosonde data. Guillory (1991) applied the PSW technique to VAS split window data. His resulting PW fields compared well with ground truth data and patterns from other PW retrieval methods, and deep moisture layers were clearly distinguishable.

A technique proposed by Kleespies and McMillin (1990) computes PW from time changes in VAS split window observations. During the time interval analyzed, the surface contribution to upwelling radiances is assumed to change while the atmospheric contribution is assumed constant. The ratio of channel transmittances is estimated from the ratio of the channel brightness temperatures resulting from the skin temperature changes. The transmittance ratio is then related to radiosonde-derived PW by regression. A case study produced PW values which compared well with those from radiosondes.

Although it is advantageous to use VAS because of its half-hourly temporal resolution, the system provides only 8 or 16 km spatial resolution in the split window channels. Some of the PW retrieval algorithms may be portable to instruments with finer spatial resolution. For example, Kleespies and McMillin (1990) were successful in applying their technique to the Advanced Very High Resolution Radiometer (AVHRR), which provides infrared data at 1 km resolution. In general, however, only limited research has investigated the potential of using split window PW retrieval algorithms on data from recently developed instruments with greatly increased resolution.

Jedlovec (1990a) obtained PW estimates from split window data collected by the airborne Multispectral Atmospheric Mapping Sensor (MAMS), which provides 100 m spatial resolution. To do so, he derived and applied an extension of the Kleespies and McMillin (1990) approach called the Split Window Variance Ratio (SWVR) technique. This technique computes PW from spatial variations in split window observations made at the same time. The ratio of channel brightness temperatures is equated to the ratio of squared channel transmittances, and both ratios are related to PW by regression. His retrieved PW images from 19 June 1986 exhibited enhanced mesoscale features which were associated with the later development of a cumulus cloud field. Jedlovec (1990b) also applied the technique to AVHRR data and found the PW results agreeing favorably with values derived from radiosondes and from other retrieval techniques. These studies showed that application of the technique to both instruments described moisture variability at scales smaller than possible with the VAS.

The principal objective of the study presented here is to examine the strengths and weaknesses of the SWVR technique. A new case study will evaluate the performance of the technique under a different set of surface and atmospheric conditions. The resulting PW fields will be analyzed for their utility in describing moisture variability within the area of interest. Sources of error in the PW retrievals will be estimated, and the effect of recent improvements to the instrument also will be assessed. The goal of the study is to achieve a more complete understanding of the detailed moisture information that is provided by the SWVR technique.

## 2. Description of the split window variance ratio technique

The SWVR technique for deriving PW (Jedlovec 1990a,b) depends on split window channel brightness temperature data having fine spatial resolution. Specifically, the SWVR is the ratio of the spatial variance of observed scene brightness temperatures in the 12  $\mu\text{m}$  channel to the corresponding variance in the 11  $\mu\text{m}$  channel, both within a small region in the imagery. Jedlovec (1990a) showed the strong inverse relationship between PW and the SWVR which is the foundation of the technique. Each value of the SWVR calculated from the imagery can be converted to a PW estimate when a regression relationship between the quantities is determined.

The regression relationship is determined in one of two ways. First, the SWVR can be computed from simulated imagery and related to the corresponding PW that was input to the simulation. A less rigorous and more indirect method is to relate PW to the ratio of squared split window channel transmittances. This is possible because of the mathematical relationship between the squared transmittance ratio and the SWVR. The derivation of this relationship that is presented below describes the physical reasoning behind the SWVR technique (Jedlovec 1990a).

Kleespies and McMillin (1990) showed that the split window channel transmittance ratio is related to the ratio of temporal changes in brightness temperatures by

$$\frac{\tau_{12}}{\tau_{11}} = \frac{\Delta T_{12}}{\Delta T_{11}} \quad (1)$$

where the subscripts correspond to the 11  $\mu\text{m}$  and 12  $\mu\text{m}$  channels,  $T$  represents brightness temperature, and  $\tau$  is the total atmospheric transmittance. This relationship is valid under the assumption that changes in brightness temperature are due only to changes in skin temperature, and not to changes in the atmosphere. It is also assumed that surface emissivity does not change between measurements. In formulating the SWVR technique, Jedlovec (1990a) assumed that the brightness temperature changes in (1) are purely spatial and proceeded from that point.

Each brightness temperature in (1) can be expanded as the sum of the spatial mean and a perturbation from that mean to give the expression

$$T = \bar{T} + \delta T. \quad (2)$$

Substituting (2) into (1), rearranging (1) in terms of products, squaring both sides, and summing both sides over  $N$  adjacent fields of view yields

$$\sum_{i=1}^N \tau_{12}^2 \delta T_{11}^2(i) = \sum_{i=1}^N \tau_{11}^2 \delta T_{12}^2(i). \quad (3)$$

Since the atmosphere is assumed to be invariant, the squared transmittances can be removed from the summation. Solving for the ratio of squared transmittances yields

$$\frac{\tau_{12}^2}{\tau_{11}^2} = \frac{\sum_{i=1}^N \delta T_{12}^2(i)}{\sum_{i=1}^N \delta T_{11}^2(i)} . \quad (4)$$

Replacing the summations with the sample variance, defined as

$$\sigma^2 = \frac{\sum_{i=1}^N \delta T^2(i)}{N-1} , \quad (5)$$

gives the following expression between the squared transmittance ratio and the SWVR:

$$\frac{\tau_{12}^2}{\tau_{11}^2} = \frac{\sigma_{12}^2}{\sigma_{11}^2} . \quad (6)$$

Equation (6) is the physical substantiation for relating the SWVR to PW because it states that, under certain assumptions, the squared transmittance ratio and the SWVR are interchangeable. The SWVR technique may then be applied via a regression relationship between PW and the squared transmittance ratio. In this way, the SWVRs calculated from split window imagery are estimates of squared transmittance ratios.

The regression relationship determined for the 16 October 1990 case studied here appears in Section 4.

The formulation of the technique presented above includes several assumptions about the image scene in which the SWVR is computed. Most significant is that the atmosphere is assumed to be invariant across adjacent fields of view within the regions where channel variances are computed. High resolution data therefore are needed in order to minimize the size of these regions. Assuming an invariant atmosphere means that changes in channel brightness temperatures are due only to variations in the underlying skin temperatures. Another important assumption is that emissivity does not vary between channels or between adjacent fields of view. Also, changes in the magnitude of this invariant emissivity are assumed not to affect the SWVR. This is because the ratio involves only variations in channel brightness temperatures and is not inherently dependent on the temperatures themselves. For this same reason, the absolute infrared calibration of any instrument used to obtain the brightness temperatures is not a concern. Section 5 will discuss the extent to which the above assumptions are satisfied in application to actual imagery.



### 3. Data

The current research utilized split window radiance measurements from the MAMS. Data from this instrument were also used in the introductory study of the SWVR technique by Jedlovec (1990a). The MAMS is a scanning instrument which is part of the high altitude research program coordinated by the National Aeronautics and Space Administration (NASA) to investigate potential instrumentation for future satellite sensors. In addition to the 11 and 12  $\mu\text{m}$  split window channels, MAMS collects data from one other infrared channel. This third channel can be either a shortwave infrared window channel centered at 3.7  $\mu\text{m}$  or a water vapor channel centered at 6.5  $\mu\text{m}$ . These two bands cannot be used simultaneously. MAMS also measures reflected radiation from the earth's surface and clouds in eight visible wavelength bands.

MAMS is normally flown at an altitude of 20 km aboard a NASA ER-2 high altitude aircraft. In the usual instrument configuration (Table 1), the ground swath width is approximately 37 km across the flight track. The horizontal resolution of each instantaneous ground field of view is about 100 m at nadir. An analog-to-digital converter is used during flight to extract raw count values from channel voltages resulting from energy received from the observed scene and the controlled

Table 1. MAMS instrument characteristics for the 16 October 1990 flight (from Jedlovec *et al.* 1989).

Spectral bands	8 visible and near infrared 3 infrared (3.7,11.1,12.6 micrometers)
Roll correction	+/- 15.0 degrees
Pixels per scan line	716
Calibration sources	2 controlled blackbodies
Scan speed	6.25 revolutions per second
Instantaneous field of view	5.0 milliradian
Ground resolution at 20 km altitude	100 meters at nadir
Total field of view	85.92 degrees
Swath width at 20 km altitude	37.2 km
Digitization	8 bit (visible), 10 bit (infrared)

blackbodies. The counts obtained from viewing the blackbodies of known temperature during each scan line are for infrared channel calibration. They are used to relate scene count values to channel equivalent blackbody temperatures (brightness temperatures). Additional details on MAMS instrument specifications and calibration procedures are reported by Jedlovec *et al.* (1989).

The 12  $\mu\text{m}$  channel, the 'dirty' channel of the split window pair, measures radiation at wavelengths where water vapor absorption is greater than in the 'clean' 11  $\mu\text{m}$  channel. Resolving this differential absorption is essential to the SWVR technique. The MAMS split window channels have spectral response curves (Fig. 1) which are centered at 11.1  $\mu\text{m}$  and 12.6  $\mu\text{m}$ . They have characteristics similar to their VAS counterparts. The narrow 12.6  $\mu\text{m}$  MAMS channel differs somewhat from the corresponding 'dirty' channel on AVHRR which is broader and shifted towards shorter, less moisture-sensitive wavelengths. Despite these differences in spectral characteristics, Jedlovec (1990a and 1990b) has shown the SWVR technique to be applicable to AVHRR as well as MAMS data.

The MAMS data for this study were collected during a flight over the Florida peninsula on 16 October 1990. The MAMS was flown along several north-south tracks during the late morning and early afternoon (Fig. 2). Data from this flight benefit from many improvements made to the instrument in the late 1980s. Among these was a change to a full aperture mirror which increased the signal-to-noise ratio in all MAMS channels. Also, improved electronics has increased the reliability of infrared calibration values. Further, the 3.7  $\mu\text{m}$  channel capability mentioned

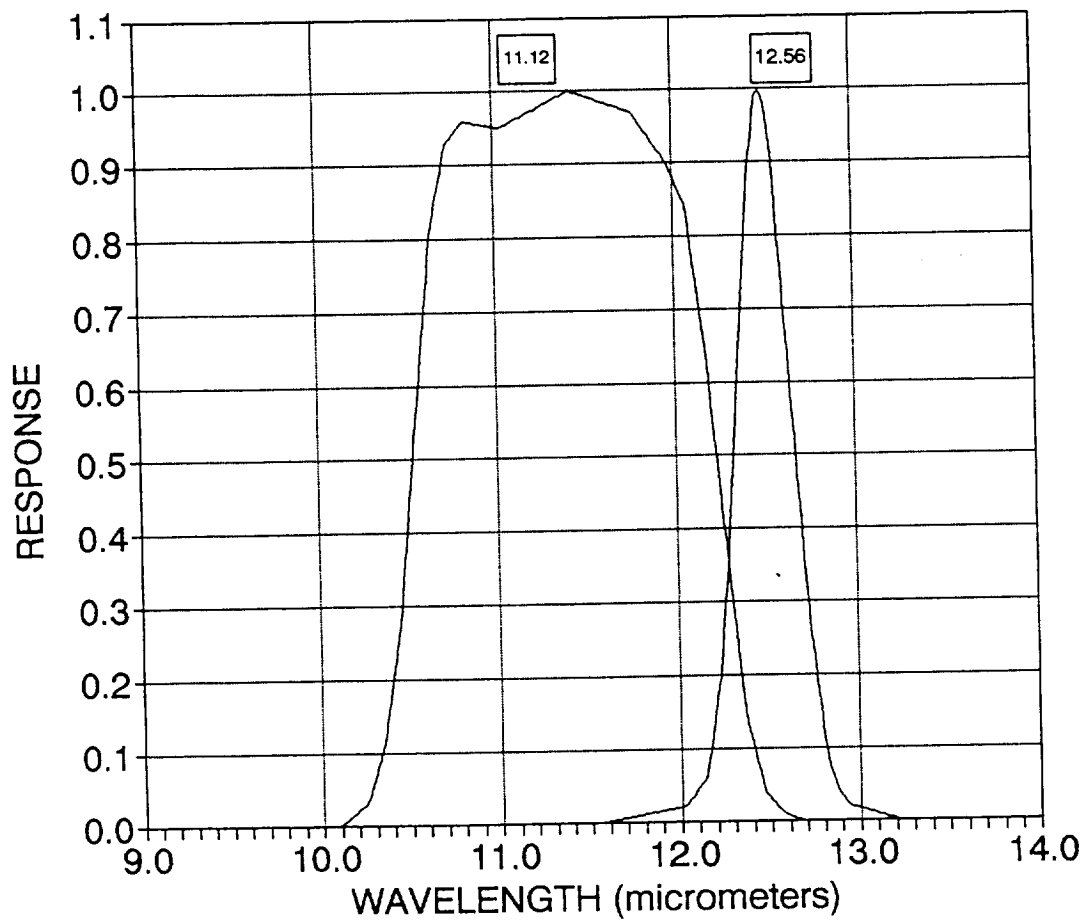


Figure 1. Normalized spectral response functions for the MAMS split window bands. The boxed values above each curve indicate the central wavelengths of the bands.

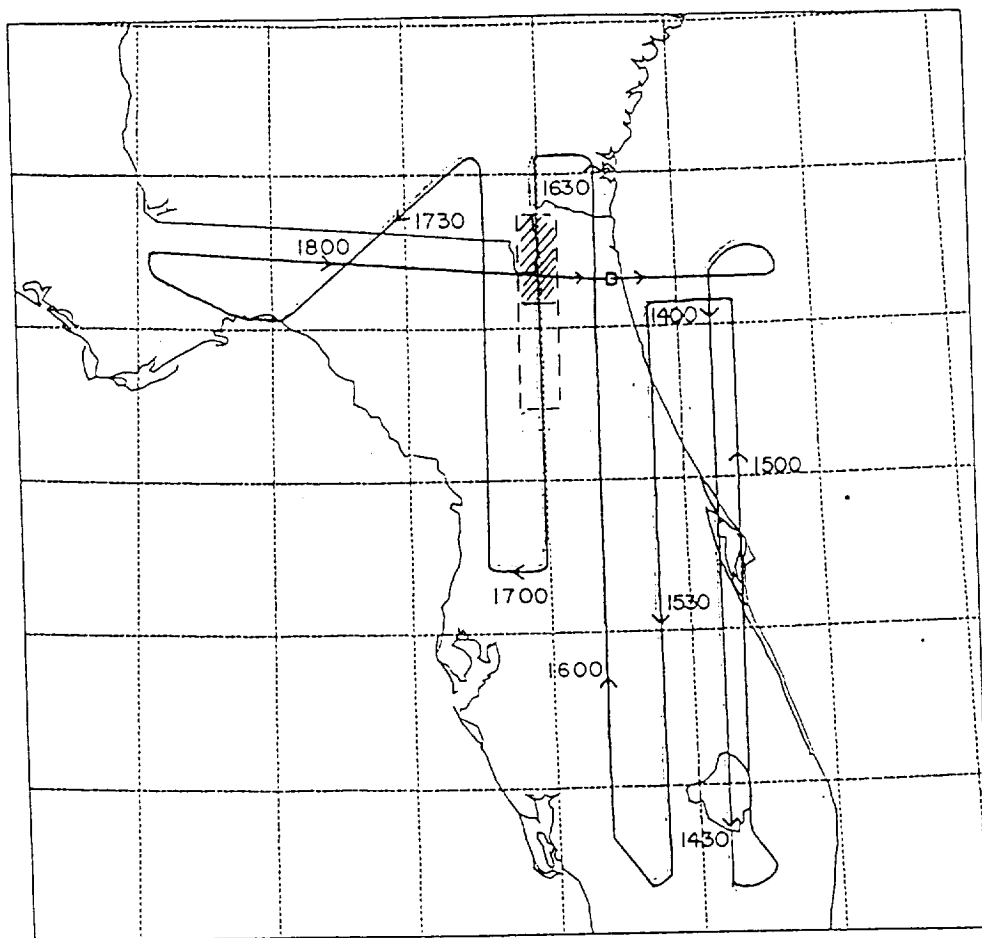


Figure 2. MAMS flight track over the Florida peninsula on 16 October 1990. The locations and directions of flight at various UTC times are indicated by the arrows. The dashed box represents the region displayed in the images in Fig. 22, while the shaded area is the region for Figs. 16-20.

previously was added in September 1986. This channel was used in place of the 6.5  $\mu\text{m}$  channel for the October 1990 flight. Important for this study is that infrared channel count values and the channel temperatures were digitized with ten bits of precision instead of only the eight bits available prior to June 1987 (Jedlovec *et al.* 1989). This change affects the accuracy of the split window channel brightness temperatures by reducing errors due to truncation. For purposes of evaluating the effect of this upgrade on results from the SWVR technique, 8 bit versions of the infrared data from the October 1990 flight were also constructed.

Truncation error in the split window data is due to discrete quantization of the calibration and actual scene temperatures. Errors for both eight and ten bit observed brightness temperatures are presented in Table 2 (Jedlovec *et al.* 1989). Clearly, the ten bit data provide significant error reduction, especially when the two error sources are considered together. The listed values are the maximum possible; truncation error is normally less than half these magnitudes.

Single sample noise in the 16 October 1990 MAMS split window data was estimated using structure functions similar to that described by Hillger and Vonder Haar (1979) and Fuelberg and Meyer (1986). Structure values were computed at a separation interval of 100 m. Noise estimates for both eight and ten bit data (Table 3) were obtained by extrapolating the structure profiles to zero separation distance. Current values are considerably lower than those for previous MAMS flights (Jedlovec *et al.* 1989) as a result of improvements to the instrument. While noise in the 11  $\mu\text{m}$  channel is the same in this case for both levels of data precision, ten bit digitization

Table 2. Maximum errors (K) in MAMS split window brightness temperatures due to truncation error in both calibration counts and scene temperatures. Errors for both 8 and 10 bit digitization correspond to a scene temperature of 300 K.

BAND (micrometers)	SCENE DATA ERRORS (K)	
	8 BIT	10 BIT
	Calibration value truncation error	
11.1	0.42	0.11
12.6	0.54	0.12
	Scene value truncation error	
11.1	0.32	0.08
12.6	0.32	0.08
	Total truncation error	
11.1	0.74	0.19
12.6	0.86	0.20

Table 3. Single sample noise estimates based on structure function analysis of 16 October 1990 MAMS split window data with 8 and 10 bit digitization.

---

---

BAND (micrometers)	SCENE DATA ERROR DUE TO NOISE (K)	
	8 BIT	10 BIT
11.1	0.050	0.055
12.6	0.118	0.081

---



yields slightly decreased noise in the 12  $\mu\text{m}$  channel.

Each of the noise estimates in both channels (Table 3) is less than half of the total truncation error for both levels of precision (Table 2). Thus, truncation error will mask much of the effect of noise on channel brightness temperatures. As a result, observed temperature variations as small as 0.2 K (the total truncation in the 12  $\mu\text{m}$  channel) are likely due to real scene variations. This suggests that the small amount of noise in the data will have little influence on computing SWVRs from actual imagery. The effects of all split window data errors on results of the SWVR technique will be discussed in Section 5.

Since the 16 October 1990 flight was not part of any major field experiment, no special ground truth information is available. However, conventional radiosonde data surrounding the location and time of the MAMS flight are utilized. Soundings taken at 12 h intervals between 1200 UTC 15 October 1990 and 1200 UTC 17 October 1990 at nine locations (Fig. 3) are included in the data set. These profiles are used in assessing the synoptic situation presented later and in developing the PW versus SWVR regression relationship that is described next.

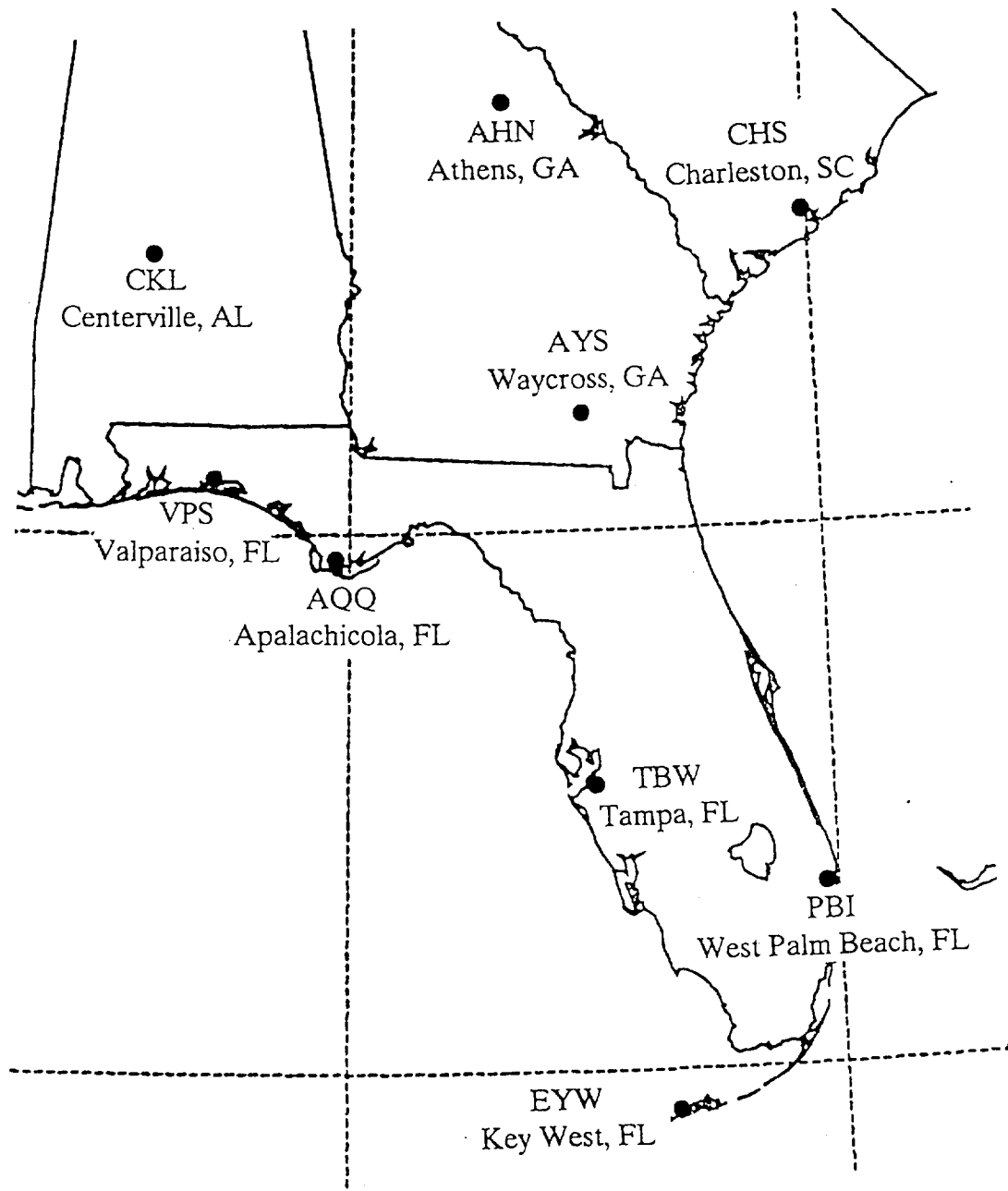


Figure 3. Locations of National Weather Service radiosonde sites from which temperature and dewpoint profiles were obtained.

#### 4. The relationship between precipitable water and the split window variance ratio

##### *a. Developing the regression line*

To apply the SWVR technique to the 16 October 1990 MAMS data, radiative transfer simulations were used to relate PW to the SWVR and, for comparison, to the squared transmittance ratio. The 34 cloud-free temperature and dewpoint profiles used as input to the simulations were extracted from the 15-17 October 1990 radiosonde data set (Fig. 3). These soundings were the best available for representing atmospheric conditions mapped by MAMS on 16 October. A dewpoint depression threshold was used to identify cloudy soundings, which were excluded because clouds are opaque at infrared wavelengths and preclude transmittance calculations.

SWVRs were computed from simulated MAMS split window data. The data was created by combining each clear-air sounding of known PW with a 25x25 pixel array, or template, of different underlying surface skin temperatures, thereby representing the atmospheric and surface radiance contributions. Since MAMS has a pixel resolution of 100 m, the simulated templates represent 2.5x2.5 km regions. Each of the radiances (computed at 1 wavenumber spectral resolution for each pixel) was converted into an equivalent blackbody temperature using an inverse Planck function. Filtering these temperatures through MAMS channel response functions (Fig. 1) yielded templates of channel brightness temperatures. Ratios of 12  $\mu\text{m}$  to 11  $\mu\text{m}$  channel

temperature variance (the SWVRs) were formed for each template. The chosen range of simulated skin temperatures (about 302 to 320 K, with an average 312 K) was determined from land surface temperature retrievals from the 16 October 1990 MAMS data, using the algorithm implemented by Jedlovec and Atkinson (1992). Based on research by Labed and Stoll (1991), and as suggested by Hayden (1988), emissivity in both channels was set to 0.96. This constant emissivity satisfies a major assumption of the technique. The invariant atmosphere assumption also was met since only one sounding was used to determine each SWVR value.

PW derived from each of the 34 input soundings is plotted against the corresponding SWVR simulation in Fig. 4a. A least squares analysis was applied to determine the slope and intercept of the best fit line. A logarithmic formulation gave the best fit to these data, as in the case presented by Jedlovec (1990a). The correlation between quantities is quite strong, as indicated by the small standard error of the points about the regression line (1.23 mm).

A similar regression relationship was calculated between PW and the squared transmittance ratio. MAMS split window channel transmittances were computed for each of the 34 input soundings by filtering simulated transmittance profiles with the channel response functions (Fig. 1). The channel transmittances were squared, and then ratios of 12  $\mu\text{m}$  to 11  $\mu\text{m}$  channel squared transmittance were formed. Results of these simulations appear in Fig. 4b. The best fit curve was determined identically to that for the SWVR (Fig. 4a). A strong correlation is again evident, and the slope, intercept, and standard error of this line are quite similar to those in Fig. 4a. At a

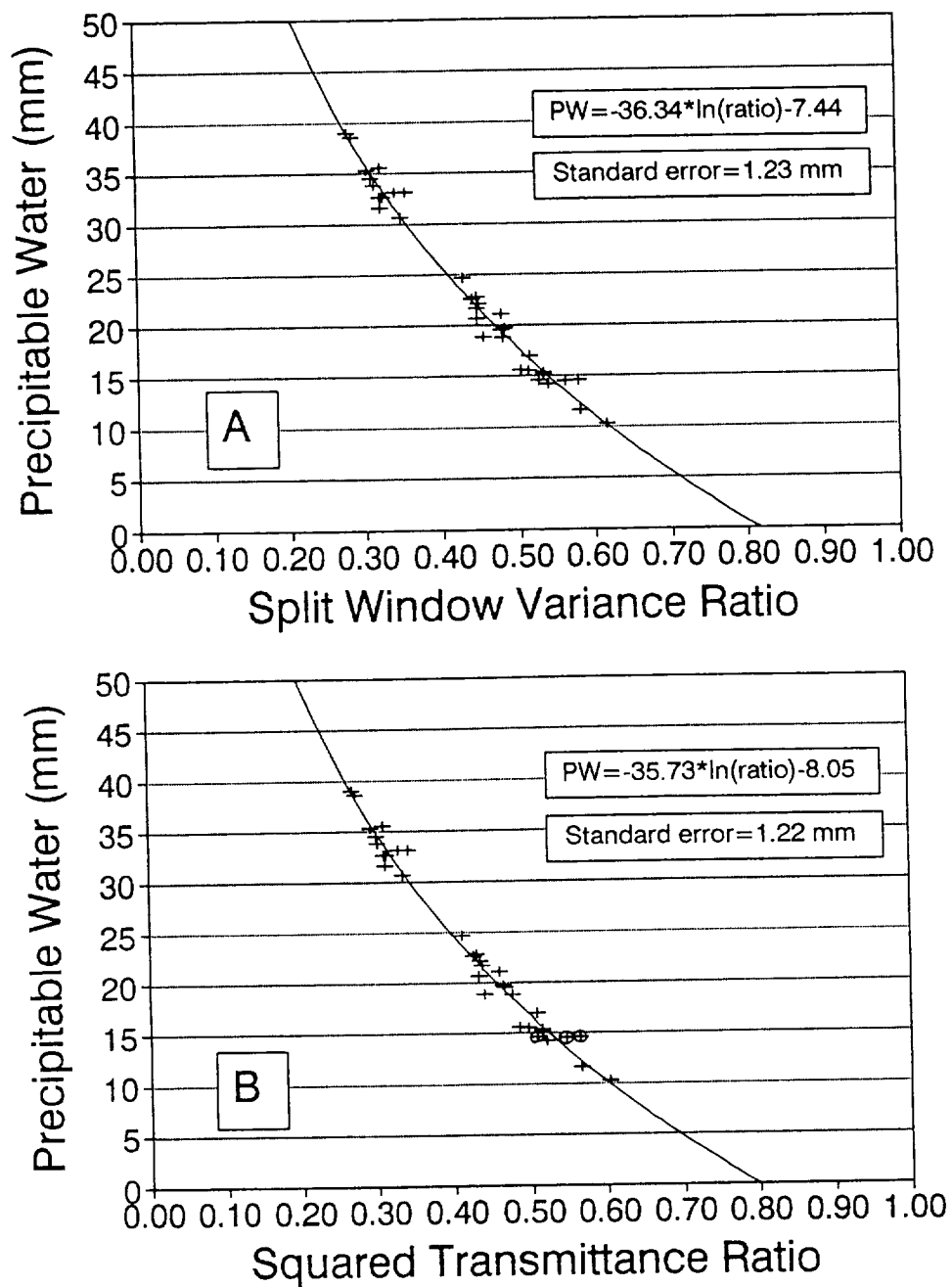


Figure 4. PW versus (A) split window variance ratio and (B) squared transmittance ratio for simulations using radiosonde data from 15-17 October 1990 (Fig. 3). The boxed equations represent the least squares fit regression line (drawn through the data points) between PW and the natural logarithm of each ratio. Standard errors correspond to these regression lines. The circled points in (B) are discussed in Section 4b.

ratio of 0.40, the two regression lines yield PWs which differ by about 1 mm. Further, both regression lines are comparable to those determined by Jedlovec (1990a) for a different case study. He computed PW and the SWVR from MAMS imagery simulated with June 1986 radiosonde data over Tennessee. Least squares analysis determined a slope of -35.13 and an intercept of -3.59 for the best fit line between PW and the natural logarithm of SWVR. For a ratio of 0.40, Jedlovec's (1990a) regression line returns a PW which is 2.75 mm larger than that using the line presented here in Fig. 4a. While this discrepancy is not insignificant, the agreement in slope of the lines indicates that PW gradients would not be dependent on the regression line used. The similarity of results between the 1986 study and the current one suggests that the PW versus SWVR relationship does not vary greatly over differing locations and atmospheric conditions. However, the relationship has yet to be evaluated in regions outside of the southeastern United States or during winter.

Results from additional simulations (discussed in Section 5) reveal that the SWVR regression line is weakly dependent on surface characteristics in the 25x25 pixel array. Each SWVR changes slightly when the average surface temperature or the value of constant emissivity is altered. For a given PW, the variance ratio regression (Fig. 4a) exhibits a slight bias towards larger ratios compared to the transmittance ratio regression (Fig. 4b). However, the transmittance ratio regression is not sensitive to surface characteristics and reflects only atmospheric conditions at one point in horizontal space. For this reason, the PW versus squared transmittance ratio relationship (Fig. 4b) was used for the 16 October 1990 case study. Thus, as

described in Section 2, SWVRs measured from actual imagery will serve as estimates of squared transmittance ratios. The above comparison convincingly verifies the near equality between the SWVR and the squared transmittance ratio.

Both regression relationships (Figs. 4a and 4b) were determined from soundings having PWs between 10 and 40 mm. Additional data points were needed to validate the extrapolation of the curves to drier and moister extremes. Modified soundings having PWs outside the 10-40 mm range were created by increasing or decreasing dewpoints in some of the original soundings. PW and the squared transmittance ratio were then recomputed for each new sounding. In Fig. 5, the additional data points (denoted by Xs) are combined with the 34 original points (the +s). The regression line from Fig. 4b is superimposed. Transmittance ratios for modified PWs as large as 70 mm appear to agree well with those of the regression line. However, at this moist end of the regression line, small changes in ratio translate into larger PW changes than at smaller PW values. Thus, even a small amount of scatter indicates significant retrieval errors. At the dry extremes, however, the original curve even less adequately represents the actual relationship between PW and the transmittance ratio.

The regression lines (Figs. 4a and 4b) intercept the abscissa (where  $PW = 0$ ) near a ratio of 0.80. This differs significantly from a ratio of 1.0 which would indicate no water vapor absorption in either split window channel under conditions of zero moisture, assuming no other absorbing constituents are present. The modified sounding points on Fig. 5 suggest still another ratio (0.68) when  $PW = 0$ . As the squared transmittance ratios approach 0.68, the  $11 \mu\text{m}$  channel transmittances approach

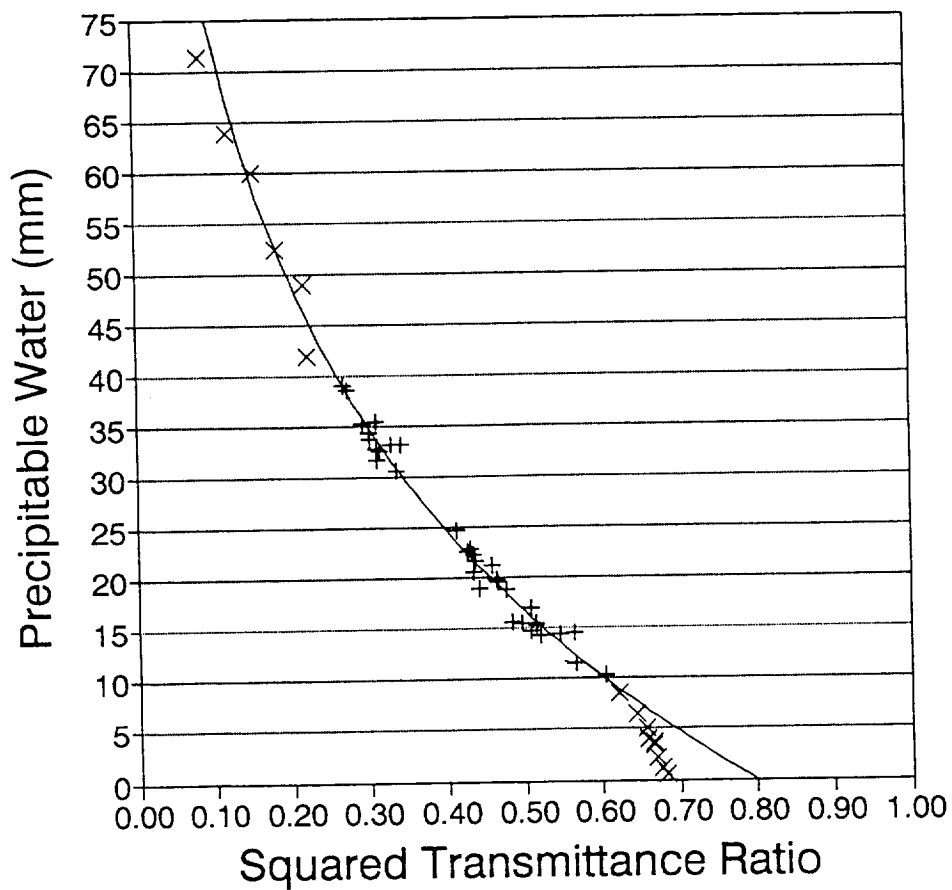


Figure 5. PW versus squared transmittance ratio for simulations using original radiosonde soundings (+) and modified versions of some soundings (X). The regression line from Fig. 4b is drawn through the data points.



0.98 (not shown). Thus, this channel becomes essentially a clear window. However, the 12  $\mu\text{m}$  channel transmittance decreases only to 0.81 because it is more sensitive to absorption by atmospheric constituents besides water vapor, including carbon dioxide and aerosols. Based on these findings, SWVRs greater than 0.60 should be related to PW using a different relationship. Jedlovec (1990a), who also observed an intercept near 0.68, used a linear fit for ratios greater than 0.58. In the current case study, however, no additional relationship for low moisture extremes is needed since PW less than 10 mm is not expected in the regions mapped by MAMS.

*b. Uncertainty in the regression relationship*

The scatter of points about the regression lines (Figs. 4a, 4b) indicates that a given ratio cannot be related to a unique value of PW, i.e., there is uncertainty. The reasons for this scatter must be understood to properly interpret gradients in derived PW imagery. Variations in the transmittance ratio at constant values of PW can be examined using soundings that were input to the simulations discussed above. Three soundings (points) used for this purpose are circled on Fig. 4b just below the PW value of 15 mm. From smallest to largest ratio, these points correspond to soundings from VPS at 1200 UTC 15 October, CKL at 0000 UTC 16 October, and CKL at 0000 UTC 17 October 1990 (station identifiers and locations were given in Fig. 3).

Table 4 lists the PWs and squared transmittance ratios for the three soundings. PWs related to each ratio on the regression line also are given. These values would result from an SWVR retrieval if the SWVR equalled the transmittance ratio. While

Table 4. Comparison of vertical moisture structure among soundings having similar amounts of total column precipitable water. Transmittances are for the total atmospheric column.

Station:	VPS	CKL	CKL
Time:	1200 UTC	0000 UTC	0000 UTC
Date:	15 Oct 1990	16 Oct 1990	17 Oct 1990
Radiosonde PW (mm)	14.67	14.50	14.59
Squared transmittance ratio	0.508	0.547	0.565
Regression line PW (mm)	16.14	13.53	12.33
Retrieval error (mm)	1.47	-0.97	-2.26
Surface dewpoint (K)	286.95	282.15	278.80
Surface-850 mb contribution to PW (%)	70.2	64.8	53.3
Level of weighting function peak (mb)	935	885	815
11 micrometer channel transmittance	0.841	0.933	0.922
12 micrometer channel transmittance	0.600	0.690	0.694

actual PW averages 14.59 mm at the three sites, retrievals would yield PWs ranging from 16.14 mm to 12.33 mm, based on SWVRs ranging from 0.508 to 0.565. The difference between retrieved PW and that calculated from radiosonde data is retrieval error. A positive error indicates an overestimate of the actual PW. The retrieval error at each of the three locations is seen graphically in Fig. 4b as the distance between the circled data point and the regression line at a constant ratio. The point with the smallest transmittance ratio is located below the regression line (positive retrieval error), while the other two points are above the line (negative retrieval errors).

The three soundings differ significantly in the lower troposphere. This is apparent in the surface dewpoints (Table 4), which are smallest where the ratio is greatest, and vice versa. There is a similar relationship between the transmittance ratio and the percentage contribution by the surface-850 mb layer to total column PW (Table 4). Clearly, the transmittance ratio responds to differences in vertical moisture structure even when PW remains constant. The ratio decreases as the concentration of moisture shifts towards progressively lower levels of the atmosphere. This is due to the differing sensitivity between the two split window channels to low level moisture. This problem suggests the need for an additional channel to provide measurements sensitive to higher-altitude moisture, to better describe vertical structure.

Profiles of split window channel transmittances (Figs. 6a,b,c) and normalized weighting functions (Figs. 6d,e,f) for the three soundings discussed above illustrate this sensitivity difference. Total atmospheric transmittances (through the entire column from the top of the atmosphere to the surface) are represented graphically by the 'x

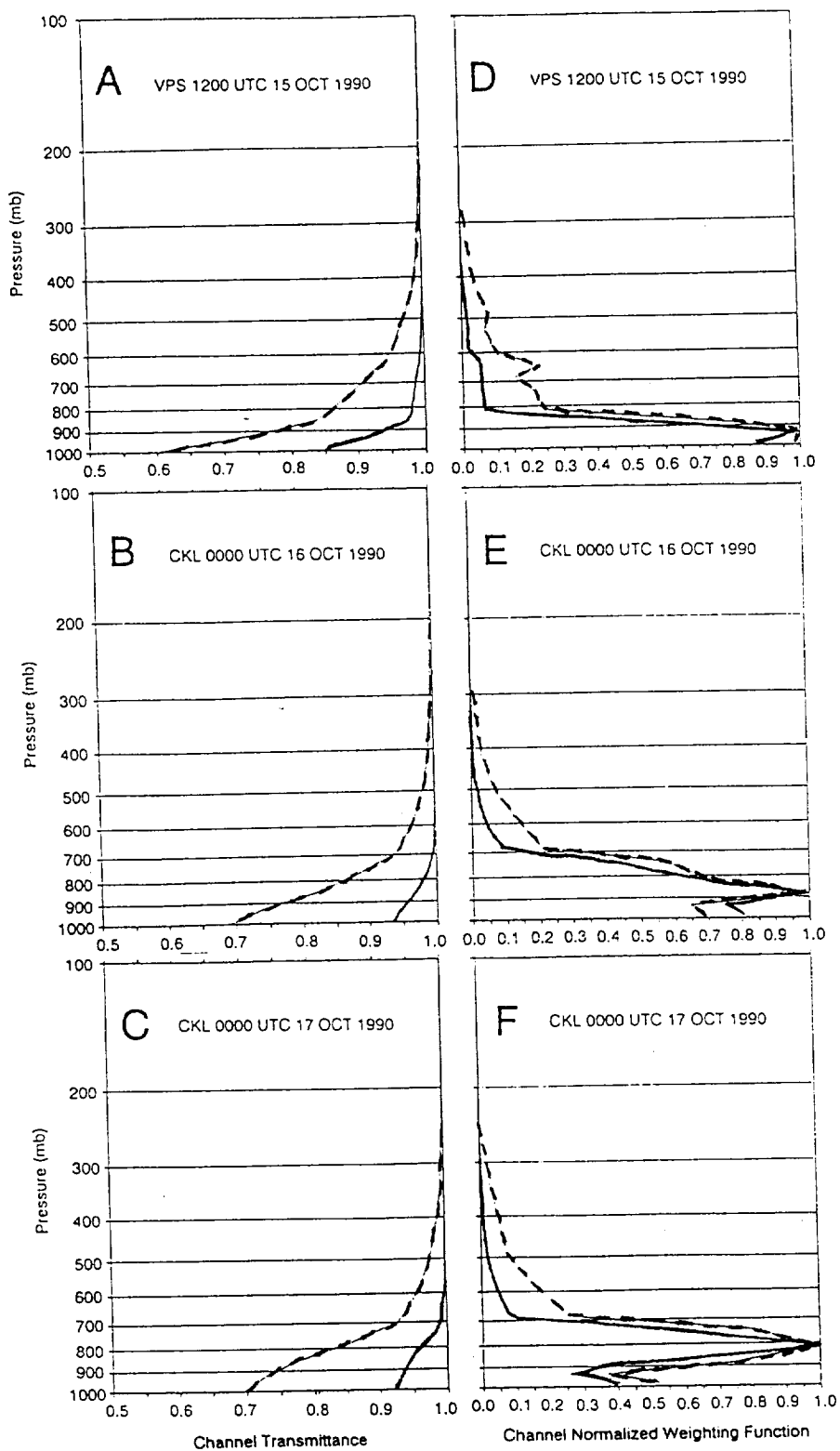


Figure 6. Profiles of split window channel transmittances (a-c) and normalized weighting functions (d-f) for the three soundings in Table 4 with similar amounts of PW. Solid lines are for the 11  $\mu\text{m}$  channel, and dashed for the 12  $\mu\text{m}$  channel.

intercepts' in Figs. 6a-c and are listed in Table 4. Results show that station VPS at 1200 UTC 15 October has the smallest transmittances in both channels (0.841 and 0.600 at 11 and 12  $\mu\text{m}$ , respectively). The 12  $\mu\text{m}$  channel value is particularly small and produces the smallest squared transmittance ratio (0.508). These smallest values occur at the sounding location with the greatest concentration of moisture near the surface (70.2% of PW is below 850 mb). Although transmittance ratios for the two soundings at station CKL increase (from 0.547 to 0.565) as the surface-to-850 mb contribution to PW decreases (from 64.8% to 53.3%), the total atmospheric transmittances in the 11  $\mu\text{m}$  channel (decreasing from 0.933 to 0.922) do not follow this trend (Table 4). This exemplifies how individual channel transmittances are not very descriptive of vertical moisture structure.

Total atmospheric transmittances at VPS (Table 4) are the smallest of the three sites despite the fact that channel transmittances down through levels between 800 mb and 900 mb are greatest (Fig. 6a-c). This occurs because VPS has the smallest percentage of moisture above 850 mb. The abrupt vertical change in transmittances corresponds to peaks in the weighting functions near 935 mb (Fig. 6d). This level is closer to the surface than in either CKL profile (Figs. 6e,f). Thus, both VPS profiles (Figs. 6a,d) respond to its greater concentration of water vapor near the surface.

Transmittance profiles for CKL (Figs. 6b,c) are similar, although values for the 16 October profile are slightly greater at middle and upper levels since moisture is concentrated closer to the surface. As a result, the weighting functions at CKL peak closer to the surface on 16 October than on 17 October (Figs. 6e,f). Overall, this

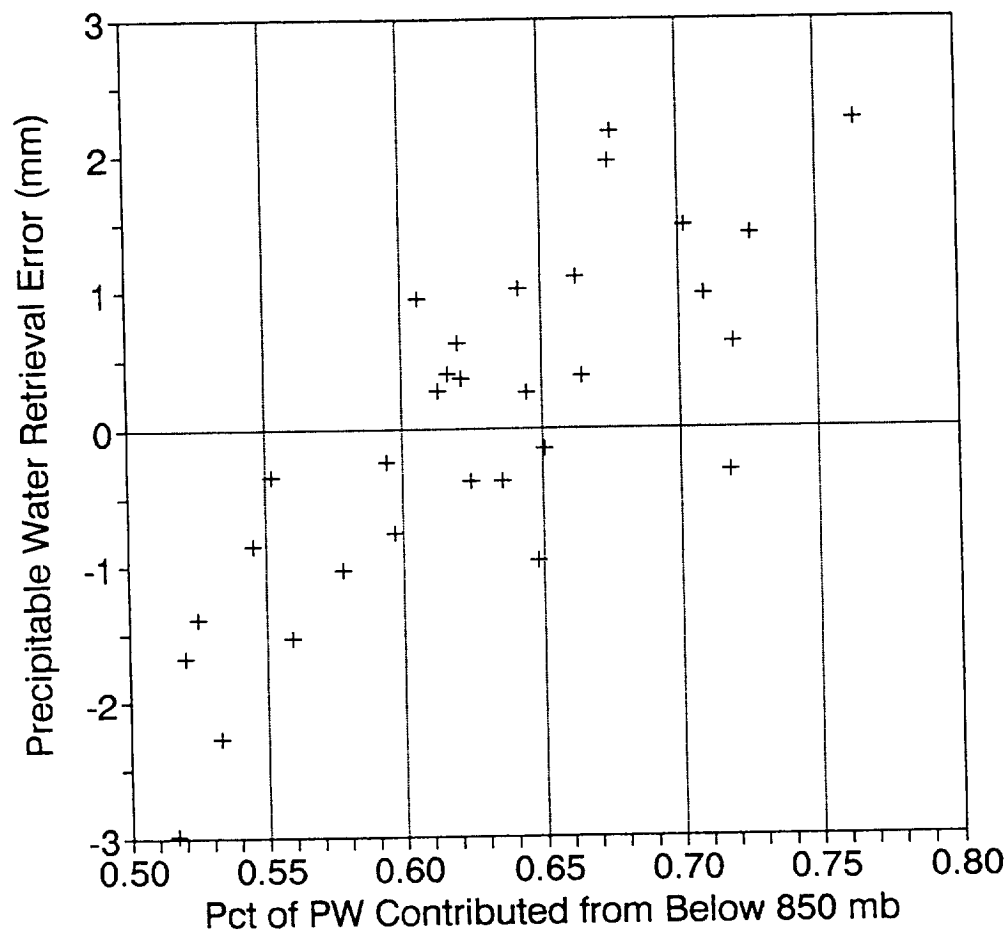


Figure 7. Error in PW retrieval versus percentage of PW contributed by the layer between the surface and 850 mb in the original soundings. Retrievals were calculated from the regression (Fig. 4b) relating PW to the squared transmittance ratio computed from the radiosonde soundings. Positive retrieval errors indicate overestimates of radiosonde values.

comparison indicates that a higher-altitude peak in the weighting function is correlated with a smaller concentration of moisture at lower levels, a greater transmittance ratio, and an increased likelihood that the SWVR retrieval will underestimate the actual PW.

Vertical variations in low level humidity also explain the scatter of the remaining data points about the regression line in Fig. 4b. This is shown in Fig. 7 by plotting retrieval error against the contribution that levels below 850 mb provide to the total column PW in the 34 soundings. The scatter diagram reveals that greater contributions by the surface-to-850 mb layer are associated with increasing overestimates of retrieved PW. In fact, with the exception of five data points, the 60% value separates overestimates from underestimates. Thus, the magnitude of this error depends on the extent to which the moisture profile at individual sounding sites deviates from the 'average' associated with the regression line. The standard errors of the regression lines (Figs. 4a and 4b) suggest that most of the PW discrepancies due to vertical moisture structure variations will normally be near 1.2 mm.

These results show that retrieved PW strongly depends on the integrated lower level moisture content. As the vapor becomes more concentrated near the surface, even in a column of constant PW, the retrieved amount increases. Thus, although retrievals may not always accurately represent the total column, they do describe the lower troposphere. This also was demonstrated by Jedlovec's (1990a) finding of a good agreement between areas of large retrieved PW and the later development of a cumulus cloud field. Thus, the SWVR technique is a useful tool for discriminating between regions which may support convection and those which may not.

## 5. Application of the technique to split window imagery

Most sources of error for the SWVR technique are not apparent by examining the regression relationships discussed in the previous section. Errors in the split window data and violation of technique assumptions were left out of the simulations used to develop the regression lines, but these are sources of error when retrievals are actually made. The effects of these errors cannot be measured directly from the imagery. Therefore, in an attempt to quantify the errors, additional simulations were performed. This section begins with a summary of results from these simulations. Next, meteorological conditions during the case study are presented. Finally, the methodology for implementing the technique concludes this section.

### *a. Split window data errors*

Errors in split window channel brightness temperatures due to truncation error (Table 2) and single sample noise (Table 3) for the 16 October 1990 MAMS data were introduced in Section 3. In the current experiment, the simulated 25x25 arrays of brightness temperature used to determine the SWVR regression line (Fig. 4a) were subjected to errors due to 8 and 10 bit digitization to analyze their effect on PW retrievals. Each of the 34 original soundings again was used separately as input to the simulations to provide an invariant atmosphere, and surface emissivity was again held



at 0.96. The methodology consisted of several steps. First, the appropriate value of single sample noise (Table 3) was randomly added to or subtracted from each of the 625 values of channel brightness temperature. Next, the temperatures were truncated to emulate 8 and 10 bit precision (in actuality, truncation is applied to raw counts and radiances; however, corresponding errors in scene temperatures can be inferred, as in Jedlovec *et al.* 1989). SWVRs then were computed from channel brightness temperature variances. Various magnitudes of variance in channel brightness temperatures (ranging from 0.5 to 25 K<sup>2</sup> and created by changing the variance in underlying skin temperature) were used to examine the effect of data errors under different surface conditions. Finally, the ratios were related to retrieved PW via the variance ratio regression line (Fig. 4a). The effect of data errors on the retrievals was then assessed by comparing the results to those from the original unaltered retrievals.

Results from this procedure, using the sounding from station CKL at 1200 UTC 16 October as an example, are shown in Fig. 8. Retrieved PW remains constant with changing variance when temperatures are not subjected to error and technique assumptions are met. Retrievals made under these conditions (from which SWVRs were used in developing the regression line in Fig. 4a) are shown graphically in Fig. 8 by the horizontal line with a PW of 15.5 mm. This value differs only slightly, due to vertical moisture structure variation, from the PW of 15.4 mm calculated from the radiosonde profile. Data errors cause deviations from the constant retrieved value. The simulated retrievals from 8 bit data fluctuate at small variances and have a 1 mm moist bias at large variances. The results using 10 bit data are less prone to

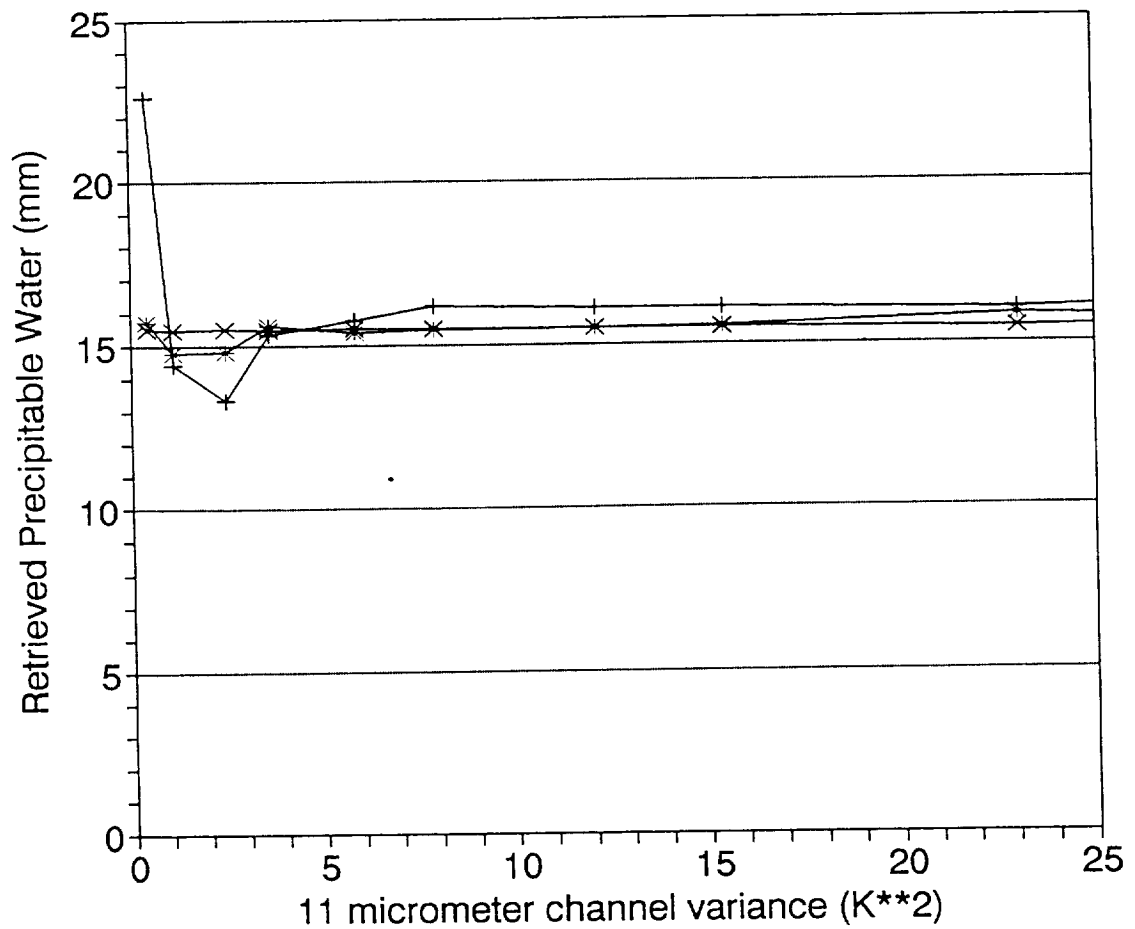


Figure 8. 11  $\mu\text{m}$  channel variance versus retrieved PW for simulations using the CKL sounding at 1200 UTC on 16 October 1990. Curves represent retrievals using input split window data with no errors (X), instrument noise with 8 bit digitization (+), and instrument noise with 10 bit digitization (\*).

fluctuations and at large variances differ little from the retrievals from unaltered data. Thus, 10 bit data provide smaller retrieval errors, particularly at small variances.

Retrieval errors for the CKL sounding just discussed are slightly less than those for most of the other 33 profiles. In Fig. 9, average absolute retrieval errors for all soundings, at both levels of data precision, are plotted against  $11 \mu\text{m}$  channel variance. The  $11 \mu\text{m}$  channel variance corresponding to each surface variance used in these simulations varies slightly from one sounding to the next due to the different amounts of moisture in each sounding. Thus, the plotted variances are averages among all the soundings. Retrievals from 10 bit data provide smaller retrieval error (nominally 0.5 mm) than those from 8 bit data, regardless of channel variance. The difference in error becomes more apparent as variances fall below  $2.5 \text{ K}^2$ . Thus, the upgrade to 10 bit data reduces the limitation of the SWVR technique at low scene variances and provides an overall improvement in retrieval accuracy. The importance of reducing retrieval error with 10 bit digitization is better assessed in conjunction with the impact of violating major assumptions of the technique. That issue is examined next.

*b. Violating the invariant emissivity assumption*

One of the basic assumptions of the SWVR technique is that emissivity remains constant. Surface emissivity was held constant at 0.96 in computing simulated SWVR values up to this point. In actual scenes, however, emissivity is likely to vary (spectrally and spatially) to an extent that depends on the types of surfaces encountered. Since emissivity cannot be measured directly, it is not possible to correct

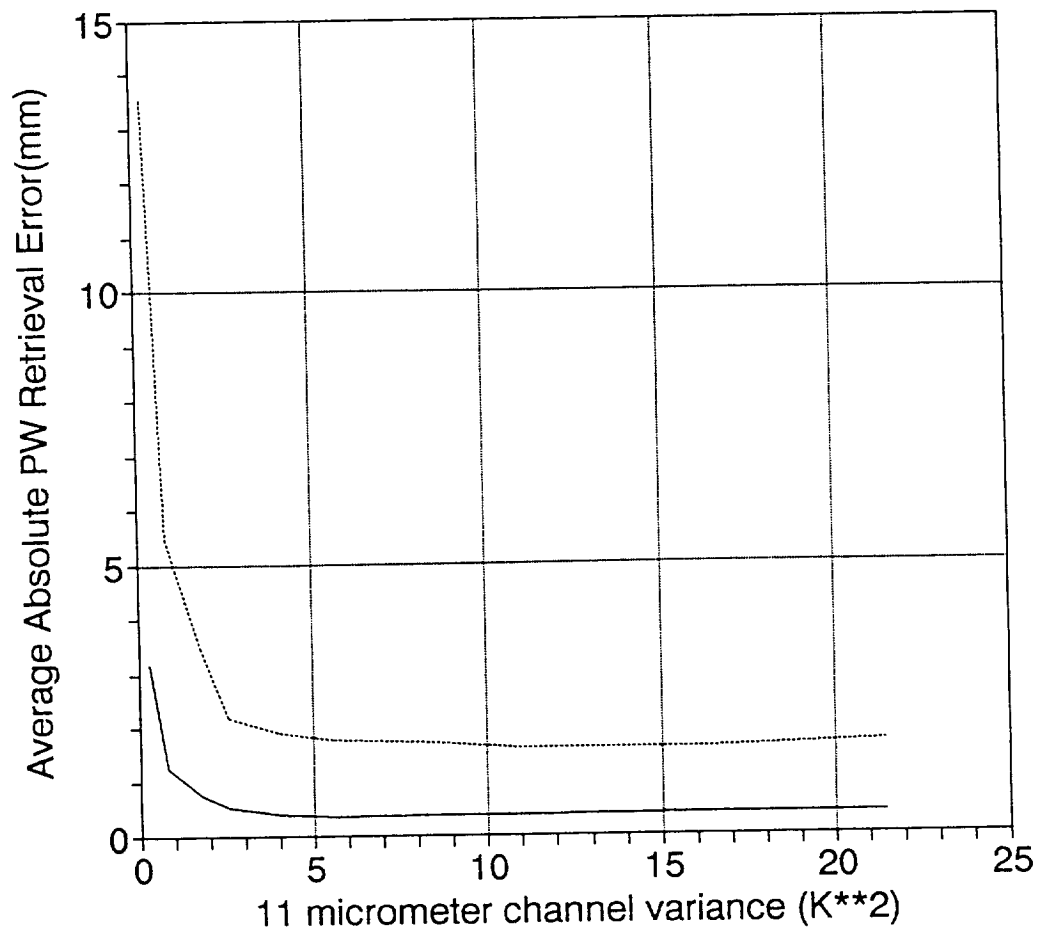


Figure 9. 11  $\mu\text{m}$  channel variance versus average absolute retrieval error from simulations using each of the 34 original radiosonde soundings. Curves represent retrievals using input split window data subjected to instrument noise as well as 8 bit (dotted) and 10 bit (solid) digitization.

for its variation, and effects on PW retrievals can only be estimated. To do so, the previously used simulated 25x25 skin temperature arrays were modified to have variations in emissivity. Three new types of simulations were performed to evaluate the effect of these variations on retrievals from templates with various magnitudes of channel variances. The first introduced spatial variation by applying emissivity values normally distributed about a mean of 0.96 to the temperatures in the array. The emissivities were applied randomly to all pixels to avoid a dependence on temperature. Three normal distributions, each having a different standard deviation (0.005, 0.01, or 0.02), were investigated. In a second simulation, emissivity was spatially invariant, but different values were used in each split window channel. Lastly, emissivity again was held constant with respect to channel and space, but the magnitude of this constant emissivity was varied. In each experiment, the atmospheric contribution to radiance was held constant by using only one sounding as input. Further, channel brightness temperatures were not subjected to the noise and truncation errors described earlier. Each resulting SWVR again was related to PW using the regression line in Fig. 4a.

The procedure imposing spatial emissivity variation was applied to the 34 soundings from sites in Fig. 3. Results for the CHS sounding at 1200 UTC 16 October are given as an example in Fig. 10. The straight line, with a PW value of 19.5 mm, again represents retrievals using error-free temperatures and a constant emissivity (0.96). Again, as described in Section 4, vertical moisture structure variations cause this value to deviate from the PW computed from the radiosonde profile (21.2 mm). The curved lines show that spatial emissivity variation causes PW

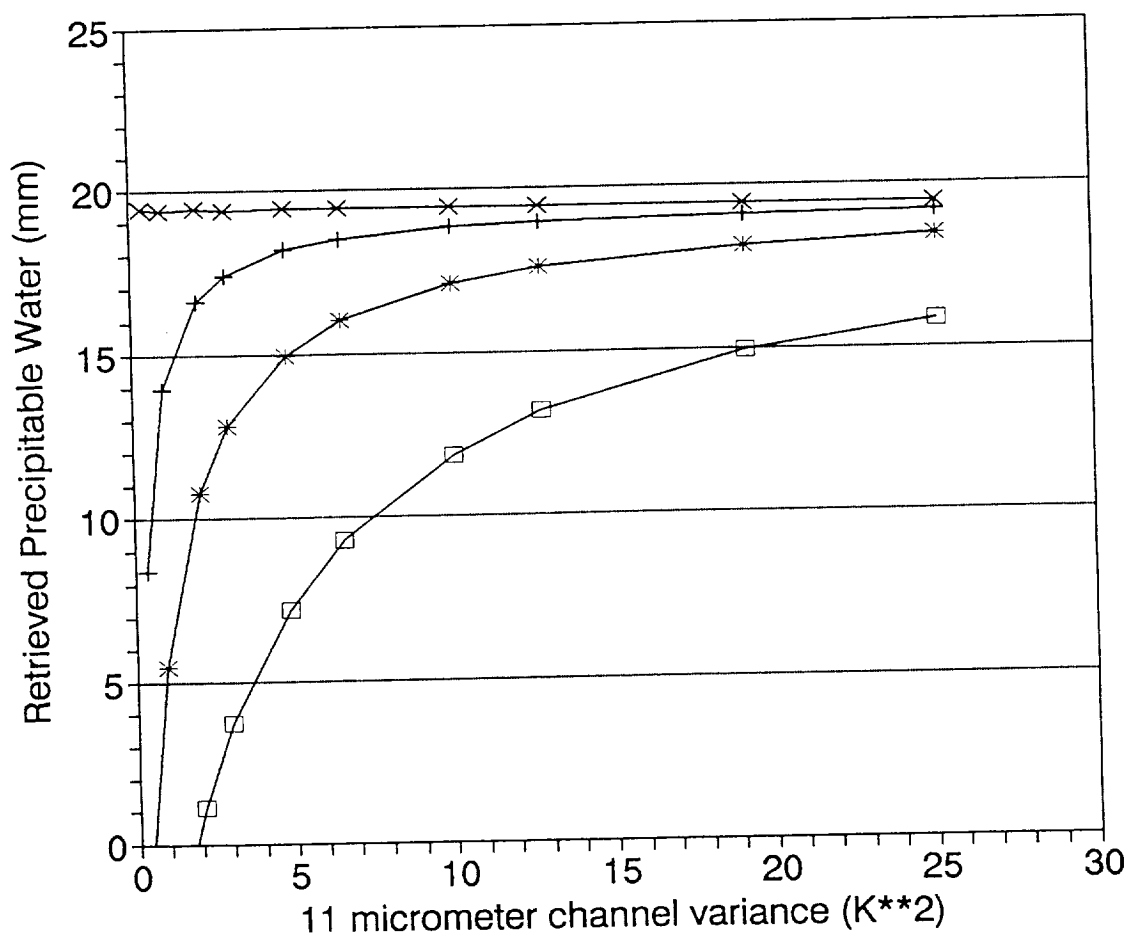


Figure 10. 11  $\mu\text{m}$  channel variance versus retrieved PW for simulations using the CHS sounding at 1200 UTC 16 October 1990. The various lines represent retrievals using a 25x25 template of channel brightness temperatures. The straight line with Xs indicates a template with an invariant surface emissivity of 0.96. The curved lines indicate templates where the emissivity is normally distributed about a mean of 0.96 with standard deviations of 0.005 (+), 0.01 (\*), and 0.02 ( $\square$ ).

retrievals to deviate from the straight line at 19.5 mm. It also causes the channel variances to increase slightly for a given value of PW (not shown). For ease of comparison, however, PWs from retrievals with emissivity variation are plotted against original 11  $\mu\text{m}$  channel variances with no emissivity variation. As the standard deviation of emissivity increases, retrieved PW decreases, with greatest errors again associated with the smallest thermal variances. This occurs because the emissivity variations increase thermal variances in both channels by similar amounts, thereby increasing the SWVR and decreasing the retrieved PW. As the variation in surface temperatures decreases, channel variances are dominated by the emissivity variations, even to the extreme that the SWVR nears unity and retrieved PW becomes negative.

The results of this simulation show that retrieval error is proportional to the amount of emissivity fluctuation within templates. Knowledge of actual spatial variations in emissivity is needed to accurately determine the magnitude of this source of error. Unfortunately, only a limited amount of research has been devoted to this topic. In a case study by Labed and Stoll (1991), average emissivity in the 8-14  $\mu\text{m}$  spectral region was estimated to be 0.959 for a flat, sparsely vegetated surface. The standard deviation of emissivity measurements spaced about 30 m apart within a 1  $\text{km}^2$  region was determined to be 0.0075, with a maximum spatial variability of 3%, or 0.029.

While the surfaces examined by Labed and Stoll (1991) may or may not be comparable to all of those mapped by MAMS in this study, their results do provide insight into the spatial variability of emissivity. Their standard deviation of 0.0075

was computed over a 1 km<sup>2</sup> region. Assuming this standard deviation to also be reasonable over the 2.5x2.5 km region used in the simulations for the current study, it corresponds to a curve in Fig. 10 which would fall in between those for values of 0.005 and 0.01 used for the simulations in this study. Based on that estimated curve and an 11  $\mu\text{m}$  channel variance of 2.7 K<sup>2</sup> (the average computed during this case study, as discussed later), a typical retrieval error due to emissivity variation would be about 4 mm. Of course, the error for a given retrieval depends on the magnitude of the 11  $\mu\text{m}$  channel thermal variance and on the actual variations in emissivity in the underlying surface. Also, in actual scenes emissivity may often be quite uniform within the template, except for isolated pixels due to small features such as roads or buildings which affect the retrieval in ways not investigated here.

Although not attempted in this study, a possible aid in estimating emissivity variation would be to calculate the variability in the Normalized Difference Vegetation Index (NDVI) within the retrieval template. The derivation of NDVI values from MAMS visible wavelength data is discussed in Jedlovec and Atkinson (1992). The NDVI could be useful because the amount of vegetative cover is often related to emissivity. Estimating emissivity variation with NDVI values would require collocated NDVIs and measured emissivities, or a detailed statistical analysis of the sensitivity of retrieved PW to NDVI, both of which are beyond the scope of the current study.

The second simulation of emissivity variation involved only differences between the split window channels. Labed and Stoll (1991) found that the effective emissivity in the 11  $\mu\text{m}$  channel of the AVHRR was 0.957, while in the 12  $\mu\text{m}$  channel it was



0.976. This difference was applied to the MAMS channels. Results (not shown) indicate that the retrieved PW differs little, on average by only 0.3 mm, from the value determined using the same emissivity in both channels. While the spectral difference in emissivity may in some cases be larger than that incorporated here, this appears to be a very minor source of error for the SWVR technique when applied over vegetated surfaces as seen in northern Florida. This error source would certainly be enhanced if the technique were applied over a surface such as bare soil or rock, where the emissivity difference between the channels would be larger.

Small retrieval errors also were found in the third simulation, in which the spatially and spectrally constant emissivity itself was changed. The emissivity was varied between 0.92 and 1.00, creating an effect similar to that caused by varying the average skin temperature. The resulting PW retrievals differed by no more than 0.2 mm for a given input sounding. These small fluctuations in retrieved PW occur because of small SWVR changes which cause slight shifts in the SWVR regression line (Fig. 4a) as discussed in Section 4. Clearly, variations in emissivity are a much greater source of error when they occur spatially.

*c. Violating the invariant atmosphere assumption*

The effect of moisture variability within templates also was examined. Emissivity was reset to the constant value of 0.96, and no errors were applied to the channel brightness temperatures. One-dimensional horizontal PW gradients of varying magnitudes were placed within the 25x25 pixel templates. This was done by replacing

original brightness temperatures with new values resulting from the same underlying surface temperature, but with PWs slightly smaller or greater than the input sounding. PW gradients of 1, 2, and 3 mm were considered in templates for the 34 soundings. The gradients were applied such that the average PW in the template was equal to the original invariant value. Again, retrievals were simulated from templates having various magnitudes of channel variances.

Results of this procedure for the AYS sounding at 1200 UTC 16 October are given in Fig. 11. Retrieved PWs from templates with moisture variability are plotted against the original 11  $\mu\text{m}$  channel variance from templates without moisture variation. As observed with emissivity variations (Fig. 10), increasing moisture variation causes PW retrievals to err towards drier values (Fig. 11) and causes channel variances to increase slightly (not shown). Retrieved PW decreases in these simulations because moisture variation induces increased brightness temperature variances in both channels. Since this effect is enhanced in the more sensitive 12  $\mu\text{m}$  channel, the SWVR increases and retrieved PW decreases. Scenes with small thermal variance again experience the greatest PW errors.

As stated earlier, with MAMS having a pixel resolution of 100 m, the 25x25 template represents a 2.5x2.5 km region. In order to identify a typical magnitude for the error produced by sub-template moisture variation, an estimate of a reasonable PW gradient over a region of this size is needed. Observational data on moisture variability at such small spatial scales, especially for specific locations, is rather limited. Thus, PW results from this study (presented in the next section) are useful

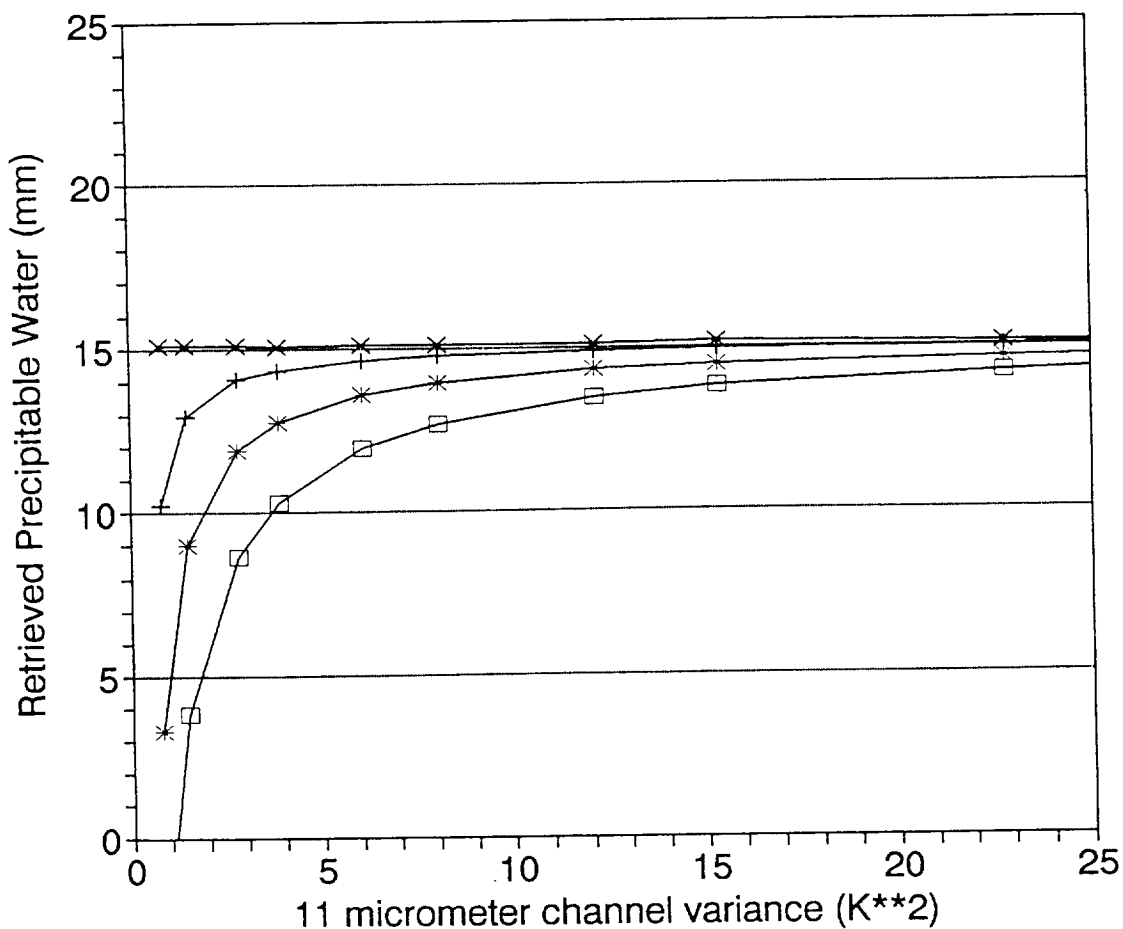


Figure 11. 11  $\mu\text{m}$  channel variance versus retrieved PW for simulations using the AYS sounding at 1200 UTC 16 October 1990. The various lines represent retrievals using a 25x25 template of channel brightness temperatures. Surface emissivity was constant at 0.96. The straight line with Xs indicates a template with invariant PW. Curved lines indicate retrievals from templates with one-dimensional horizontal PW gradients of 1 mm (+), 2 mm (\*), and 3 mm ( $\square$ ). Gradients were applied such that the average PW in the template was equal to the original value from the sounding.

for estimating sub-template moisture variation. A PW gradient of 8 mm was found over a distance of 30 km. By extrapolation, this corresponds to a gradient of 0.7 mm per 2.5 km. The retrieval errors due to a sub-template gradient of this magnitude would be similar to those indicated in Fig. 11 by the curve corresponding to a PW gradient of 1 mm. Assuming an 11  $\mu\text{m}$  channel variance of 2.7  $\text{K}^2$  (the average determined in this case study, as assumed for the emissivity variation simulations), a typical retrieval error due to sub-template moisture variation would be about 1 mm. As presented earlier, for the same 11  $\mu\text{m}$  channel variance, a typical amount of emissivity variation produces a 4 mm retrieval error. Thus, emissivity variation is likely a more significant source of error for the SWVR technique than moisture variation.

As with emissivity variations, the amount of moisture variability within the template is itself quite variable, making this source of error difficult to assess for each retrieval. One would suspect that the likelihood of a strong PW gradient within the template decreases as the size of the template decreases. Emissivity variations, however, likely do not depend as strongly on template size and could be large even in a small template. Of course, channel variances also typically decrease as the template becomes smaller, thereby enhancing retrieval errors produced by whatever moisture or emissivity variability is present (Figs. 10, 11). Since significant emissivity variability can more readily occur regardless of the template size, it is in general more likely to be a greater source of error than moisture variability.

Table 5 summarizes the estimated typical magnitudes of retrieval error due to the

Table 5. Typical PW retrieval errors (mm) due to major sources of error for the application of the SWVR technique on 16 October 1990.

---

---

Error Source	Avg PW Error (mm)
Vertical moisture distribution	1.25
Data errors (10 bit)	0.5
Sub-template emissivity variation	4.0
Sub-template moisture variation	1.0

---

major sources discussed to this point. Emissivity variation has been determined to be the most influential error source (typical error of 4 mm). Vertical moisture distribution, related to scatter about the regression lines as discussed in Section 4, causes errors comparable to those caused by sub-template moisture variation. Since all of these errors are generally larger than those due to the 10 bit digitization of the input data (nominal error of 0.5 mm), improvements in instrumentation do not seem to have the potential for optimizing the SWVR technique. Violating major assumptions in the theoretical development are the more significant sources of error for applying the technique to the case study presented below.

*d. Case study overview*

The MAMS mapped a large portion of the Florida peninsula containing significant contrasts in moisture and cloud cover during the period from 1330 to 1830 UTC on 16 October 1990 (Fig. 2). Surface synoptic conditions over the eastern United States at 1200 UTC 16 October (Fig. 12) indicate that Florida was in a transition zone between different air masses. A region of high pressure was centered over the border between Virginia and West Virginia. While the weather in northern Florida was influenced by this cool, dry air mass, the southern portion of the state remained warm and moist. The analysis of PW at 1200 UTC 16 October (Fig. 13) computed from radiosonde soundings (Fig. 3) reveals a strong north-to-south horizontal moisture gradient spanning northern Florida. The contours in this analysis reflect only a strict linear interpolation between values at the radiosonde sites and do not account for the

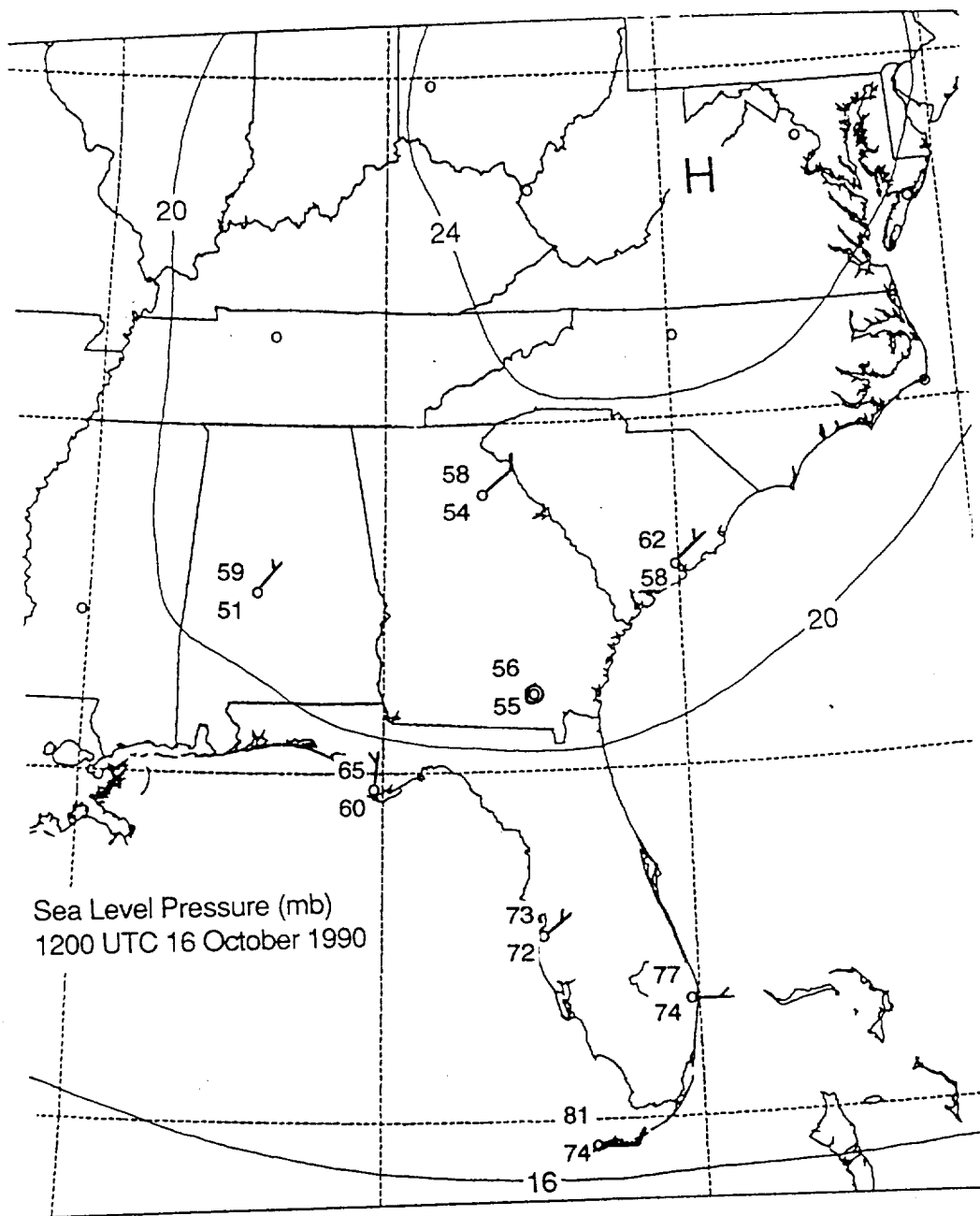


Figure 12. Synoptic conditions for the surface at 1200 UTC 16 October 1990. Solid contours indicate sea level pressure. Note the center of high pressure over the border between Virginia and West Virginia. Station model plots at radiosonde sites provide surface temperature (F), dewpoint (F) and wind speed (kts).

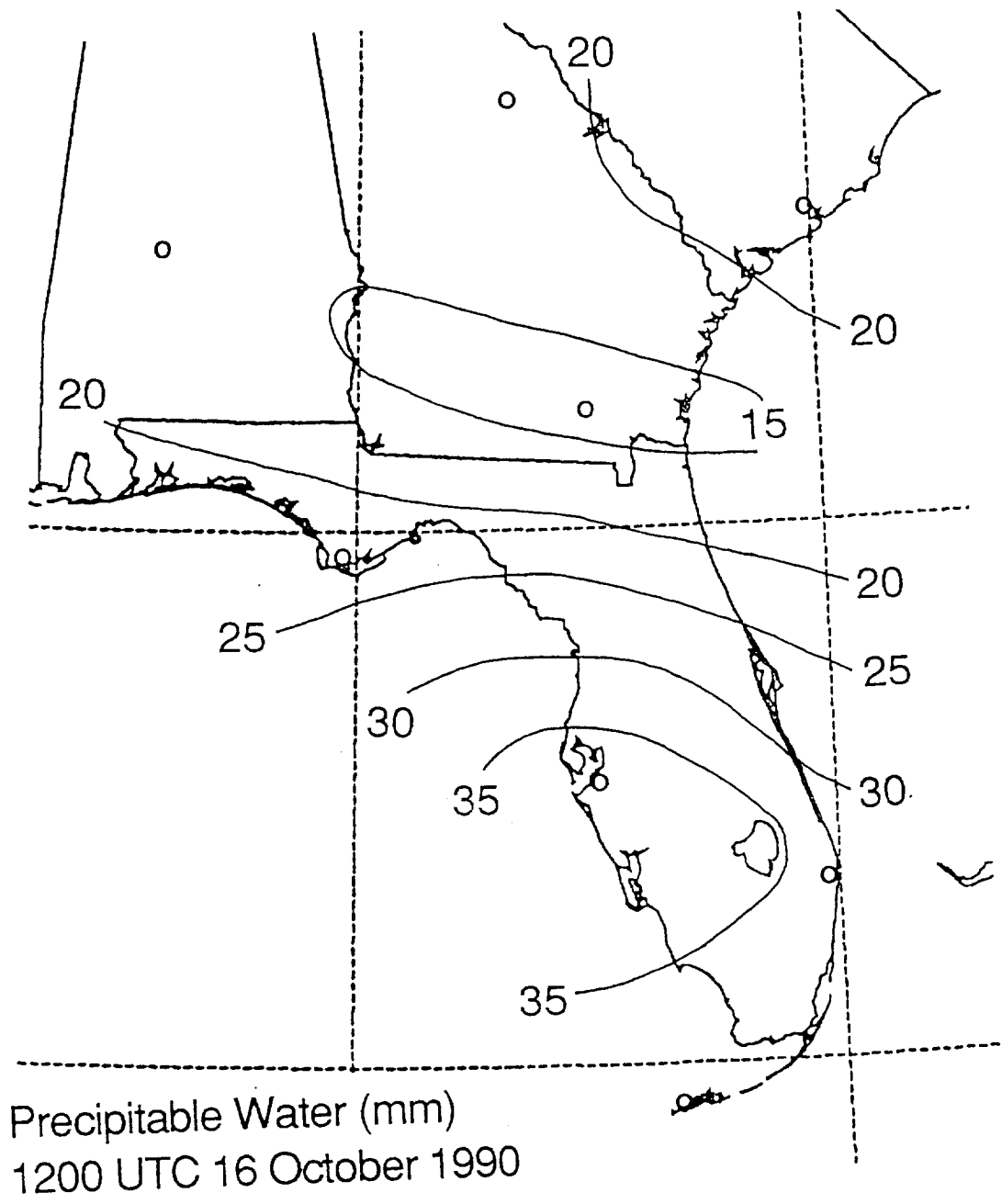


Figure 13. Analysis of total column PW (mm) computed from radiosonde sites (indicated by the circles and identified in Fig. 3) at 1200 UTC 16 October 1990.



effects of the onshore easterly flow. The strong gradient was located near the remnants of a frontal boundary along the southern edge of the high pressure. This front was not analyzed by the National Weather Service at this time (Fig. 12), although they had indicated the front further north in analyses 12 hours earlier (not shown). The several flight tracks through this region (Fig. 2) placed the MAMS in an optimum position for describing in more detail the horizontal structure of the moisture gradient.

Throughout the day on 16 October, a large cloud mass covered much of central Florida, corresponding to the zone of moisture transition. Significant rainfall totals were reported in the vicinity of Cape Canaveral. Skies remained clear in the northern part of the state, while a dense cumulus cloud field developed during the morning and persisted in regions south of the precipitation area. An early afternoon GOES visible image from 1630 UTC 16 October (Fig. 14) shows the distinct boundary between clear skies over north Florida and southern Georgia and the variable cloudiness to the south. Due to the cloud cover, SWVR retrievals could not be made from MAMS data collected over southern half of the state, i.e., prior to 1615 UTC (Fig. 2).

By 1620 UTC, the aircraft had passed northward over the cloud boundary and was well into the clear skies over the St. John's River (Fig. 14). Unfortunately, this body of water was large enough to produce numerous templates containing small thermal variances. The small variances produced unreliable SWVRs over most of the flight segment from 1615 to 1630 UTC. The southbound leg from 1635 to 1650 UTC tracked over cloud-free land surfaces (Fig. 14) which yielded larger variances.

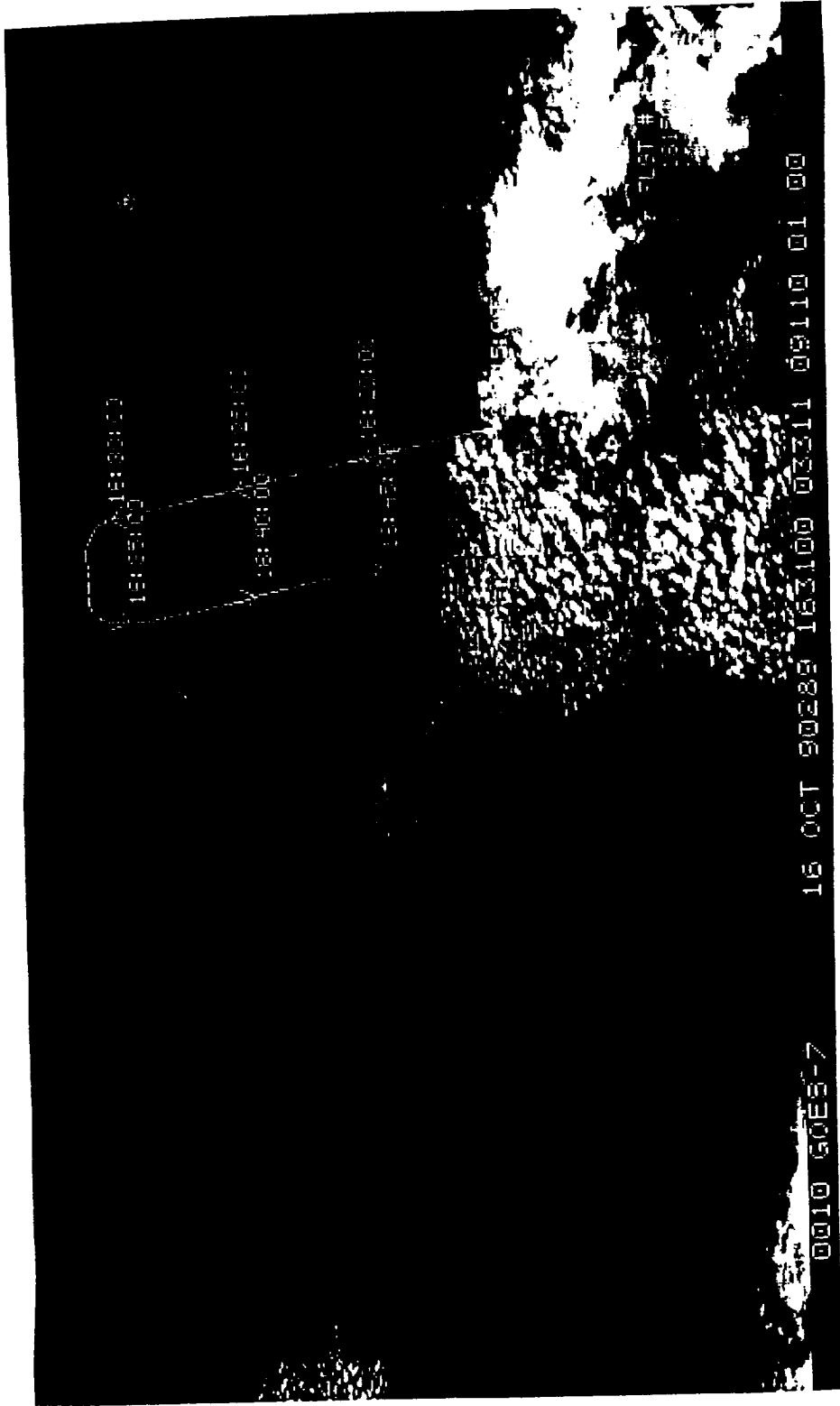
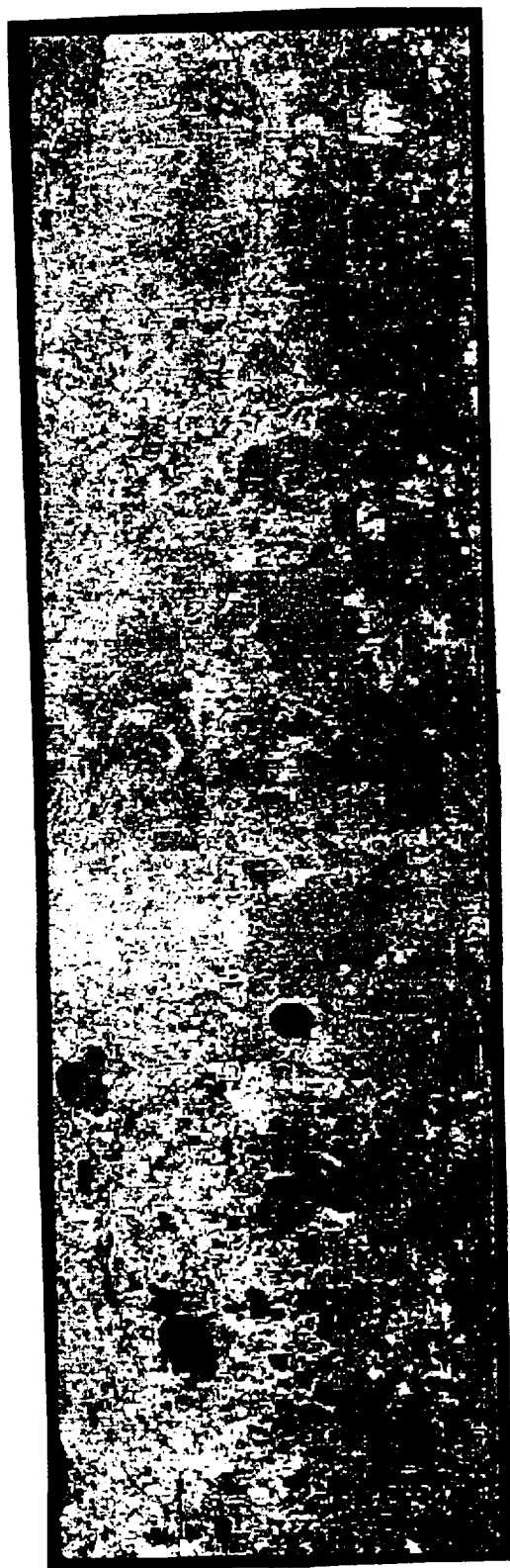


Figure 14. GOES visible image at 1630 UTC on 16 October 1990 over northern Florida. The MAMS flight track is superimposed with times in UTC next to arrows indicating the position and direction of flight.

Although flight segments from 1700 to 1830 UTC also provided data suitable for PW retrievals, the 1635-1650 UTC period yielded the best depiction of the moisture gradient in the region. The 37x120 km region mapped during this flight leg, indicated by the dashed rectangular region in Fig. 2, is therefore the focus of the case study. The specific methods by which PW retrievals were made are described next.

*e. Application to MAMS data on 16 October 1990*

PW images were constructed from the MAMS split window imagery collected between 1635-1650 UTC 16 October. The MAMS visible image from this flight leg (Fig. 15) shows a complete absence of clouds. This is advantageous for assessing the behavior of the technique apart from the undesirable influences that clouds can have on the results. The first step in applying the technique was to compute channel variances within templates throughout the area. To reduce the amount of computer time needed for these calculations, templates were centered at every other MAMS pixel (in terms of both lines and elements) instead of at each pixel. Such closely-spaced templates contain a large percentage of common pixels and do not represent unique atmospheric columns. This overlapping provides PW retrievals spaced at scales smaller than the size of the templates. This allows for estimating sub-template moisture variation and for determining the sensitivity of retrievals to small changes in central location. However, since PW variations at scales below template size indicate a violation of the invariant atmosphere assumption for retrievals, the gradients in the PW image can only be inferred at the horizontal scale of the template size or larger.



NORTH -->

Figure 15. MAMS visible image for 1635-1650 UTC flight leg on 16 October 1990, corresponding to the dashed region in Fig. 2.

Five template sizes were investigated, i.e., square templates which were 9, 17, 25, 33, and 41 MAMS image pixels across. Since the imagery has a resolution of 100 m at nadir, the width of the templates varied from approximately 0.9 to 4.1 km. The smaller templates provide very high resolution retrievals and require little computer time, but channel variances often are small, resulting in unreliable retrievals. Conversely, larger templates provide greater variances and a smoother PW field. However, the assumptions of an invariant atmosphere and a constant surface emissivity become increasingly invalid as template size increases. The analysis of PW retrievals from the five template sizes, presented in the next section, investigates which size provides the best compromise between these considerations. Each template size was applied to both the 8 and 10 bit versions of MAMS data to determine if 10 bit data provide more reliable retrievals, especially under conditions of small scene variance.

The simulations presented earlier showed that data errors and variations of moisture and emissivity within the templates (Figs. 9, 10, 11) have a stronger effect on retrieved PW as channel variances decrease. Retrieval errors were most significant when the 11  $\mu\text{m}$  channel variance was less than unity. Therefore, only retrievals from templates with an 11  $\mu\text{m}$  channel variance of at least 1.0  $\text{K}^2$  were considered valid in the case study. Retrieval locations failing the threshold test later were assigned a PW by interpolating between valid nearby values. While this subjectively chosen threshold does not eliminate all influences of error, their effects are greatly reduced. A larger threshold would produce unacceptably large gaps in the PW image.

After applying the threshold test, the ratio of channel variances in each template

was formed to yield the SWVR. Each SWVR was related to PW using the regression line between PW and the squared transmittance ratio (Fig. 4b). Each PW then was modified to account for the varying lateral scan angle ( $\Theta$ ) between the MAMS and the surface. As the MAMS scans away from nadir towards both edges of the swath width, the depth of the observed atmospheric column becomes larger. Jedlovec (1990a) showed that reducing the retrieved PW by the factor  $\sec(\Theta)$  removes this effect. This reduction was applied to all retrievals in this case study. The scan angle corrected PW values were transformed into an image format. Images resulting from various combinations of template size, digitization, and filtering are discussed next.

## 6. Analysis of precipitable water imagery

The SWVR technique was applied to the 1635-1650 UTC MAMS flight leg of 16 October 1990 which mapped a 37x120 km region in northeast Florida (dashed rectangle in Fig. 2). The first part of this section investigates the effects of the choice of template size on retrieved PW. Next, results obtained with data having 8 and 10 bit precision are compared. Finally, PW gradients along the entire 1635-1650 UTC flight leg are evaluated, focusing on the meteorological knowledge gained.

### *a. Comparison of results using different template sizes*

The determination of the most appropriate template size for SWVR retrievals is a subjective determination. The intent of this discussion is not to quantitatively determine the template size which produces the most accurate retrievals. However, the results from different template sizes are compared to identify the advantages and disadvantages of using each size. To investigate the implications of template size, results from the northern half of the flight leg are examined in detail. PW images covering a 37x50 km area (hatched in Fig. 2) appear in panel 'a' of Figs. 16-20. These five images were created from 10 bit input data and represent the five template sizes listed earlier. As described in the previous section, the variance threshold test (the 11  $\mu\text{m}$  channel variance must exceed 1  $\text{K}^2$ ) was applied during the calculations.

Panel 'b' in Figs. 16-20 represents the identical region shown in panel 'a', indicating in black the areas which failed the variance threshold test for the given template size.

These images (Figs. 16-20) show that increasing the template size causes distinguishable differences in results. Pixel-to-pixel variability in the PW images (panel 'a') decreases substantially, and the number of pixels failing the variance threshold test (panel 'b') also decreases. On a larger scale, each PW image depicts a north-to-south moisture gradient with greatest PW (the lightest shades) to the southeast. Clearly, the spatial scales at which PW gradients can be accurately interpreted varies with the template size used. Results for individual template sizes are examined below. Retrieval statistics were computed over the 37x50 km region (Table 6) to quantify the image differences. PW statistics in the table refer only to retrievals passing the threshold test.

The PW image created with 9x9 templates (Fig. 16a) exhibits strong variability between pixels in many areas. Most regions with little variability are locations where retrievals failed the variance threshold test (black areas in Fig. 16b). PW pixels in these areas are averages from surrounding retrievals which passed the test (white areas in Fig. 16b). These interpolated PWs change more gradually in the horizontal than values for valid retrievals. As a result, the image exhibits regions of high variability superimposed upon a larger-scale, smooth PW gradient arising from the interpolation process. Compared to larger template sizes (Table 6), the 9x9 template yields the most failures of the variance threshold test (only a 62% pass rate). Although many retrievals are considered invalid, PW gradients on a large scale (much greater than



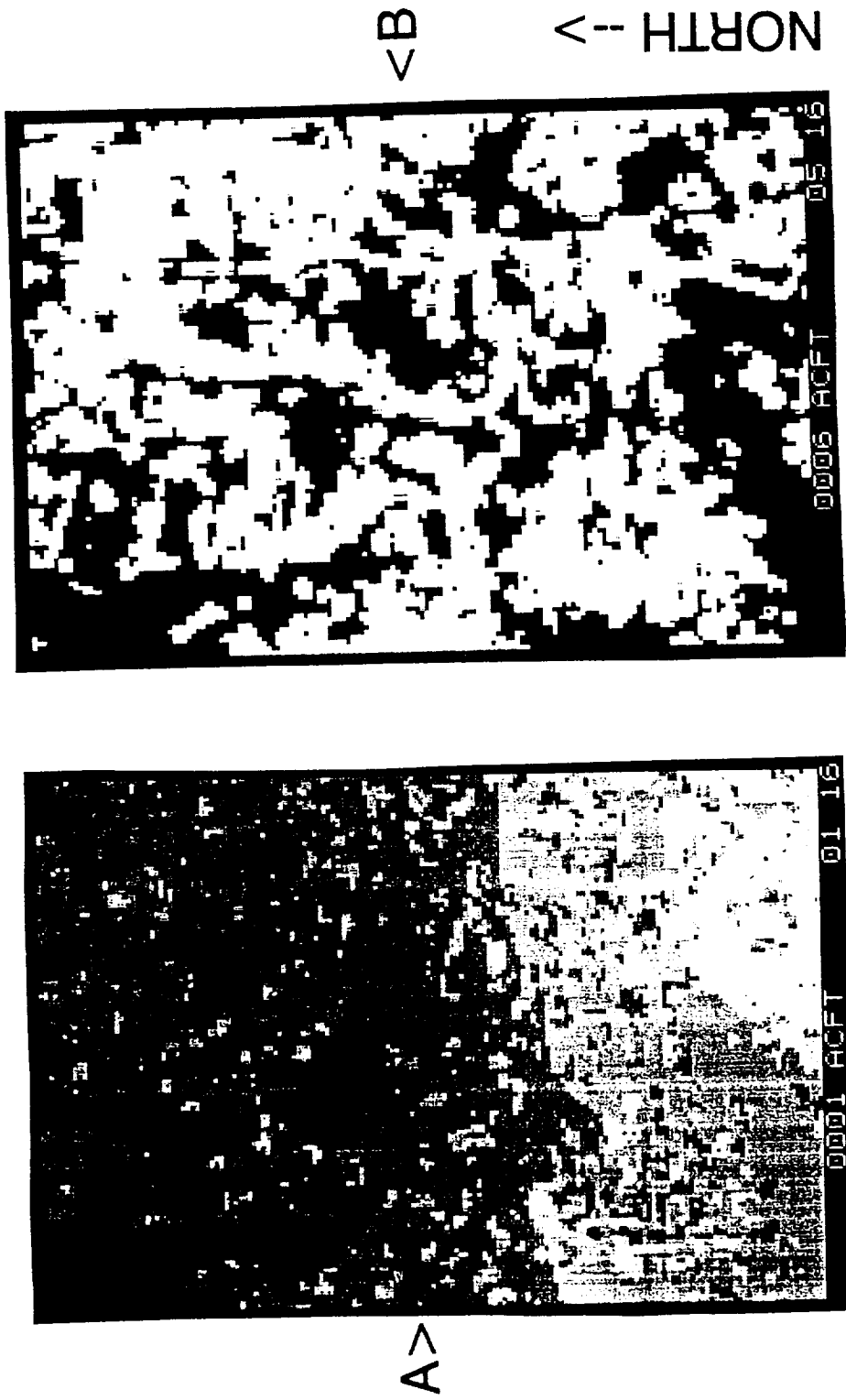


Figure 16. Images of retrieved PW (A) and 11  $\mu$ m channel variance (B) for retrievals made with a 9x9 template over the 37x50 km region hatched in Fig. 2. In (A), lighter regions indicate greater PW. Darkest regions indicate PW below 12 mm. Each shade represents a range of about 3 mm. In (B), black regions denote variances below 1  $K^2$ , while white regions denote variances above 1  $K^2$ .

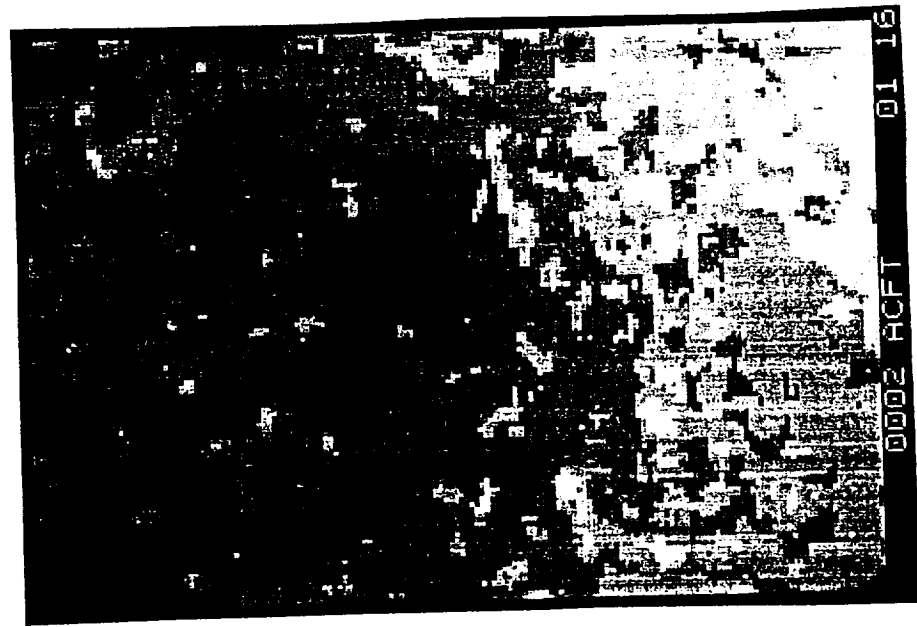
Table 6. Comparison of statistics from all retrievals made with five different template sizes, from 10 bit input data, within the 37x50 km region represented in Figs. 16-20. The PW statistics represent only those retrievals with 11  $\mu\text{m}$  channel variance above 1.0  $\text{K}^2$ . Statistics for 11  $\mu\text{m}$  channel variance include all values above and below 1.0  $\text{K}^2$ .

Template Width (pixels)	Retrieved Precipitable Water (mm)				11 micrometer channel variance ( $\text{K}^2$ )				
	Std				Std				
	Avg	Dev	Min	Max	Avg	Dev	Min	Max	Pct > 1.0
9	22.80	3.19	9.42	40.61	2.12	2.57	0.03	34.96	62.2
17	21.99	2.64	11.90	35.11	2.54	2.34	0.09	33.43	76.1
25	21.48	2.30	11.08	31.51	2.72	1.94	0.20	25.09	84.3
33	21.15	2.11	9.42	28.17	2.88	1.87	0.24	21.24	90.9
41	20.84	2.05	10.13	26.81	2.98	1.22	0.46	21.08	94.1

retrieval spacing) can still be detected by interpolating between valid retrievals.

Increasing the template size generally yields larger variances, and thus a larger percentage of retrievals that pass the threshold test (Table 6). Also, the range and standard deviation of those PWs becomes smaller with increasing template size (Table 6). These differences are visible when comparing the PW images from the 9x9 (Fig. 16a) and 17x17 (Fig. 17a) templates. The PW image from the larger template exhibits slightly less variability from pixel to pixel, reflecting the smaller standard deviation of PWs from valid retrievals (Table 6). The averaging across failed retrievals (black areas in Fig. 17b) again contributes to a smooth background PW gradient; however, it is less evident than before because 76% of the retrievals now have an 11  $\mu\text{m}$  channel variance greater than 1.0  $\text{K}^2$  (Table 6).

Moist and dry regions are better described as the template size is increased to 25x25 (Fig. 18a), 33x33 (Fig. 19a), and 41x41 (Fig. 20a). This occurs for two main reasons. First, the number of retrievals passing the threshold test continues to rise with increasing template size (Table 6). This is seen visually in panel 'b' of Figs. 18-20 by the greater coverage of white regions. Therefore, less and less interpolation across regions of failed retrievals was required. Second, the valid PW retrievals from the larger templates have less pixel to pixel variation than those from smaller templates. This is reflected by the smaller PW standard deviations for the three largest template sizes (Table 6). The overall result is that the detailed structure of the gradual north-to-south PW gradient from the small templates (Figs. 17a and 18a) is described by valid retrievals which are as not disrupted by strong pixel-to-pixel variability.



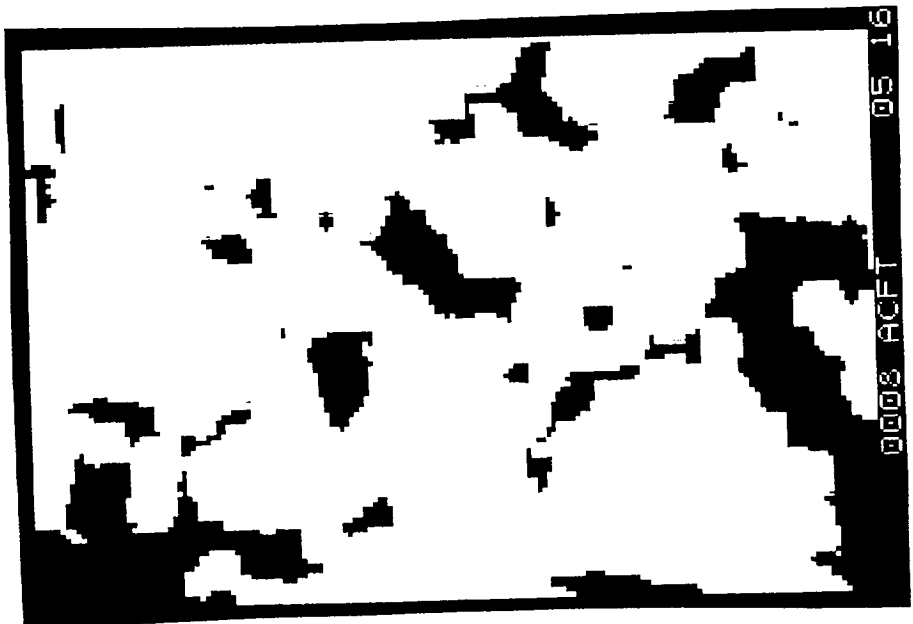
A>



<B

NORTH -->

Figure 17. As in Fig. 16 but for retrievals made with a 17x17 template.



<B

<-- NORTH -->

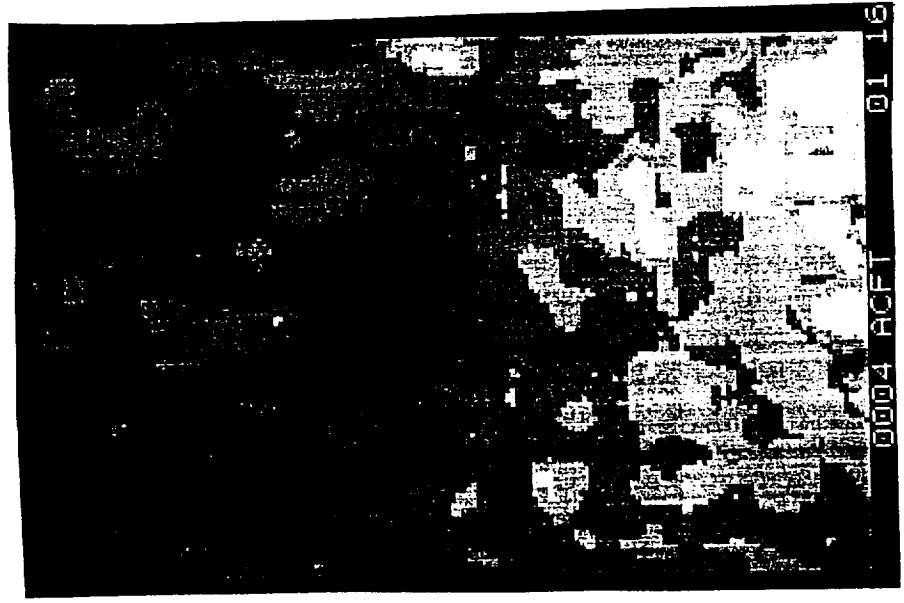


A>

Figure 18. As in Fig. 16 but for retrievals made with a 25x25 template.



<B  
<-- NORTH -->



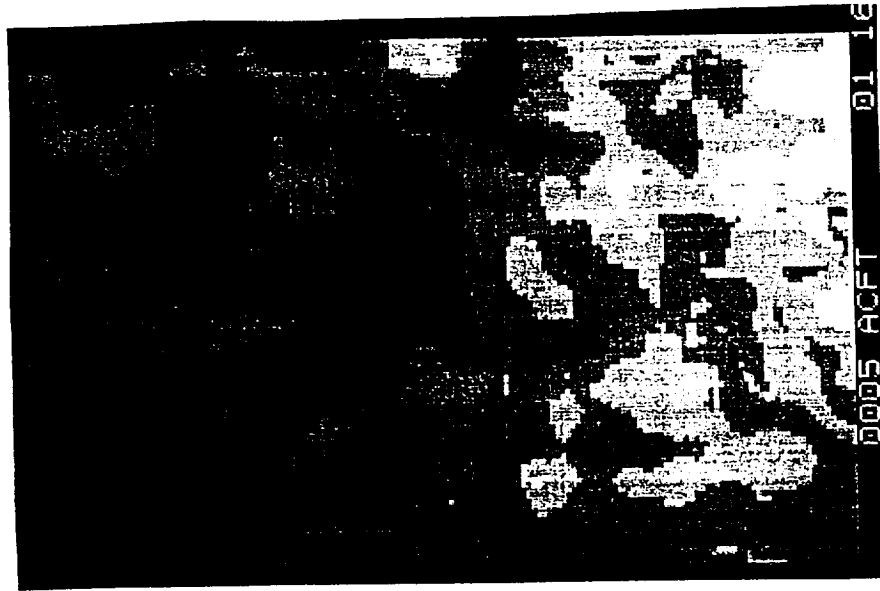
A>

Figure 19. As in Fig. 16 but for retrievals made with a 33x33 template.



<B

<-- NORTH



A>

Figure 20. As in Fig. 16 but for retrievals made with a 41x41 template.

The above comparisons clearly show that template size greatly influences the appearance of the resulting PW imagery. Correspondingly, the amount of reliable moisture gradient information also depends on template size. The PW gradients determined with a small template (9x9 and 17x17) are unreliable because they are adversely affected by the channel variances in two ways. First, variances often become quite small, thereby amplifying the effects of several error sources discussed earlier (Figs. 8-11). A large percentage of retrievals must then be omitted (using the threshold test) from the PW image, requiring a significant amount of interpolation. Second, even when variances are above  $1.0 K^2$ , they are highly variable and cause the strong horizontal variability in PWs seen in Figs. 17a and 18a. The abrupt variance fluctuations occur because small numbers of pixels in templates cause individual pixels to have a greater influence. The PW field is correspondingly affected because unreliable SWVRs are formed from the variances. The unrealistically large PWs (Table 6) retrieved with smaller templates (maximum PW of 40.6 mm for the 9x9 template) are attributable to this problem as well. Since the variances fluctuate mostly in response to surface characteristics, the problem in forming the SWVRs is most likely related to emissivity variation.

The use of larger templates (25x25, 33x33, 41x41) overcomes many problems encountered with smaller templates. The strong pixel-to-pixel variability in the PW images is greatly decreased, and fewer retrievals are omitted by the variance threshold test. Variances usually increase with template size simply because the larger number of temperatures usually contain a wider variety of values. The PW images created



with the larger templates (Figs. 18a, 19a, 20a) thus describe moisture variability more accurately. However, as template size becomes very large, detail is sacrificed somewhat. Use of the 41x41 template produces a PW image (Fig. 20a) with little variability at the scale of a few pixels. While this can be viewed as eliminating undesired abrupt fluctuations, a point is reached when large templates cause poor resolution of moisture features. Further, because real moisture features at the pixel-to-pixel scale go increasingly undetected, the assumption of an invariant atmosphere becomes increasingly invalid. Fig. 11 showed that sub-template moisture gradients can introduce significant retrieval errors. Thus, while larger templates avoid some of the difficulties with smaller sizes, other sources of error become more of a problem.

In summary, the choice of template size for use with the SWVR technique is a compromise between advantages that can be gained or lost. The expected variability of the surface and atmosphere, as well as other considerations such as available computer time and the expected amount of instrument noise, affect the choice. The above discussion showed that very small templates are not desirable. How large the template must be, so that PW fluctuations at scales as small as the template width reflect real moisture features, is a very subjective determination. In this case study, the 25x25 template seems qualitatively to offer a good compromise between the advantages and disadvantages of using smaller or larger sizes.

*b. 8 bit versus 10 bit input data*

The effects of using data at 8 versus 10 bit precision on PW images for the 1635-

1650 UTC flight leg were investigated. One should recall that simulated retrieval errors (Fig. 9) were nominally 0.5 mm for 10 bit data and 2.0 mm for 8 bit data. Thus, collocated retrievals using the two levels of precision are expected to differ by about 1.5 mm. Examination of PW imagery indicates that images from 8 bit input data (not shown) do differ slightly from the 10 bit versions. Fig. 21 shows a plot of PWs along one image line near the middle of the flight leg. These values were obtained prior to applying the variance threshold test. Both sets of retrievals used 25x25 templates. This example is typical of the case study in that, while the differing data precision causes some discrepancies in PW, many locations are unaffected. More importantly, although individual PWs differ, horizontal gradients from the two types of input data are similar. PW fluctuations at locations more than 5 km west of nadir (negative distances) are due to variances below the minimum threshold. The similarity of the two curves in that region shows that the upgrade to 10 bit data does not overcome the problems caused by these low variances. Thus, the influences of many other sources of retrieval error are not diminished by using more precise input data.

*c. Evaluation of observed surface features and precipitable water gradients*

The variety of surface and atmospheric conditions encountered in this case study tests the ability of the SWVR technique to resolve moisture gradients without influence from the underlying surface. This section summarizes moisture features in the PW imagery, their relationship to surface features, and their meteorological implications. Fig. 22 shows results from applying the technique to the entire 1635-1650 UTC

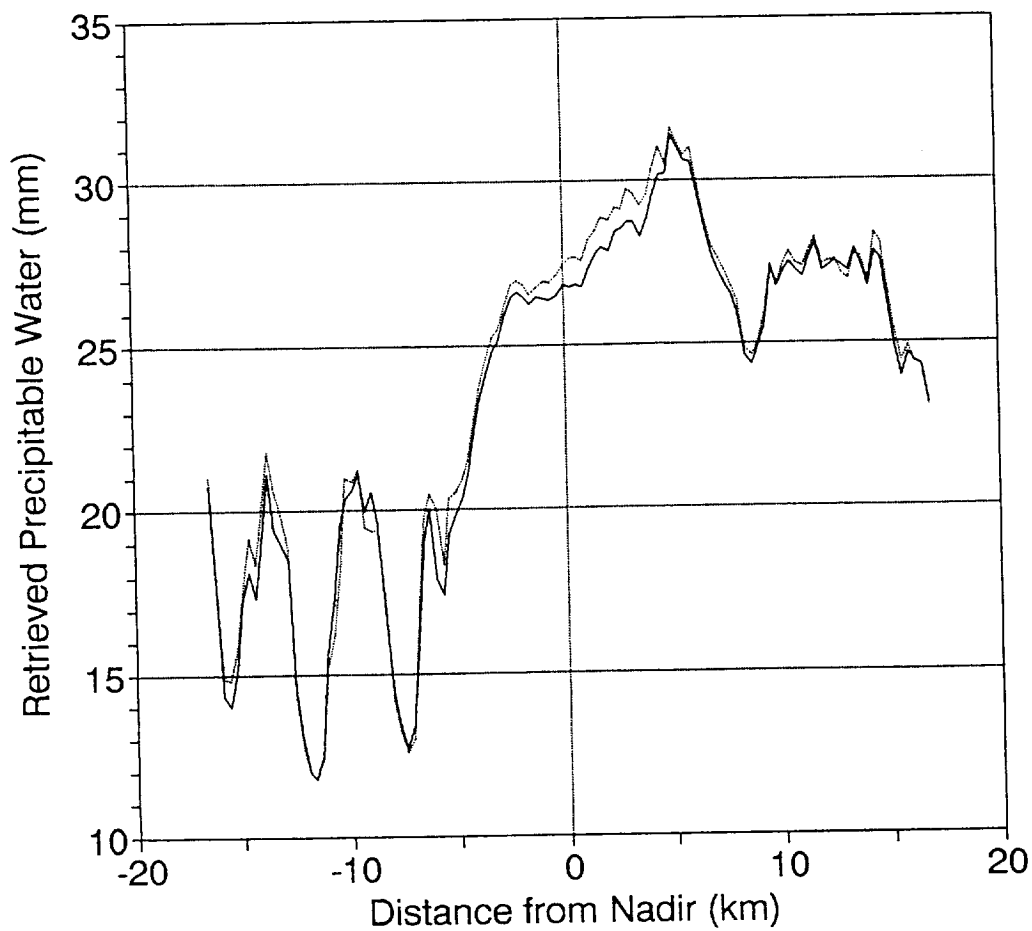


Figure 21. Retrieved PW (prior to applying the variance threshold test and using a 25x25 template) versus distance of the retrieval from nadir. Retrievals are along a single scan line located 59.7 km south of the beginning of the flight leg. Negative distances indicate locations west of nadir. The solid line represents retrievals made from 10 bit data, and the dotted line indicates 8 bit data.

MAMS flight leg using a 25x25 template. Fig. 22a is the PW image covering the 37x120 km region indicated by the dashed rectangle in Fig. 2. Fig. 22b is the corresponding image of 11  $\mu\text{m}$  channel variance used to compute the SWVR at each retrieval location. All variances, regardless of magnitude, are included. This image differs from those in panel 'b' of Figs. 16-20 in which only passes and failures of the variance threshold test were denoted. The larger variances, some of which exceed 20  $\text{K}^2$ , are indicated by the lighter shades.

Comparing the variance image (Fig. 22b) to the MAMS visible image for this flight leg (Fig. 15) explains some of the variance patterns. In the southern half of the visible image, numerous small lakes can be seen. Some of these lakes are collocated with strong minima in the 11  $\mu\text{m}$  channel variance (Fig. 22b). The small variances are a response to the uniform temperatures of the water surfaces. However, the lakes also create a significant amount of land-surface temperature contrast in the region. An example is the area of rather large channel variances in the south central part of the image (the brightest regions in the lower half of Fig. 22b). Visual comparison of the variance and PW images (Figs. 22a,b) suggests that there is little correlation between centers of large or small variance and gradients in the PW imagery. This is encouraging since it indicates that the SWVRs and the retrieved PWs are responding to atmospheric and not surface variability. 11  $\mu\text{m}$  channel variances (Fig. 22b) are influenced by PW (as discussed below) but are mostly dependent on the surface.

The relationship between retrieved PW and variance in the image discussed above was also analyzed quantitatively. Fig. 23 is a scatter plot of retrieved PW (before

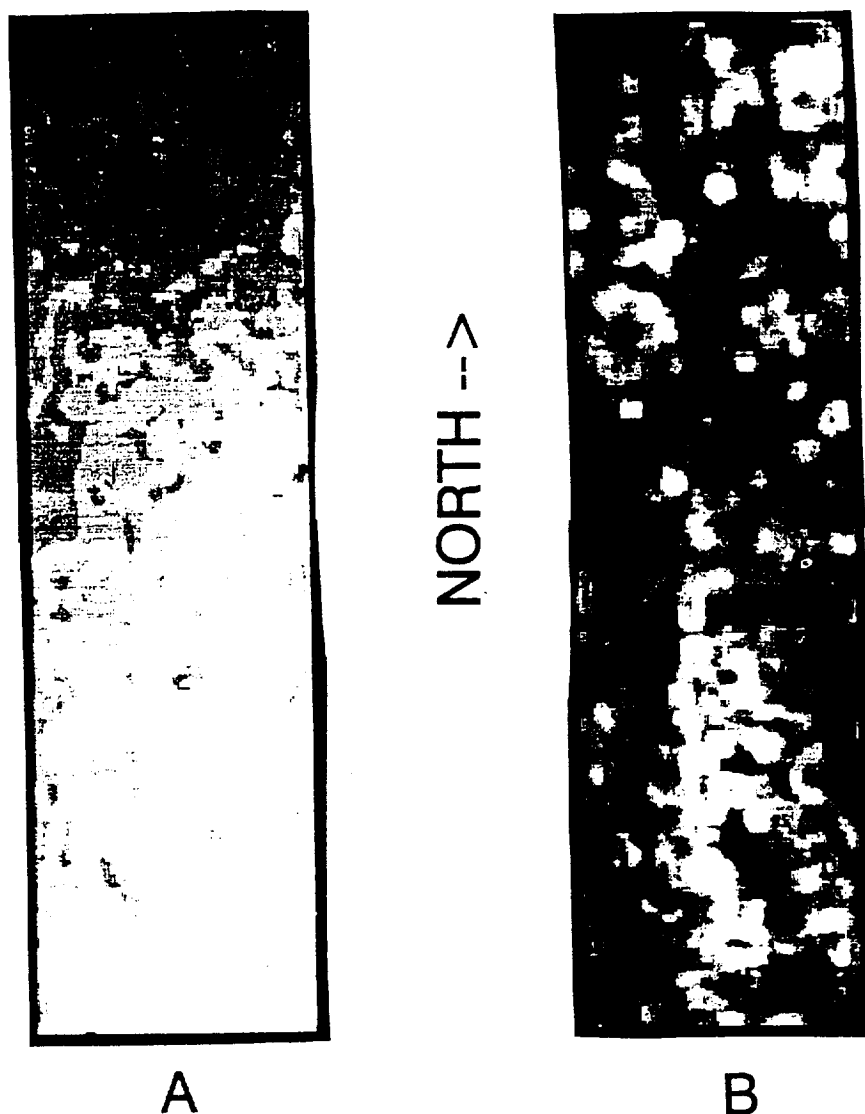


Figure 22. Images of retrieved PW (A) and  $11 \mu\text{m}$  channel variance (B) for retrievals made with a  $25 \times 25$  template over the  $37 \times 120$  km region (dashed rectangle in Fig. 2) mapped during the entire 1635-1650 UTC flight leg. In (A), lighter regions indicate greater PW. The darkest shade indicates PW below 12 mm, and the lightest shade denotes values greater than 40 mm. Each shade represents a range of about 3 mm. In (B), lighter shades indicate larger variance. The lightest shade denotes variance above  $10 \text{ K}^2$ , and each shade represents a range of about  $1 \text{ K}^2$ .

applying the variance threshold test) versus  $11 \mu\text{m}$  channel thermal variance for all retrievals (spaced 300 m apart) in the 1635-1650 UTC flight leg. Clearly, for PWs between 15 and 35 mm, retrievals having the same PW resulted from a wide variety of  $11 \mu\text{m}$  channel variances. No strong bias in retrieved PW is seen in response to the variances. This same lack of correlation was seen in scatter plots of retrieved PW versus  $11 \mu\text{m}$  channel variance from retrievals spaced 5 and 10 km apart (not shown).

Some important features in this diagram (Fig. 23) reveal certain characteristics of the technique. First, as retrieved PW increases, the maximum variance among the retrievals decreases. This is not surprising since increased moisture in the template increasingly obscures the surface from the instrument and decreases brightness temperature variance. Another feature is the absence of variances above  $10 \text{ K}^2$  for PWs between 20 and 25 mm, which is simply due to the lack of highly variable surfaces in regions of PW having those magnitudes. Finally, extremely small PWs occur only when variances are small. In fact, all PWs below 10 mm correspond to an  $11 \mu\text{m}$  channel variance below the threshold of  $1.0 \text{ K}^2$ . This is also expected, based on the simulations in Section 5 (Figs. 8-11) which showed that when channel variances are small, the major sources of error become enhanced and tend to cause PWs to err towards drier values. Thus, the variance threshold test successfully omitted obviously erroneous retrievals. However, the threshold test eliminated PWs ranging from near zero up to 35 mm, indicating that the exclusion of retrievals with low variances is not completely biased towards low values. Overall, while variances gradually decrease with increasing PW, there is no strong correlation between the

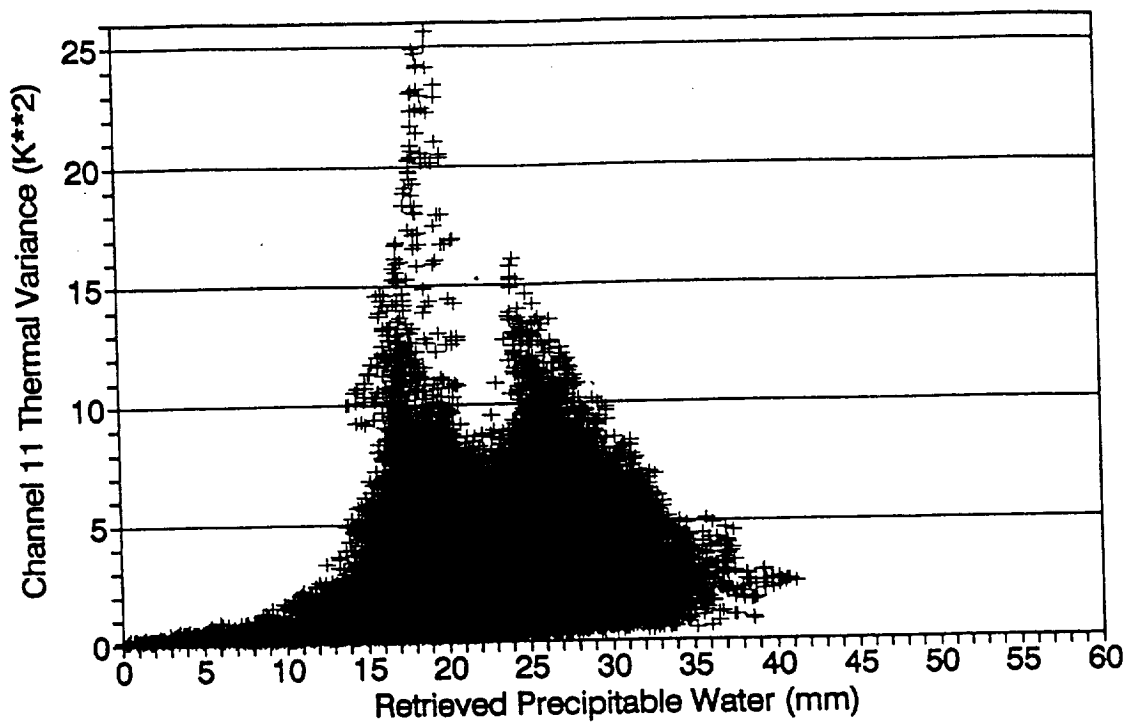


Figure 23. Scatter plot of retrieved PW versus 11  $\mu\text{m}$  channel variance for all actual retrievals made at 300 m spacing in the 1635-1650 UTC MAMS flight leg (corresponding to the 37x120 km dashed region in Fig. 2).

variance and the retrieved PW.

The northern portion of the PW image in Fig. 22a (also shown separately in Fig. 18a) exhibits a well defined transition into the more uniform, moist regions in the southern portion of the leg. To more quantitatively evaluate this north-to-south gradient, an average PW was computed for each horizontal (east-to-west) line in the PW image. These average PWs are plotted against distance along the flight leg in Fig. 24. This diagram clearly reveals the strength of the gradient. In the area between 20 and 50 km south of the initial point, horizontally averaged PW increases from 17 to 26 mm, translating into a gradient of about 0.3 mm per km. This transition is more abrupt and occurs further north than suggested by the early morning radiosonde-derived PW analysis (Fig. 13). Thus, the technique describes moisture variability at scales well below that resolvable with synoptic-scale radiosondes.

PWs in the region south of the intense gradient show a gradual increase. This is most pronounced near the end of the leg where individual PWs (before averaging) are near 40 mm. The flight leg ends just north of the cloud boundary that persisted across north-central Florida throughout the day on 16 October (Fig. 14). Thus, the SWVR technique successfully depicts the difference between clear, dry air and moisture-laden air capable of supporting significant cloud cover. This region of transition most likely represents the remnants of the frontal boundary which moved south after being analyzed north of this region on 15 October.

Without 'ground truth' PW measurements, the accuracy of PWs and PW variations (especially at scales as small as template size) in each portion of the image (Fig. 22a)



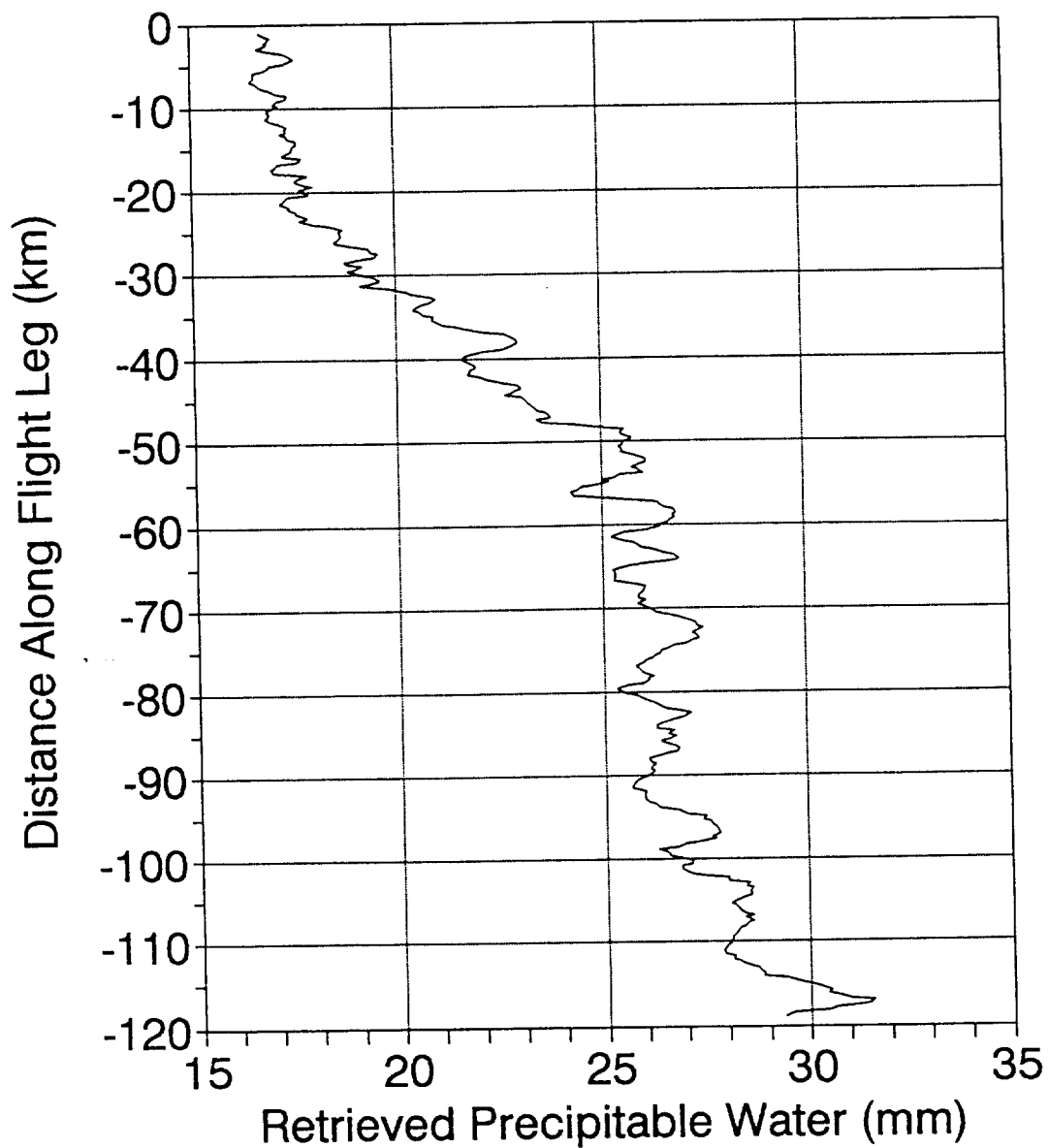


Figure 24. Retrieved precipitable water averaged along each scan line in the 1635-1650 UTC flight leg versus the distance along the flight leg of the corresponding scan line.

is not certain. Considering the number of error sources which influence the technique (Sections 4 and 5), further research is needed to confirm the validity of the results. However, the results presented in this section show that the PW image has little dependence on the surface and qualitatively reflects expected meteorological conditions in the region (i.e., a north-to-south gradient). The range of retrieved PWs in this flight leg (15-40 mm) is comparable to the range of values from radiosondes, suggesting that the retrieved PW values are generally reasonable.

## 7. Summary and conclusions

This study has investigated the theory and application of the SWVR technique for estimating precipitable water from high resolution split window imagery. Earlier studies demonstrating the utility of the technique provided the motivation to seek a better understanding of its strengths and weaknesses. The technique was applied to a case study of 16 October 1990 over Florida. PW estimates were derived from split window data at 100 m resolution obtained from the airborne MAMS instrument. Temperature and dewpoint profiles from conventional radiosonde sites were used as input for the numerous radiative transfer simulations performed in the study.

Based on simulated radiance data, the regression relationships between PW and SWVR, and between PW and the squared transmittance ratio, were found to be nearly identical. This confirmed the theoretical equality between the two ratios. More importantly, it verified the relation between the SWVR, a statistical quantity, and the physically meaningful parameter PW. PW was strongly inversely correlated with the SWVR when the major assumptions of the technique were met. The slope and intercept of the regression line agreed well with those of previous studies. That the relationship seems to vary little between summertime cases over the southeast United States suggests that the technique may not require direct prior knowledge of atmospheric conditions over a particular region of interest.

Several sources of error for the technique were quantified. While the effects of each source cannot be documented precisely, an approximate error budget was formulated. The least influential source was errors in the split window data. When 10 bit digitization was used, the combined effects of truncation and instrument noise caused an average retrieval error of only 0.5 mm. While the upgrade to 10 bit from 8 bit data did provide reduced retrieval errors in simulations, in actual application the improvement was largely masked by the effects of other sources of error.

Horizontal and vertical moisture variations were found to cause comparable retrieval errors. Variability in the vertical moisture profile produced scatter about the PW versus SWVR regression line. Thus, the standard error of that relationship (about 1.25 mm) was an acceptable measure of the typical retrieval error from that source. Horizontal moisture variation within the templates used to compute the SWVR is assumed to be zero; however, such gradients do exist and become increasingly influential with larger template sizes. If a template size of 25x25 MAMS pixels is used, PW gradients of 1 mm within the template will typically cause PW retrievals to be incorrect by 1 to 2 mm, depending on the magnitude of channel variances. However, isolated regions of stronger moisture transition can significantly increase the effect of this error source. These larger moisture gradients were detected in the PW imagery of this case study.

Sub-template variations in emissivity are the most difficult source of error to quantify, and they are likely the most troublesome to the SWVR technique. This is because emissivity can vary greatly within either small or large templates. If one

assumes that the standard deviation of emissivity in a template is not greater than 0.01, corresponding retrieval errors will generally range between 2 and 8 mm of PW. Again, the error depends on the channel thermal variances. Obviously, the degree of horizontal emissivity variation is itself highly variable, and, therefore, so is its influence on the retrievals.

The PW images produced over northern Florida detected a strong moisture gradient associated with a frontal boundary. Compared to the PW analysis from radiosondes, the high resolution retrievals more precisely defined the region of most intense transition and described moisture variability at much smaller scales. The range of retrieved PWs was comparable to that of surrounding radiosonde values. Since 'ground truth' PW information was not available, the reliability of PW variations, especially at scales as small as the template sizes, is not certain. Further research is needed to examine the accuracy of the technique at all spatial scales.

The greatest weakness of the technique was found to be its performance in regions of small scene variance. This condition amplifies the effects of almost every source of error. However, avoiding such regions when making retrievals can reduce the associated errors. Although areas of low variance were frequent in this case study, their avoidance yielded moisture gradients in the final image product that appeared realistic and useful for diagnosing moisture variability. Thus, an important strength of the technique is that, although individual retrieval errors may be significant in some locations, the relative accuracy of the PW imagery appears to be high.

Results using various template sizes were compared. PW images from using small

templates (9x9, 17x17) were susceptible to strong horizontal variations which did not reflect real moisture features. The small templates also often resulted in small channel variances. Small variances sometimes were found with larger templates, but to a lesser extent. While larger templates (33x33, 41x41) increase variances, they also increasingly invalidate the assumptions of an invariant atmosphere and constant emissivity. Further, detail in the PW imagery is sacrificed somewhat with the use of a large template. The choice of template size is thus a subjective determination. Perhaps, further research could quantitatively determine the best template size via calculations which show a minimum influence of the problems of small and large sizes. An intermediate size of 25x25 MAMS image pixels was qualitatively chosen in this study as the most appropriate choice.

Moisture fields from templates such as 25x25 retain excellent resolution when 100 m resolution MAMS data are used as input. Although very small templates cannot be used reliably with the technique, an increased knowledge of surface emissivity might permit the development of procedures for using smaller templates. Finally, the technique also has shown utility when applied to data of coarser resolution (such as AVHRR at 1 km resolution). Thus, with technological advancements, the technique perhaps can be used with instruments on future polar or even geostationary platforms.

## REFERENCES

- Baker, M. N., 1992: Precipitable water variations over central Florida as derived from the VAS split window channels. Masters thesis, Florida State University, 60 pp.
- Birkenheuer, D., 1991: An algorithm for operational water vapor analyses integrating GOES and dual-channel microwave radiometer data on the local scale. *J. Appl. Meteor.*, **30**, 834-843.
- Chesters, D. L. W. Uccellini, and W. D. Robinson, 1983: Low-level water vapor fields from the VISSR Atmospheric Sounder (VAS) split window channels. *J. Clim. Appl. Meteor.*, **22**, 725-743.
- \_\_\_\_\_, W. D. Robinson, and L. W. Uccellini, 1987: Optimized retrievals of precipitable water from the VAS split window. *J. Clim. Appl. Meteor.*, **26**, 1059-1066.
- Fuelberg, H. F., and P. J. Meyer, 1986: An analysis of mesoscale VAS retrievals using statistical structure functions. *J. Climate Appl. Meteor.*, **25**, 60-76.
- Guillory, A. R., 1991: A physical split window technique for deriving precipitable water utilizing VAS data. Masters thesis, Florida State University, 70 pp.
- Hayden, C. M., 1988: GOES-VAS simultaneous temperature-moisture retrieval algorithm. *J. Appl. Meteor.*, **27**, 705-733.
- Hillger, D. W., and T. H. Vonder Haar, 1979: An analysis of satellite infrared soundings at the mesoscale using statistical structure and correlation functions. *J. Atmos. Sci.*, **36**, 287-305.
- Jedlovec, G. J., 1985: An evaluation and comparison of vertical profile data from the VISSR Atmospheric Sounder (VAS). *J. Atmos. Oceanic Tech.*, **2**, 559-581.
- \_\_\_\_\_, 1987: Determination of atmospheric moisture structure from high resolution MAMS radiance data. Ph.D. Dissertation, University of Wisconsin-Madison, 187 pp.

- \_\_\_\_\_, K. B. Batson, R. J. Atkinson, C. C. Moeller, W. P. Menzel, and M. W. James, 1989: Improved capabilities of the Multispectral Atmospheric Mapping Sensor (MAMS). NASA Tech. Memo. 100352, Marshall Space Flight Center, 80 pp.
- \_\_\_\_\_, 1990a: Precipitable water estimation from high resolution split window radiance measurements. *J. Appl. Meteor.*, **29**, 851-865.
- \_\_\_\_\_, 1990b: Retrieval of precipitable water from AVHRR split window imagery. Preprints, *Fifth Conf. on Satellite Meteor. and Ocean.*, London, Amer. Meteor. Soc., 89-93.
- \_\_\_\_\_ and R. J. Atkinson, 1992: Variability of geophysical parameters from aircraft radiance measurements (for FIFE). In press.
- Kleespies, T. J., and L. M. McMillin, 1990: Retrieval of precipitable water from observations in the split window over varying surface temperature. *J. Appl. Meteor.*, **29**, 851-862.
- Labeled, J. and M. P. Stoll, 1991: Spatial variability of land surface emissivity in the thermal infrared band: spectral signature and effective surface temperature. *Remote Sens. Environ.*, **38**, 1-17.
- McMillin, L. M., D. G. Gray, H. F. Drahos, M. W. Chalfant and C. S. Novak, 1983: Improvements in the accuracy of operational satellite soundings. *J. Climate Appl. Meteor.*, **22**, 1948-1955.
- Smith, W. L., 1983: The retrieval of atmospheric profiles from VAS geostationary radiance observations. *J. Atmos. Sci.*, **40**, 2025-2035.
- \_\_\_\_\_, G. S. Wade and H. M. Woolf, 1985: Combined atmospheric sounding/cloud imagery -- a new forecasting tool. *Bull. Amer. Meteor. Soc.*, **66**, 138-141.



## BIOGRAPHICAL SKETCH

Richard D. Knabb was born June 20, 1968, in Elmhurst, Illinois. He attended elementary school in Ft. Lauderdale, Florida and then attended secondary schools in Katy, Texas. He received a B. S. in Atmospheric Science in May 1990 at Purdue University in West Lafayette, Indiana. In August 1990, he entered Florida State University to pursue a M. S. in Meteorology. This thesis marks the completion of that goal.

THE FLORIDA STATE UNIVERSITY  
COLLEGE OF ARTS AND SCIENCES

A COMPARISON OF SEVERAL TECHNIQUES  
FOR ESTIMATING SOIL MOISTURE  
OVER COMPLEX TERRAIN

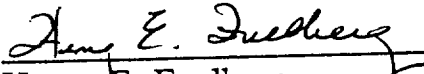
By

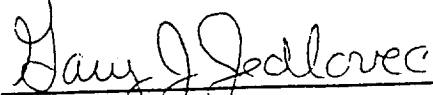
MICHAEL W. NICHOLS

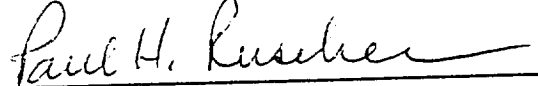
A Thesis submitted to the Department of Meteorology  
in partial fulfillment of the requirements for the degree of  
Master of Science

Degree Awarded:  
Summer Semester, 1993

The members of the Committee approve the thesis of Michael W. Nichols  
defended on 23 April, 1993

  
Henry E. Fuelberg  
Professor Directing Thesis

  
Gary J. Jedlovac  
Outside Committee Member  
NASA / Marshall Space Flight Center  
Huntsville, Alabama

  
Paul H. Ruscher  
Committee Member

  
Peter S. Ray  
Committee Member

## DEDICATION

This thesis is dedicated to my Dad, Charles R. Nichols, who always encouraged me to solve my own math problems, who continually stimulated my interest in natural and scientific phenomena, and who spent so much time with his three sons at the Smithsonian Institute and many other interesting places. My Dad's exemplary fathering helped me to be a better father in a time when many fathers give such little priority to their families.

## ACKNOWLEDGEMENTS

I would like to thank my major professor, Dr. Henry Fuelberg for his exemplary and dedicated guidance throughout this research endeavor. Special thanks go out to Dr. Gary Jedlovec of NASA's Marshall Space Flight Center for providing the MAMS data, additional guidance, and use of his transmittance code and various MAMS processing software; to my other committee members Dr. Paul Ruscher for his assistance with the operation of the boundary layer model, and Drs. Stephen Stage and Peter Ray for their suggestions. Additional thanks go out to Rick Knabb for the use of his precipitable water routine, and to Mr. Paul Meyer of NASA's Marshall Space Flight Center for providing topographic data.

Appreciation goes out to Dr. JoAnn Logan of the University of Tennessee for supplying soil temperature data and Mr. L. Wayne Hamberger of the Tennessee Valley Authority for supplying additional rain gauge data. Also, special thanks to Jeff Orrock for help with the figures.

Finally, my heartfelt gratitude goes out to my wife, Jean Ann, for her patience and endurance with me during my graduate studies. It takes a very special person to put up with all the trials and tribulations of graduate student life, and indeed, she is that special person.

This research was sponsored by NASA Grant number NAG8-653 under the auspices of the Marshall Space Flight Center.

## TABLE OF CONTENTS

	Page
LIST OF TABLES.....	vii
LIST OF FIGURES.....	viii
ABSTRACT.....	xii
1. Introduction.....	1
2. Boundary layer model physics.....	8
<i>a. The boundary layer component.....</i>	9
<i>b. The surface layer.....</i>	13
<i>c. The soil layer.....</i>	14
<i>d. The surface energy balance.....</i>	15
<i>e. Boundary layer clouds.....</i>	17
<i>f. Radiation.....</i>	17
<i>g. Shelter air temperature.....</i>	18
<i>h. Model initiation and use.....</i>	19
3. Data and methodology.....	21
<i>a. Data sources.....</i>	21
1. Vegetation index - NDVI.....	23
2. Precipitable water - (PW).....	26
3. Land surface temperature (LST).....	27
<i>b. Roughness length.....</i>	29
<i>c. Soil moisture.....</i>	30
1. The antecedent retention index.....	31

2.	MAMS / PBL model regressed soil moisture.....	35
3.	NDVI / LST slope method.....	39
d.	<i>Mixing layer height estimation from MAMS.....</i>	39
e.	<i>Cloud fraction estimation from MAMS.....</i>	40
4.	Results.....	43
a.	<i>Selection of the best ARI “ground truth” .....</i>	43
b.	<i>MAMS LSTs, LST changes and soil moisture.....</i>	54
1.	MAMS LSTs as accurate ground truth LST.....	54
2.	LST changes and soil water availability.....	57
c.	<i>MAMS LST change / PBL regression soil moisture estimation.....</i>	62
d.	<i>NDVI / LST relationships to soil moisture.....</i>	71
e.	<i>Estimation of other parameters.....</i>	83
1.	Maximum shelter air temperature.....	83
2.	MAMS LST vs. modeled LST from different input soil moisture.....	85
3.	Mixing layer height.....	85
4.	Boundary layer clouds.....	88
5.	Conclusions.....	96
	APPENDIX A.....	101
	REFERENCES.....	102
	BIOGRAPHICAL SKETCH.....	109

## LIST OF TABLES

Table	Page
1. MAMS instrument specifications (after Jedlovec <u>et al.</u> , 1989). . . .	6
2. Mean error contributions (%) to mixing layer heights estimated from cloud shadows. . . . .	87



## LIST OF FIGURES

Figure	Page
1	Rain gauge locations within the study area. Flight tracks appear in Fig. 2. Sites marked with an asterisk (*) were cirrus contaminated during the first pass. Sites marked with "t" are classified rough terrain. Major lakes along the Tennessee River are marked "G" for Guntersville, and "W" for Wheeler Lake. . . . . 10
2	Flight tracks of the NASA U2 high altitude research aircraft on which the MAMS instrument was flown. First pass (a) from 1441 to 1550 UTC; second pass (b) flown from 1555 to 1700 UTC on 18 August 1988. . . . . 24
3	Regression fit between MAMS split-window variance ratio and precipitable water. Data were from summer soundings during 1988 (see text for equation). . . . . 28
4	Behavior of the evaporation reduction function, $F$ , in the evapotranspiration term for the ARI calculation (see text for equation). 33
5a	Examples of ARI calculations for the EvapARI model (with explicit evaporation included). . . . . 36
5b	Same as Fig. 5a, but for ARI without evaporation term for the same two sites. . . . . 37
6	Example of regression calculation from PBL modeled LST difference from 10 AM to noon local time. Separate regressions were done at each location where MAMS surface temperature changes were observed. Note the discontinuity around 0.20 soil moisture value (see text). . . . . 41
7	Example of a typical scatter plot between NDVI and LST over a 5 x 5 km region in the study area. More examples are given in chapter 4. . . . . 42

8	Observed in situ maximum soil temperatures at various depths near the study region. Data were taken from 15 locations in southern Tennessee, northeastern Mississippi on 18 August 1988. The arrow corresponds to the average MAMS LST during the second overpass. . . . .	46
9	Soil moisture profiles (average and range) fit through final NoEvapARI soil moisture values. The average was done for 55 sites shown in Fig. 1. . . . .	47
10	Same as Fig. 9., except profiles were fit through final soil moisture model from EvapARI model. . . . .	48
11	Soil temperature differences at various depths between PBL model output and observed data (forecast minus observed). The observed values were averaged from all sites where in situ temperatures were measured. . . . .	50
12	Composite MAMS LST image taken during the first pass (see Fig. 2 for flight tracks). Hottest values appear red (45 - 50° C); coolest appear purple (30-35° C). . . . .	56
13	Normalized MAMS LST change from 10 AM to noon local time. . . . .	59
14	Cumulative rainfall (in) from 1 June through 18 August 1988. . . . .	60
15	Scatter plot of MAMS LST change ( $^{\circ}\text{C h}^{-1}$ normalized from 10 AM to noon) vs. ARI-derived soil water availability (ratio of actual to maximum saturation value) for 34 sites in the study region. A Log fit to the data yields a correlation coefficient of -0.63. All sites are characterized by a relatively small roughness parameter. . . . .	63
16	Observed MAMS LST differences compared to PBL model regressed soil moisture for (a) all sites, and (b) only those with relatively flat terrain. Note the very little difference in R values. . . . .	66

17	ARI-derived soil water availability vs. PBL regressed availability from MAMS LST differences. The ARI values, on average, are 23 % drier than the PBL-derived values. . . . .	69
18	Histogram of differences between ARI and PBL-regressed soil water availability. Mean difference (PBL - ARI) is 0.23 with a standard deviation of 0.26. . . . .	70
19	Composite MAMS Normalized Differenced Vegetation Index (NDVI) over the study region. See Fig. 2 for flight track times. Green (0.6 - 0.8) correspond to high vegetation density; black areas are low vegetation density (NDVI from 0.0 to 0.1). White areas are where NDVI < 0.0 (water bodies and clouds). . . . .	73
20	Averaged NDVI vs. ARI-derived soil water availability for 34 sites in the study area. (R = 0.33). NDVI values were averaged from first and second MAMS overpasses. . . . .	75
21	Two contrasting examples of NDVI / LST scatter plots for estimating soil moisture. Top (a) was made over a wet location; bottom (b) over a dry location. The ARI availability (day 231) was 91% for (a) and only 23% for (b). . . . .	76
22	Average slopes of NDVI / LST scatter plots versus ARI - derived root zone soil moisture availability. Slopes were only included if a correlation < -0.40 was achieved for the scatter diagram for both MAMS overpasses. . . . .	79
23	Same as Fig. 22 but NDVI compared with PBL - regressed soil moisture from MAMS LST change slope ( R = 0.60). . . . .	81
24	PBL-regressed soil moisture compared to second pass NDVI only (R = 0.60). Data for all sites are included regardless of terrain. . . . .	82
25	Slope of NDVI / LST plots vs. local time of the second MAMS overpass (R = -0.59). . . . .	84

26	Imaged terrain (1 km resolution) over study region (data courtesy of United States Geological Survey). Brightest areas are highest elevations. Elevations range from 50 to 670 m. . .	90
27	Mean and standard deviation cloud fractions (%) vs. time for all sites with minimum terrain influence. Arrows correspond to the times of MAMS overpasses. . . . .	92
28	Histogram of differences between forecast and observed cloud fraction (%) with MAMS-PBL regressed soil moisture input to the PBL model. . . . .	94
29	Same as Fig. 28. except for ARI modeled soil moisture into PBL. . . . .	95

# A COMPARISON OF SEVERAL TECHNIQUES FOR ESTIMATING SOIL MOISTURE OVER COMPLEX TERRAIN

Michael W. Nichols  
The Florida State University, 1993  
Major Professor: Henry E. Fuelberg, Ph. D.

Three different techniques for estimating soil moisture are compared over northern Alabama / southern Tennessee: 1. An antecedent retention index (ARI) with and without explicit evaporation physics, 2. A remotely sensed land surface temperature (LST) - modeling technique in which separate regression equations are developed at each site using a one-dimensional planetary boundary layer (PBL) model to predict soil moisture based on LST changes from 10 AM to noon; and, 3. A method which exploits the relationship between soil moisture availability and the slope of normalized differenced vegetation index (NDVI) vs. LST on scatter diagrams. Observed soil moisture data were not available for the study. Therefore, results of the various methods are intercompared to assess their strengths and weaknesses. Additionally, remotely sensed LSTs from the Multispectral Atmospheric Mapping Sensor (MAMS) are compared to in situ and PBL-modeled LSTs.

Results show significant differences between these estimation methods over complex terrain. The most reliable method is found to be the LST - modeling approach. There is a correlation of -0.9 between time changes in LST and regressed soil moisture, regardless of terrain

influences. Moreover, the slope of the fitted regression line is similar to those of previous investigations where in situ measurements of soil moisture and soil temperatures were available.

The indexed technique (ARI) apparently underestimates root zone soil moisture when compared to PBL-regressed soil moisture. Terrain slope may account for some of the differences, in addition to the simplicity of the ARI model parameters. The correlation between ARI soil moisture and 2 h LST changes is found to be -0.63 over sites characterized by relatively flat terrain. This is reduced to -0.50 when sites with significant terrain were included. The NDVI / LST slope procedure is found to be easily contaminated by changes in solar insolation. This solar contamination must be removed in order to infer soil moisture estimates. Both ARI-derived and LST - PBL model regressed soil moisture estimates are input to a PBL model to predict such variables as LST, mixed layer (ML) height, cloud fractions, and surface fluxes.

Comparison of MAMS LSTs with in situ soil temperatures show agreement within 1 to 3° C. The soil moisture model producing the smallest differences between remotely sensed and modeled LST is found to be the MAMS / PBL- regressed method. It produces a mean difference of -2.3 ° C versus a mean difference of -4.7° C for model runs with the ARI input soil moisture.

No relationship is found between any soil moisture model and ML growth. There are inherent large errors in the procedure (a cloud shadow

technique is employed), and the ML observations were taken during the rapid phase of ML growth.

Both ARI and model-regressed techniques lead to similar errors (-11 %) in forecast cloud fraction when these soil moisture values are input to the PBL model. Important processes which cannot be resolved by a one-dimensional model most likely are influencing PBL cloud growth.

## 1. Introduction

A major objective within NASA's planned Earth Observing System (EOS) is to better understand interactions between the land surface and the atmosphere (NASA, 1987). These interactions and associated convective cloud development play an important role within the context of global climate studies (Ramanathan, 1989). Indeed, a major concern today is the radiative role that clouds have on regional and large scales. EOS will explore how these interactions are seen from remote sensing platforms. NASA currently plans to develop and deploy high spectral and spatial resolution sensors for these types of studies. The Multispectral Atmospheric Mapping Sensor (MAMS; Jedlovec *et al.* 1986, 1989) is an airborne instrument for this purpose. Future instruments on space platforms include the Moderate-Resolution Imaging Spectrometer (MODIS), the High Resolution Imaging Spectrometer (HIRIS) for the imaging of vegetation and land surface temperature (LST), and the Synthetic Aperture Radar (SAR) for estimating root zone soil moisture and other parameters. Several studies have suggested



the possibility of inferring root zone soil moisture based on LST differences (Wetzel and Woodward, 1987; Carlson *et al.*, 1981; Schmugge, 1978; Jackson *et al.*, 1977; Lahouari, 1992).

Previous studies, both observational and modeling, have shown the importance of surface characteristics on convective cloud development. Yan and Anthes (1988) demonstrated that “inland sea breezes” generated in response to soil moisture gradients can be as strong as the land/sea breeze circulations found near coastal areas. Furthermore, they supported the earlier hypothesis (Anthes, 1984) that mesoscale variations in vegetative cover could enhance convective precipitation in normally semiarid regions under weak synoptic conditions with sufficient instability.

These “nonclassical mesoscale circulations” occur on scales between 20-200 km and develop not only due to soil moisture gradients, but near any “perturbed area” where the surface sensible heat flux is enhanced or suppressed compared to its surroundings (Segal and Arritt, 1992). This enhancement or suppression can result from spatial variations of evapotranspiration, surface albedo and thermal storage. Chang and Wetzel (1988) suggested that differential soil moisture and evapotranspiration, and their associated mesoscale circulations, may have been the forcing mechanism which initiated the thunderstorm that eventually spawned the Grand Island, Nebraska tornado of 1980. They concluded that spatial variations of soil moisture increased the LST gradient and thus produced the thermally direct ageostrophic circulation which caused mesoscale surface moisture convergence and upward motion.

Bradshaw and Fuelberg (1993) also studied the effect of the underlying surface on convective cloud initiation as part of a validation study for the High-resolution Interferometer Sounder (HIS). They found that areas of initial cumulus onset coincided with locations of relatively large Bowen ratio estimated from HIS soundings.

Recently, Rabin *et al.* (1990) used visible and infrared (IR) satellite imagery combined with detailed landscape information to study the effects of the land surface on the ensuing convective cloud field during weak environmental forcing. They used a one-dimensional planetary boundary layer (PBL) model to simulate a developing cloud field for comparison with satellite imagery. Their results indicated that for a relatively dry boundary layer, clouds formed first over areas with large sensible heat flux (large Bowen ratio) and were initially suppressed over areas with large latent heat flux (small Bowen ratio). With a moist boundary layer, they found that convective clouds formed first over moist ground with small Bowen ratio.

Various combinations of visible, IR, and near-IR wavelengths can be used to infer information about the land/atmosphere interface (e.g., see the review by Sellers *et al.*, 1990). For example, vegetated areas can be described using the normalized difference vegetation index (NDVI) which combines radiances from near-IR and visible channels. The NDVI is related to the amount of illuminated chlorophyll in the land surface cover (Tucker, 1979; Asrar *et al.*, 1984; Brest and Goward, 1987) and can be related to transpiration processes at the surface (see Running and Nemani, 1988). The NDVI also has been used in conjunction with LST data to estimate root zone

soil moisture availability (Nemani and Running, 1989; Carlson *et al.*, 1990). Much of the current research in land/atmosphere studies has utilized data sets from the Advanced Very High Resolution Radiometer (AVHRR) and the Land Remote Sensing Satellite (Landsat) Multispectral Scanner.

MAMS shows great potential in studies of the land/atmosphere interface and has been used in NASA's high altitude research program (see Jedlovec *et al.*, 1986). MAMS is spectrally similar to Landsat, and Table 1 gives its technical specifications. MAMS has four (9 and 10 being redundant) IR channels, and 8 visible/near-IR channels. When carried on a U2/ER2 aircraft at an altitude of 20 km, MAMS has a spatial resolution of 100 m at nadir, providing details at the meso-, micro- $\beta$  and micro- $\alpha$  scales (Orlanski, 1975). There have been several significant improvements to the MAMS instrument since its inception (Jedlovec *et al.*, 1989), including better signal to noise characteristics and 10 bit IR digitization versus the previous 8 bit. Jedlovec (1990) and Knabb (1993) have demonstrated the use of MAMS to derive small scale variations of precipitable water and LSTs using a split window technique.

The current study focuses on four primary objectives:

- 1) Compare three different techniques for estimating soil moisture.

One method is based on the best "ground truth" data available, the antecedent retention index (ARI). In the current study, I compare two forms of the ARI, one with explicit evaporation physics and one without, and select the best "ground truth" based on several factors. Of primary importance is the best forecast maximum soil temperatures compared to in situ soil temperature data.

For the second method, I calculate MAMS remotely sensed temporal LST differences and regress these to PBL modeled LST differences to infer soil moisture. This aspect of the research differs from previous studies in two significant ways. First, I examine time changes of LST during a short time interval (approximately 10 AM to noon local time), whereas other studies have examined them from the time of minimum to maximum LST. During the 10 AM to noon time interval, the time rate of change of LST exhibits an approximately linear relationship (Idso *et al.*, 1975; Schmugge, 1978); which increases significantly with smaller soil moisture content. Furthermore, clouds are minimal at this time over much of the region being examined. Second, I take advantage of high resolution MAMS visible and IR imagery over the study region. For the third method, a technique that relates NDVI / LST scatter diagrams to soil moisture (Running and Nemani, 1988; Carlson *et al.*, 1990) will be compared to the other soil moisture estimation techniques. An intercomparison between the three methods will be carried out.

2) Investigate several MAMS-derived products such as LST and atmospheric corrected NDVI. The NDVI is used to infer vegetation fraction and is a necessary input parameter to the PBL model. The roles of solar angle on values of NDVI will be investigated over areas with similar viewing geometry. MAMS LST will be compared to in situ LST and will be used as verification for LSTs from the PBL model. LSTs will be forecast with the various input soil moisture models for comparison.

3) Use MAMS data where possible, to determine characteristics of the land surface and observe where boundary layer cloud formation is

Table 1. Specifications for the MAMS sensor (after Jedlovec *et al.*, 1989)

Scan speed	25 rps
Instantaneous field of view (ifov)	5.0 mrad
Ground resolution at nadir (20 km altitude)	100 meters
Total field-of-view (fov)	85.92 degrees
Swath width (20 km altitude)	37.2 km
Digitization	8 bit (vis)/ 10 bit (IR)
Roll correction	$\pm 15$ degrees
Pixels per line	716
Calibration sources	2 controlled blackbodies
<u>Bandwidth (@50% response)</u>	<u>Channel</u> (micrometers)
1	0.42-0.45
2	0.45-0.52*
3	0.52-0.60*
4	0.57-0.67
5	0.60-0.73*
6	0.65-0.83
7	0.72-0.99*
8	0.83-1.05
9	3.47-3.86
10	3.47-3.86
11	10.55-12.24
12	12.32-12.7

\* Similar to Landsat channel.

avored. Reasons for first formation over preferred regions in the study area will be sought. Factors to be included are NDVI, LST, soil moisture variations and terrain.

4) Determine how well a simple one-dimensional PBL model predicts cloud fractions, LSTs, and mixed layer (ML) heights in comparison to those estimated from the MAMS data.

The next chapter describes important features of the PBL model. Chapter three describes the data sources and methodology used in this study. Chapter four focuses on results, and, finally, a concluding discussion appears in chapter five.

## 2. Boundary layer model physics

Planetary boundary layer (PBL) modeling was performed for two primary purposes. First, model runs were used to develop predictive regression relationships for soil moisture using LST changes during the time of the MAMS overpasses. Chapter three gives details of this regression technique. Second, the model was used to predict several boundary layer parameters: LST, shelter temperature, boundary layer height, cloud fraction, and Bowen ratio. The Bowen ratios were compared qualitatively to soil moisture values and cloud fractions. The PBL model runs were made over the locations shown in Fig. 1 during the synoptically quiescent day of 18 August 1988. These sites were chosen because each recorded rainfall (thus allowing a calculated value of the ARI), and some also recorded maximum and minimum shelter temperatures.

The first order closure Oregon State University one-dimensional PBL model (Ek and Mahrt, 1989; version 1.0.3) was used for this study. Only a brief summary is presented; however, pertinent references are given for each

major component of the model. The main advantage of using this simple model is the ability to do many simulations in a short time. The Oregon State model has been tested under a variety of atmospheric conditions and has been shown to perform relatively well compared to more sophisticated models (Pan and Mahrt, 1987; Mahrt and Pan, 1984). Since there is no large scale advection during this particular study period, a simple one-dimensional model is justified. The model was originally developed to be part of a global spectral model at the United States Air Force Geophysical Laboratory (Brenner *et al.* 1984). For the current study, it was used as a stand alone model and was run for 12 hours from 7 AM to 7 PM local time. Section 2a describes the boundary layer component, 2b describes the surface layer portion, section 2c the soil model, and 2d the surface energy balance. Lastly, the cloud model and radiation portions are described in sections 2e and 2f, respectively. The shelter temperature is described in section 2g and lastly, the model usage is outlined in section 2h.

*a. The boundary layer component*

A detailed description of the boundary layer component of the model appears in Troen and Mahrt (1986). The set of prognostic equations for potential temperature ( $\theta$ ), specific humidity ( $q$ ), and horizontal wind ( $V_h$ ) is given by (Ek and Mahrt, 1989) as:

$$\frac{\partial V_h}{\partial t} = \frac{\partial}{\partial z} \left( K_m \frac{\partial V_h}{\partial z} \right) - w \left( \frac{\partial V_h}{\partial z} \right) \quad (1a)$$

$$\frac{\partial \theta}{\partial t} = \frac{\partial}{\partial z} \left[ K_h \left( \frac{\partial \theta}{\partial z} - \gamma \theta \right) \right] - w \left( \frac{\partial \theta}{\partial z} \right) \quad (1b)$$



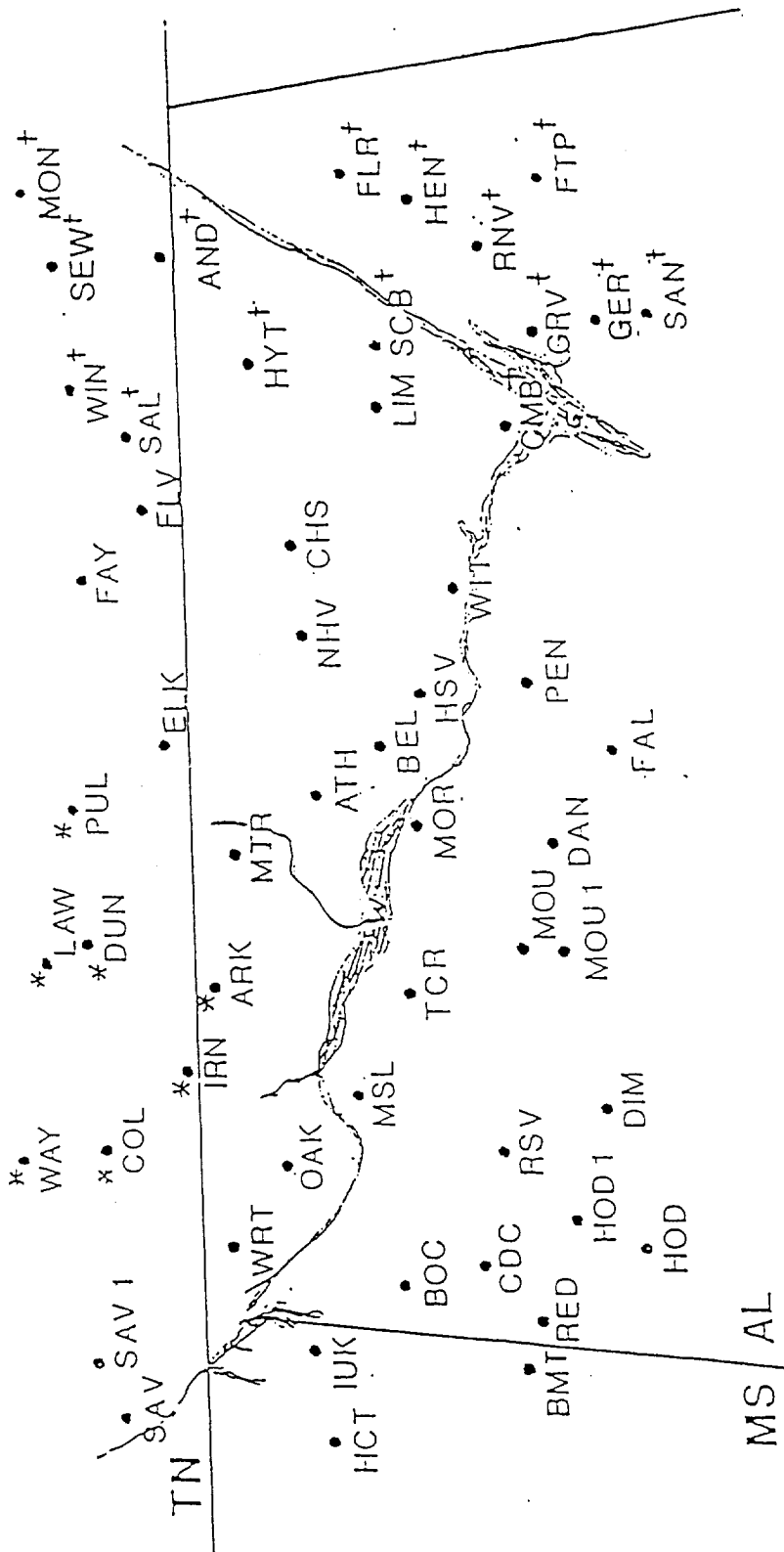


Fig. 1. Rain gauge locations within the study area. Flight tracks appear in Fig. 2. Sites marked with an asterisk (\*) were cirrus contaminated during the first pass. Sites marked with "t" are classified rough terrain. Major lakes along the Tennessee River are marked "G" for Guntersville, and "W" for Wheeler Lake.

$$\frac{\partial q}{\partial t} = \frac{\partial}{\partial z} \left( K_h \frac{\partial q}{\partial z} \right) - w \left( \frac{\partial q}{\partial z} \right), \quad (1c)$$

where  $\gamma_\theta$  is the potential temperature counter-gradient correction used when the stratification is unstable (see Deardorff, 1966). This correction is necessary to avoid using physically unrealistic negative values of the eddy diffusivity,  $K$ .

The model utilizes a vertically varying eddy diffusivity given by

$$K_m = w_s h k \frac{z}{h} \left( 1 - \frac{z}{h} \right)^p \quad (2)$$

for the unstable case, where  $p$  is set to 2. Also, for  $p=2$ ,  $K_m$  assumes a cubic profile in the vertical. The subscript  $s$  denotes the surface. The von Kármán constant,  $k$  is taken to be 0.4. The boundary layer height,  $h$  is given by (6) below. For the stable case (Brost and Wyngaard, 1978)

$$K_m = u^* \phi_m^{-1} h k \frac{z}{h} \left( 1 - \frac{z}{h} \right)^p, \quad (3)$$

where  $z$  is the height above the ground. The nondimensional profile function for momentum,  $\phi_m$  is given by

$$\phi_m = \left\{ \begin{array}{ll} 6.0 & \text{,very stable} \\ 1.0 + 5.0 \frac{z}{L} & \text{,stable} \\ \left( 1.0 - 15 \frac{z}{L} \right)^{-1/3} & \text{,unstable} \end{array} \right\}, \quad (4)$$

where  $L$  is the Monin-Obukhov length scale (Stull, 1988). These formulations are from Businger et al. (1971) with modifications by Holtstlag

(1987) and Ruscher (1988).

The parametrization for the coefficient of eddy heat diffusivity,  $K_h$  is given by

$$K_h = K_m Pr^{-1} , \quad (5)$$

where  $Pr$  is the nondimensional Prandtl number (Troen and Mahrt, 1986). The nondimensional profile function for heat,  $\phi_h^{-1}$  is the same as for momentum except for the unstable case where the exponent is  $-1/2$  instead of  $-1/3$ .

One should note that the model boundary-layer height is computed diagnostically as

$$h = \frac{Ri_{cr} \theta_{0v} |V_1|^2}{g (\theta_v(z) - \theta_{0v}^*)} , \quad (6)$$

where  $Ri_{cr}$  is the nondimensional critical Richardson number ( $=0.5$ ),  $\theta_{0v}^*$  is the reference virtual potential temperature at the first model level above the ground,  $g$  is gravitational acceleration,  $\theta_v(z)$  is virtual potential temperature at model level  $z_1$  (60 m for the unstable case and 20 m for the stable case), and  $V_1$  is horizontal wind velocity at the first model level above ground. The low-level virtual potential temperature ( $\theta_{0v}$ ) is modified under unstable stratification (Troen and Mahrt, 1986)

$$\theta_{0v}^* = \left\{ \begin{array}{ll} \theta_{0v} & , \text{ stable} \\ \theta_{0v} + C \frac{\overline{(w'\theta_v')_s}}{w_s} & , \text{ unstable} \end{array} \right\} . \quad (7)$$

*b. The surface layer*

Surface fluxes are parameterized for the stable case as in Mahrt (1987), and for the unstable case as in Louis *et al.* (1982) with modifications by Holtslag and Beljaars (1989). They are given by

$$u_*^2 = C_m |V_0| \quad (8a)$$

$$\overline{(w'\theta')}_s = C_h (\theta_s - \theta_0) \quad (8b)$$

$$\overline{(w'q')}_s = C_h (q_s - q_0) , \quad (8c)$$

where  $C_m$  and  $C_h$  are the exchange coefficients for momentum and heat, respectively, and are defined below. Surface values of potential temperature ( $\theta_s$ ) and specific humidity ( $q_s$ ) are calculated from the surface energy budget equations described in section 2d.

The surface layer ( $z < 0.1 h$ ) forecast equations (the same as (1a-c)) are matched to the PBL using modified forms of eddy diffusivities for momentum and heat as

$$K_m = u_* k z \phi_m^{-1} \left(\frac{z}{L}\right) \left(1 - \frac{z}{h}\right)^p \quad (9)$$

and

$$K_h = K_m \text{Pr}^{-1} , \quad (10)$$

respectively. Note that the profile functions now have a  $z_s/L$  dependence instead of on  $z/L$ . The term  $(1 - z/h)^p$  remains for proper matching with the mixed layer  $K_m$  as a modification. The only remaining variables needed to

close the surface layer model are  $\theta_s$  and  $q_s$  which are calculated in the soil model and the surface energy balance, discussed below.

*c. The soil layer*

This portion of the model is described in detail in Mahrt and Pan (1984) and Pan and Mahrt (1987). The forecast equation for volumetric soil water content ( $\Theta$ ) is

$$\frac{\partial \Theta}{\partial t} = \frac{\partial}{\partial z} \left( D(\Theta) \frac{\partial \Theta}{\partial z} \right) + \frac{\partial K(\Theta)}{\partial z}, \quad (11)$$

where  $D$ , the coefficient of diffusivity, and  $K$ , the hydraulic conductivity, both are functions of volumetric water content and soil type (see Mahrt and Pan, 1984). *These coefficients can vary by several orders of magnitude through the extremes of wet and dry soil conditions.*

Total model evaporation is found by determining direct, canopy, and transpiration components following Ek and Mahrt (1989). Total evaporation is not allowed to exceed the potential rate. "Surface specific humidity"  $q_s$  is calculated as a function of the total evaporation, i.e.,

$$q_s = q_0 + \frac{E}{\rho_0 C_h}, \quad (12)$$

where  $q_0$  is the specific humidity of the first model level,  $\rho_0$  is the air density at the surface, and  $C_h$  is the exchange coefficient for moisture. Soil temperature ( $T$ ) is forecast according to the prognostic equation

$$C(\Theta) \frac{\partial T}{\partial t} = \frac{\partial}{\partial z} \left( K_T(\Theta) \frac{\partial T}{\partial z} \right), \quad (13)$$

where  $C(\Theta)$  is the volumetric heat capacity and  $K_T(\Theta)$  is the thermal conductivity of the soil. The heat capacity is a linear function of  $\Theta$ ; the thermal conductivity, however, is a highly nonlinear function that can vary several orders of magnitude with soil moisture changes. The soil model provides the soil heat flux discussed in the next section, and also provides the surface potential temperature,  $\theta_s$  (an upper boundary condition in the soil model). The entire model is now closed with the exception of potential evaporation (described next).

*d. The surface energy balance*

The surface energy balance equation is given by

$$(1-\alpha)S\downarrow + L\downarrow - \sigma\theta_s^4 = G + H + L_v \cdot E , \quad (14)$$

where each term is expressed in  $W\ m^{-2}$ . The first term on the left-hand side of (14) is downward solar radiation (positive downward) where  $\alpha$  is the surface albedo. The second term on the left-hand side is downward atmospheric long wave radiation (positive downward). Both the solar and long wave radiation are described in more detail below. The third term on the left-hand side is upwelling terrestrial radiation with blackbody surface temperature  $\theta_s$  (positive upward). The first term on the right of (14) is the soil heat flux (positive downward) discussed earlier. The second term on the right-hand side is the sensible heat flux (positive upward) defined as

$$H = \rho_0 c_p C_h (\theta_s - \theta_0) , \quad (15)$$

where  $\rho_0$  is the air density,  $c_p$  is the specific heat of air,  $C_h$  is the surface exchange coefficient, and the potential temperature difference in parentheses is between the surface and the first model layer. The last term on the right-hand side of (14) is the latent heat flux (positive upward), where  $L_v$  is the latent heat of vaporization and  $E$  is the total evaporation.

Since the surface temperature is not known initially, the usual Penman relationship cannot be used to compute the potential evaporation,  $E_p$  (which is required in the present model). Instead, as a first step, the surface energy balance is computed using a reference state of saturated soil (keeping the albedo constant) as

$$(1-\alpha)S\downarrow + L\downarrow - \sigma\theta_s'^4 = G + H' + L_v \cdot E_p, \quad (16)$$

where the primed variables now denote a fictitious potential surface temperature ( $\theta_s'$ ) and sensible heat flux ( $H'$ ). This fictitious surface temperature is the temperature the surface would have if the soil were sufficiently wet and the evaporation were to proceed at the potential rate. The fictitious heat flux ( $H'$ ) is the value corresponding to saturated soil with soil temperature of  $\theta_s'$ . The potential evaporation and sensible heat flux are calculated as

$$E_p = \rho_0 C_h (q_s^*(\theta_s') - q_0) \quad (17)$$

and

$$H' = \rho_0 c_p C_h (\theta_s' - \theta_0), \quad (18)$$

respectively. The variable  $q_s^*$  is the saturation specific humidity for the fictitious surface temperature  $\theta_s'$ . This fictitious surface temperature is used

to temporarily evaluate the momentum exchange coefficient ( $C_m$ ).

*e. Boundary layer clouds*

Fractional cloud cover (CLC) is formulated according to Slingo (1980) as

$$CLC = \left( \frac{RH - RH_{crit}}{1 - RH_{crit}} \right)^c, \quad (19)$$

where  $RH_{crit}$  is the critical relative humidity for cloud formation and  $c$  is an empirically derived constant (assumed 2.0) based on experimental data. For the stable case,  $RH$  is taken to be the maximum relative humidity in the lowest 2000 m of the model, and  $RH_{crit}$  is prescribed to be 0.8. For the unstable case, the fractional cloud cover is the maximum that occurs from (19) with  $RH_{crit}$  set to 0.7 or 0.8. The temperature and mixing ratio from the lowest model level are used for computing the lifting condensation level (LCL). The maximum of the two methods ensures a smooth transition between stable and unstable regimes with no large jumps in cloud cover. This also allows for stratiform or cumuliform boundary layer clouds.

*f. Radiation*

Incoming clear sky solar radiation ( $S\downarrow$ ) is given by Kasten and Czeplak, (1980) as

$$S\downarrow = S\downarrow [1 - (1 - \tau) CLC^n] (1 - \alpha), \quad (20)$$

where  $S\downarrow$  is reduced by solar elevation angle and boundary layer clouds ( $n$  is



an experimentally derived exponent set to 1; Ek and Mahrt, 1989), and the transmission function ( $\tau$ ) is parameterized according to Liou (1976) for shallow boundary layer cumulus clouds as

$$\tau = 0.06 + 0.17 \cos \theta , \quad (21)$$

where  $\theta$  is the solar elevation angle ( $0^\circ$  overhead and  $90^\circ$  at the horizon). In this simple approximation cloud thickness and liquid water content are not treated.

Downwelling long wave radiation from the atmosphere is formulated according to Satterlund (1979) as

$$L\downarrow = \varepsilon \sigma T_{\text{ref}}^4 + c2 \cdot \text{CLC} , \quad (22)$$

where  $\varepsilon$  is atmospheric emissivity (a function of the temperature and the moisture at the reference model level of 2000 m; Satterlund, 1979),  $\sigma$  is the Stefan-Boltzmann constant,  $T_{\text{ref}}$  is the atmospheric reference temperature at model level 200 m, and  $c2$  is an experimentally-derived constant ( $60 \text{ W m}^{-2}$ ; Paltridge and Platt, 1976).

g. *Shelter air temperature*

The two meter (shelter) air temperature is calculated according to Holtslag and de Bruijn (1988) as

$$T_2 - T_1 = \frac{\theta^*}{k} \left[ \ln \left( \frac{z_2}{z_1} \right) - \psi_H \left( \frac{z_2}{L} \right) + \psi_H \left( \frac{z_1}{L} \right) \right] - \Gamma_d(z_2 - z_1) , \quad (23)$$

where  $T_2 - T_1$  is the temperature difference between two levels  $z_2$  and  $z_1$ ,  $k$  is

the von Kármán constant,  $\Gamma_d$  is the dry adiabatic lapse rate,  $\psi_H$  is the stability function for heat, which is a function of  $z$  and the Monin-Obukhov length scale  $L$ , as

$$L = \frac{u_*^2}{k \frac{g}{T} \theta_*} . \quad (24)$$

In (24),  $g$  is gravitational acceleration,  $T$  is air temperature, and  $\theta_*$  is the turbulent temperature scale obtained from

$$H = - \rho c_p u_* \theta_* , \quad (25)$$

where  $\rho c_p$  is the volumetric heat capacity of air at constant pressure and  $u_*$  is the friction velocity. Once the temperature difference is known between two levels, it is a simple matter to find the two meter temperature.

#### *h. Model initialization and use*

Input data needed by the model are a vertical sounding of temperature, mixing ratio, winds and synoptic scale vertical velocity. A detailed sounding from Redstone Arsenal, Alabama was used for this study. For the background synoptic scale vertical velocity, the kinematic method (Holton, 1979) was employed with the 1200 UTC 18 August 1988 soundings from Athens, Georgia, Nashville, Tennessee and Centreville, Alabama. The Bellamy (1949) triangulation method was employed to estimate the synoptic scale divergence. A typical value of vertical velocity above the PBL was  $0.2 \mu\text{b s}^{-1}$  downward.

Several other model parameters must be specified via an input control file. Relevant parameters are discussed in the context of results in chapter 4. Values were estimated from various data sources. The shading factor,  $\sigma_f$ , used in the PBL model was estimated by calculating the vegetation fraction (Chang and Wetzel, 1988) from atmospheric corrected (Lacis and Hansen, 1974) MAMS NDVI data (see discussion in chapter 3 (27)). Another parameter estimated from MAMS is the root zone (upper 5 cm) soil moisture. Soil moisture profiles may be initially specified with up to 10 layers in a 1 meter depth of soil. Techniques for doing this are given in the next chapter.

The albedo was estimated from published values of mean August values (Brest and Goward, 1987) based on four land use classifications: farm ( $\alpha=0.165$ ), suburb ( $\alpha=0.139$ ), city ( $\alpha=0.122$ ), and forest ( $\alpha=0.166$ ).

The aerodynamic roughness length was estimated as a function of the variance in topography (Lettau, 1969). One kilometer resolution topography data from the United States Geological Survey were used. In flat areas where topography was not a significant factor, published values based on land use (Stull, 1988) were employed. Details of this procedure appear in chapter 3.

Soil type was estimated from soil maps (Depts. of Agriculture in Tennessee, Alabama, and Mississippi).

### 3. Data and methodology

#### *a. Data sources*

The region of study is primarily northern Alabama and southern Tennessee. The study date is 18 August 1988. Figure 2 shows the MAMS flight tracks and overpass times. The MAMS flight began with west to east flight leg one over the Tennessee-Alabama border starting at 1441 UTC, then proceeded southward in a zig-zag fashion (legs two and three; Fig. 2a). Flight leg four picks up in Fig. 2b and tracks east to west starting around 1555 UTC. Flight leg six was last, ending around 1700 UTC.

Upper air and surface data for the case study were obtained and processed using the General Meteorological Package (GEMPAK; NASA, 1988) software which operates on the Florida State University Department of Meteorology's Vax and Sun computers. In addition to standard hourly surface data, National Weather Service (NWS) cooperative observer data and Tennessee Valley Authority rain gauge data were used. Each of the NWS coop sites logs daily precipitation amounts. No rain was observed at any of

the sites (Fig. 1) on 18 August. Two sites noted small amounts (less than 0.25 in (6.4 mm)) on 17 August. In the two cases where amounts were missing, a standard estimation technique based on surrounding station data and normals was used (Linsley *et al.*, 1982). In situ maximum and minimum soil temperature data for various depths and two surface types (bare soil and sod covered) were obtained at 15 sites from the University of Tennessee and from NWS cooperative observers in Mississippi and Alabama.

Most of the visible and IR imagery used in this study were taken from the MAMS instrument (see Table 1) flown aboard NASA's ER2 research aircraft at an altitude of 20 km and nominal airspeed of around 200 m s<sup>-1</sup>. Some of this imagery will be presented in the next chapter. The MAMS imagery calibration was corrected using a running 100 pixel moving average to smooth digital IR count values in channels 11 and 12 (11.1 and 12.7  $\mu\text{m}$ , respectively). Additionally, GOES 1 km visible loops were also used in conjunction with the MAMS data to observe cloud fractions over most of the sites shown in Fig. 1. Seven locations (marked with asterisks in Fig. 1) were cirrus contaminated such that LST and NDVI could not be calculated on the first pass. All of the imagery was visualized with the PC McIDAS (Man-computer Interactive Data Analysis System).

Several parameters needed for the PBL runs were calculated from the MAMS data as part of this study. The methodology for these calculations is described in the following paragraphs.

### 1. Vegetation index - NDVI

The Normalized Difference Vegetative Index (NDVI) is needed for two reasons. First, to compare with the LST on a pixel by pixel basis to estimate soil water availability, and second, to estimate the vegetation fraction required for the PBL model runs. Both of these techniques are described below.

Two of the eight MAMS visible channels were used to diagnose NDVI (Jedlovec and Atkinson, 1992) according to the expression:

$$\text{NDVI} = \frac{R_7 - R_5}{R_7 + R_5}, \quad (26)$$

where  $R$  is the radiance ( $\text{W m}^{-2} \mu\text{m}^{-1}$ ) and the subscripts indicate the MAMS channel number (see Table 1). The denominator in the above expression normalizes the channel differences for various scene illuminations. The NDVI has been shown to be well correlated with exposed green leaf area due to the differential absorption by chlorophyll between near-IR and visible (specifically, red) wavelengths (e.g., Tucker, 1979; Sellers, 1985; Asrar *et al.*, 1984). Chlorophyll strongly absorbs in the visible (red) and strongly reflects in the near - IR part of the spectrum. The form of the NDVI given in (26) was used in conjunction with LST for the NDVI / LST slope soil moisture technique discussed in section 3c below.

One of the parameters needed for the boundary layer model runs is the shading factor for vegetation cover. This can be calculated from the NDVI. "Synthesized" AVHRR (Advanced Very High Resolution Radiometer) atmospheric-corrected NDVIs were calculated to estimate this approximate vegetation fraction (Chang and Wetzell, 1988). This "synthesized" NDVI was

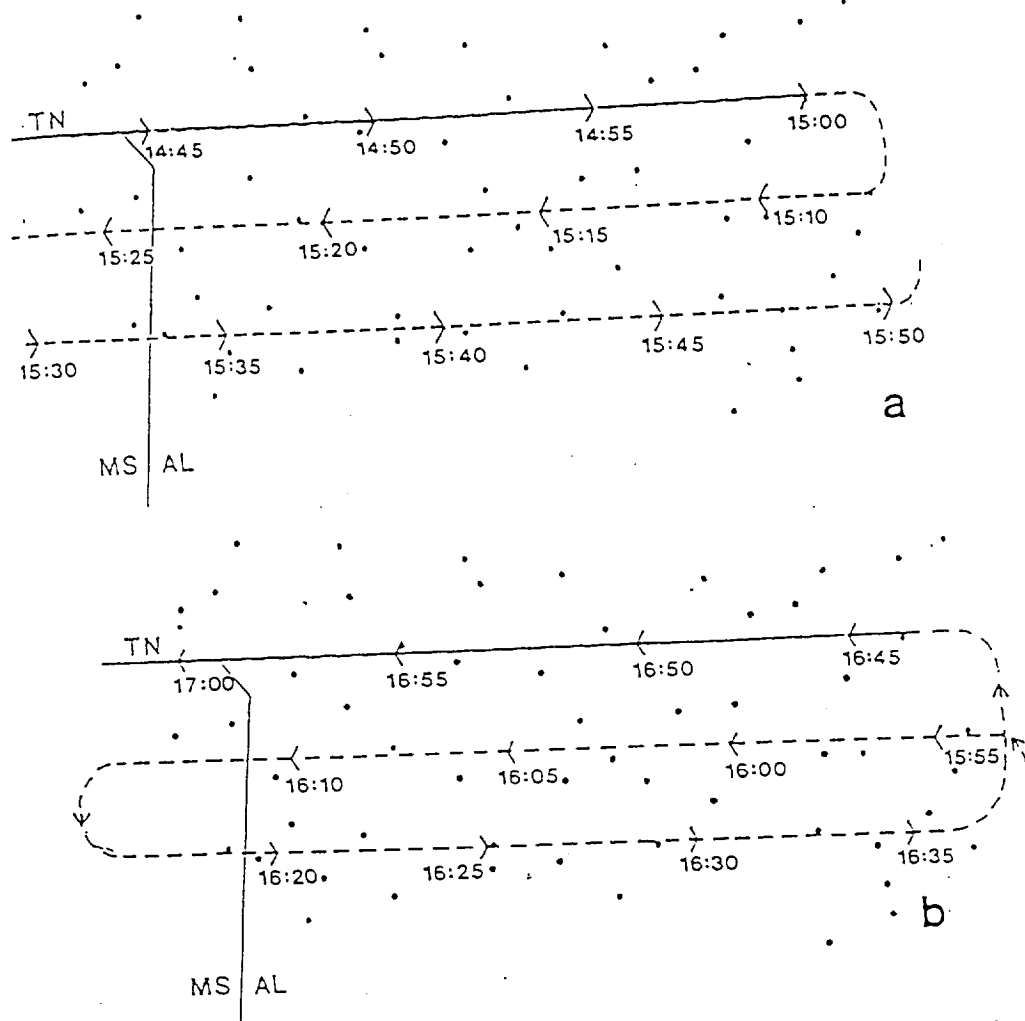


Fig. 2. Flight tracks of the NASA U2 high altitude research aircraft on which the MAMS instrument was flown. First pass (a) from 1441 to 1550 UTC; second pass (b) flown from 1555 to 1700 UTC on 18 August 1988.

calculated by adding three MAMS channels (3-5) to approximate AVHRR channel 1 (analogous to channel 5 in (26)), and MAMS channels 7 and 8 to approximate AVHRR channel 2 (analogous to channel 7 in (26)) used in the standard AVHRR calculation of NDVI. Typical values of the synthesized NDVI were around 0.51. This value corresponds to a mean value of 0.36 calculated directly from MAMS data using (26). The vegetation fraction,  $\sigma_f$  was computed as an estimate of the shading factor according to (Chang and Wetzel, 1988)

$$\sigma_f = \begin{cases} 1.5 (\text{NDVI} - 0.1) & \text{NDVI} \leq 0.547 \\ 3.2(\text{NDVI}) - 1.08 & \text{NDVI} > 0.547 \end{cases}, \quad (27)$$

where the MAMS "synthesized" AVHRR NDVI was used. Typical computed values of vegetation fractions were near 60%.

Archived maps of soil type and land use were compared with the MAMS-derived NDVIs and corresponding vegetation fraction. Results of the vegetation fraction calculation compared favorably to land use maps over the area. Land use is principally agricultural and forested with a few small urban areas. Huntsville, Alabama is the largest urban area with a population of about 150,000. Soil type over the region varies from predominantly sandy soils along the Tennessee River basin to soils with high clay content in other locations. Land use is basically one of three types: agricultural, forested, and, to a minor extent, urban. There are a few small areas of significant bare soil.

The near infrared radiances used to compute NDVI values were corrected for atmospheric attenuation according to Lacis and Hansen (1974).



This required an estimate of precipitable water.

## 2. *Precipitable water. (PW)*

A statistical relationship for estimating PW over the study area was derived using RAOB soundings. Summer soundings from 1988 were chosen at nearby locations to get a variety of humidity distributions representative of the region. Simulated MAMS channel 11 and 12 transmittances were calculated by inputting the RAOB soundings into an appropriate transmittance code (McMillin *et al.*, 1979). Ratios of squared channel 11 to channel 12 transmittances were then regressed to the precipitable water values. Jedlovec (1990) has shown that the ratio of the variances of the channel 11 to channel 12 brightness temperatures in a scene is a good approximation to the ratio of the transmittances in the respective channels. This technique is referred to as the “split-window variance ratio” (SWVR) method (Jedlovec, 1987,1990).

Figure 3 shows the relationship between values of the split-window variance ratio and precipitable water for the current case. A complete error analysis of this procedure appears in Knabb (1993), who has shown that such PW values are accurate to within 6 to 7 mm in an absolute sense on a per retrieval basis. The PW regression equation obtained for this study was:

$$PW \text{ (mm)} = - 41.55 [\ln (\text{SWVR})] - 5.43 \quad , \quad (28)$$

where SWVR is the ratio of the variances of 11.1 to 12.7  $\mu\text{m}$  brightness temperatures across a 37 x 37 pixel (4 x 4 km) template. The standard error of the regression procedure was just over 2 mm, the squared correlation

coefficient ( $R^2$ ) was 0.94, and the mean computed value of PW for the first MAMS flight (1441 to 1550 UTC) was 42 mm. The mean PW value for the second pass (1555 to 1700 UTC) was found to be 36 mm. For comparison purposes, the 1200 UTC rawinsonde-derived value of PW from the Redstone Arsenal sounding was computed to be 31 mm. These differences between RAOB and MAMS - derived PW are reasonable in light of previous studies that have shown significant mesoscale PW gradients (Knabb, 1993; Hoepner and Fuelberg, 1992; Guillory *et al.*, 1992; Jedlovec, 1990). For example, Jedlovec (1987) showed that PW gradients of 5 to 8 mm over tens of kilometers were common.

### 3. *Land surface temperature (LST)*

LSTs were generated from a statistical regression equation developed from forward radiative transfer code (McMillin *et al.*, 1979) in a manner similar to that of the PW equation (28). Using representative RAOB soundings in the area, various values of the skin temperature were input to the forward code to generate MAMS channel 11 and 12 brightness temperatures. The regression equation developed was

$$LST(K) = 28.913 + 0.905 T_{bb11} + 1.192 (T_{bb11} - T_{bb12}) \quad , \quad (29)$$

where the subscripts indicate the MAMS channel number (Table 1). An  $R^2$  value of 0.96 for zenith angles from 0 to 35° was found between input sounding LST and calculated values from (29). Note that scan angle influences are corrected for in this equation. It is believed that scan angle was

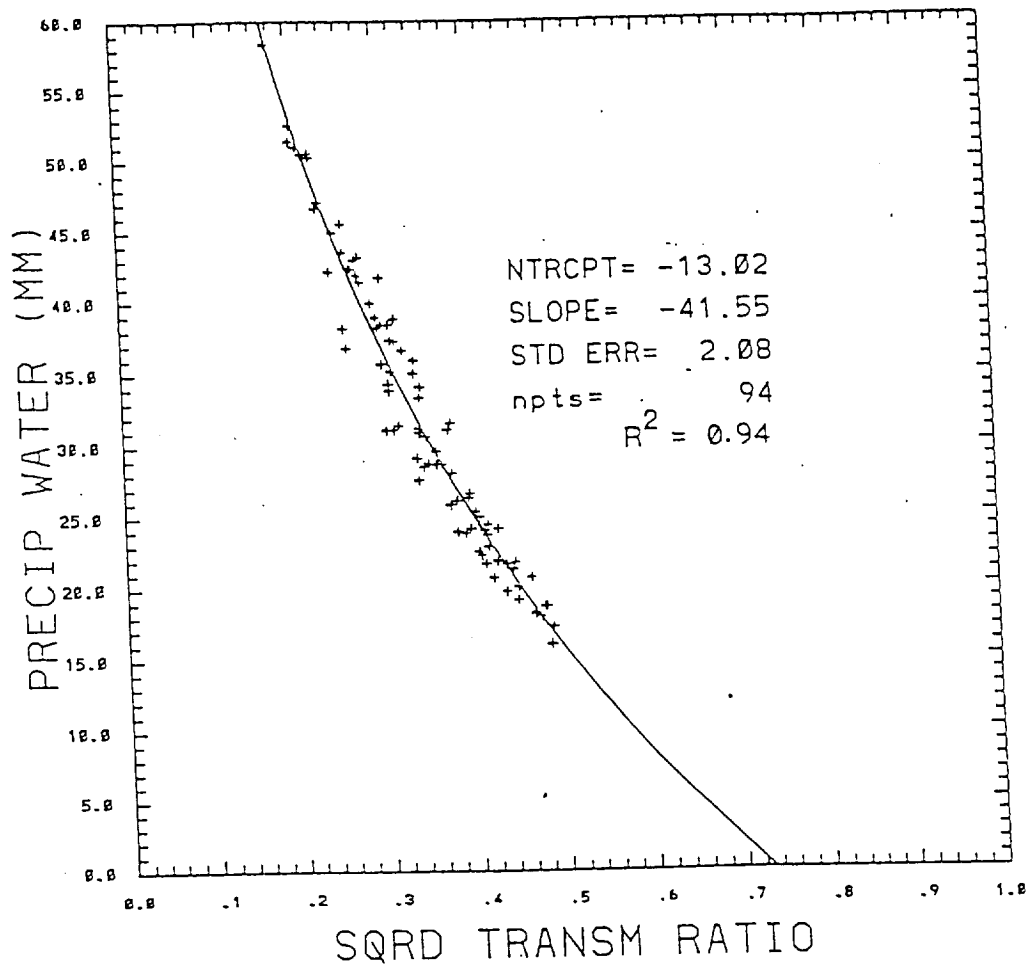


Fig. 3. Regression fit between MAMS split-window variance ratio and precipitable water. Data were from summer soundings during 1988 (see text for equation).

not a factor when LST changes were computed, since viewing geometry was similar during both overpass times. LSTs in this study were generally 2 to 3° C warmer than in Jedlovec and Atkinson (1992), i.e., their equation produced LSTs about 2 to 3° C cooler than with (29) for the same input raw data. This arises because an emissivity of 0.96 was assumed in the current study instead of 1.00. Previous work with calculated MAMS sea surface temperatures showed a high degree of accuracy (within 1° C; Moeller *et al.*, 1989). These investigators derived an LST equation similar to that used in this study. A comparison of MAMS LSTs with in situ soil temperatures appears in the next chapter.

*b. Roughness length*

Topographic data were used to estimate surface roughness (Lettau, 1969) for input to the PBL model. High resolution (1 km) United States Geological Survey topography data were imaged on PC McIDAS. Originally, the topographic data were at 3 arcsecond resolution; the data were then reduced to 1 km intervals. Lettau's (1969) technique estimates the roughness parameter from the variance of the elevation, the number of roughness elements in an area (with each element having the same assumed basic conical shape), and the cross-sectional area of each element (assumed as a function of the base and height of the roughness elements). This technique has been used in other studies (e.g., Stage, 1991, personal communication). When the terrain exhibited no significant variance of roughness elements, published values of surface roughness based on land use were employed (Stull, 1988).

An image of the terrain data appears in chapter 4.

*c. Soil moisture*

Volumetric soil moisture in a 1 m soil layer is a necessary input to the PBL model. The user may specify up to 10 levels in the 1 m soil layer. This section describes several methods that were used to estimate soil moisture. The first is a modeled retention index technique, which has been used as “ground truth” in the literature (e.g., Wetzels and Woodward, 1987; Heymsfield and Fulton, 1992). *Although modeled indexed techniques have been frequently used as “ground truth” in the literature, most of these studies considered relatively flat terrain. In the current case, however, the terrain is anything but flat. Thus, the ARI is referred to as “ground truth” solely for consistency with the literature. An intercomparison of this and two other soil moisture estimators will be the major thrust of this study, and it will become apparent that the ARI is not necessarily the best choice for “ground truth” over complex terrain. This comparison is based on how well each soil moisture model, when input to a PBL model, predicts parameters such as LST, temporal changes in LST, mixed layer (ML) height, and cloud cover. Additionally, the results are compared to earlier work utilizing in situ soil moisture and soil temperature data.*

The second technique is the MAMS / PBL-regression procedure where separate regression equations over each site were developed to estimate root zone soil moisture from PBL modeled changes in LST. The third procedure is the NDVI / LST slope method where scatter plots of LST vs. NDVI were

used to compute slopes of the fitted least squares regression line over each of the sites.

1. The antecedent retention index (ARI)

The first method (denoted "EvapARI") uses a modified antecedent retention index (ARI; see Saxton and Lenz, 1967) for the top soil layer (0 to 5 cm) according to

$$ARI(i)_{top} = [ARI(i-1)_{top} + c_i \cdot precip(i-1)] \cdot k_{top} - Evap(i-1), \quad (30)$$

where the subscript  $i$  is the day number;  $c_i$  is the canopy interception factor (assumed constant at 0.85; see Linsley *et al.*, 1982);  $precip$  is the precipitation amount;  $k_{top}$  is the retention factor for the top layer (0.92); and  $Evap$  is the evaporation function that is modeled following Brutsaert (1982) as

$$Evap(i) = panEvap(i) \cdot F, \quad (31)$$

where

$$F = \max \cdot \left[ 1 - \exp\left(\frac{-b \cdot wsoil(i-1)_{top}}{\maxwet}\right) \right]. \quad (32)$$

The author is unaware of any previous studies which included actual pan evaporation as part of the ARI calculation. Most studies assume a  $k$  value (which varies from 0.85 to 0.95) with constant (or no explicit) evaporation and no canopy interception factor. In (31),  $panEvap$  is the measured pan evaporation data at the Huntsville, Alabama NWS office. The function  $F$  is a

soil evaporation reduction function that acts as a filter to reduce the evaporation from the soil as the soil moisture is depleted. The function  $F$  is graphed against the ratio in the exponential argument in Fig. 4.  $Max$  is the maximum allowable percentage of evaporation from the soil based on experimental pan data (Brutsaert, 1982) and was estimated to be 0.8. This means physically that for saturated soil, the most that can be evaporated from the top layer is 80% of the measured pan evaporation value. In the exponential argument of (32),  $b$  is an empirically-derived constant equal to 10.6.  $Maxwet$  is the saturation point of the soil that varies according to soil type (Linsley, 1982); a typical value is about 0.4.  $W_{soil_{top}}$  is the volumetric soil moisture calculated from the ARI according to

$$W_{soil_{top}} = ARI_{top} \cdot maxwet . \quad (33)$$

The ARI was never allowed to exceed 1.0 (any precipitation in excess of 2.00 inches (51 mm) was assumed runoff); the ARI was set to 1.0 if two inches or more rainfall occurred during a 24 h period. Evaporation and gravitational drainage completely stop when the wilting point (also a function of the soil type) is reached; i.e., the soil moisture stays at the wilting point until rain occurs. For the top layer, the soil moisture was allowed to go as low as 0.001 based on experimental data for the uppermost 5 cm layer (Carlson et al., 1990). The soil water availability,  $f_{top}$ , was taken to be the soil moisture divided by the maximum available or

$$f_{top} = \frac{\text{Actual moisture}}{\text{Maxwet}} . \quad (34)$$

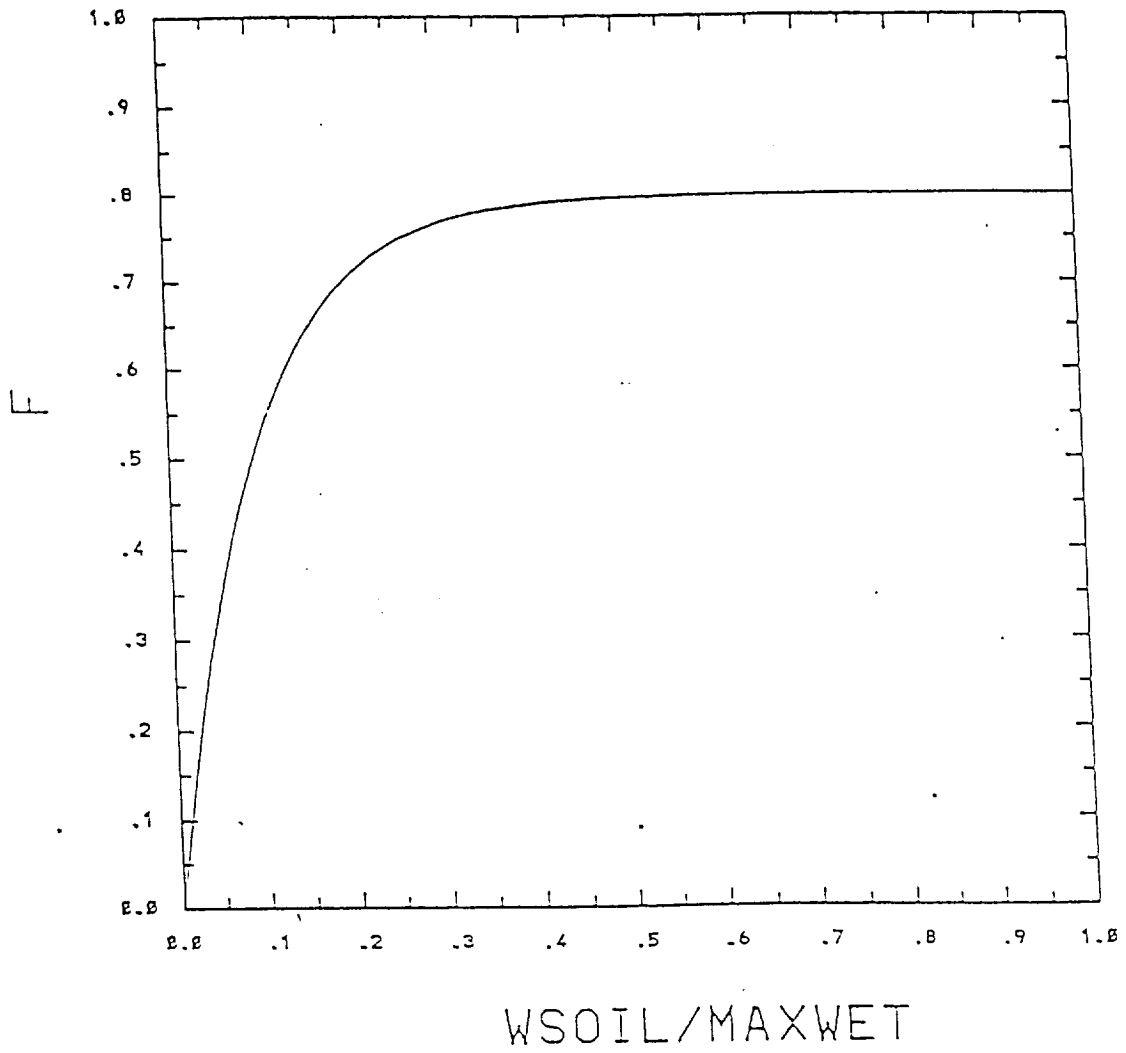


Fig. 4. Behavior of the evaporation reduction function,  $F$ , in the evapotranspiration term for the ARI calculation (see text for equation).



The ARI for the bottom layer (25 cm) was modeled as

$$\text{ARI}(i)_{\text{bot}} = (1 - k_{\text{top}}) \cdot \text{ARI}(i - 1)_{\text{top}} + \text{ARI}(i - 1)_{\text{bot}} \cdot k_{\text{bot}} \quad , \quad (35)$$

where  $k_{\text{top}}$  and  $k_{\text{bot}}$  were set to 0.92. These constants parameterize the effects of gravitational drainage and root uptake in the layers. The 25 cm level was chosen based on typical wetting front speeds through a soil typical of the study region (Dunne and Leopold, 1978). Notice that evaporation does not reduce the bottom layer moisture and that upward diffusion is not treated. Again, soil moisture approaches a constant as the bottom layer moisture approaches the deep soil wilting point (a function of each soil type, but typically around 0.12). The wilting point occurs when evapotranspiration completely stops. Initially, the 0th day ( $i=0$ ) is taken as the day when the soil is assumed saturated at maxwet; usually this occurs after a series of heavy rain days. Both top and bottom layers are assumed to be saturated at day 0. Figure 5a shows typical plots of ARI-derived soil moisture. Notice that the top layer shows much greater temporal variability than the bottom, and that the amplitude of the bottom layer values lags the top by two to three days.

The above mentioned EvapARI technique was compared to a simpler model (“NoEvapARI”) in which only depletion ( $k_{\text{top}} = k_{\text{bot}} = 0.92$ ) and canopy interception factor (= 0.85; top layer only) were used for the top (5 cm) and bottom (25 cm) levels; no explicit evaporation data were employed. The depletion coefficients,  $k_{\text{top}}$  and  $k_{\text{bot}}$ , vary from 0.85 to 0.95 (Linsley *et al.*, 1982) in the literature, and some do not use a canopy interception factor

(e.g., Borland, 1990). Figure 5b shows results of the simpler ARI model calculation for the same two locations in Fig. 5a. Notice how the top and bottom layer remain moister for the simpler model, and notice the difference in dry down rates for the top layers. The top layer dries out much faster for the EvapARI case than for the NoEvapARI case.

Both versions of the final ARI model results for day 231 (18 August) at all 55 sites were fitted to a  $1/7$  power profile to estimate soil water content at the intermediate levels between the 5.0 cm and 25 cm depths. The equation is given by

$$\Theta = c \cdot [1.0 - \exp(Y)]^{1/7} + b, \quad (36)$$

where the constants  $c$  and  $b$  for each site were based on the soil moisture at 5 and 25 cm ( $Y$  in negative cm). These vertical profiles of soil moisture were chosen to represent profiles from typical field data (Carlson *et al.*, 1990) during a long dry period. Examples of the mean and extremes of these fitted profiles will be shown in the next chapter. Both ARI models (EvapARI and NoEvapARI) also will be compared in the next chapter. The choice for ground truth was based on soil temperature comparisons (see chapter 4) between PBL-modeled LST (with each respective input soil moisture model) and observed LST.

## 2. MAMS / PBL model regressed soil moisture

This technique utilizes observed LST differences (normalized from 10 AM to noon) between the first and second MAMS overflights at each precipitation site. The normalization was a simple linear extrapolation of the

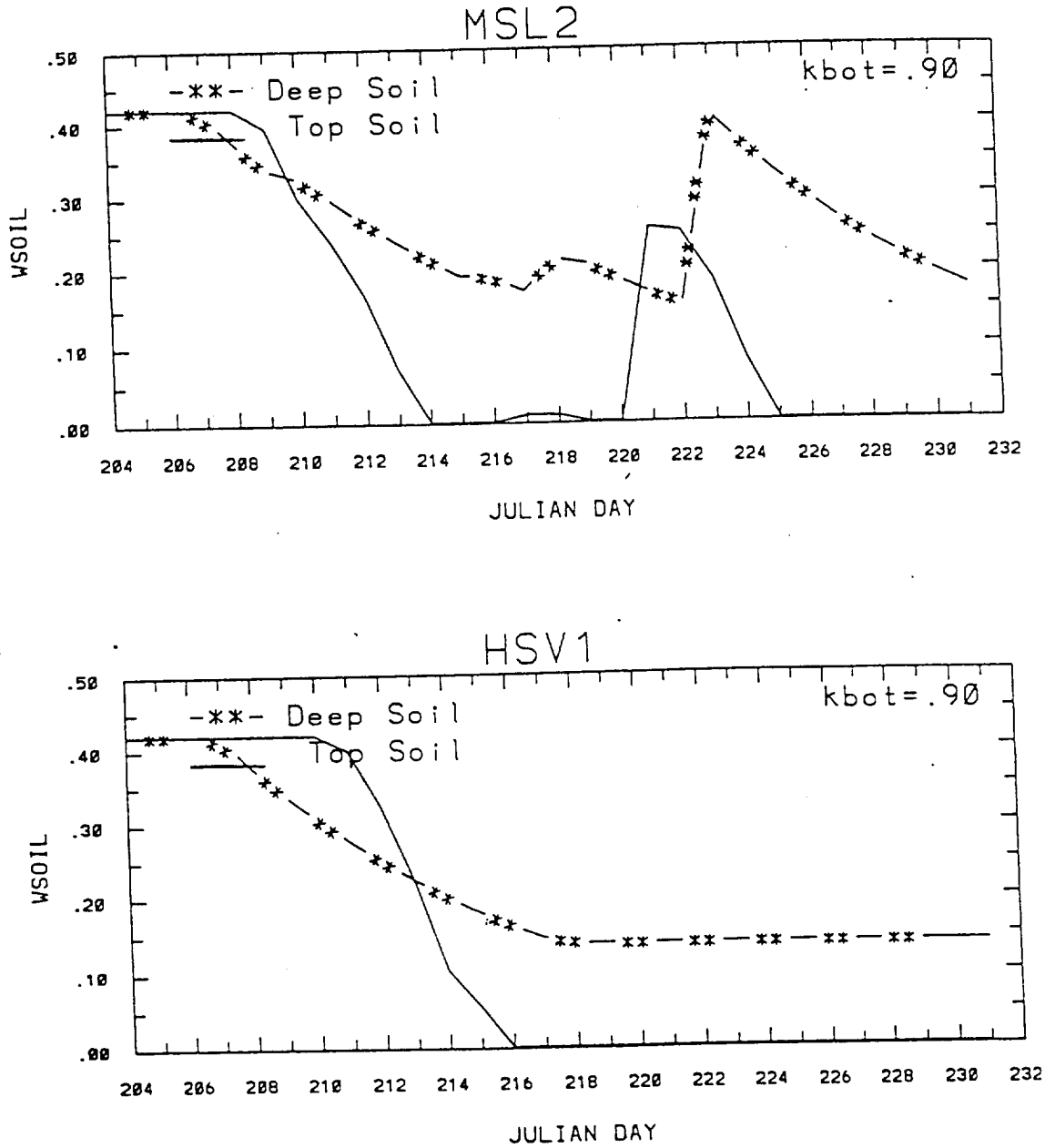


Fig. 5a. Examples of ARI calculations for the EvapARI model (with explicit evaporation included).

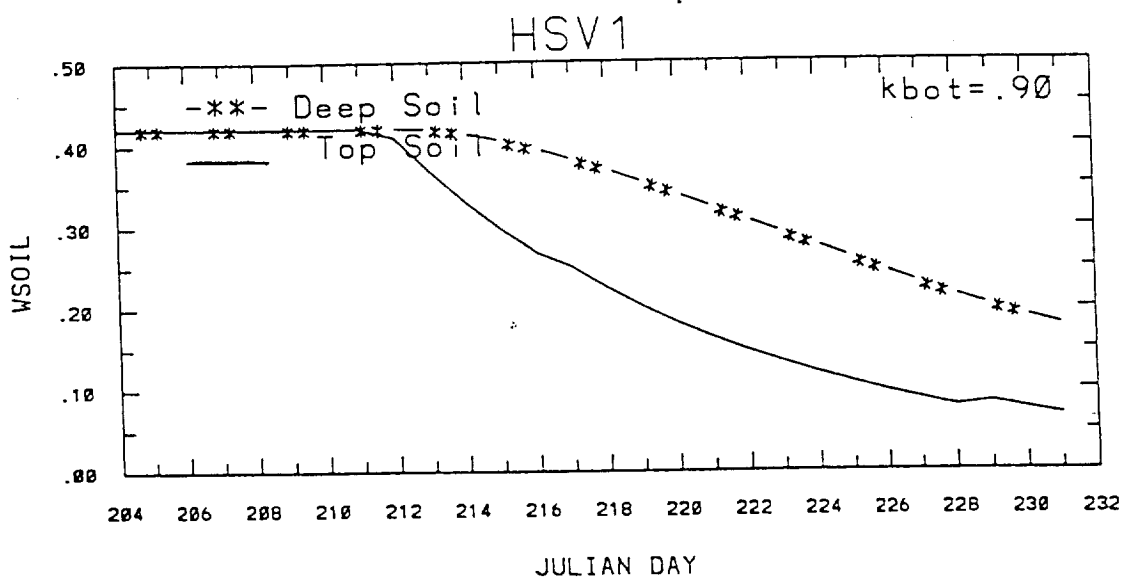
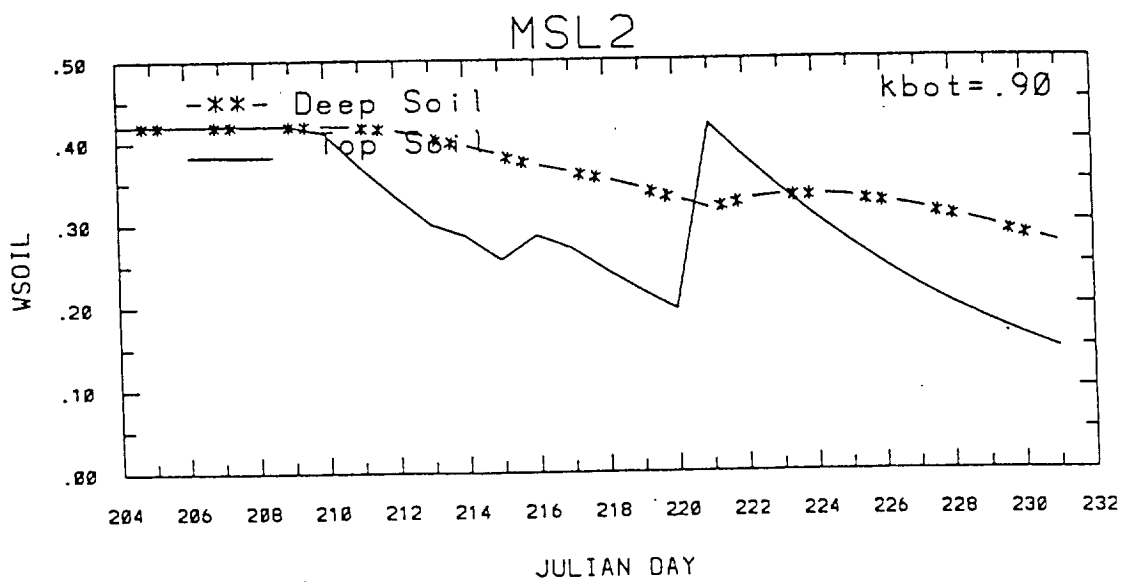


Fig. 5b. Same as Fig. 5a, but for ARI without evaporation term for the same two sites.

slope of the temperature change observed between the two MAMS overpasses. As stated earlier, some locations were cirrus contaminated during one or both passes such that LSTs could not be calculated. Accurate LST differences required utmost care in navigating the MAMS images. This was done using landmark identification in order to correct for navigation drift of the aircraft.

The physical reasoning behind this technique is that for moist soil there will be a smaller temperature change than for dry soil. Alternatively stated, there is greater thermal inertia (a strong function of soil moisture) for dry soil because more solar energy goes into heating the soil instead of evaporating soil moisture and cooling the soil (Schmugge, 1978). A separate regression equation was developed for each site taking into account soil type, vegetation fraction, and surface roughness (estimated from the topography data). A flow chart of this procedure appears in Appendix A. Volumetric soil moisture values for a two layer (0 to 5 cm and 5 to 1 m) soil model in the overall PBL model were varied from 0.001 to 0.30 in increments of 0.01. Resulting LSTs from the PBL model at 10 AM and noon were used to estimate the slope of the LST temperature change for each site. Thus, with the regression relationship established, one can estimate soil moisture in approximately the upper 5 cm based on the MAMS observed LST differences (normalized from 10 AM to noon) from pass 1 to pass 2. Normalized LST changes ranged from  $0.5^{\circ} \text{C h}^{-1}$  to  $5.6 \text{ C h}^{-1}$ . A typical regression plot is shown for one of the sites in Fig. 6. Correlation coefficients (R values) generally were between 0.7 and 0.95. One should note the discontinuity that occurs near the soil moisture

value of 0.20. This is the value where potential evaporation begins in the PBL model; it will be discussed further in the next chapter. This technique is compared with the others in the next chapter.

### 3. NDVI / LST slope method

This technique for estimating soil moisture utilizes the relationship between the NDVI and LST at each pixel. The physical reasoning is that the slope of the fitted line (assuming a reasonable fit to the scatter plot) is related to the soil water availability parameter. Figure 7 shows an example of a typical plot, along with a line fitted to the data. Correlation values were generally between 0.6 to 0.8 for those sites where cloud or cloud shaded contamination was not a problem. This technique has been used over forested regions with limited success in previous studies (Running and Nemani, 1989). The steeper the slope of the fitted line, the less soil water is available for evapotranspiration.

#### *d. Mixing layer height estimation from MAMS*

A cloud shadow technique was employed to estimate mixing layer heights from the height of the cloud base above ground. This was done to assess the performance of the PBL model's mixing layer growth rate and to study the effect of varying soil wetness on PBL height. To the author's knowledge, this procedure has not been utilized previously. Several parameters from the visible imagery were required for this calculation: the time of the overpass, the cloud latitude and longitude, and the secant squared

corrected (for off nadir viewing angles) horizontal distance from the edge of the cloud to the edge of the shadow. Solar elevation angles were calculated at each location (Stull, 1988), and mixing layer heights were computed from the tangent of the elevation angle and the distance from the corrected cloud edge to the shadow edge. This technique assumes that the top of the mixed layer corresponds to the height of the cloud base; in reality, the cloud base may be higher than the mixing layer due to convective overshoot. The results of this method along with a complete error analysis will be given in the next chapter.

*e. Cloud fraction estimation from MAMS*

Cloud fractions were estimated by counting pixels above a threshold brightness value in the visible imagery. These observed cloud fractions were compared to model output cloud fractions at each time in order to assess the accuracy of the model over complex terrain. Cloud fractions were estimated from MAMS as well as GOES imagery. Results of these comparisons appear in the following chapter.

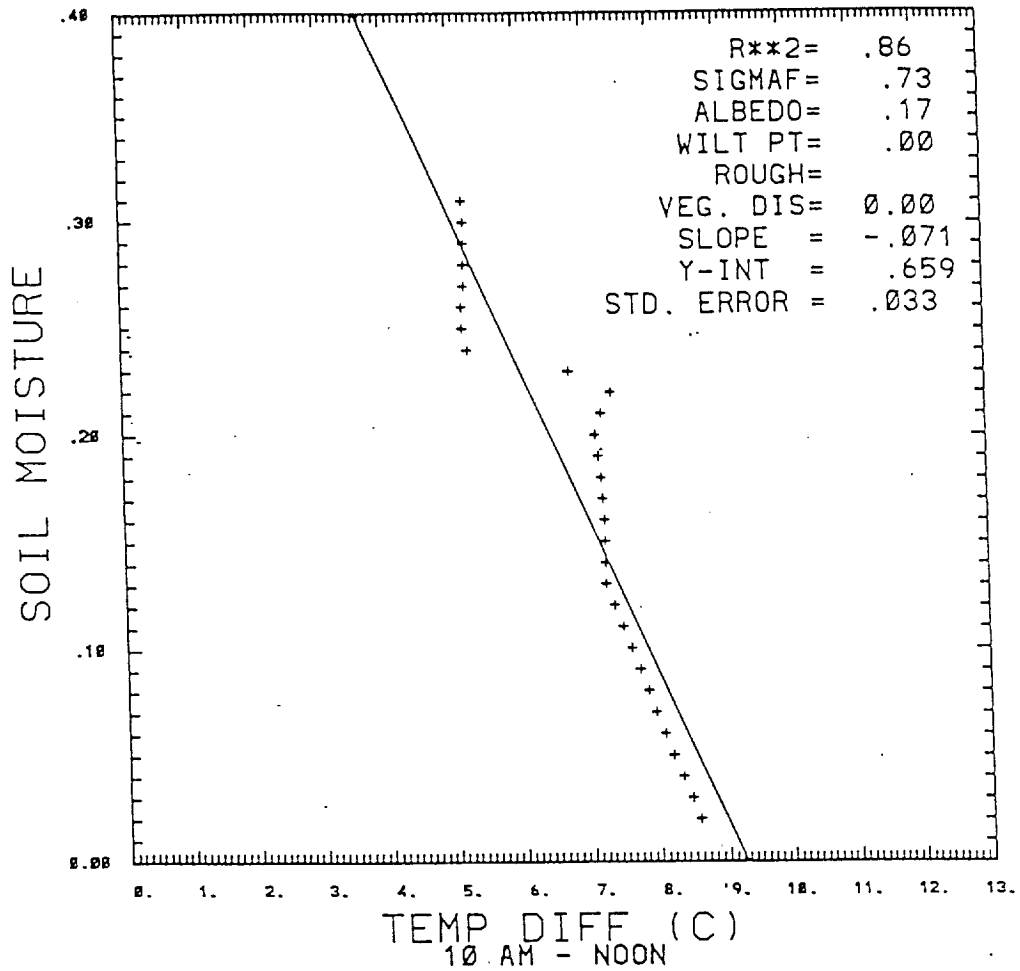


Fig. 6. Example of regression calculation from PBL modeled LST difference from 10 AM to noon local time. Separate regressions were done at each location where MAMS surface temperature changes were observed. Note the discontinuity around 0.20 soil moisture value (see text).



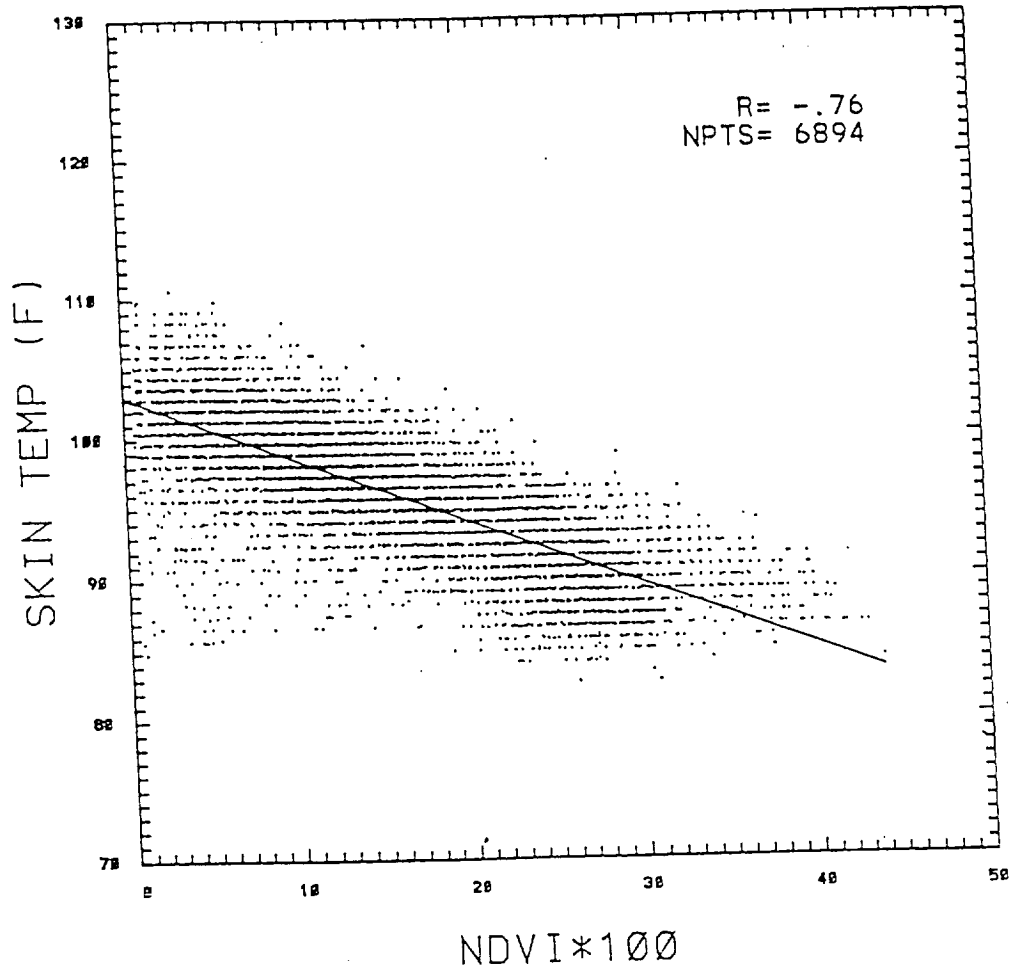


Fig. 7. Example of a typical scatter plot between NDVI and LST over a 5 x 5 km region in the study area. More examples are given in chapter 4.

## 4. Results

### *a. Selection of the best ARI "ground truth"*

The selection of the best "ground truth" ARI model was based primarily on how well maximum soil temperatures were predicted by the PBL model with the different types of ARI input. The reason for denoting the ARI as "ground truth" is that, barring in situ observations, indexed approaches to estimating soil moisture typically have been used as ground truth in the literature (e.g., Wetzal and Woodward, 1987; Heymsfield and Fulton, 1992). These studies were done over flat terrain. *My research indicates that the ARI apparently does not yield the best ground truth over complex terrain.* The question here is, if no in situ soil moisture observations are available, which modeled / parameterized approach is best over complex terrain? The results of this study will be compared to those of previous in situ soil moisture investigations.

Figure 8 shows average observed in situ maximum soil temperatures at various depths from fifteen locations near the study area. Most of the locations were in southern Tennessee and northeastern Mississippi; only one site (SAN; see Fig. 1) was actually in the MAMS study region. These stations recorded temperatures at various depths, not all of which were the same. The most common recording depth was  $-0.1$  m. Some stations reported soil temperatures below bare soil, some below sod, and some under both types of surfaces. Notice that the sod covered temperature composite is considerably cooler ( $4.5$  to  $5.0^{\circ}$  C) than the bare soil composite at the  $-0.1$  m depth. Soil temperatures at  $-0.1$  m have a standard deviation of  $2^{\circ}$  C for bare soil and  $1.5^{\circ}$  C for sod covered soil. Temperatures warm much faster upward toward the surface for bare soil than for sod covered soil. The range of temperatures at the  $-0.02$  m depth for bare soil was  $42.8^{\circ}$  to  $43.9^{\circ}$  C. The author would have preferred to have soil temperatures at every depth at each of the sites, but these data were not available.

The observed maximum soil temperatures (Fig. 8) were compared to PBL model forecast maximum temperatures generated using two different ARI-derived average soil moisture profiles (Figs. 9 and 10). The ARI soil moisture modeling procedure was outlined in chapter 3. Chapter 3 showed examples of both EvapARI and NoEvapARI model behavior for two of the sites in the study area. The ARI values were calculated at two depths, 5 cm and 25 cm, and the assumed soil moisture profile function (36) was then fit to these levels at each site (also described in chapter 3). Figure 9 was generated by averaging the soil moisture data from the model having no evaporation

physics (hereafter referred to as “NoEvapARI”) at 10 levels for the 55 sites in the study region (see Fig. 1). Figure 10 was computed in a similar manner, but with data from the “EvapARI” model (with explicit evaporation included). Recall from chapter 3 that the major difference between these two soil moisture models was the use of explicitly parameterized evaporation in “EvapARI”, and no explicit evaporation in “NoEvapARI”.

One should note that the major contrast between the two soil water profiles (Figs. 9 and 10) is that the average EvapARI profile moistens considerably slower with depth than the one from NoEvapARI. This is expected with the explicit use of evaporation. For example, at the -0.1 m depth, the EvapARI model yields a mean volumetric moisture value of about 0.1, while the NoEvapARI model produces 0.25; i.e., the no evaporation version is about two and one-half times wetter! Recall that the pan evaporation data used in the EvapARI calculations were taken at the Huntsville, AL WSO and assumed for all precipitation sites. It would have been desirable to have evaporation data at each site, but this was not possible. Previous work (Brutsaert, 1982) has shown that many local factors such as cloud cover, soil conditions, vegetation type and density, and winds, can influence actual evapotranspiration rates.

Figure 11 compares observed maximum temperatures to those calculated from the two different soil moisture profiles (Figs. 9 and 10) as input to the PBL model. The mean observed temperatures were calculated by averaging values at each reporting depth under each type of surface, i.e., bare and sod covered soil. The modeled soil temperatures were obtained by

### Composite in-situ Soil Temperature ( $^{\circ}\text{C}$ )

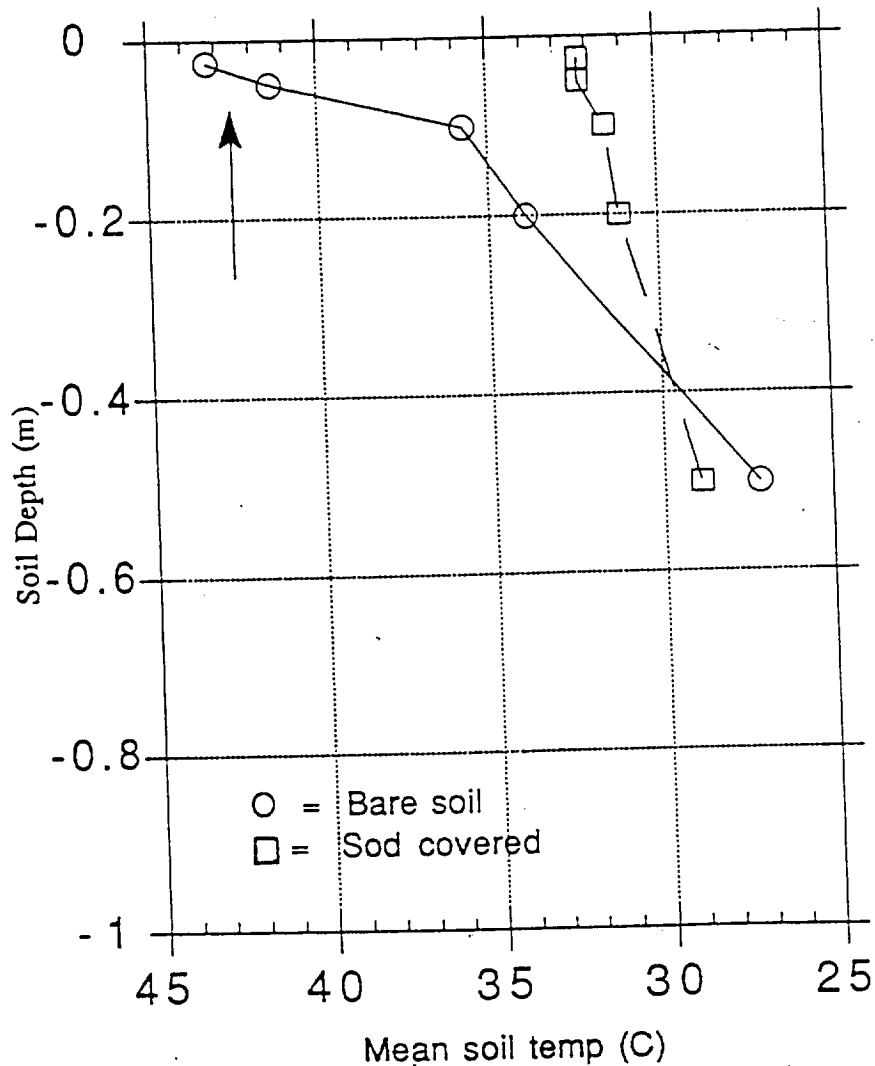


Fig. 8. Observed in situ maximum soil temperatures at various depths near the study region. Data were taken from 15 locations in southern Tennessee, and northeastern Mississippi on 18 August 1988. The arrow corresponds to the average MAMS LST during the second overpass.

### Average and Range of Soil Moisture Profiles ("NoEvapARI")

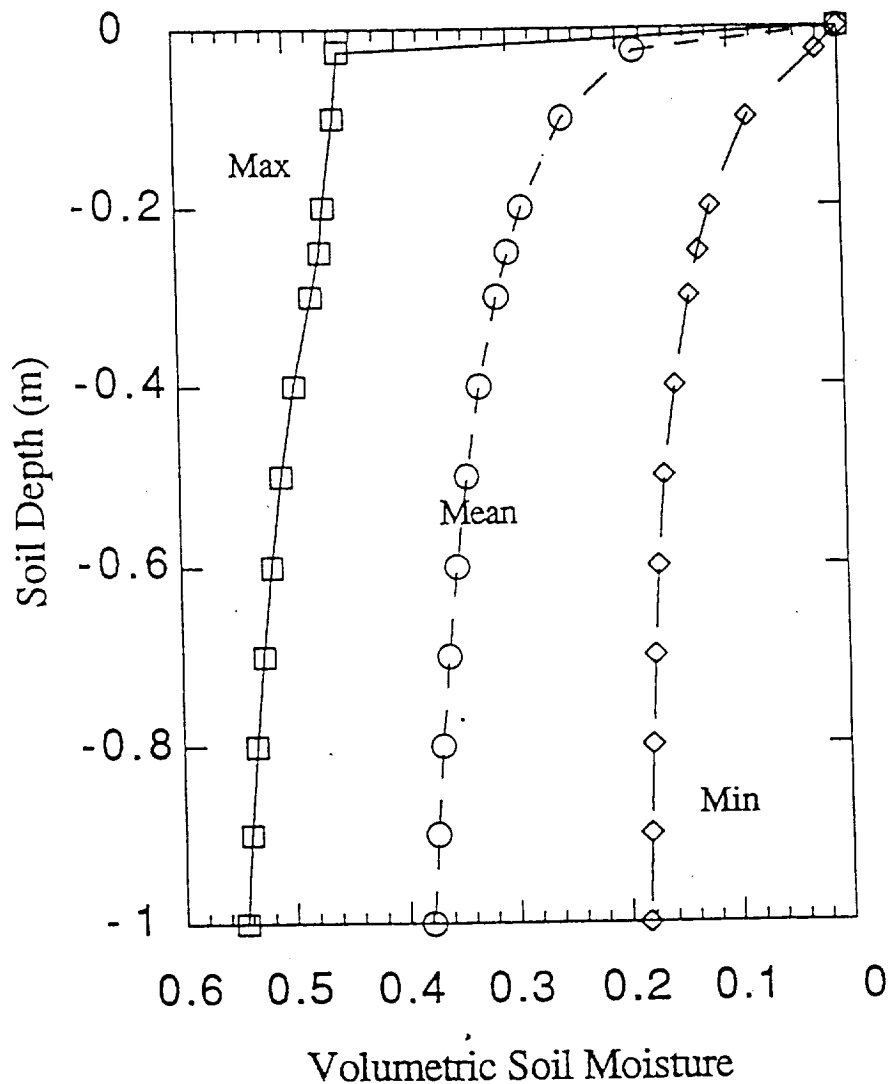


Fig. 9. Soil moisture profiles (average and range) fit through final NoEvapARI soil moisture values. The Average was done for 55 sites shown in Fig. 1.

### Average and Range of Soil Moisture Profiles ("EvapARI")

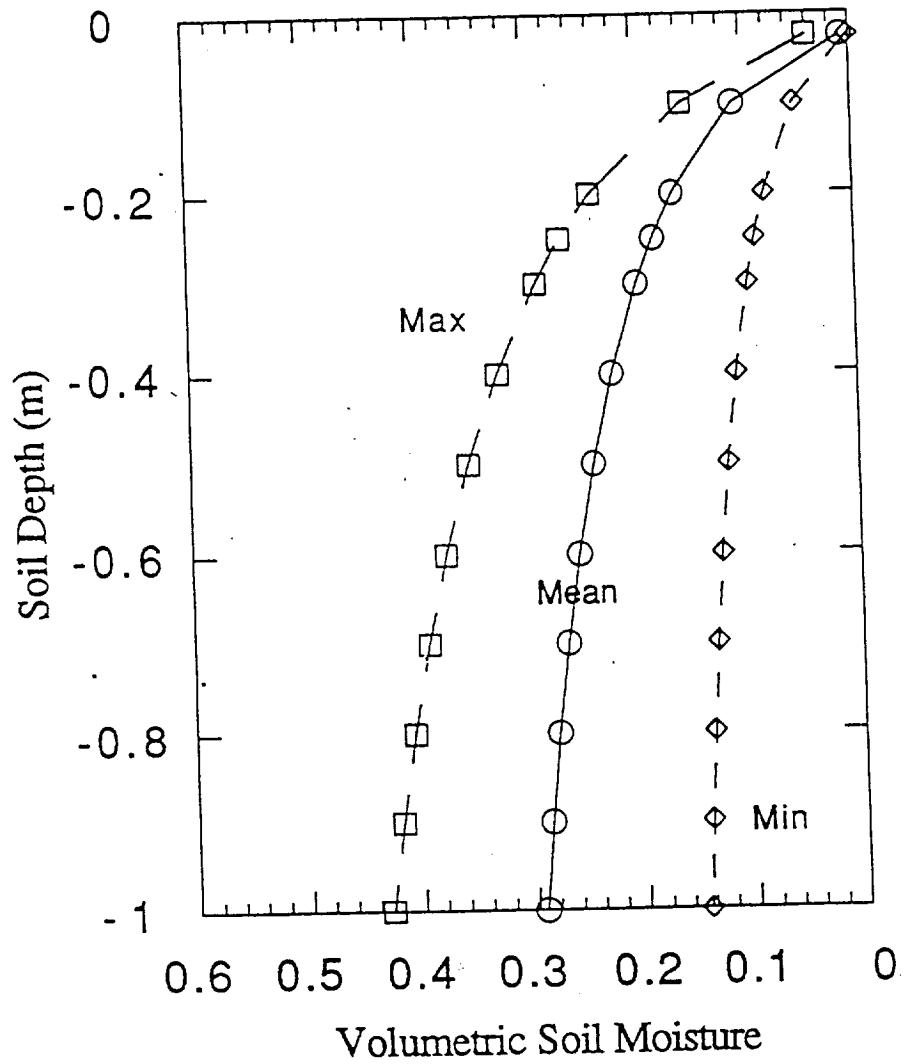


Fig. 10. Same as Fig. 9., except profiles were fit through final soil moisture model from EvapARI model.

inputting the mean soil moisture profiles at 10 depths from NoEvapARI and EvapARI (Figs. 9 and 10, respectively) for bare soil (PBL modeled vegetation fraction set to 0.0%) and sod covered soil (PBL modeled vegetation fraction set to 100%). The mean temperature differences suggest, for both bare and sod covered soils, that the NoEvapARI soil moisture profile (solid symbols in Fig. 11) yields the best temperature results. It produces the smallest overall deviations from the observed profiles. At every level, this model yields soil temperatures within 1 to 2 °C of the observed maxima. The overall mean absolute difference between modeled and observed maximum temperatures (for all levels, both bare and sod covered soils) is 2.0° C for the EvapARI model and 1.2° C for the NoEvapARI. The worst errors for the EvapARI model occur at the -0.02 m and -0.2 m level. For sod covered soil near the surface, the EvapARI model (open diamonds in Fig. 11) yields a temperature difference approximately 5° C warmer than observed. Thus, soil moisture dries out too quickly with depth in the upper soil layer. Temperatures at the deepest level (-0.5 m) are approximately the same regardless of the input moisture for each type of surface. Furthermore, the overall stability of fit to the data seems best for the simpler NoEvapARI model. There is considerable variation in the temperature differences closest to the surface. Therefore, later sections will use additional observed LST data to compare with those from the PBL. MAMS LSTs will be used for this purpose (described below).

Two sensitivity tests were performed using the ARI data. The first test was to determine whether it was advantageous to use a 10 layer soil moisture profile instead of a simpler 2 layer profile in the PBL model. For the 2 layer



## Mean Soil Temperature Differences - Modeled vs Observed

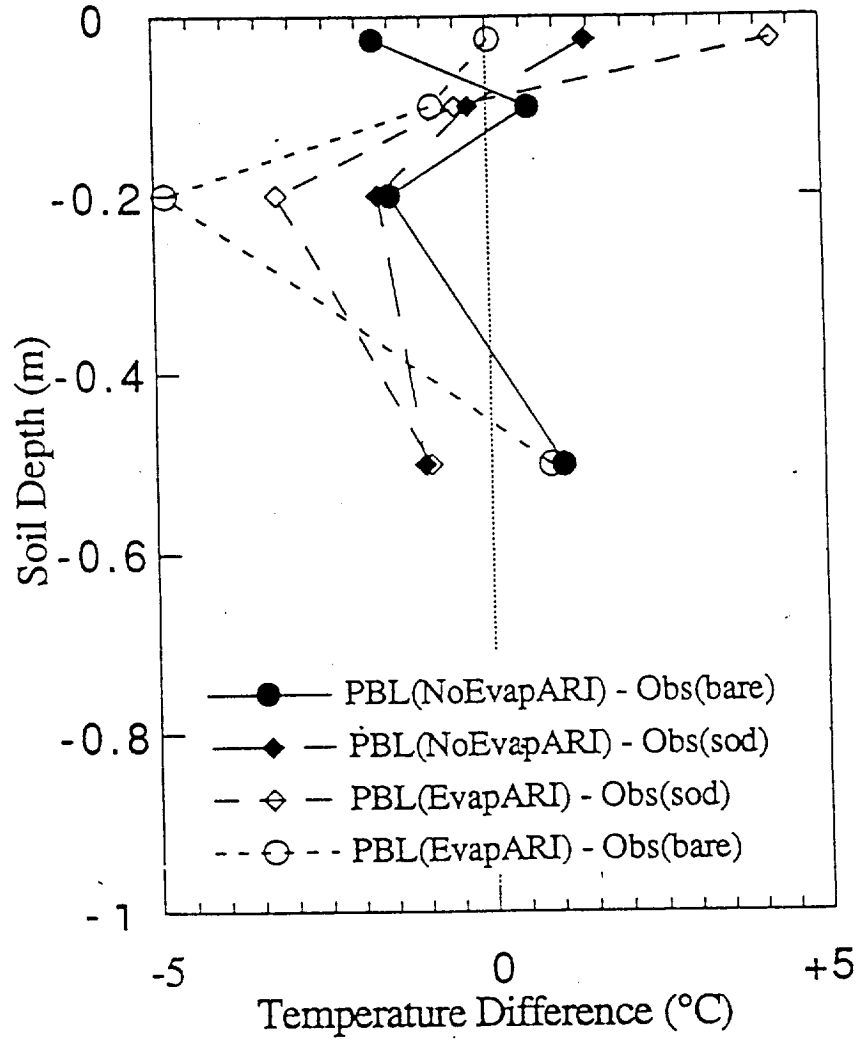


Fig. 11. Soil temperature differences at various depths between PBL model output and observed data (forecast minus observed). The observed values were averaged from all sites where in situ temperatures were measured.

version, only ARI-derived soil moisture values at the 5 cm and 1 m depths were input to the PBL model. Results (not shown) indicate that no additional information is gained using the 10 layer model, i.e., forecast LSTs are approximately the same for the two types of input soil water profiles. For example, the RMS difference between forecast and MAMS observed LSTs (chapter 3 and discussed below) was the same ( $5.6^{\circ}\text{C}$ ) for both the 10 layer and 2 layer profiles. This 2 layer case will be referred to as the “ARI2Wet” test case. These test results seem to justify use of the simpler 2 layer version.

The second sensitivity test examined one of the greatest uncertainties to the ARI approach — how far downward soil moisture travels with time. The depletion coefficients ( $k_{\text{top}}$  and  $k_{\text{bot}}$  in chapter 3) can vary from 0.85 to 0.95 (Linsley *et al.*, 1982); a constant of 0.9 was used for this study. The speed of this “wetting front” through the soil depth is a function of porosity, vegetation cover, soil type, and the vertical gradient of soil moisture (Arya, 1988; Linsley *et al.*, 1982). Dunne and Leopold (1978) show how a typical wetting front travels through a sandy soil. They showed that moisture moves through different soil depths at different speeds. *This suggests that the recession coefficients are not constant in time.* Most ARI models assume constant  $k$  values, and this was also the procedure followed here. With this in mind, sensitivity tests were conducted to note changes in PBL modeled LSTs and surface fluxes when only the bottom (1 m) value of soil moisture was changed. The motivation for this test was to note the PBL model’s forecast LST sensitivity and to examine the importance of surface fluxes on convective cloud development (Rabin *et al.*, 1990; Bradshaw and Fuelberg, 1993).

When the ARI-derived moisture values at 10 cm were assumed for the moisture values at 1 m in the PBL runs, the mean RMS LST temperature difference between model forecast and MAMS observed values dropped from 5.6 to 4.8° C (referred to as the “ARI2Dry” test case). This improvement suggests that the deep (1 m) soil moisture may have been overestimated with the ARI model. These results show that PBL modeled LST is sensitive to changing the deeper soil water values when the top layer is unchanged.

Results from the ARI2Wet and ARI2Dry tests also indicate significant differences in surface fluxes between cases. For example, average sensible heat flux (SHflx) for the ARI2Dry case (at all 55 precipitation sites) is 67 W m<sup>-2</sup> (44%) larger than for the ARI2Wet case. This increased SHflx is accompanied by an 81.7 W m<sup>-2</sup> decrease in the average latent heat flux (LHflx). These changes in flux correspond to an increase in the average Bowen ratio from 0.7 to 1.7. This is a significant increase, considering that typical Bowen ratios vary from about 0.5 over grassy areas to 5.0 over semi-arid regions (Stull, 1988). This test result indicates the sensitivity of the PBL model’s flux calculations to changes in deep soil moisture. It may also help explain some of the differences between other modeled and observed parameters such as cloud cover amount that will be described in later sections.

Other uncertainties with the ARI approach to soil moisture include estimating the runoff threshold and the initial starting value of ARI in the deep soil layer. There is considerable uncertainty in the deeper layer soil moisture, as evidenced by the scatter of those temperatures in Fig. 11. Borland (1990)

also found similar uncertainties using an ARI model. He assumed that any precipitation greater than 1.00 in. (2.54 cm) produced runoff, whereas in the present study, any rainfall in excess of 2.00 in. (5.0 cm) was assumed runoff. Two inches was used here since this was a summertime study where the soil was extremely dry prior to the study period. Furthermore, it is critical to know the initial value of the bottom soil moisture at the start of the ARI index modeling. Although the two layers are assumed to be saturated initially, this was probably not the case in reality. This is also a possible reason why the deeper layer soil moisture may be incorrect.

To summarize, comparison with the limited in situ soil temperature data suggests that the NoEvapARI scheme yields the best “ground truth” estimate of soil moisture. This result is surprising. It was hoped that the inclusion of detailed evaporation might improve the ARI approach, but this was not the case. One possible explanation is the performance of the evaporation reduction function,  $F$  in (32) that is used in calculating the ARI. Most indexed soil moisture models do not include explicit evaporation as part of the calculation; some use a constant (e.g., Borland, 1990; Saxton and Lenz, 1967). It was hoped that inclusion of daily pan evaporation data, along with a reduction function based on field data (Brutsaert, 1982) would produce better indexed soil moisture estimates. However, this function seems to allow too much water to be removed from the soil when it is dry. Previous studies have shown that the currently used PBL model can forecast shelter air temperatures relatively well (Borland, 1990; Holtslag and De Bruijn, 1990), with  $R^2$  values ranging from 0.63 to 0.98. A comparison of shelter air

temperatures appears in section e1 below. Comparison between measured in situ soil moisture and antecedent indexed estimated moisture have been shown to agree relatively well, *albeit over flat terrain* (Blanchard *et al.*, 1981; Choudhury and Blanchard, 1983). A later section will investigate the role of terrain in greater detail. Hereafter, “ARI” will refer to the NoEvapARI model.

*b. MAMS LST, LST changes and soil moisture*

1. MAMS LST as accurate ground truth LST

Figure 12 shows a composite MAMS LST image for flight legs 2 and 3 shown in Fig. 2a. This image was computed using the regression relationship in (29). The  $R^2$  value between LST input to the forward radiative transfer code and LST calculated from (29) was 0.96. Temperatures from this equation are generally within 2 to 3° C of those obtained from an equation derived by Jedlovec and Atkinson (1992). Previous studies have shown MAMS sea surface temperatures to be accurate to within 1° C (Jedlovec *et al.*, 1989; Moeller *et al.*, 1989). The hottest areas in Fig. 12 (45 to 50° C) appear as red, while the coolest areas (30 to 35° C), corresponding to water and forested areas, are purple. White pixels are cloudy; cirrus contamination is evident in the northwestern portion of the image. One should note that the easternmost part of the LST image contains a “seam” which corresponds to a temperature change from the time of the beginning of leg 2 to the end of leg 3. There is no seam on the western part of the image because the times of these overpasses are more nearly the same (Fig. 2).

The spatial emissivity variations that occur in nature are unaccounted for in the LST equation (29); an emissivity of 0.96 was assumed everywhere. However, the emissivity of most vegetated land surfaces only varies around 1% of this value within the 11 and 12  $\mu\text{m}$  "window" region (Zhang, 1990). Water has an emissivity closer to 1.00, and for this reason the water temperatures in the MAMS image (Fig. 12) could be as much as 3-5° C warmer than actually occurring.

MAMS senses radiation emanating from the uppermost surface molecules (Jedlovec, 1993, personal communication). In the present study, the average MAMS LST is 42.7° C during the second pass (nearest to the time of the maximum soil temperature); the arrow in Fig. 8 indicates this temperature. The exact time of maximum soil temperatures is not known for this case, but climatologically, the maximum temperature near the surface occurs about 1 h after local noon (Stull, 1988). This is between 1 and 2 h after the second MAMS overpasses here.

The average MAMS temperature appears closer to the bare soil temperature than the sod covered value (Fig. 8). The pixels used to compute second pass MAMS average surface temperatures mainly included farm and forested regions, with a minor contribution from secondary roads and small areas of bare soil; no pixels over water or major urban centers such as Huntsville were included in the MAMS average (42.7 C). Consider the following calculation, assuming a reasonable vertical soil temperature gradient of 0.5° C  $\text{mm}^{-1}$  through the first 20 mm of bare soil and a corresponding gradient of 0.25° C

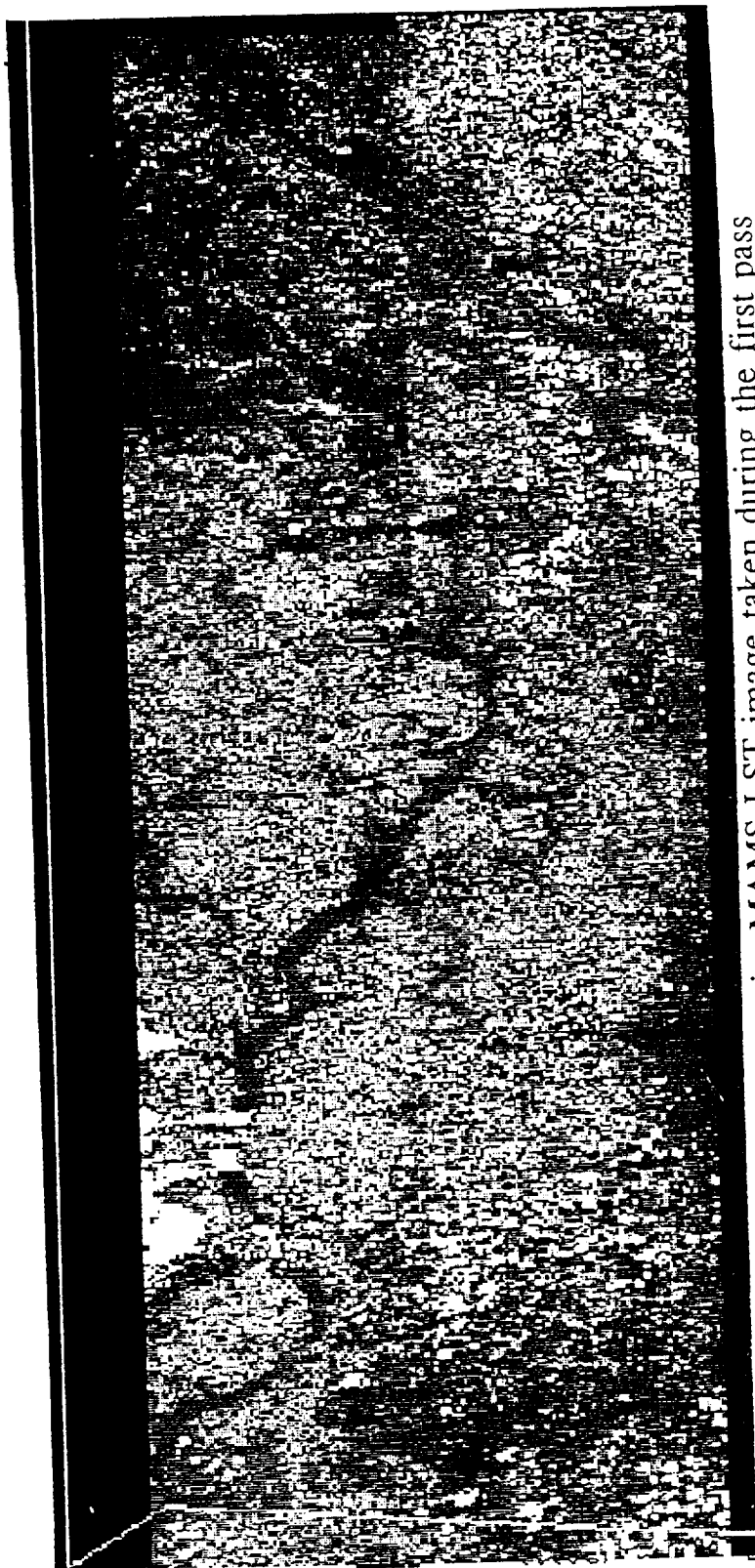


Fig. 12. Composite MAMS LST image taken during the first pass (see Fig. 2 for flight tracks). Hottest values appear red (45 - 50° C); coolest appear purple (30 - 35° C).

mm<sup>-1</sup> for sod covered soil (Garratt, 1992). Referring to Fig. 8 and starting with a bare soil temperature of 43.2° C and a sod covered temperature of 32.2° C at the -0.02 m depth, and further noting that the majority of the MAMS image (say 60%) is covered with vegetation (and 40% is bare or other “hot” surfaces), the average soil temperature at the air / soil interface can be approximated as

$$\bar{T} \cong 0.4 (53.2) + 0.6 (37.2) = 43.6^{\circ} \text{ C} . \quad (37)$$

This value is within 1° C of the average seen by MAMS (42.7° C). The calculation (37) is based on extrapolated surface temperatures only. *This result, along with the R<sup>2</sup> value of 0.96 given earlier, justify the use of MAMS for providing accurate ground truth LST; a result that is crucial to properly evaluate soil moisture estimates described later.*

## 2. LST changes and soil water availability

There is a direct relationship between the soil’s thermal inertia and its water content (Idso *et al.*, 1975; Schmugge, 1978; Stull, 1988). Thermal conductivity and thermal diffusivity are both highly dependent on soil water content (Mahrt and Pan, 1984). There is an important application from this: Time changes in soil temperature can be used to estimate soil moisture. Previous studies have related diurnal changes in soil temperature to soil water availability. They have used both 2 h (Wetzel and Woodward, 1987) and diurnal (Carlson *et al.*, 1981; Schmugge, 1978; Idso *et al.*, 1975) time intervals. I investigated whether MAMS-derived LST changes between



approximately 10 AM and noon local time could be related to soil moisture. These time differences actually ranged from 0.78 to 1.5 h, depending on the flight track configuration.

Figure 13 shows an analysis of MAMS-derived normalized LST changes from 10 AM to noon local time. This was done for just the 20 sites in the figure (a representative sample) by calculating the average LST in a 5 x 5 km box at each site and time and then differencing. This temperature difference was then divided by the appropriate time interval to obtain the rate of change. This linear change is assumed to occur during the 2 h period from 10 AM to noon. The normalization was necessary because of the differing times of the MAMS overpasses at each location. Figure 14 shows cumulative precipitation totals from 1 June through 18 August 1988. When the basic patterns of Figs. 13 and 14 are compared, the axis of minimum rainfall generally corresponds to the region of greatest LST increase which runs across northern Alabama along a SAV-MSL-HSV-SCB line. Similarly, rainfall maxima correspond to minima in normalized LST changes. A similar pattern correspondence was noted for three week (28 July to 18 August) cumulative rainfall totals (not shown). However, one week (11 August to 18 August) totals showed little relationship to LST changes due to the small variability of rainfall during this period. No rain was observed on 18 August at any of the sites, and only small amounts (less than 0.25 in.; 0.64 cm) were observed at two sites on 17 August. LST changes were not computed on a pixel by pixel basis as done in Jedlovec and Atkinson (1992), where some unexpected decreases in LST were noted during the morning

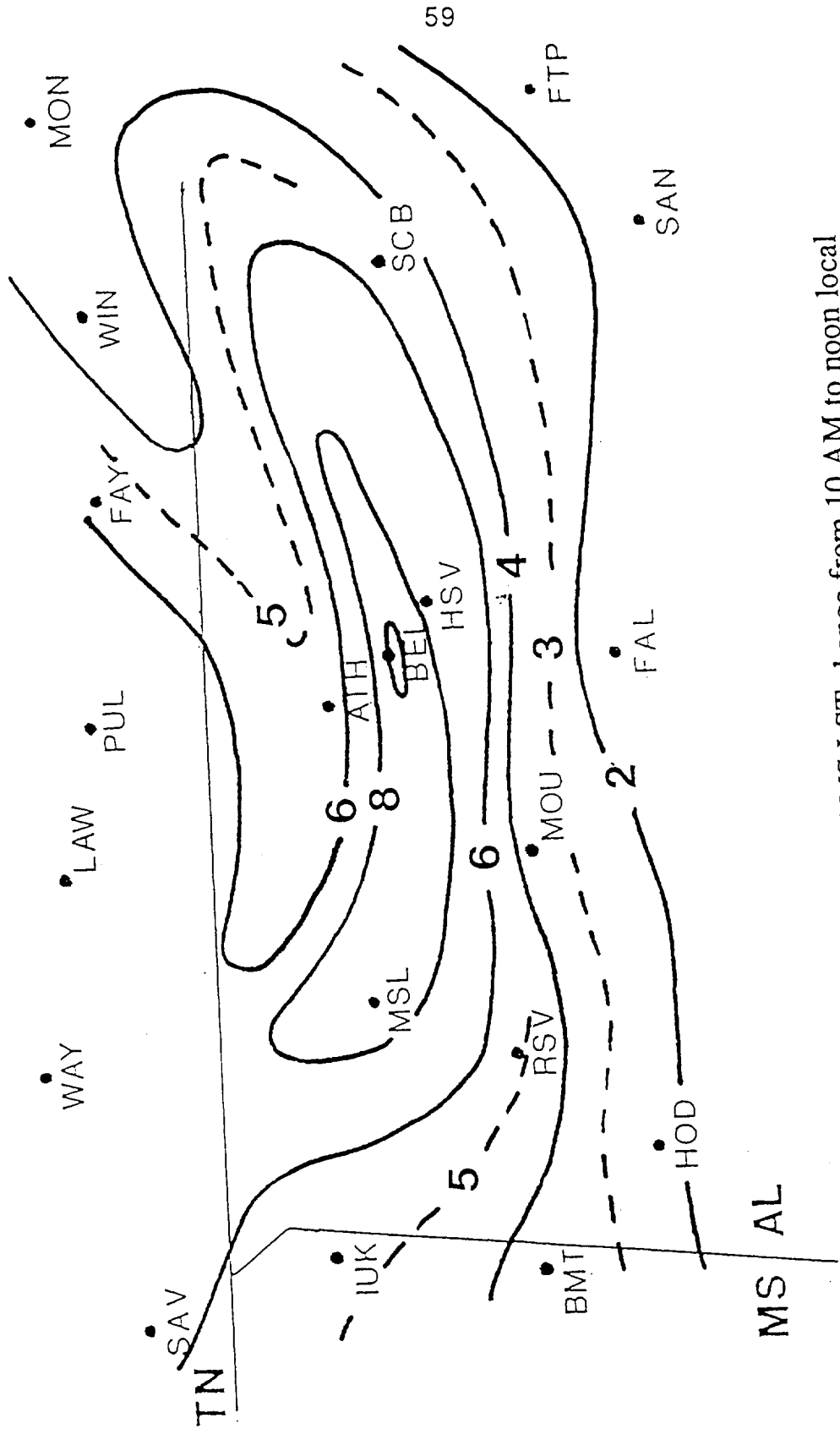


Fig. 13. Normalized MAMS LST change from 10 AM to noon local time ( $^{\circ}\text{C}$ ).

TOTAL PRECIPITATION JUNE - AUGUST 18, 1988

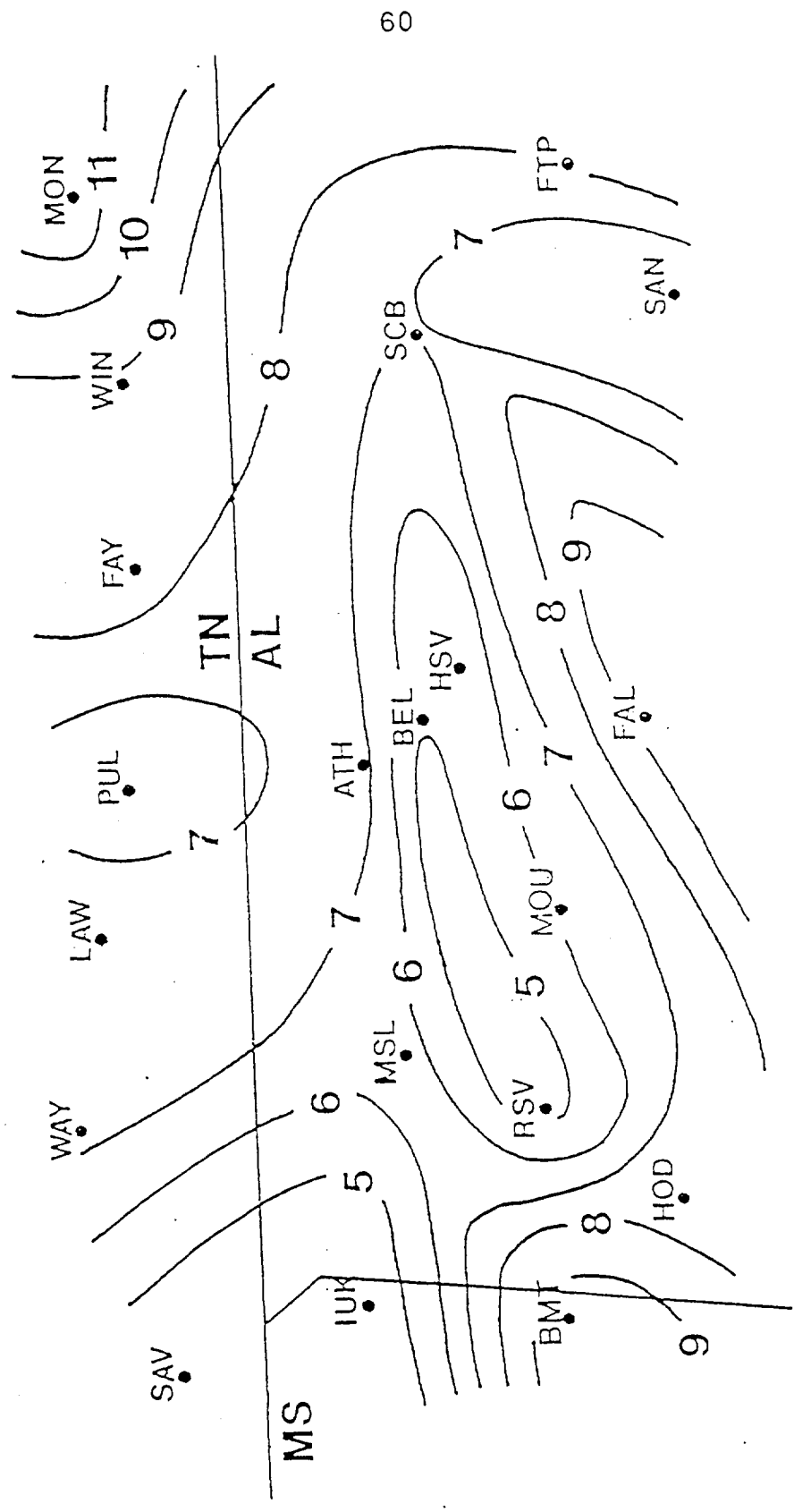


Fig. 14. Cumulative rainfall (in) from 1 June through 18 August 1988.

hours. In the current case, no temperature decreases were indicated between the first pass and second passes at the stations examined.

Figure 15 shows ARI-derived soil water availability versus the computed normalized time change in LST from 10 AM to noon. The 34 sites that were plotted (see Fig. 1) were characterized by a small roughness parameter computed according to Lettau (1969) and described in chapter 3. Any sites whose roughness parameter was greater than 1 m were not considered. The correlation coefficient for the relatively flat sites is  $-0.63$  (log fit). When all sites are included (not shown), the correlation is reduced to  $-0.50$ . This degradation is expected since sloping terrain affects values of the availability parameter ( $f_{top}$  and  $f_{bot}$ ; see (34)). No terrain parameterization was included as part of the ARI calculations. Current correlations are somewhat less than those of Idso *et al.* (1975), and they show considerably more scatter, even for the flat terrain locations. These investigators found a correlation of  $-0.86$  between in situ soil temperatures at 0 - 2 cm and observed (gravimetric) soil water content, with an availability intercept of about 0.90 (for no temperature change). Furthermore, the terrain in the Idso *et al.* study (Phoenix, Arizona) was comparatively flatter and more homogeneous than the area currently being investigated. With a linear fit to the data in Fig. 15 (not shown), the correlation is reduced to  $-0.58$  and the y-intercept is only 0.66. The above mentioned results suggest a significant limitation to the ARI approach: the effects of terrain slope. The ARI approach probably underestimates (overestimates) the actual soil moisture in valleys (on hills), assuming all other parameters in the ARI formulation are accurate. Even

small changes in slope can affect soil water movement (Arya, 1988; Linsley *et al.*, 1982).

The influence of cloud cover is a limitation to this approach for assessing soil moisture. Clouds and cloud shaded areas must be avoided when determining LST changes from IR imagery. Microwave data have been shown to overcome cloud limitations. It may be possible to estimate soil moisture profiles through the first 4 cm of topsoil using microwave frequencies near 1.4 GHz (Njoku and Kong, 1977). For the microwave approach, soil moisture is related to microwave brightness temperature which changes with surface emissivity (Heymsfield and Fulton, 1992). However, a significant drawback to the microwave approach is its large footprint size, approximately 15 to 25 km depending on frequency. At the very least, microwave data afford the possibility of mesoscale soil moisture monitoring with other frequencies (6.6 and 10.7 GHz; Heymsfield and Fulton, 1992).

*c. MAMS LST change / PBL regression soil moisture estimation*

A related approach for estimating soil water availability utilizes a regression technique whereby measured LST differences and other parameters are used as predictors in a boundary layer model to estimate predictands such as soil moisture and surface fluxes. One such study that used diurnal LSTs was carried out by Carlson *et al.* (1981). Their results showed marked surface dryness over urban areas with corresponding high values of SHflx. They suggested that the nocturnal heat island was primarily caused by surface dryness and increased heat storage, rather than by spatial variations in thermal

LST Change  
vs.  
ARI Moisture Availability

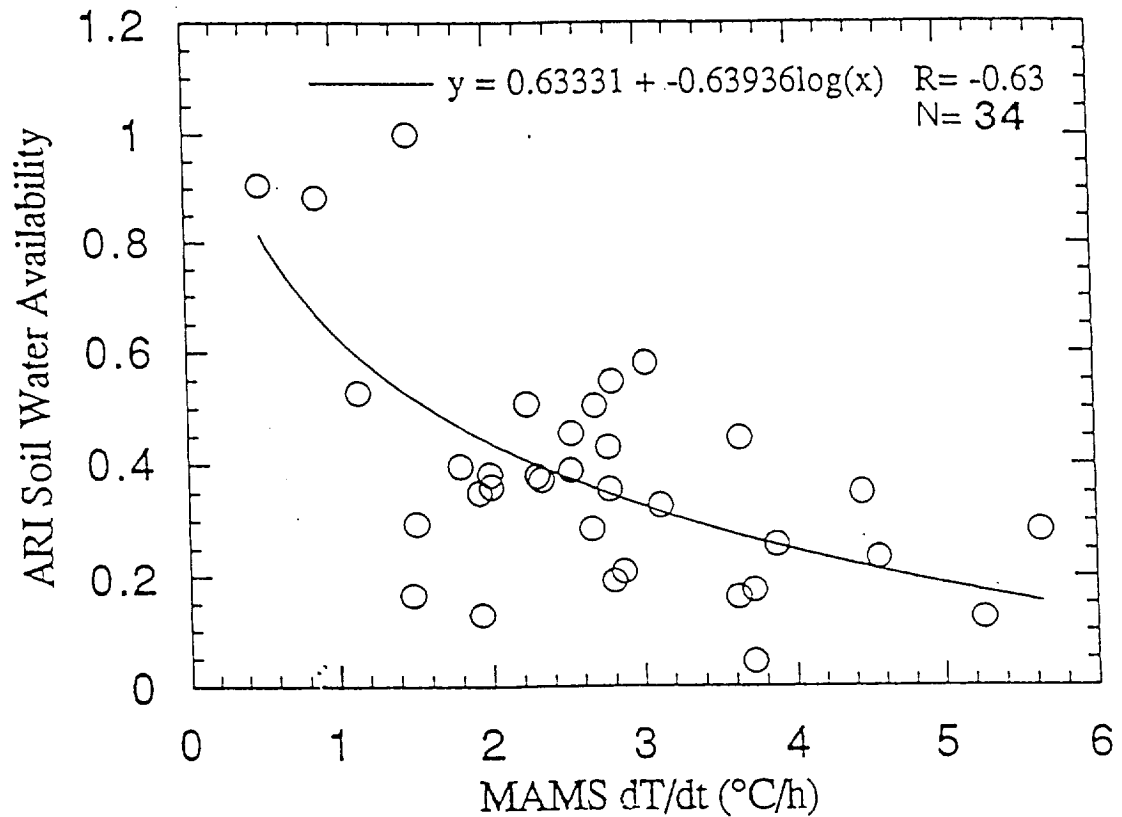


Fig. 15. Scatter plot of MAMS LST change ( $^{\circ}\text{C h}^{-1}$  normalized from 10 AM to noon) vs. ARI-derived soil water availability (ratio of actual to maximum saturation value) for 34 sites in the study region. A log fit to the data yields a correlation coefficient of -0.63. All sites are characterized by a relatively small roughness parameter.

conductivity. Other studies have also used the LST-modeling approach (Soer, 1977, 1980; Kahle, 1977; Dabberdt and Davis, 1978).

Current procedures differ from those of previous investigations in two ways. First, this study is the first to use MAMS high resolution LSTs for the purpose of estimating soil moisture. Second, a 2 h normalized LST change from approximately 10 AM to noon was used, instead of the diurnal changes employed in many previous cases. Three important factors justify this 2 h time window for LST time differencing. First, there is a nearly linear increase in surface temperature during mid-morning. Second, the largest difference between temperature changes of wet and dry soil typically occurs during this time interval (Stull, 1988). Schmugge (1978) (his Fig. 1) had values ranging from  $3.0^{\circ} \text{C h}^{-1}$  for bare wet soil to  $6.5^{\circ} \text{C h}^{-1}$  for dry soil in Phoenix, Arizona. Third, the usual absence of convective clouds early in the day makes this an ideal time for utilizing IR imagery. Cloud shading can alter LST changes which otherwise would occur due to soil / surface characteristics alone.

A pair of related studies which employed 2 h morning LST time differences (from 8 to 10 AM) were done by Wetzel *et al.* (1984) and Wetzel and Woodward (1987) using 8 km IR GOES data for LST calculations. Their research was carried out during a five day period over the flat Kansas-Nebraska prairie. They found good agreement ( $R^2 = 0.71$ ) between model estimated soil moisture and “observed” (indexed) soil moisture. The primary variables that were determined to influence PBL model estimated soil moisture were (in decreasing order of importance): LST changes, winds, roughness

length, and vegetation biomass. Current procedures have accounted for all of these variables (winds were not a factor in this study since it was a meteorologically quiescent period) by using separate regression equations at each site. Chapter 3 described the current regression methodology in more detail.

An obvious advantage with this technique for estimating soil moisture, one that was not included for in the ARI procedure, is the minimization of terrain effects. Specifically, since the PBL model relates LST changes (and other important influences such as soil type, vegetation type and amount) to soil moisture, terrain effects should be “built into” the relationship for each site, regardless of terrain. In other words, the PBL model predicts soil moisture based on physical LST changes in the surface energy balance equations. The model has no information about terrain except the roughness parameter for turbulent energy exchange. Figure 16 indicates this important advantage. The observed MAMS temperature change at all 39 sites (Fig. 16a) shows a strong correlation ( $R = -0.90$ ) to MAMS / PBL regressed soil moisture availability, despite the variations of terrain. When all eleven sites with rough terrain are excluded (Fig. 16b), the fit to the data remains nearly the same ( $R = -0.91$ ). This result suggests that the ARI approach (e.g., Fig. 15) with  $R = -0.63$  ( $R = -0.5$  with all sites) may not be as good for estimating soil moisture as the MAMS LST-PBL regressed approach over complex terrain. Moreover, this is further evidence that the ARI approach needs to be terrain adjusted. The slopes of the fitted lines in Fig. 16 are similar to those previously attained using in situ 0 to 4 cm soil temperature data (Idso *et al.*,



## MAMS LST Change vs. Regressed. Soil Moisture

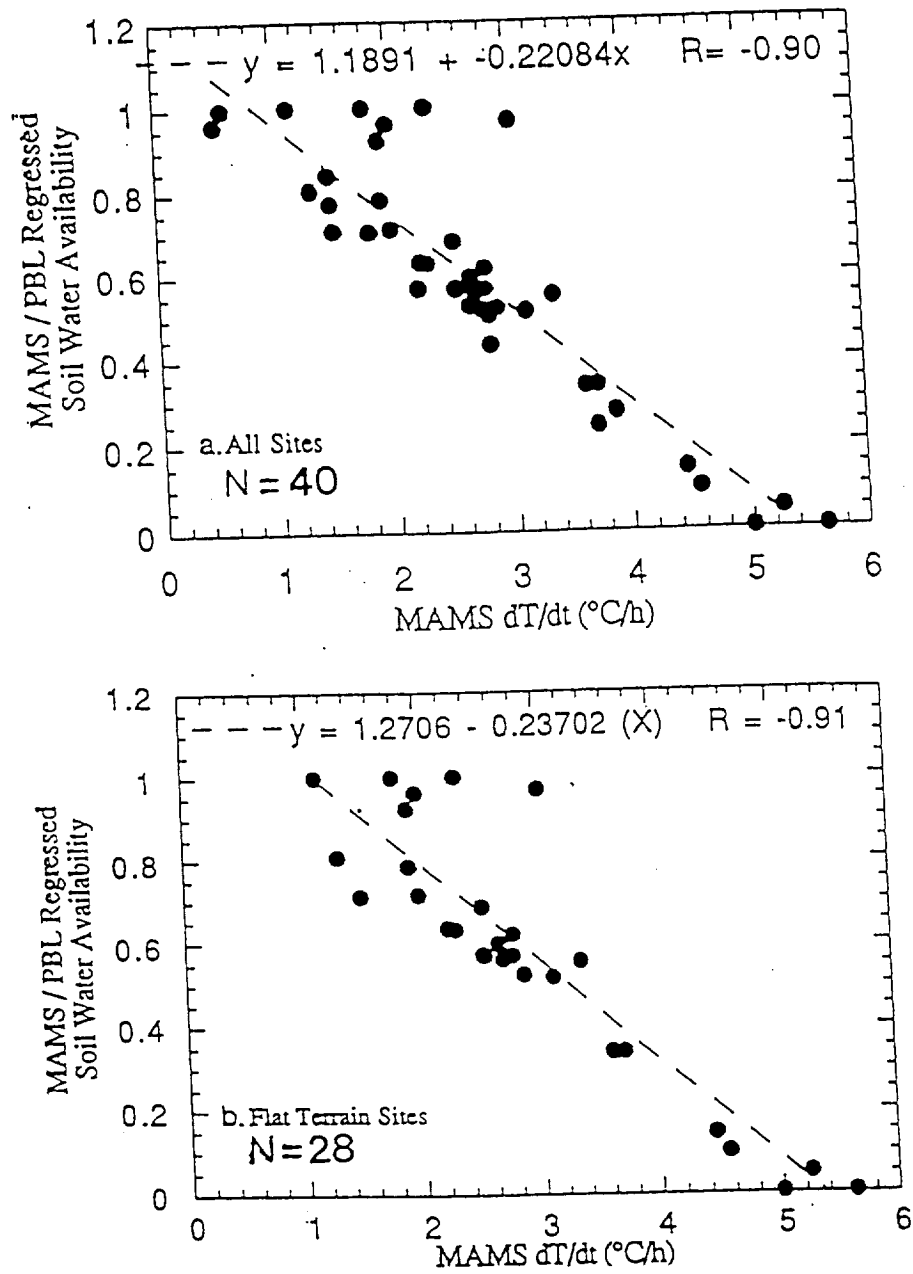


Fig. 16. Observed MAMS LST differences compared to PBL model regressed soil moisture for (a) all sites, and (b) only those with relatively flat terrain. Note the very little difference in R values.

1975), despite the fact that there are significant differences in soil and vegetation type between this study and theirs. This similarity lends further credence to the current procedures and resulting findings.

There are several disadvantages to this method that are related to specifying parameters needed by the PBL model. One uncertainty is specifying the value of root zone soil moisture at which evaporation proceeds at the potential rate. This soil moisture value required by the PBL model was assumed constant (0.20) based on previous investigations using this same model (Troen and Mahrt, 1986). Evaporation is allowed to proceed at the potential rate (see chapter 2) when the soil moisture equals or exceeds this value. In reality, this potential evaporation threshold is a complex function of soil type, organic matter content, atmospheric humidity, wind speed, and other variables (Brutsaert, 1982). This threshold parameter has a significant impact on PBL cloud development. For example; an increase in soil moisture of just 5% over the potential evaporation threshold leads to as much as a 40% increase in forecast cloud fractions in certain cases.

Other uncertainties of the technique are specifying the vertical distribution of soil moisture, which can influence drainage rates into the soil, and knowing the condition of the vegetation; i.e., stressed vegetation will respond differently to soil moisture changes than healthy vegetation. In the present PBL model, the health of the vegetation cannot be realistically simulated. In fact, the addition of detailed plant canopy physics would be major improvement to the PBL model. In its present form, the PBL model includes a simple "plant coefficient" (it can vary from 0.0 to 1.0; assumed

constant at 0.50 in this study) that attempts to parameterize plant stomatal resistance (Ek and Mahrt, 1989).

Figure 17 shows estimated MAMS / PBL regressed soil moisture availability compared to ARI-derived availability for the top (0-5 cm) soil layer (flat terrain sites only). Figure 18 shows a histogram of these differences (PBL model minus ARI). The model regressed values are considerably moister compared to the ARI-derived values; the mean difference is +0.23. In fact, for 73% of the cases, MAMS / PBL soil moisture values are wetter than ARI values. The range of differences is from +0.65 to -0.28.

In summary, the LST-PBL modeling approach to estimating soil moisture provides a better fit to the observed MAMS LST temperature differences than do moisture estimates from the ARI techniques (Figs. 15 and 16). The reader is reminded that most studies involving "ground truth" ARI soil moisture have been conducted over relatively flat terrain (e.g., Schugge, 1978; Wetzel and Woodward, 1987; Heymsfield and Fulton, 1992). *An important conclusion is that the LST PBL model - regressed approach, which contains explicit soil physics, is the preferred technique for estimating soil moisture over complex terrain when no in situ data are available.* Comparison of model regressed and ARI-derived soil moisture suggests that root zone ARI values may be underestimated (Fig. 17) due to the complexity of the terrain and other factors mentioned previously. Most of the rainfall sites being utilized here tend to be located in comparatively low lying areas, where the ARIs may be larger than calculated. Furthermore, the ARI values may be more representative of a very shallow soil layer near the surface, whereas the

### ARI vs. Model Regressed Soil Water Availability

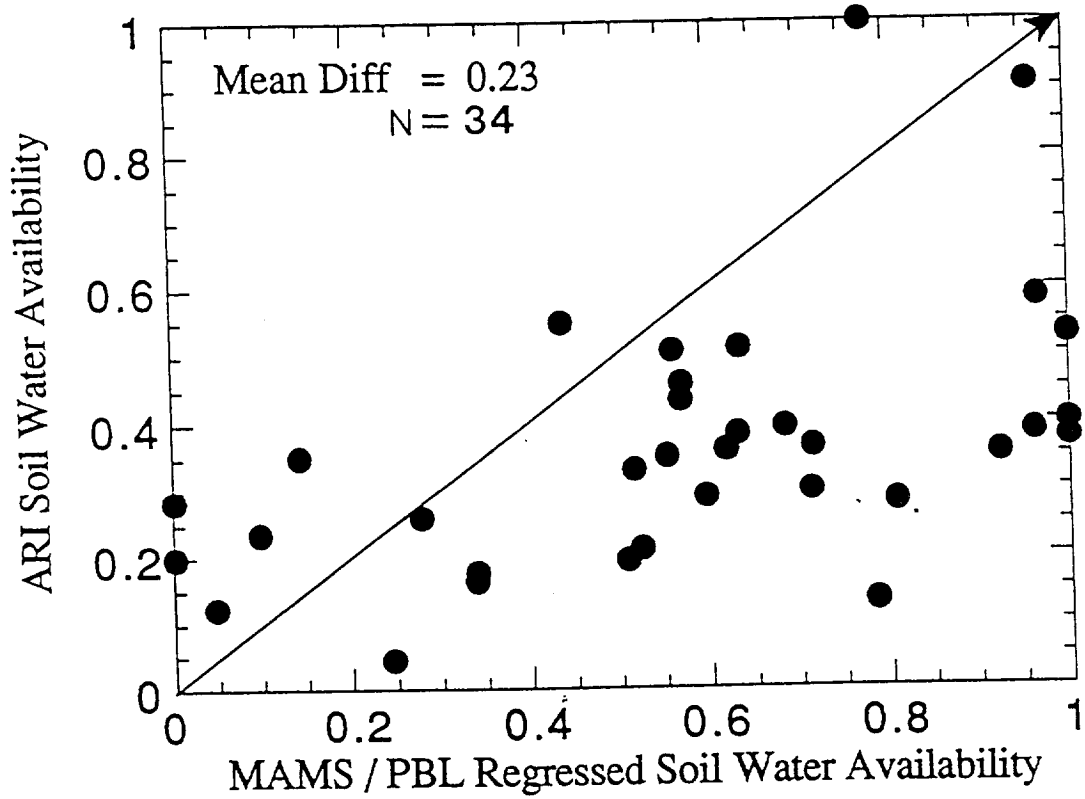


Fig. 17. ARI-derived soil water availability vs. PBL regressed availability from MAMS LST differences. The ARI values, on average, are 23 % drier than the PBL-derived values.

Soil Availability Difference  
(MAMS / PBL - ARI)

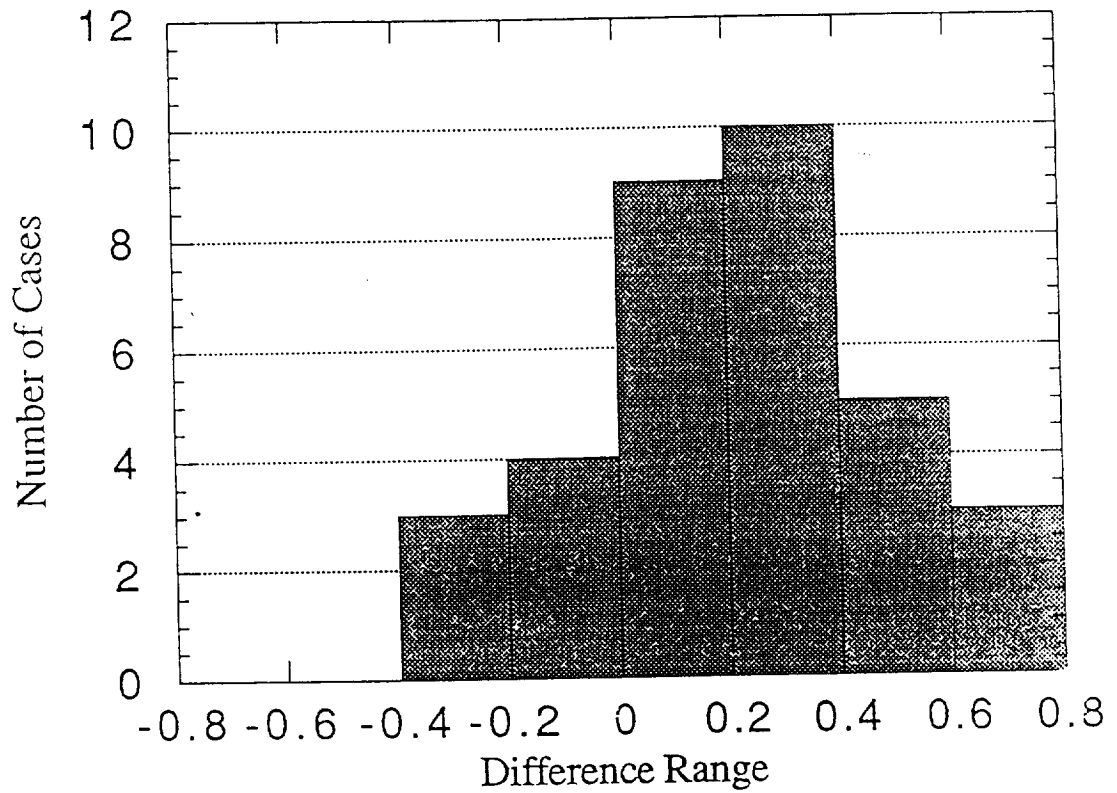


Fig. 18. Histogram of differences between ARI and PBL-regressed soil water availability. Mean difference (PBL - ARI) is 0.23 with a standard deviation of 0.26.

PBL model can infer soil moisture in a deeper layer(s).

*d. NDVI / LST relationships to soil moisture*

Figure 19 shows the composite MAMS NDVI image for the first overpass that corresponds to the composite LST image in Fig. 12. The NDVI procedure was described in chapter 3 (see (26)). NDVI values range from -0.15 to 0.80, representing areas of no vegetation to high vegetation density, respectively. Huntsville, Alabama stands out as a black area near the center of the image. A large forested area (blue / dark green) is apparent in the northeastern corner. One should note the general inverse relationship between LST and NDVI (Figs. 12 and 19). Generally, smaller NDVI values (black, orange and yellow) correspond to larger values of LST. The green areas (large NDVIs) over the northeastern part of the image are densely forested and have the smallest values of LST. These LSTs have been shown to be more representative of the canopy temperature (Jedlovec and Atkinson, 1992).

It is encouraging to note that no significant NDVI changes are observed between the first and second aircraft passes (not shown). The mean difference in NDVI over the study area from the first to second pass is only -0.02, or about 5.7% of the areal mean value over the study area (0.35). This change probably is due to varying solar insolation and minor changes in viewing geometry during the two overpasses.

Since NDVI is related to plant chlorophyll, one might expect a relationship between NDVI and the soil water available for photosynthesis;

i. e., the wetter the soil, the more robust (green) the vegetation. However, this is not the case. The NDVI has been shown to be well correlated with vegetation density and the amount of exposed green leaf area (the so-called “leaf area index”; Tucker, 1979; Asrar *et al.*, 1984) Thus, it is possible to have the same soil moisture content with fundamentally different vegetation density (NDVI). Figure 20 shows the relationship between root zone (0-5 cm) ARI-derived moisture availability (with no explicit evaporation physics) and NDVI averaged from both MAMS overpasses for 34 sites in the study region (Fig. 1). NDVI was calculated in 5 x 5 km boxes at each site and then averaged to produce a single value for both times. The averaging was used to smooth out solar insolation influences between overpasses. With a correlation of only 0.33, this result confirms the expected poor relationship between these two variables.

The slope of NDVI / LST scatter diagrams has been shown to be related to soil moisture availability and canopy resistance (Nemani and Running, 1989). As vegetation closes (opens) its stomata due to decreasing (increasing) moisture availability, the temperature of the canopy increases (decreases). Jedlovec and Atkinson (1992) examined scatter diagrams of NDVI vs. LST and found a similar inverse relationship between these two variables. They suggested that the slopes of the scatter diagrams are mainly dependent on solar insolation and, moreover, that the scatter in the NDVI vs. LST diagrams may fluctuate with changes in other variables such as soil moisture, type and density of vegetation, and photosynthetic activity. A strong negative relation between NDVI and LST is best achieved for an intensely sunlit landscape with

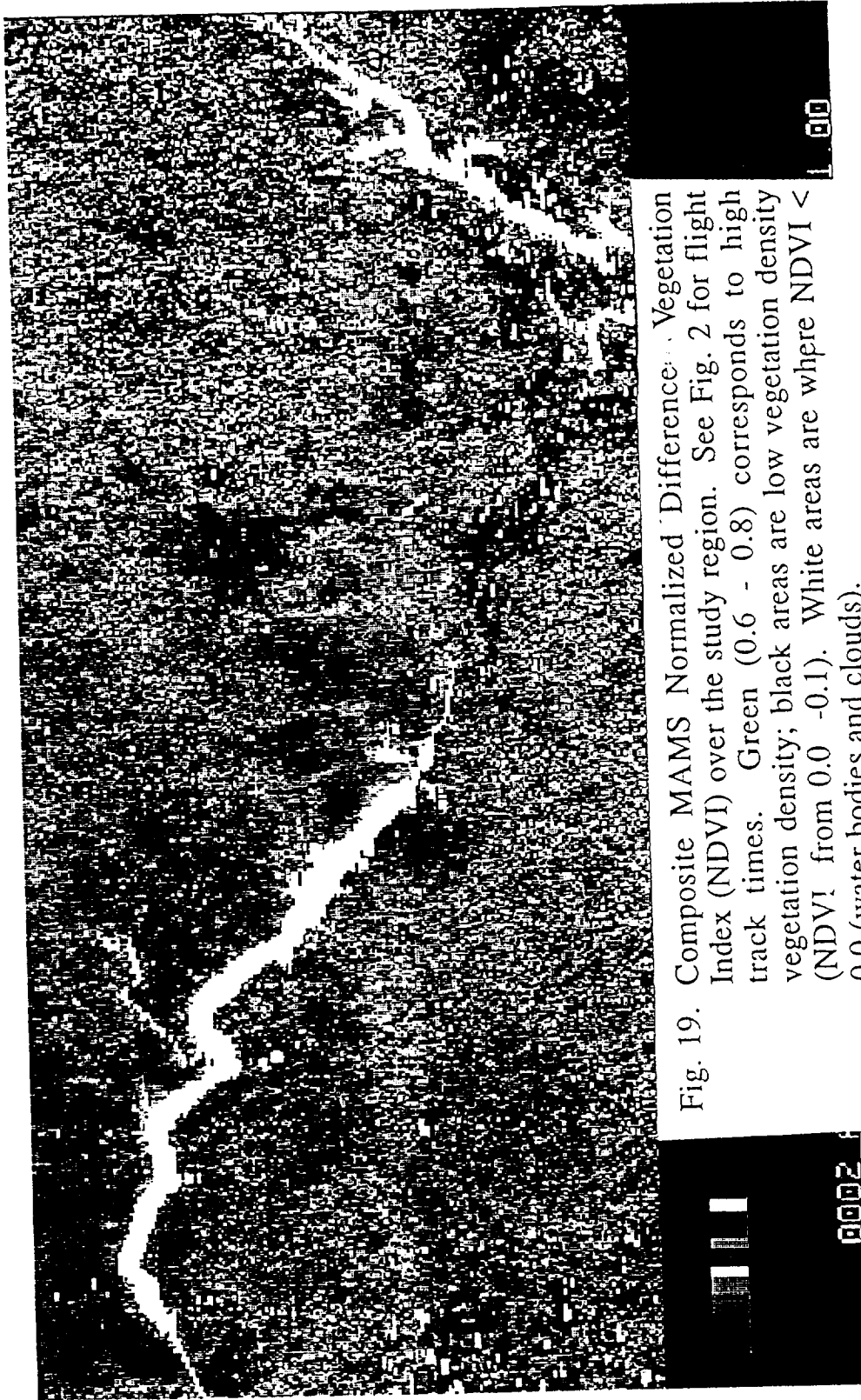


Fig. 19. Composite MAMS Normalized Difference Vegetation Index (NDVI) over the study region. See Fig. 2 for flight track times. Green (0.6 - 0.8) corresponds to high vegetation density; black areas are low vegetation density (NDVI from 0.0 - 0.1). White areas are where NDVI < 0.0 (water bodies and clouds).



dry soil. The slope reduces for wet soil because incoming solar radiation goes to evaporation, producing reduced LST with little corresponding change in NDVI. Jedlovec and Atkinson (1992) have also shown that NDVI is sensitive to sun-sensor-viewing geometry. In the present study, viewing geometry was not a factor due to the similarities of each MAMS overpass.

NDVI / LST scatter diagrams were calculated for 41 sites in Fig. 1. Figure 21 shows two NDVI vs. LST scatter diagrams for the current study period. An example for a comparatively “wet” location appears in Fig. 21a; a plot for a dry location in Fig. 21b. The “wet” site in Fig. 21a had an ARI availability of over 90% (for day 231), whereas the dry site (Fig. 21b) had an availability of only 23%. Each plot was obtained by computing LST and NDVI, pixel by pixel, over 5 x 5 km areas nearest its location (Fig. 1). The slopes were found by fitting a linear least squares line to the data. One should note the different slopes for these two example sites. The “wet” location (Fig. 21a) shows a less steep negative slope (-0.19) than the drier location (-0.33), and the fit to the data is worse for the wet site ( $R = -0.58$  vs.  $-0.83$ ). Correlations between NDVI and LST for all 41 sites (not shown) range from -0.3 to -0.85. More work needs to be done to determine a better interpretation for these data.

Carlson *et al.* (1990) referred to NDVI vs. LST scatter diagrams as “axes of variation”, suggesting that they are a “crucial aspect” for estimating root zone soil moisture. They utilized an extrapolation technique whereby bare soil temperatures were estimated by finding the LST temperature that corresponded to an NDVI value near 0.1 from the fitted regression line.

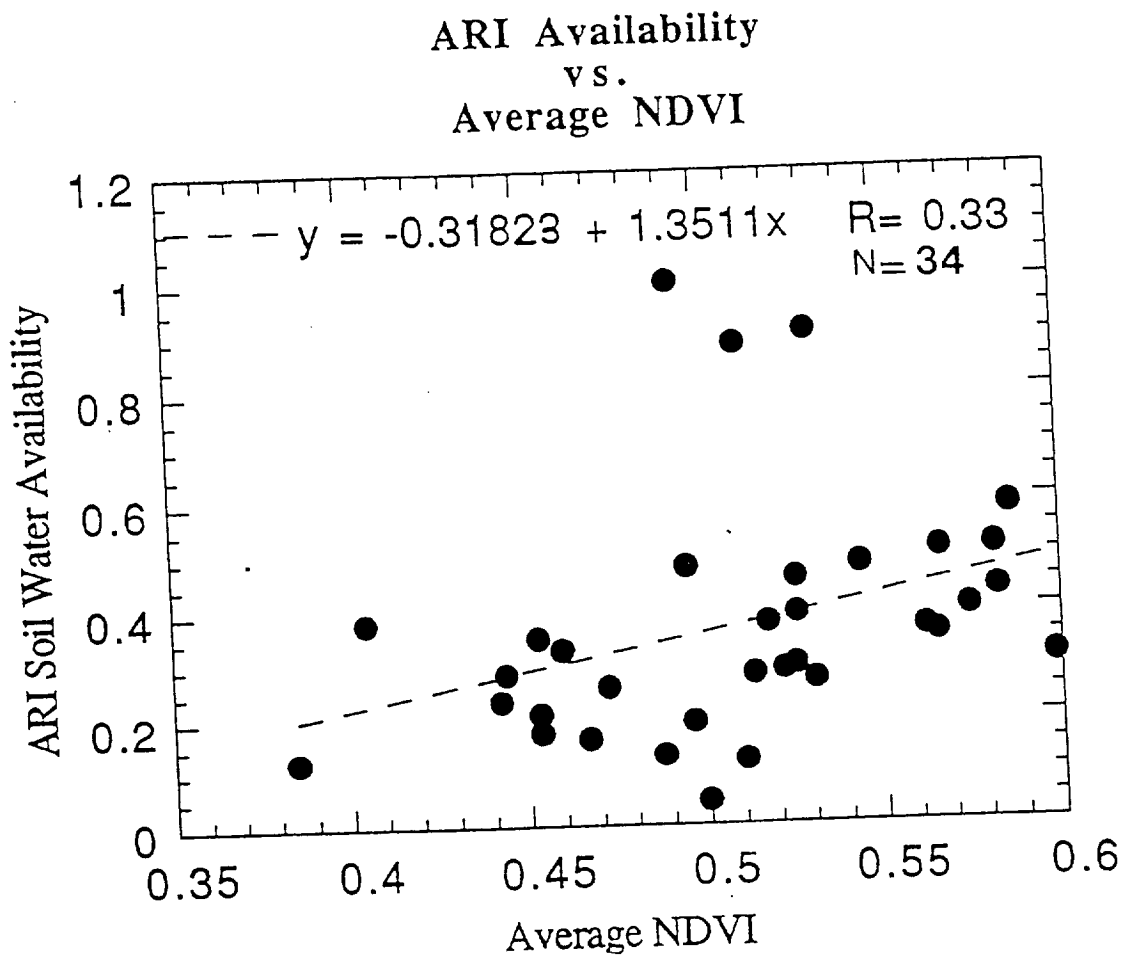


Fig. 20. Averaged NDVI vs. ARI-derived soil water availability for 34 sites in the study area ( $R = 0.33$ ). NDVI values were averaged from first and second MAMS overpasses.

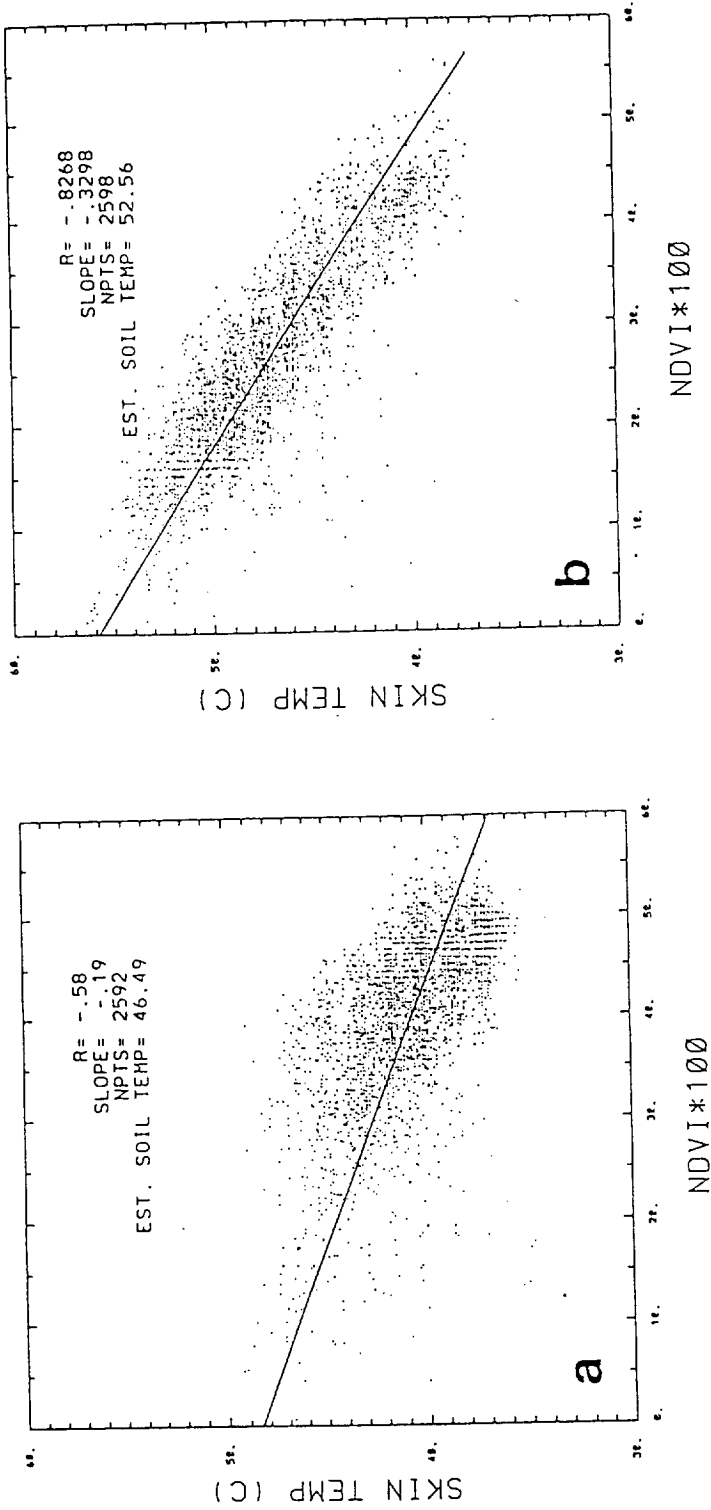


Fig. 21. Two contrasting examples of NDVI / LST scatter plots for estimating soil moisture. Top (a) was made over a wet location; bottom (b) over a dry location. The ARI availability (day 231) was 91% for (a) and only 23% for (b).

Soil moisture was then estimated by forcing agreement (tuning appropriate model parameters) between these extrapolated bare soil temperatures and PBL-modeled temperatures at one time during the day. A similar procedure was followed for the current case. One should note the differences in estimated bare soil temperature (Fig. 21). The “wet” site has an estimated bare soil temperature near  $46.5^{\circ}\text{C}$ , while the estimated value is  $52.6^{\circ}\text{C}$  for the dry location. These temperatures are reasonable, considering the measured bare soil temperatures within one week of irrigation were found to be  $45^{\circ}\text{C}$  in the Carlson *et al.* (1990) study. When these extrapolated bare soil temperature changes are compared to soil water availability at 21 sites (not all 41 could be used for reasons discussed below), more evidence supporting the model-regressed approach is revealed. When these temperatures changes are compared to the ARI values (not shown), a correlation of -0.38 is obtained; however, when compared to model-regressed soil water values (also not shown), the correlation improves to -0.67.

When NDVI / LST slopes from the various sites are compared to soil water availability, an interesting relation becomes apparent. Figure 22 shows slopes of the NDVI / LST plots (averaged for both MAMS overpasses) compared to ARI estimated soil moisture availability ( $f_{\text{top}}$ ) in the root zone (0-5 cm) layer. Only sites whose correlations were better than -0.40 were utilized in this analysis. A total of 21 sites (40% of the total) met this criterion (as well as being cloud free and having good site collocation) for both the first and second overpasses. A total of 26 sites (49%) were used for just the second overpass. The average slope between both overpasses was used to

smooth out any changes due to solar insolation effects. Scatter plots of NDVI vs. LST could not be prepared over some locations due to the presence of clouds and / or cloud shadows. Figure 22 shows a poor relationship between ARI soil water availability and average slopes of NDVI vs. LST ( $R = 0.42$ ). *Since a relationship has been established between these slopes and soil moisture in past studies, this poor correlation here suggests further that the ARIs are underestimated.*

For the first MAMS overpass (not shown), slopes range from -0.19 to -0.29, and from -0.15 to -0.40 for the second overpass. The average change in slope from the first to second overpass at the various sites is -0.02, or approximately 6% of the average slopes between the two overpasses (-0.33). In the worst case, these slope changes are as great as -28% of the average. Positive slope changes also are as great as 18%. These results suggest that, in addition to soil moisture, processes such as solar insolation and vegetation type and density, are influencing the slopes of these plots. This agrees with Jedlovec and Atkinson (1992).

When slopes of *only the second overpass* are compared to ARI moisture availability, the correlation is reduced from 0.42 for the mean (Fig. 22) to 0.26 (not shown). Since the correlation gets worse for the second pass, dew is probably not an influence. This degradation is probably due to slight errors in site collocation and differing scene illuminations from changes in solar insolation between the overpasses. Nemani and Running (1989) showed a strong correlation ( $R^2 = 0.92$ ) between model simulated canopy resistance (mostly a function of soil water availability) and the slopes

ARI Availability  
vs.  
NDVI / LST Slopes

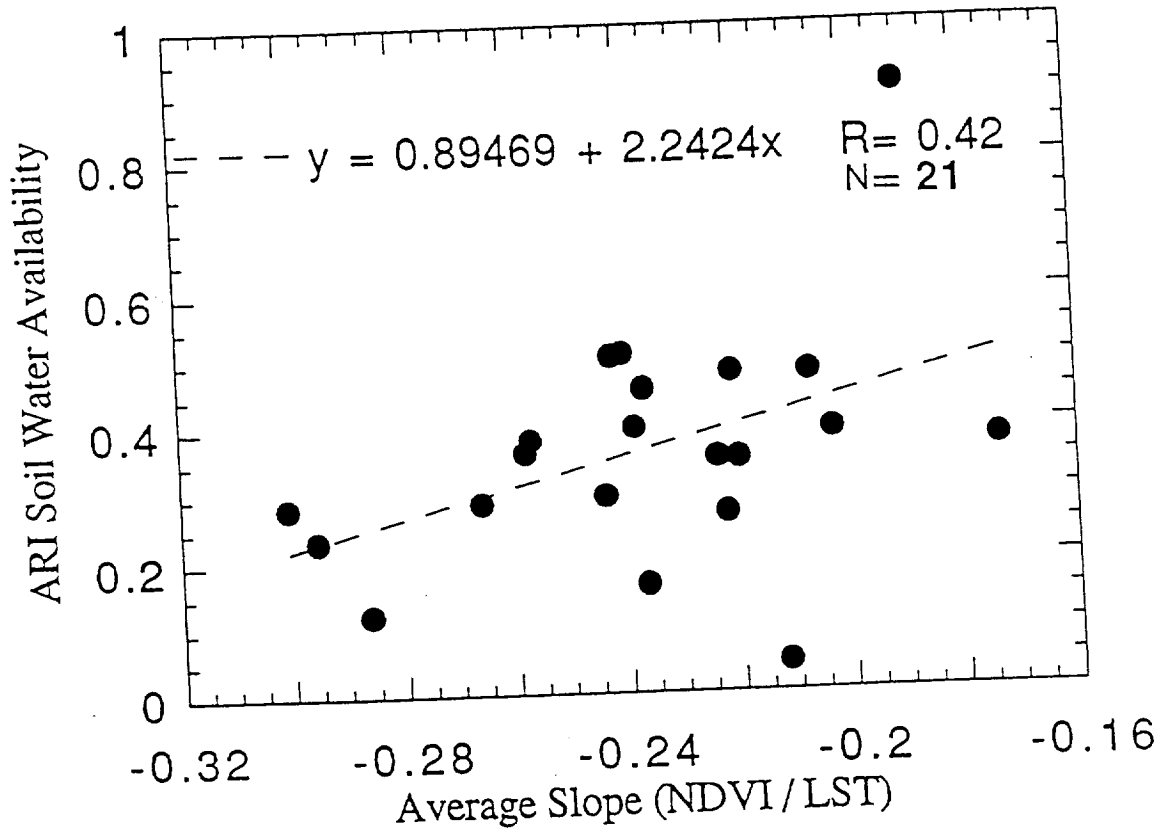


Fig. 22. Slopes of NDVI / LST scatter plots versus ARI - derived root zone soil moisture availability. Slopes were included only if a correlation better than -0.40 was achieved for the scatter diagram for both MAMS overpasses.

of NDVI vs. LST, although their results were based on only 8 data points (their Fig. 5). They speculated that this relationship may only be valid over forest canopies.

When the average NDVI / LST slopes (from both overpasses) are compared to MAMS / PBL regressed soil moisture availability (Fig. 23), the fit to the data becomes significantly better ( $R = 0.61$ ) than seen earlier with the ARI data (Fig. 22). However, unlike the previous comparison, the correlation is essentially unchanged ( $R = 0.60$ ; see Fig. 24) when just the second pass data are used. This suggests that as much as 37% of the variance of soil moisture may be explained by slopes of NDVI / LST. This result also shows more evidence of the PBL-regressed soil moisture values over the ARIs.

The superiority of the MAMS / PBL moisture results (cf. Figs. 23 and 24) over the ARI version is further evidence that the "ground truth" ARI-derived soil moisture values may be underestimated due to the complexity of the terrain and other reasons discussed earlier. Furthermore, they suggest that the MAMS LST-modeling approach may yield better estimates of root zone soil moisture over complex terrain.

Current results confirm the work of Jedlovec and Atkinson (1992) in that NDVI vs. LST slopes seem to be influenced by changes in solar insolation. Figure 25 shows the relationship between NDVI / LST slopes versus the exact time of the second aircraft overpass. A correlation of  $-0.59$  is found for all 26 sites; the slopes tend to steepen (in a negative sense) as time progresses. This solar influence needs to be removed if information about

PBL-Regressed Availability  
vs.  
NDVI / LST Slopes

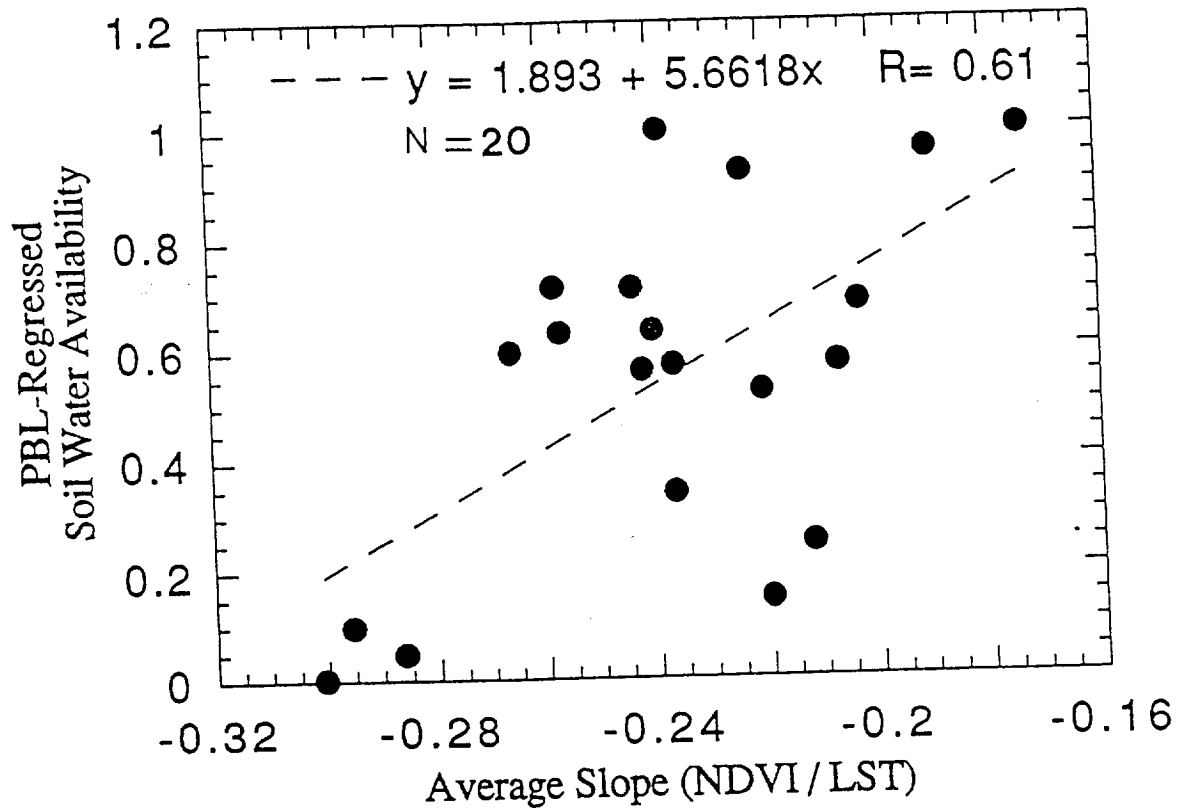


Fig. 23. Same as Fig. 22 but NDVI compared with PBL - regressed soil moisture from MAMS LST change slope ( $R = 0.61$ ).



PBL-Regressed Availability  
vs.  
NDVI / LST Slopes - 2nd Pass

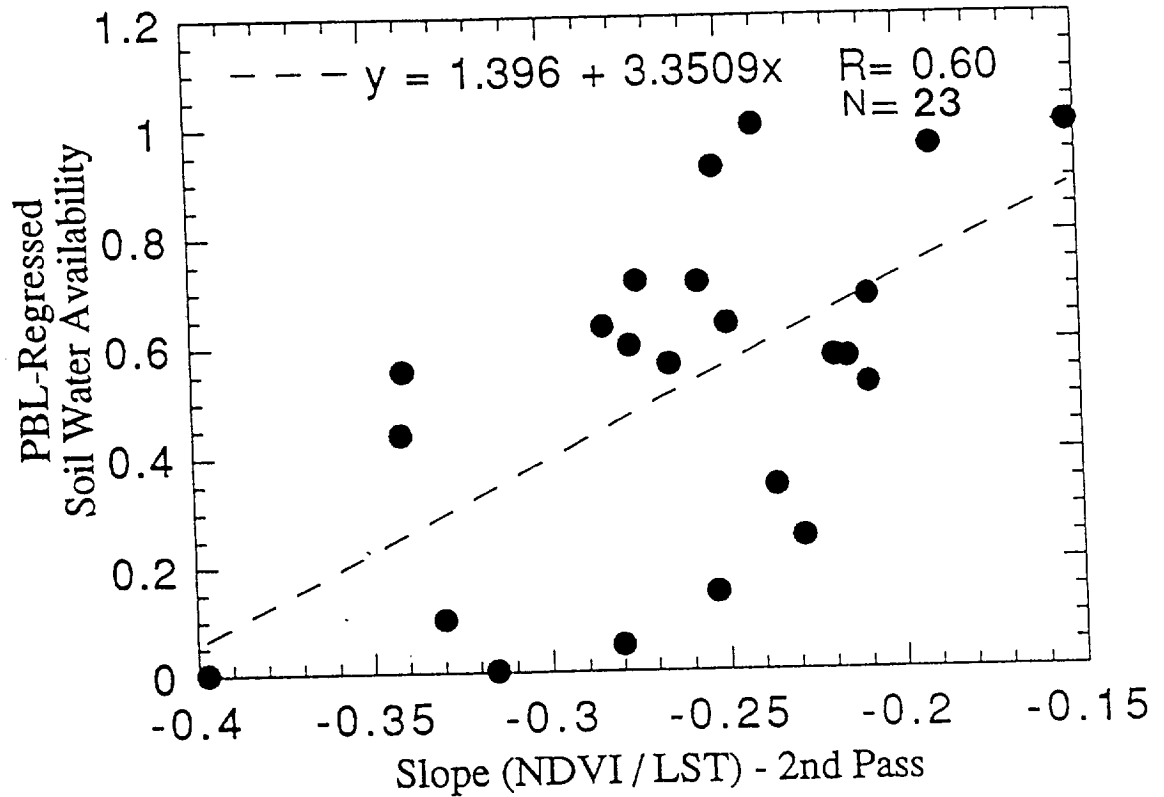


Fig. 24. PBL-regressed soil moisture compared to second pass NDVI only ( $R = 0.60$ ). Data for all sites are included regardless of terrain.

soil moisture is desired.

In summary, the NDVI / LST slope procedure for estimating soil moisture is inferior to the MAMS / PBL-regressed soil moisture technique. Furthermore, the regression method is superior to the ARI approach. The extrapolated bare soil temperature changes calculated as in Carlson *et al.* (1990) are better correlated with the regressed soil moisture values than those from the ARI. One can only question ARI as “ground truth” over complex terrain since no terrain parameterization is included in this method. The PBL-regressed technique shows more realistic relationships between soil moisture and LST changes when compared to previous in situ studies. Nonetheless, the NDVI vs. LST slope method is easily contaminated by sun-sensor-viewing geometry, and these solar influences must be removed in order to, at best, obtain only qualitative soil moisture information.

*e. Estimation of other parameters*

1. Maximum shelter air temperature

Another means of gauging the success of a soil moisture model is to compare PBL forecast and observed maximum shelter air temperatures. The equation for model calculated shelter temperature was given previously in (23). This comparison could only be made at 12 locations in the study area (not all locations recorded maximum and minimum temperatures). RMS values of maximum shelter air temperatures (forecast minus observed) are found to be slightly worse using the ARI input soil moisture profiles than

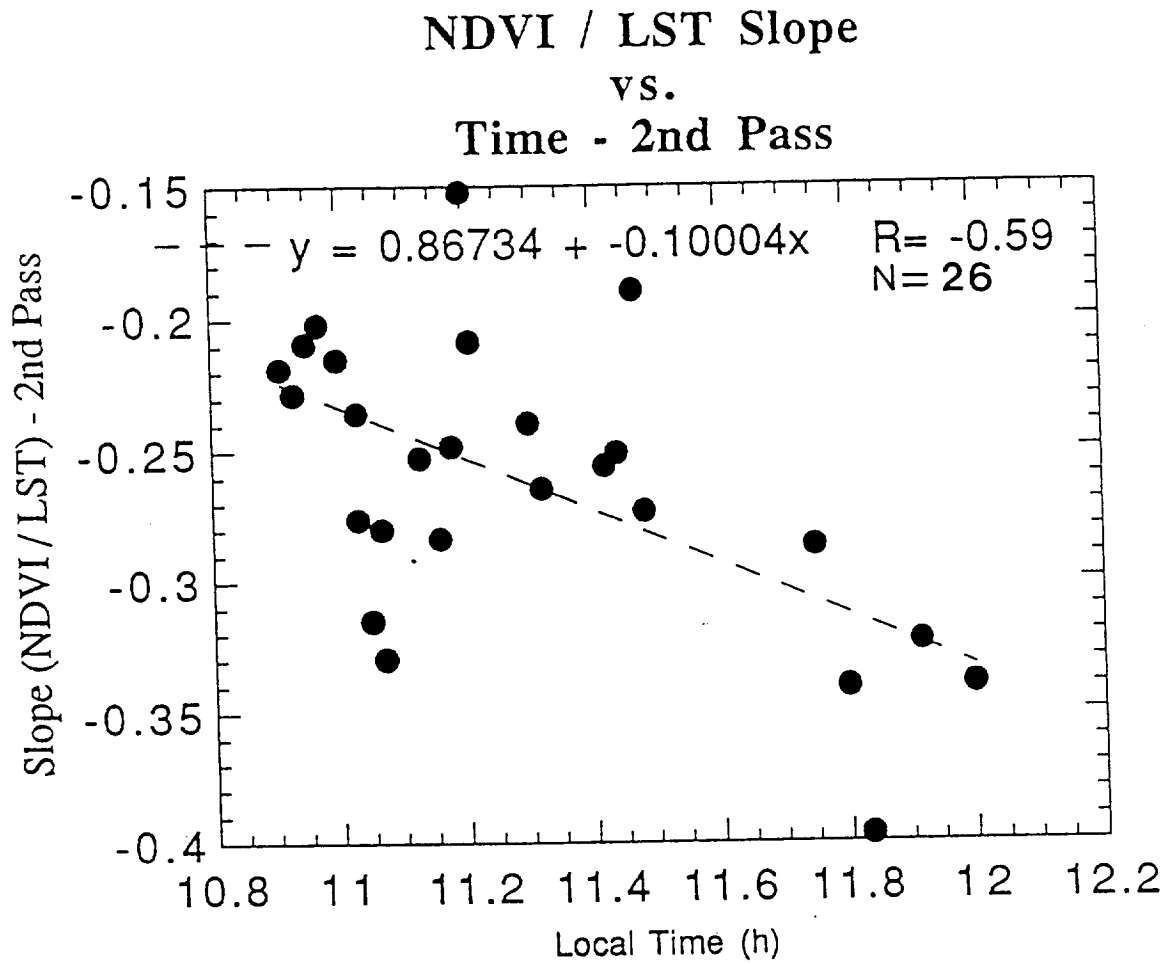


Fig. 25. Slope of NDVI / LST plots vs. local time of the second MAMS overpass ( $R = -0.59$ ).

using PBL-regressed soil moisture values. Specifically, an RMS maximum temperature difference of  $2.7^{\circ}\text{C}$  is found for the regression method, while the RMS maximum temperature difference is  $3.5^{\circ}\text{C}$  for the 2 layer ARI model. These results again suggest that the MAMS-LST regressed soil moisture values may be closer to ground truth than the ARI-derived values. Sensitivity tests show that when the deeper soil moisture is as much as 25% smaller (refer to ARI2Dry test above), the RMS differences are within  $1^{\circ}\text{C}$ , suggesting further that there is good reason to be skeptical of ARI deep layer soil moisture estimates.

## 2. MAMS LST vs. modeled LST from different input soil moisture

A comparison of modeled and MAMS-observed LSTs also suggests that the regressed soil moisture technique outperforms the ARI (with no explicit evaporation). The average difference (forecast minus observed) between MAMS LST and PBL modeled LST, with the regressed soil moisture values as input, is  $-2.3^{\circ}\text{C}$  (for all 34 sites). The same comparison with the ARI soil moisture as input is  $-4.7^{\circ}\text{C}$ . These LST differences between observed and forecast were calculated from both MAMS overpasses. However, the RMS values are only slightly better for regressed soil moisture ( $0.4^{\circ}\text{C}$  lower) than for the ARI input soil moisture values.

## 3. Mixing layer height

It is informative to compare model predicted mixing layer (ML) heights (with various input soil moisture) to observed heights. Surface fluxes are

critical to the evolution of the ML, and soil moisture is perhaps the most important forcing mechanism partitioning surface flux between sensible and latent components (Stull, 1988; Troen and Mahrt, 1986; Ookouchi *et al.*, 1984; Zhang and Anthes, 1982). Stull (1988) and Troen and Mahrt (1986), for example, have shown that the ML growth rate is related to SHflx and the amount of surface evaporation. During convectively active conditions and light background wind, the fastest ML growth rates occur over surfaces with largest SHflx. These large SHflxs, in turn, are associated with small soil moisture availability. Therefore, it may be possible to infer soil moisture from the observed ML growth rates (Troen and Mahrt, 1986).

A cloud shadow procedure was developed to estimate PBL heights (see chapter 3 for description of the procedure). Table 2 shows results of an error analysis of this technique. The errors for each factor were obtained by incrementing each variable in the ML calculation by an estimated observed error at each of the 30 sites. The estimated observed error was determined subjectively from PC McIDAS imagery measurement uncertainty. Absolute errors were found by computing each factor separately, while “turning off” the errors for all other factors. The percent differences in ML were calculated by dividing the ML estimates (with the errors included) by the ML calculation without the errors. Results show that the two greatest error sources are distance from the cloud edge to shadow edge ( $\Delta X$ ) and the variance in topography. Together, these two error sources (9.8 and 2.2%, respectively) account for over 99% of the total error (12.05%).

*Changes in mixed layer height* were calculated at the eighteen sites

where cumuliform clouds were observed within 5 km during *both* MAMS overpasses. The mean first pass ML height is  $1146 \pm 137$  m; for the second pass, the mean height is  $1579 \pm 189$  m. This corresponds to an average height increase of  $433 \pm 163$  m from the first to second pass, i.e., a mean time rate of change of  $541 \pm 204$  m h<sup>-1</sup> ! Height changes at individual sites range from -133.25 to 1380 m.

Since the average height increase of 433 m is greater than the worst case average error (163 m), the increase may be physically meaningful. However, cloud shadow ML height estimates most likely overestimate growth rates, especially the higher values, even though it is possible to obtain large growth rates in nature.

Table 2. Mean error contributions (%) to mixing layer heights estimated from cloud shadows.  $\Delta X$  is the error in horizontal distance from cloud edge to shadow, Lat is latitude, and Lon is longitude.

Error Source	Time	$\Delta X$	Lat	Lon	Nadir Angle	Topography Variance	TOTAL
	0.03	9.8	0.01	0.01	$10^{-6}$	2.2	12.05

For example, in a convectively active boundary layer, a decrease in surface dew point of 2°C together with an increase in air temperature of 4°C during a 2 h interval produces an increase in the convective condensation level (CCL) of about 350 m h<sup>-1</sup> (from a simple calculation on a Skew-T diagram).

Furthermore, Stull (1988) indicated that during the rapid growth phase of the mixed layer, these large ML growth rates ( $625 \text{ m h}^{-1}$ ) are not uncommon for convectively active MLs. For the eighteen locations where a calculation could be made, there is a correlation coefficient of  $-0.32$  between ARI root zone soil moisture availability and observed boundary layer growth rate. When the same comparison is made for MAMS / PBL regressed soil moisture values, an even poorer correlation ( $R = +0.06$ ) is realized. These poor results for both types of soil moisture suggest that the cloud shadow technique, when applied during rapid ML phase of boundary layer growth, is not suitable for estimating soil moisture. Synthetic Aperture Radar (SAR) will be carried on future satellite platforms and should yield better estimates of ML growth (NASA, 1987).

#### 4. Boundary layer clouds

Boundary layer clouds first form when the entrainment zone overlaps the lifting condensation level (LCL) zone (Stull, 1988). Rabin *et al.* (1990) and others have shown that clouds form preferentially over locations having large (small) Bowen ratio for relatively dry (moist) atmospheres. Additionally, horizontal variations in surface fluxes can produce “nonclassical mesoscale circulations” (NCMCs). These can generate clouds because their flow can be as strong as the sea breeze when there are large gradients in soil moisture (Ookouchi *et al.*, 1984; Segal and Arritt, 1992).

In addition to horizontal variations in soil moisture, NCMCs can be generated in response to horizontal variations in soil texture—even when there

is uniform moisture content (Zhang and Anthes, 1982). Other influences on NCMCs include contrasting surface land use, such as a forest next to farm land (Segal and Arritt, 1992). Such a case is evident from inspecting Fig. 12. The white features on the LST image at 1535 UTC correspond to the first cumiform clouds of the morning. Note that the initial cloud cover is located over the southwestern part of the image between a large area of relatively cool ground (forested area) and a large area of relatively warmer farm / range land. Irrigated farmland adjacent to dry land also produces gradients of surface flux (Segal and Arritt, 1992). However, there were no irrigation influences to consider for the present study (United States Dept. of Commerce, Census Bureau, 1980).

Terrain variations and associated slope flows compound the problem of diagnosing NCMCs and associated clouds that are due to soil moisture variations. Upslope flow can produce clouds regardless of the soil moisture, given the right terrain / atmospheric characteristics. Figure 26 shows an image of the 1 km resolution terrain data used in this study (United States Geological Survey), where brightest values correspond to highest elevations. Elevations range from 670 m over the northeastern part of the region to 50 m in the Tennessee River Valley. The method for obtaining these data was described in chapter 3. If locations of initial cloud development (Fig. 12) are compared to the terrain (Fig. 26), one notices that some areas of large terrain gradient are preferred regions for initial development. The organized cloud development over the southeastern part of the image near Gunterville Lake on the Tennessee River is especially evident.



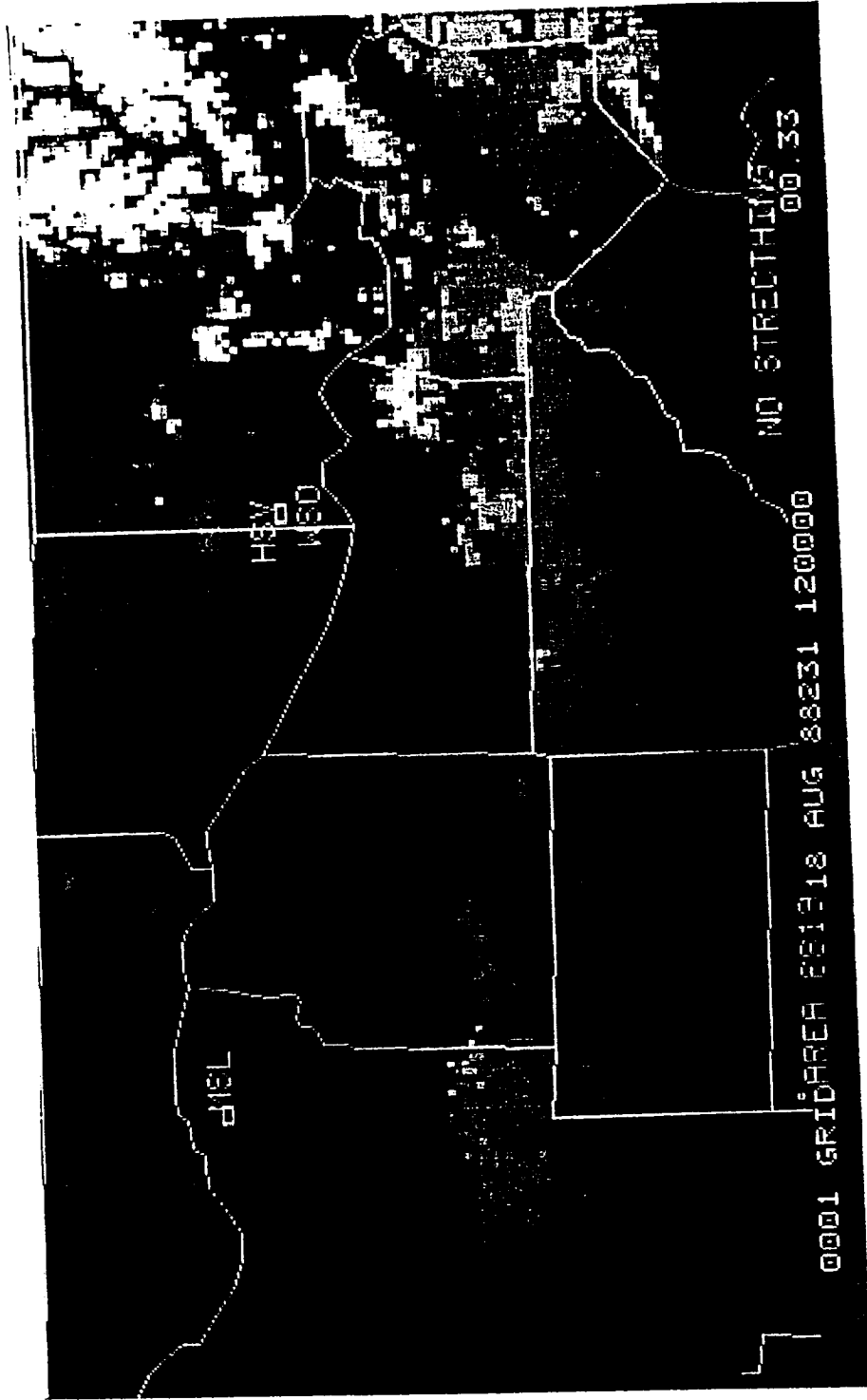


Fig. 26. Imaged terrain (1 km resolution) over the study region (data courtesy of United States Geological Survey). Brightest areas are highest elevations. Elevations range from 50 to 670 m.

To minimize the effects of topography on cloud development, I limit the current discussion to areas of flat terrain; i.e., those areas where the roughness parameter is less than 0.5 m (based on the Lettau (1969) method). Figure 27 shows the mean and standard deviation of cloud fraction as a function of time for all 41 sites with flat terrain. Mean values were obtained by averaging those GOES 1 km visible pixels exceeding a specified brightness value in a 10 x 10 km area centered over each site. Standard deviations were calculated from all sites at each time. The arrows in Fig. 27 correspond to the MAMS overpass times. The average onset time of clouds is near 1500 UTC, with the greatest average cloud fraction (34%) occurring near 1630 UTC. Cloud fraction decreases gradually between 1600 - 1900 UTC, and more rapidly thereafter. The rapid increase from 1500 to 1630 UTC indicates rapid overlapping of the entrainment and LCL zones. The boundary layer was undergoing rapid ML growth (Stull, 1988) during this time period, and this may explain why there was little relationship between soil moisture and ML growth (discussed above).

Forecast and observed cloud fractions were compared during the second MAMS overpass for flat terrain sites only. The second pass was chosen because many sites were clear during the first pass. The cloud model was described in chapter 3. Results indicate that both soil moisture models (ARI and PBL-regressed) input to the PBL model produce about the same differences between forecast and observed clouds. Figure 28 shows a histogram of differences (forecast - observed) between PBL-modeled and observed cloud fractions at 30 sites, using the MAMS-LST-regressed soil

### Observed Cloud Fraction vs. Time

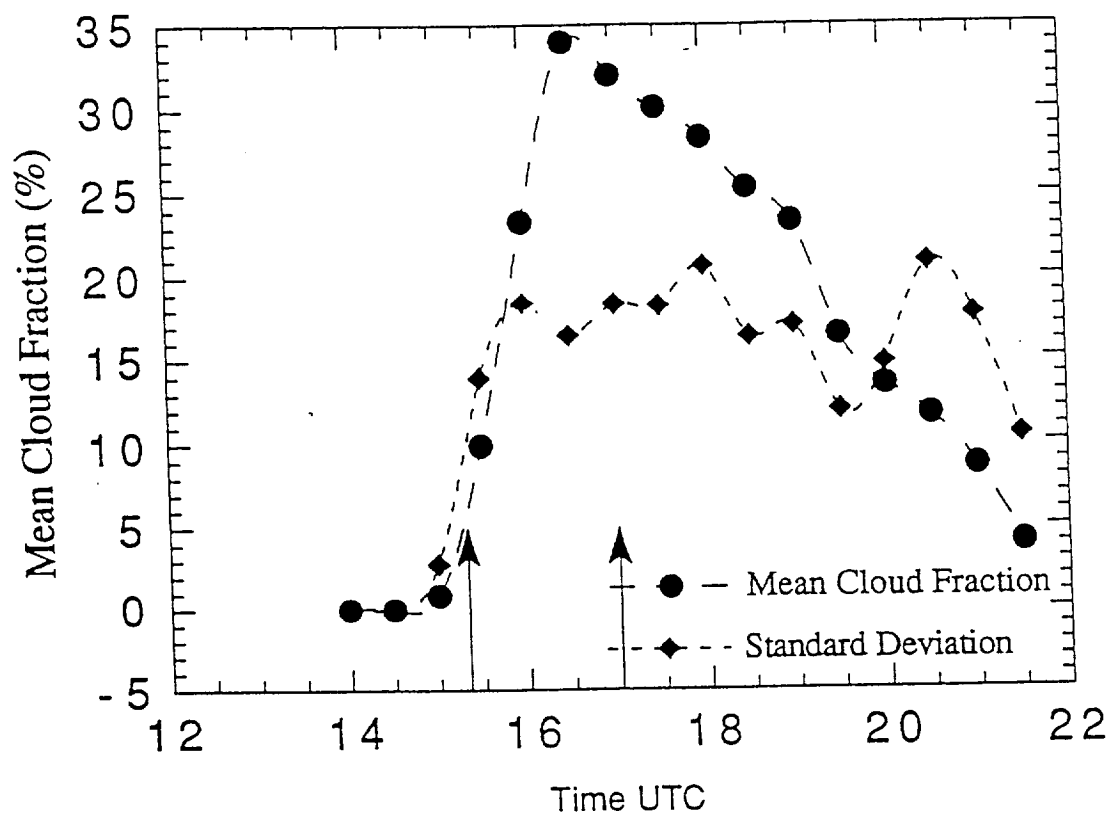


Fig. 27. Mean and standard deviation of cloud fractions (%) vs. time for all sites with minimum terrain influence. Arrows correspond to the times of MAMS overpasses.

moisture as input to the PBL model. A mean difference of -11.4% (RMS = 14%) is found; i.e., the PBL model generally underforecasts clouds. Similarly, a mean difference of -11.2% (RMS 14.5%) is found when the ARI-derived (with no explicit evaporation) soil moisture was used for the model runs (Fig. 29). This suggests that both soil moisture models perform about the same, as far as cloud forecasts are concerned.

These errors in cloud fraction forecasts are probably due to several factors. NCMCs probably occur over the region in response to small scale spatial variations of terrain, land use, SHflxs and LSTs. A one-dimensional PBL model cannot resolve these two- and three-dimensional circulations. Another source for uncertainty, alluded to previously, is selecting the proper potential evaporation threshold. Significant changes in PBL model cloud forecasts were noted with small changes in this parameter as the soil moisture approached this threshold (volumetric soil moisture = 0.20).

The PBL model currently is being modified to include parameterized mesoscale advection (Craig Sloan, personal communication, 1993). A new cloud model is also being tested (Ek and Mahrt, 1991). These changes should produce improved cloud forecasts in the future.

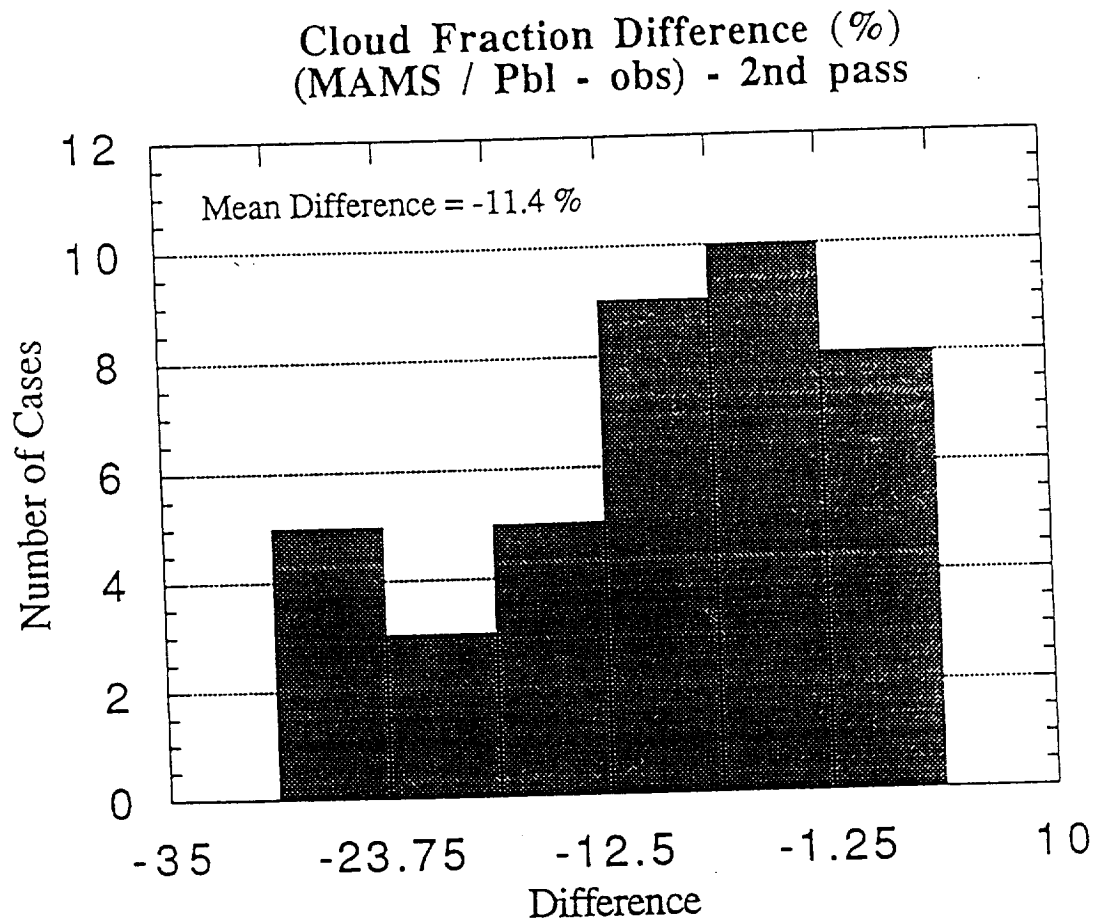


Fig. 28. Differences between forecast and observed cloud fraction (%) with MAMS-PBL regressed soil moisture input to the PBL model.

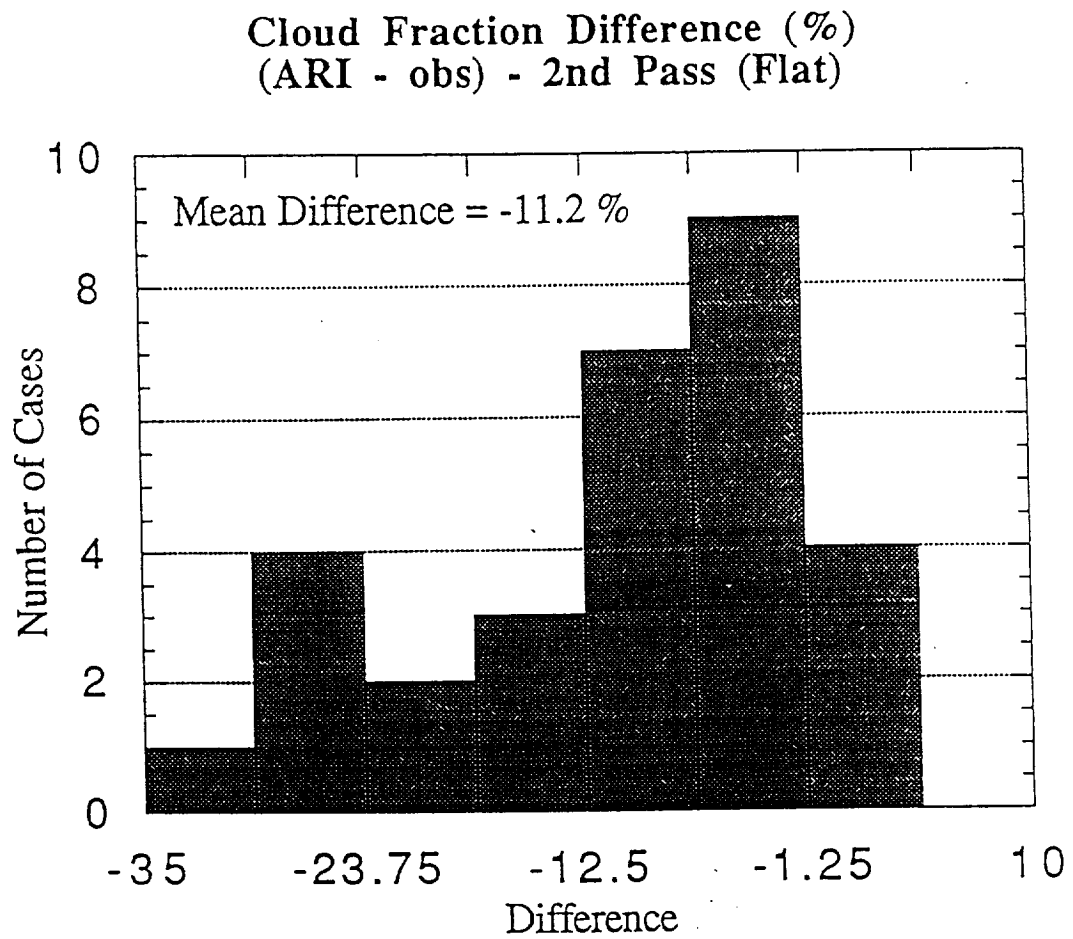


Fig. 29. Same as Fig. 28. except for ARI modeled soil moisture into PBL.

## 5. Conclusions

Three techniques for estimating soil moisture have been intercompared during a summer day over northern Alabama and southern Tennessee. In situ soil moisture data were not available for these calculations. These techniques were: 1) The antecedent retention index (ARI); often used as “ground truth” in the literature. Two forms of the ARI were considered, one with, and one without explicit evaporation physics, 2) A planetary boundary layer (PBL) model-regressed technique whereby 2 h land surface temperature (LST) differences during the morning were regressed onto soil moisture from a one-dimensional PBL model. Other parameters, such as vegetation amount, soil type, and terrain roughness were site specific for each location where a regression was calculated, 3) A technique that exploited the relationship between vegetation density and LST. Specifically, scatter diagrams of normalized difference vegetation index (NDVI) and LST were compared to both ARI-derived and PBL-model regressed soil water availability.

Data from the Multispectral Atmospheric Mapping Sensor (MAMS) were used to calculate LSTs. However, MAMS LSTs were compared to in situ soil temperatures from 15 locations in southern Tennessee and northeastern Mississippi. MAMS LSTs were shown to be within 1 to 2° C of observed values when they were extrapolated upward from the highest measured depth (2 cm). The LST equation developed in this investigation yielded temperatures that were generally 2 to 3° C warmer than those from a corresponding MAMS LST equation used in previous studies. One major difference between this study and previous ones using MAMS LSTs was the assumed emissivity. For the current study, an emissivity of 0.96 was assumed everywhere; earlier investigations used 1.00. A correlation of 0.96 was found between calculated LSTs and the input LSTs to the forward radiative transfer code.

Results from the soil moisture model intercomparison suggested that an indexed (ARI) approach may not be the best “ground truth” over complex terrain. Instead, a more sophisticated technique such as a PBL model-regressed method appeared to yield better estimates of soil moisture. Previous studies that have utilized indexed soil moisture as “ground truth” have been carried out over relatively flat terrain where they have been shown to give good estimates of soil moisture when compared to in situ data. The present study is carried out over terrain with significant variations, and this is one of the primary reasons that the author believes soil moisture was underestimated with the ARI technique. Another reason for uncertainty was the simplicity of the ARI formulation for different soils, and that assumed recession



coefficients probably were not representative of actual soil water recession. Surprisingly, including explicit evaporation physics into the ARI calculation exaggerated the underestimation of root zone (0 - 5 cm) soil moisture. It is believed that the evaporation reduction function,  $F$ , used in the ARI calculation including evaporation, was not sufficiently slowing the evaporation rate once the soil started to dry.

When a simple ARI model was run without explicit evaporation, a comparison between ARI soil water availability and 2 h morning LST changes was found to be sensitive to significant terrain influences. Specifically, a correlation of  $-0.63$  ( $R^2 = 0.40$ ) between LST differences and ARI values was found for sites with minimal terrain influence. When all sites were included in the regression, the correlation decreased to  $-0.50$  ( $R^2 = 0.25$ ).

When PBL model-regressed soil moisture availability was compared to 2 h morning LST changes, a much better correlation ( $R = -0.9$ ) was noted, regardless of terrain influences. In fact, the regression plot of PBL model-regressed soil water availability and LST differences was similar in slope and intercept to those of previous research which utilized both in situ soil temperatures and soil moisture data. When the soil moisture values from this method were compared to those from the ARI method, the ARI values were, on average, 23% drier than the PBL-regressed values.

LST forecasts provided further evidence of the model-regressed method's superiority. When both soil moisture models were input into the PBL model, forecast LSTs from PBL model-regressed soil moisture were closer to the MAMS observed LSTs than were ARI-derived values.

Specifically, mean differences between forecast and observed LSTs were  $-4.7^{\circ}\text{C}$  for the model runs with ARI input soil moisture, and  $-2.3^{\circ}\text{C}$  for runs with PBL-regressed soil moisture as input.

The NDVI / LST soil moisture technique was found to be easily contaminated by temporal changes in solar insolation. Although there was some relationship between soil moisture and the slopes of NDVI / LST scatter diagrams, a significant part of the variability ( $\sim 36\%$ ) of the NDVI / LST slopes could be explained by changes in solar insolation as well as other factors such as soil moisture, vegetation type and density. This solar contamination was noted by previous investigators. There was some correlation ( $R = 0.6$ ) between the slopes of these scatter diagrams and PBL-regressed soil water availability.

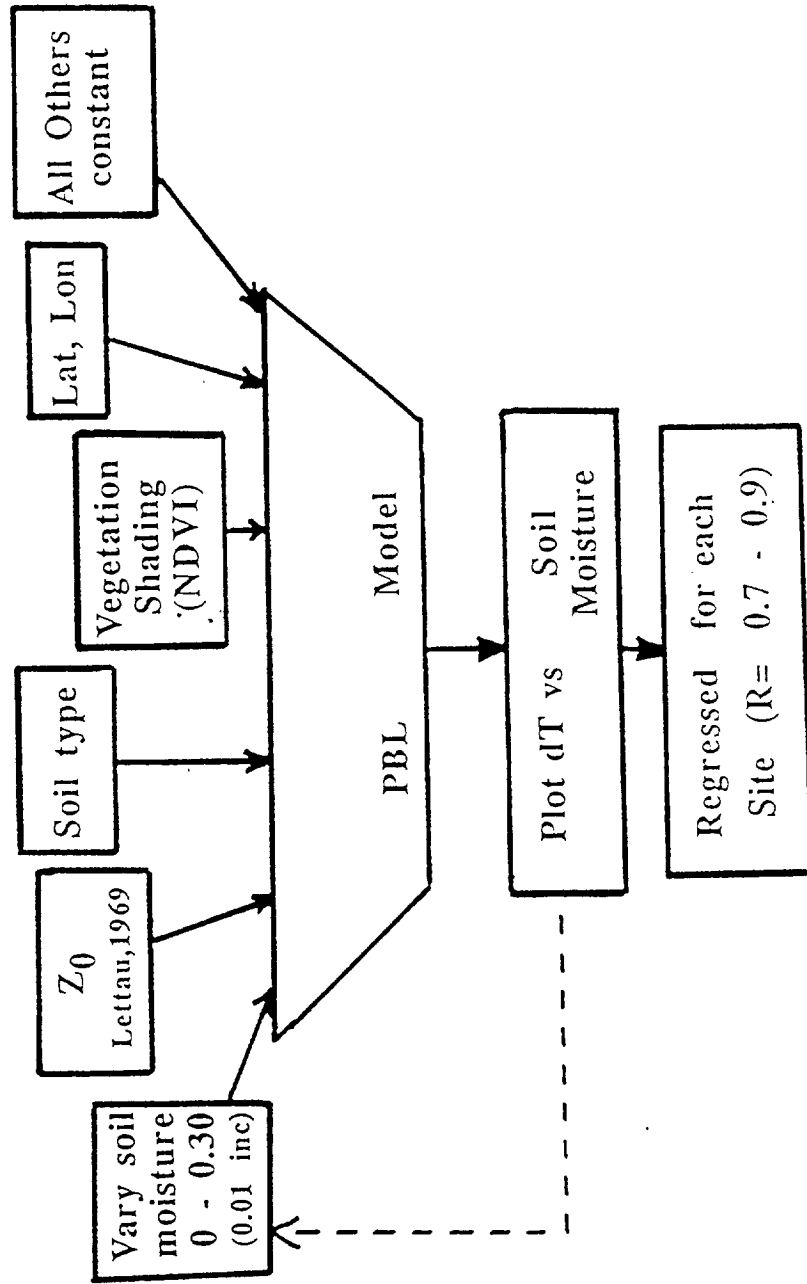
Both the ARI and the PBL-regressed soil moisture models led to similarly small errors ( $\sim 11\%$ ) in boundary layer cloud fractions computed by the PBL model. It is believed that processes not resolved by a one-dimensional model influenced cloud development over the area. These include ageostrophic circulations in response to contrasting land use and terrain gradients.

Finally, a technique for estimating mixed layer (ML) height was developed based on cloud shadows from visible MAMS imagery. It was hoped that there would be a relationship between the rate of ML growth and soil water availability, but this was not observed. Large errors were associated with the procedure, and the MAMS flights were made during the time of most rapid ML growth.

Certainly, in situ measurements afford the most accurate soil moisture data. However, in the absence of “true ground truth” data, the best soil moisture estimates over complex terrain appear to come from a more sophisticated PBL model when LST data are available. Furthermore, even with detailed soil physics, the PBL model used in this study can easily be run on an inexpensive personal computer.

APPENDIX A- Model Regression procedure flow chart for soil moisture estimation.

Model Regression Flow Chart



## REFERENCES

- Anthes, R.A., 1984: Enhancement of convective precipitation by mesoscale variation in vegetative covering in semiarid regions. *J. Clim. Appl. Meteor.*, **23**, 541-554.
- Arya, S.P.S., 1988: Introduction to Micrometeorology, Academic Press, London, 307 pp.
- Asrar, G., M. Fuchs, E.T. Kanemasu, and J.L. Hatfield, 1984: Estimating absorbed photosynthetic radiation and leaf index from spectral reflectance in wheat. *Agron. J.*, **76**, 300-306.
- Bellamy, J. C., 1949: Objective calculations of divergence, vertical velocity and vorticity. *Bull. Amer. Meteor. Soc.*, **30**, 45-49.
- Blanchard, B.J.M., M.J. McFarland, T.J. Schmugge, and E. Rhoades, 1981: Estimation of soil moisture with API algorithm and microwave emission. *Water Resour. Bull.*, **17**, 767-774.
- Borland, T.J., 1990: Short-range forecasting using a one-dimensional planetary boundary layer model. M.S. Thesis, Florida State University, 86 pp.
- Bradshaw, J. T., and H. E. Fuelberg, 1993: An evaluation of high-resolution interferometer soundings and their use in mesoscale studies. *J. Appl. Meteor.*, **32**, 522-538.
- Brest, C.L., and S.N. Goward, 1987: Deriving surface albedo measurements from narrow band satellite data. *Int. J. Remote Sensing*, **8**, 351-367.
- Brenner, S., C. -H. Yang, and K. Mitchell, 1984: The AFGL Global Spectral Model: Expanded Resolution Baseline Version. Rept. No. AFGL-TR-84-0308, Air Force Geophysics Laboratory, Hanscom AFB, 72 pp. [ADA160370].
- Brost, R.A., and J.C. Wyngaard, 1978: A model study of the stably stratified boundary layer. *J. Atmos. Sci.*, **8**, 1427-1440.
- Brutsaert, W., 1982: Evaporation into the Atmosphere, Dordrecht, Holland, 299 pp.

- Businger, J. A., J. C. Wyngaard, Y. Izumi and E. F. Bradley, 1971: Flux-profile relationships in the atmospheric surface layer. *J. Atmos. Sci.*, **28**, 181-189.
- Carlson, T.N., J.K. Dodd, S.G. Benjamin, and J.N. Cooper, 1981: Satellite estimation of the surface energy balance, moisture availability, and thermal inertia. *J. Appl. Meteor.*, **20**, 67-87.
- \_\_\_\_\_, E. M. Perry, and T.J. Schmugge, 1990: Remote estimation of soil moisture availability and fractional vegetation cover for agricultural fields. *Agri. and Forest Meteor.*, **52**, 45-69.
- Chang, J.T. and P.J. Wetzel, 1988: Effects of spatial variations of soil moisture and vegetation on the initiation of a local severe storm. Preprints, 15th Conference on Severe Local Storms: Boston, American Meteorological Society. J75-82.
- Choudhury, B., and B. Blanchard, 1983: Simulating soil water recession coefficients for agricultural watersheds. *Water Resour. Bull.*, **19**, 241-247.
- Dabberdt W.F., and P.A. Davis, 1978: Determination of energetic characteristics of urban rural surfaces in the greater St. Louis area. *Bound.-Layer Meteor.*, **14**, 105-121.
- Deardorff, J. W., 1966: The counter gradient heat flux in the lower atmosphere and in the laboratory. *J. Atmos. Sci.*, **23**, 503-506.
- Dunne, T. and L.B. Leopold, 1978: Water in Environmental Planning. Freeman, NY, p. 180.
- Ek, M. and L. Mahrt, 1989: OSU 1-D PBL Model User's Guide. Oregon State University, 120 pp.
- \_\_\_\_\_, 1991: A formulation for boundary-layer cloud cover. *Ann. Geophysicae*, **9**, 716-724.
- Garratt, J. R., 1992: Extreme maximum land surface temperatures. *J. Appl. Meteor.*, **31**, 1096-1105.
- Guillory, A.R., G.J. Jedlovec, and H.E. Fuelberg, 1993: A technique for deriving column-integrated water content using VAS split-window data. *J. Appl. Meteor.*, in press.

- Heymsfield, G. M., and R. Fulton, 1992: Modulation of SSM/I microwave soil radiances by rainfall. *Rem. Sens. Env.*, **39**, 187-202.
- Hoepner, W.A., and H.E. Fuelberg, 1992: The use of VAS retrievals for thunderstorm forecasting at the Kennedy Space Center. Preprints, 6th Conf. on Sat. Meteor. and Oceanog., American Meteorological Society, Atlanta, Ga., J31-J35.
- Holton, J.R., 1979: An Introduction to Dynamic Meteorology. 2nd ed., Academic Press, 391 pp.
- Holtslag, A. A. M., 1987: Surface fluxes and boundary layer scaling; models and applications. KNMI Sci. Rep. 87-02.
- \_\_\_\_\_, and A. C. M. Beljaars, 1989: Surface flux parameterization schemes; developments and experiences at KNMI. ECMWF Workshop on Parameterization of Fluxes and Land Surfaces, 24-26 Oct., 198, pp.121-147, Reading, England.
- \_\_\_\_\_, and E.I.F. De Bruijn, 1988: Applied modeling of the nighttime surface energy balance over land. *J. Appl. Meteor.*, **27**, 689-704.
- \_\_\_\_\_, and E.I.F. De Bruijn, 1990: A high resolution air mass transformation model for short-range weather forecasting. *Mon. Wea. Rev.*, **118**, 1561-1575.
- Idso, S. B., T. J. Schmugge, R. D. Jackson, R. J. Reginato, 1975: The utility of surface temperature measurements for the remote sensing of soil water status. *J. Geophys. Res.*, **80**, 3044-3049.
- Jackson, R.D., R. J. Reginato and S.B. Idso, 1977: Wheat canopy temperature: A practical tool for evaluating water requirements. *Water Res. Man.*, **13**, 651-656.
- Jedlovec, G. J., W.P. Menzel, R.J. Atkinson, G.S. Wilson, and J. Arvesen, 1986: The multispectral atmospheric mapping sensor (MAMS): Instrument description, calibration, and data quality. NASA Tech Memo. 86565, Marshall Space Flight Center, Huntsville, 37 pp., [Available NTIS].

- \_\_\_\_\_, K.B. Batson, R.J. Atkinson, C.C. Moeller, W.P. Menzel, and M.W. James, 1989: Improved capabilities of the Multispectral Atmospheric Mapping Sensor (MAMS) NASA Tech Memo. 100352, Marshall Space Flight Center, Huntsville, 72 pp. [Available NTIS].
- \_\_\_\_\_, 1987: Determination of atmospheric moisture structure from high resolution MAMS radiance data. Ph.D dissertation, Univ. of Wisconsin-Madison, 156 pp.
- \_\_\_\_\_, 1990: Precipitable water estimation from high-resolution split window radiance measurements. *J. Appl. Meteor.*, **29**, 863-877.
- \_\_\_\_\_ and Atkinson, 1992: Variability of geophysical parameters from aircraft radiance measurements (for FIFE). *J. Geophys. Res.*, **97**, 18913-18924.
- Kahle, A., 1977: A simple thermal model of the earth's surface for geologic mapping by remote sensing. *J. Geophys. Res.*, **82**, 1673-1680.
- Kasten, F. and G. Czeplak, 1980: Solar and terrestrial radiation dependent on the amount and type of cloud. *Solar Energy*, **24**, 177-189.
- Knabb, R.K., 1993: A sensitivity study analysis of the split-window variance technique for precipitable water estimation. M.S. Thesis, Florida State University, 81 pp.
- Lacis, A. A., and J. E. Hansen, 1974: A parameterization for the absorption of solar radiation in the earth's atmosphere, *J. Atmos. Sci.*, **31**, 118-133.
- Lahouari, B., 1992: Land surface processes and climate modeling. Ph. D. dissertation, Florida State University, 196 pp.
- Lettau, H., 1969: Note on aerodynamic roughness parameter estimation on the basis of roughness element description., *J. Appl. Meteor.*, **8**, 828-832.
- Linsley, R.K., M.A. Kohler, J.L.H. Paulhus, 1982: Hydrology for Engineers, 3rd ed., McGraw-Hill, 508 pp.
- Liou, K.-N., 1976: On the absorption, reflection and transmission of solar radiation in cloudy atmospheres. *J. Atmos. Sci.*, **33**, 798-805.



- Louis, J.-F., M. Tiedtke and J.F. Geleyn, 1982: A short history of the operational PBL parameterization of ECMWF. Workshop on Boundary layer parameterization, European Centre for Medium Range Weather Forecasts, Sheffield Park, Reading, Berks, U.K.
- Mahrt, L., 1987: Grid-averaged surface fluxes. *Mon. Wea. Rev.*, 115, 1550-1560.
- , and H. Pan, 1984: A two-layer model of soil hydrology. *Bound. Lay. Meteor.*, 29, 1-20.
- Mahrer, Y., and R. A. Pielke, 1978: The meteorological effect of the changes in surface albedo and moisture. *Isr. Meteorol. Res. Pap.*, 2, 55-70.
- McMillin, L. M., H.E. Fleming, and M.L. Hill, 1979: Atmospheric transmittance of an absorbing gas, a computationally fast and accurate transmittance model for absorbing gases with variable mixing ratios in inhomogeneous atmospheres. *Appl. Optics.*, 18, 1600-1606.
- Moeller, C. C., L. E. Gumley, K. I. Strabala, and W. P. Menzel, 1989: High resolution depiction of SST and SSC from MAMS data. Proceedings of Fourth Conference on Satellite Meteorology and Oceanography, American Meteorological Society, Boston, Mass., 208-212.
- NASA, 1987: From Patterns to Process: The Strategy of the Earth Observing system, E.O.S. Steering Committee Report, 2, 140 pp.
- NASA, 1988: GEMPAK user's guide, NASA / Goddard, 190 pp.
- Nemani, R.R., and S.W. Running, 1989: Estimation of regional surface resistance to evapotranspiration from NDVI, and thermal-IR AVHRR data. *J. Appl. Meteor.*, 28, 276-284.
- Njoku, E. G., and J. Kong, 1977: Theory for passive microwave remote sensing of near-surface soil moisture. *J. Geophys. Res.*, 82, 3108 - 3118.
- Ookouchi, Y., M. Segal, R. C. Kessler, and R. A. Pielke, 1984: Evaluation of soil moisture effects on the generation and modification of mesoscale circulations. *Mon. Wea. Rev.*, 112, 2281-2292.
- Orlanski, I., 1975: A rational subdivision of scales for atmospheric processes. *Bull. Amer. Meteor. Soc.*, 56, 527-530.

- Paltridge, G. W., and C. M. R. Platt, 1976: Developments in Atmospheric Science. Elsevier Scientific, Amsterdam, 318 pp.
- Pan, H. L., and L. Mahrt, 1987: Interaction between soil hydrology and boundary-layer development. *Bound. Lay. Meteor.*, **38**, 185-202.
- Rabin, R. M., S. Stadler, P.J. Wetzel, D.J. Stensrud, and M. Gregory, 1990: Observed effects of landscape variability on convective clouds. *Bull. Amer. Meteor. Soc.*, **71**, 272-280.
- Ramanathan, V., 1989: Cloud-radiative forcing and climate: Results from the earth radiation budget experiment, *Science*, **243**, pp. 57-63.
- Running, S. W. and R.R. Nemani, 1988: Relating seasonal patterns of the AVHRR vegetation index to simulated photosynthesis and transpiration of forests in different climates. *Rem. Sens. Environ.*, **24**, 347-367.
- Ruscher, P. H., 1988: Parameterization of the very stable boundary layer in a simple model. *Proceedings, Eighth Symposium on Turbulence and Diffusion*, San Diego, CA; Amer. Meteor. Soc., 299-301.
- Satterlund, D. R., 1979: Improved equation for estimating longwave radiation from the atmosphere. *Water Resources Res.*, **15**, 1649-1650.
- Saxton, K.E. and A.T. Lenz, 1967: Antecedent retention indexes predict soil moisture. *J. Hydraulics Div. Proc. Am. Soc. Civil Engr.*, **H44**, 228-241.
- Segal, M., and R.W. Arritt, 1992: Nonclassical mesoscale circulations caused by surface sensible heat-flux gradients. *Bull. Amer. Meteor. Soc.*, **73**, 1593-1604.
- Sellers, P.J., S.I. Rasool, and H.-J. Bolle, 1990: A review of satellite data algorithms for studies of the land surface. *Bull. Amer. Meteor. Soc.*, **71**, 1429-1447.
- \_\_\_\_\_, 1985: Canopy reflectance, photosynthesis and transpiration. *Int. J. Remote Sensing*, **6**, 1335-1372.
- Slingo, J.M., 1980: A cloud parameterization scheme derived from GATE data for use with a numerical model. *Quart. J. Roy. Met. Soc.*, **106**, 747-770.

- Soer, G.J.R., 1977: The tergra model, a mathematical model for the simulation of daily behavior of crop surface temperature and actual evapotranspiration. Netherlands Technical Memo. Series, Publ. No. 46, Delft, The Netherlands.
- \_\_\_\_\_, 1980: Estimation of regional evapotranspiration and soil moisture conditions using remotely sensed crop surface temperatures. *Remote Sensing Environ.*, **9**, 27-45.
- Schmugge, T., 1978: Remote sensing of surface soil moisture. *J. Appl. Meteor.*, **17**, 1549-1557.
- Stull, R. B., 1988: Boundary Layer Meteorology, Kluwer, The Netherlands, 666 pp.
- Troen, I. B. and L. Mahrt, 1986: A simple model of the atmospheric boundary layer; sensitivity to surface evaporation. *Bound. Layer Meteor.*, **37**, 129-148
- Tucker, C.J., 1979: Red and photographic infrared linear combinations for monitoring vegetation. *Rem. Sens. Environ.*, **8**, 127-150.
- Wetzel, P.J., D. Atlas, and R. H. Woodward, 1984: Determining soil moisture from geosynchronous satellite infrared data: A feasibility study. *J. Clim. Appl. Meteor.*, **23**, 375-391.
- \_\_\_\_\_, and R.H. Woodward, 1987: Soil moisture estimation using GOES VISSR IR data: A case study with a simple statistical method. *J. Clim. Appl. Meteor.*, **26**, 107-117.
- Yan, H. and R. A. Anthes, 1988: The effect of variations in surface moisture on mesoscale circulations. *Mon. Wea. Rev.*, **116**, 192-208.
- Zhang, H. Y. , 1990: The spectral variation of surface emissivity within the 8-12 micrometer "window", M. S. Thesis, Univ. of Wis., Madison, 70 pp. (Available University Microfilms International, Ann Arbor, MI)
- Zhang, D.L., and R. A. Anthes, 1982: A high resolution model of the planetary boundary layer-sensitivity tests and comparisons with SESAME-79 data. *J. Appl. Meteor.*, **21**, 1594-1609

## BIOGRAPHICAL SKETCH

Michael W. Nichols was born in Arlington, Virginia on July 25, 1959. He graduated from Rockville High School in Rockville, Maryland in 1977. He obtained his Bachelor of Science in Meteorology from Pennsylvania State University in November, 1981. He was employed as a Radio and Television Production Meteorologist in Washington, D.C., and then as a Television Meteorologist from 1984 to 1988 in the Huntington / Charleston, West Virginia area. He is married to the former Jean Ann Cook of Charleston, West Virginia and is the father of Jessica Mae, born 15 October 1987.